



UCTEA Turkish Chamber of Civil Engineers
TMMOB İnşaat Mühendisleri Odası

Turkish Journal of Civil Engineering

formerly
Teknik Dergi

Volume 35
Issue 2
March 2024



Turkish Journal of Civil Engineering (formerly Teknik Dergi) Publication Principles

Turkish Journal of Civil Engineering (TJCE), a non-profit, open access scientific and technical periodical of UCTEA Chamber of Civil Engineers, publishes papers reporting original research work and major projects of interest in the area of civil engineering. TJCE annually publishes six issues and is open to papers in English and Turkish. It should be noted that TJCE (formerly, Teknik Dergi/ Technical Journal of Turkish Chamber of Civil Engineers) is being published regularly for more than 30 years since 1990. Main publication principles of TJCE are summarized below:

1. Articles reporting original scientific research and those reflecting interesting engineering applications are accepted for publication. To be classified as original, the work should either produce new scientific knowledge or add a genuinely new dimension to the existing knowledge or develop a totally new method or substantially improve an existing method.
2. Articles reporting preliminary results of scientific studies and those which do not qualify as full articles but provide useful information for the reader can be considered for publication as technical notes.
3. Discussions received from the readers of the published articles within three months from publication are reviewed by the Editorial Board and then published together with the closing remarks of the author.
4. Manuscripts submitted for publication are evaluated by two or three reviewers unknown to the authors. In the light of their reports, final decision to accept or decline is taken by the Editorial Board. General policy of the Board is to get the insufficient manuscripts improved in line with the reviewers' proposals. Articles that fail to reach the desired level are declined. Reasons behind decisions are not declared.
5. A signed statement is taken from the authors, declaring that the article has not been published as a "journal article or book chapter". In case the Editorial Board is in the opinion that the article has already been published elsewhere with minor changes or suspects plagiarism or a similar violation of ethics, then not only that article, but none of the articles of the same authors are published.
6. Papers reporting works presented as conference papers and developed further may be considered for publication. The conference it was presented to is given as a footnote in the first page.
7. Additionally, a document signed by all authors, transferring the copyright to UCTEA Chamber of Civil Engineers is submitted together with the manuscript.



UCTEA Turkish Chamber of Civil Engineers
TMMOB İnşaat Mühendisleri Odası

Turkish Journal of Civil Engineering

formerly
Teknik Dergi

Volume 35
Issue 2
March 2024



UCTEA Turkish Chamber of Civil Engineers
TMMOB İnşaat Mühendisleri Odası

Necatibey St. No: 57, Kızılay 06440 Ankara, Turkey

Tel: +90.312.294 30 00 - Faks: +90.312.294 30 88

E-mail: imo@imo.org.tr - www.imo.org.tr

Publisher (Sahibi):

Taner YÜZGEÇ

On behalf of UCTEA Turkish Chamber of Civil Engineers

Administrative Officer (Yazı İşleri Müdürü):

Özer AKKUŞ

Volume 35 - Issue 2 - March 2024 (*Cilt 35 - Sayı 2 - Mart 2024*)

Published bi-monthly. Local periodical. (*İki ayda bir yayınlanır, yerel süreli yayın*)

Date of Print: January 1, 2024 (*Baskı Tarihi: 1 Mart 2024*)

Number of copies: 800 (*800 adet basılmıştır*)

Quotations require written approval of the Editorial Board.

(*Yayın Kurulunun yazılı onayı olmaksızın alıntı yapılamaz.*)

ISSN: 2822-6836

Turkish Journal of Civil Engineering (formerly Teknik Dergi) is indexed by

- Science Citation Index Expanded
- Scopus
- Journal Citation Reports / Science Edition
- Engineering Index
- Concrete Abstracts (American Concrete Institute)
- National Technical Information Service (US NTIS)
- CITIS
- Ulrich's International Periodical's Directory
- Google Scholar
- TR Index

Turkish Journal of Civil Engineering (formerly Teknik Dergi) is a peer reviewed open access periodical publishing papers of original research and interesting practice cases. It addresses both the research community and the practicing engineers.

Printed by (Baskı):

Ziraat Gurup Matbaacılık Ambalaj San. Tic. A.Ş.

Bahçekapı Mah. 2534 Sok. No: 18 Şaşmaz, Etimesgut / Ankara

Tel: 0.312.384 73 44 - Faks: 0.312.384 73 46

Turkish Journal of Civil Engineering (formerly Teknik Dergi)

Editor-in-Chief:

Alper İLKİ

Editors:

İsmail AYDIN

Özer ÇİNİCİOĞLU

Metin GER

Gürkan Emre GÜRCANLI

Kutay ORAKÇAL

İsmail ŞAHİN

Özkan ŞENGÜL

Tuğrul TANKUT

Kağan TUNCAY

Ufuk YAZGAN

Emine Beyhan YEĞEN

Drafting Languge Check:

İsmail AYDIN

Özer ÇİNİCİOĞLU

Metin GER

Polat GÜLKAN

Gürkan Emre GÜRCANLI

İsmail ŞAHİN

Özkan ŞENGÜL

Mehmet UTKU

Emine Beyhan YEĞEN

Editorial Assistant:

Çağlar GÖKSU AKKAYA

Secretary:

Cemal ÇİMEN

Advisory Board:

Prof. M. Aral, USA

Prof. D. Arditı, USA

Prof. A. Aydilek, USA

Prof. K. Beyer, Switzerland

Prof. N. Çatbaş, USA

Prof. M. Çetin, USA

Prof. M. Dewoolkar, USA

Prof. T. Edil, USA

Prof. K. Elwood, New Zealand

Prof. M. Fardis, Greece

Prof. G. Gazetas, Greece

Prof. P. Gülkan, Türkiye

Prof. J. Han, USA

Prof. I. Hansen, Netherlands

Prof. T. Hartmann, Germany

Prof. F. Imamura, Japan

Prof. T. Kang, Korea

Prof. K. Kusunoki, Japan

Prof. S. Lacasse, Norway

Prof. R. Al-Mahaidi, Australia

Prof. K. Özbay, USA

Prof. H. Özer, USA

Prof. G. Özmen, Türkiye

Prof. S. Pampanin, Italy

Prof. A. J. Puppala, USA

Prof. M. Saatçioğlu, Canada

Prof. C. Santamarina, Saudi Arabia

Prof. S. Sheikh, Canada

Prof. E. C. Shin, South Korea

Prof. J. Smallwood, South Africa

Prof. M. Sümer, Türkiye

Dr. H. A. Şentürk, Türkiye

Dr. S. S. Torisu, Japan

Prof. E. Tutumluer, USA

Prof. M. Tümer, USA

Reviewers:

This list is renewed each year and includes reviewers who served in the last two years of publication.

Şükran AÇIKEL	Ali Fırat ÇABALAR	Saadet Gökçe GÖK	Özgür KURÇ	Haluk SUCUOĞLU
Kamil Bekir AFACAN	Barlas Özden	Tansu GÖKÇE	Hasan KURTARAN	Erol ŞADOĞLU
Bülent AKBAŞ	ÇAĞLAYAN	Serdar GÖKTEPE	Murat KURUOĞLU	Yuşa ŞAHİN
Sami Oğuzhan AKBAŞ	Ferit ÇAKIR	Semih GÖNEN	Akif KUTLU	Zekai ŞEN
Zühal AKBAY ARAMA	Melih ÇALAMAK	Rahmi GÜÇLÜ	Merih KÜÇÜKLER	Burak SENGÖZ
Rıfat AKBİYİKLİ	Gülben ÇALIŞ	Ali GÜL	Abdullah KÜRKCÜ	Gülüm TANIRCAN
Sarven AKCELYAN	Umut ÇALIŞKAN	Fazlı Erol GÜLER	Todd LİTMAN	Serhan TANYEL
Burcu AKÇAY	Süheyla Pelin	İlgin GÜLER	Fağih MAARİF	Mucip TAPAN
ALDANMAZ	ÇALIŞKANELLİ	M. Fethi GÜLLÜ	Müslüm Murat MARAŞ	Ergin TARI
Cihan Taylan AKDAĞ	Mehmet Alper ÇANKAYA	Adil GÜLTEKİN	Halit Cenani MERTOL	Yüksel TAŞDEMİR
Bekir AKGÖZ	Serdar ÇARBAŞ	Fırat GÜMGÜM	Mahmoud MIARI	Ali Şahin TAŞLIGEDİK
Cem AKGÜNER	Dilay ÇELEBİ	Gürkan GÜNAY	Mehmet Murat MONKUL	Hasan TATLI
Fevziye AKÖZ	Tevfik Kutay	Taylan GÜNAY	Nihat MOROVA	Gökmen TAYFUR
Erkan AKPINAR	ÇELEBİOĞLU	Murat GÜNAYDIN	Yetiş Şazi MURAT	Serdal TERZİ
Muhammet Vefa	Ahmet Ozan ÇELİK	Samet GÜNER	Sepanta NAİMİ	Berrak TEYMUR
AKPINAR	Oğuz Cem ÇELİK	Burcu GÜNEŞ	Salih OFLUOĞLU	Hüseyin Onur TEZCAN
Atakan AKSOY	Ozan Cem ÇELİK	Oğuz GÜNEŞ	Fuad OKAY	Mesut TİGDEMİR
Hafzullah AKSOY	Hilmi Berk ÇELİKOĞLU	Mehmet Şükri GÜNEY	Didem OKTAY	Salih TİLEYLİOĞLU
Tülay AKSU ÖZKUL	Kemal Önder ÇETİN	Tuba GÜRBÜZ	Derviş Volkan OKUR	Onur Behzat TOKDEMİR
Uğurhan AKYÜZ	Mecit ÇETİN	BÜYÜKKAYIKÇI	Sezan ORAK	Nabi Kartal TOKER
Alper ALDEMİR	Elif ÇİÇEK	Aslı Pelin GÜRGÜN	Engin ORAKDÖĞEN	Ali TOPAL
Cenk ALHAN	Emin ÇİFTÇİ	Tefarruk HAKTANIR	Şeref ORUÇ	Cem TOPKAYA
Gülşay ALTAY	Hüseyin ÇİLSALAR	Soner HALDENBİLEN	Okan ÖNAL	Kamil TOSUN
Sinan ALTIN	Erdal ÇOKÇA	Murat HAMDERİ	Akin ÖNALP	FELEKOĞLU
Adlen ALTUNBAŞ	Semra ÇOMU	Ingo A. HANSEN	Bihra ÖNÖZ	Gökçe TÖNÜK
Yalçın ALVER	Turgay ÇOŞGUN	Umut HASGÜL	Cihan ÖSER	Erkan TÖRE
Mustafa M. ARAL	Atilla DAMCI	Emre HASPOLAT	Yiğit ÖZÇELİK	Kemal Dirgen TÖZER
Davit ARDITI	Yakup DARAMA	Mustafa HATİPOĞLU	Gökhan ÖZDEMİR	Nursu TUNALIOĞLU
Yalın ARICI	Kutlu DARILMAZ	Lucas HOGAN	Zuhal ÖZDEMİR	Gürsoy TURAN
Deniz ARTAN İLTER	Tayfun DEDE	Zeynep İŞİK	Murat ÖZEN	Hasan Nuri
Deepankar Kumar	Cem DEMİR	Sabriye Banu İKİZLER	Pelin ÖZENER	TÜRKMEÑOĞLU
ASHISH	Selçuk DEMİR	Okan İLHAN	Ekin ÖZER	Cüneyt TÜZÜN
Ayşegül ASKAN	Uğur DEMİR	Erol İSKENDER	Hasan ÖZER	Eren UÇKAN
GÜNDOĞAN	Ender DEMİREL	Medine İSPİR ARSLAN	Hakkı Oral ÖZHAN	Latif Onur UĞUR
Ali Osman ATAHAN	Mehmet Cüneyd	Recep İYİŞAN	Mehmet Fatih ÖZKAL	Mehmet Baran ULAK
Hakan Nuri ATAHAN	DEMİREL	Nuray Işık KABDAŞLI	Zeynep Huri ÖZKUL	Dilay UNCÜ
Güzide ATASOY ÖZCAN	Murat DİCLELİ	Volkan KALPAKÇI	BİRGÖREN	Berna UNUTMAZ
Ali Osman ATEŞ	Seyyit Ümit DİKMEN	Muhammet KAMAL	Aşkın ÖZOCAK	Mehmet UTKU
Özgür AVŞAR	Ahmet Anıl DINDAR	Reza KAMGAR	Sadık ÖZTOPRAK	Volkan Emre UZ
Cem AYDEMİR	Mustafa DOĞAN	Hakan Alper	Turan ÖZTURAN	İbrahim Mert UZUN
Metin AYDOĞDU	Marco DOMANESCHİ	KAMİLOĞLU	Gözde Başak ÖZTÜRK	Deniz ÜLGEN
Ülker Güner BACANLI	Gökhan DÖK	Elif Çağda KANDEMİR	Mustafa ÖZUYSAK	Mehmet Barış Can
Selim BARADAN	Cemalettin DÖNMEZ	Tanay KARADEMİR	Tolga Yılmaz	ÜLKER
Eray BARAN	İsmail DURANYILDIZ	Hüseyin Faruk	ÖZÜDOĞRU	Yurdanur ÜNAL
Özgür Uğraş BARAN	Cengiz DÜNDAR	KARADOĞAN	Atilla ÖZÜTOK	Ali ÜNAY
Türkay BARAN	Nurhan ECEMİŞ ZEREN	Ümit KARADOĞAN	Nilüfer ÖZYURT	Cüneyt VATANSEVER
Efe BARBAROS	Özgür EKİNCİOĞLU	Mustafa Erkan	ZİHNİOĞLU	Ahmet YAKUT
Bekir Oğuz BARTIN	Serkan ENGİN	KARAGÜLER	Erhan Burak PANCAR	Erkut YALÇIN
Zeynep BAŞARAN	Murat Altuğ ERBERİK	Halil KARAHAAN	Seval PINARBAŞI	Aslı YALÇIN
BUNDUR	Ali ERCAN	Oğuz KAYABAŞI	ÇUHADAROĞLU	Mustafa Sinan YARDIM
Mustafa Gökçe	Barış ERDİL	İlker KAZAZ	Elişan Filiz PİROĞLU	Anıl YAZICI
BAYDOĞAN	Sinan Turhan ERDOĞAN	Saeid KAZENZADEH	Bora POLATSU	Shehata E. Abdel
Cüneyt BAYKAL	Şakir ERDOĞDU	AZAD	RAHEEM	Gökhan YAZICI
Mehmet BERİLGEN	Esin ERGEN PEHLEVAN	Mustafa Kubilay	KELEŞOĞLU	Halit YAZICI
Katrin BEYER	Yusuf Çağatay ERŞAN	Elçin KENTEL	Selçuk SAATÇI	Cem YENİDOĞAN
Niyazi Özgür BEZGİN	Kağan ERYÜRÜK	Hadi	Selman SAĞLAM	Mehmet YETMEZ
Ozan BİLAL	Esra Ece ESELLER	KHANBAZADEH	Mehmet SALTAN	İrem Zeynep YILDIRIM
Senem BİLİR	BAYAT	Ufuk KIRBAŞ	Altuğ SAYGILI	Berivan YILMAZER
MAHÇİÇEK	Tuğba ESKİŞAR TEFÇİ	Serdar SELAMET	Nuri SERTESER	POLAT
İlknur BOZBEY	Burak FELEKOĞLU	Veyssel Şadan Özgür	KIRCA	Ercan YÜKSEL
Ali BOZER	Mahmut FIRAT	Mehmet Amil	KIZILASLAN	Yeliz YÜKSELEN
Mehmet Bakır BOZKURT	Onur GEDİK	Esat Selim KOCAMAN	Salih KOÇAK	AKSOY
Zafer BOZKUŞ	Abdullah GEDİKLİ	Mete KÖKEN	Baha Vural KÖK	Ahmet Şahin ZAİMOĞLU
Zekai CELEP	Ergun GEDİZLİOĞLU		Serdar SOYÖZ	Abdullah Can ZÜLFİKAR
Cihan CENGİZ	Ahmet Talha GEZGİN		Rifat SÖNMEZ	
Halim CEYLAN	Sadık Can GİRGIN		Tayfun Altuğ SÖYLEV	
Joao Ramoa CORREIA	Zehra Canan GİRGIN			

CONTENTS

RESEARCH ARTICLE

- Modeling of Asphalt Pavement Surface Temperature for Prevention of Icing on the Surface 1
Hüseyin AKBULUT, Lale ATILGAN GEVREK, Murat AY
- Application of Endurance Time Method in Seismic Assessment of RC Frames Designed by Direct Displacement-Based Procedure 23
Nisar Ahmad KARIMZADA, Amir SHIRKHANI, Engin AKTAŞ
- From Cut-in to Qanats - Ancient Groundwater Extraction Techniques 65
Hartmut WITTENBERG, Hafzullah AKSOY
- A Quantitative Investigation on the Effects of Flexure-Dominated Reinforced Concrete Column Characteristics on the Dissipated Energy 87
Ziya MÜDERRISOĞLU, Ahmet Anıl DINDAR, Ali BOZER, Hasan ÖZKAYNAK, Ahmet GÜLLÜ, Bilal GÜNGÖR, Furkan ÇALIM, Serkan HASANOĞLU
- Corrosion Rate-Based Adjustment of Plastic Hinge Parameters of Corroded RC Elements 103
Mustapha BENREDOUANE, Nouredine BOURAHLA, Anouar GHODBANE, Hala KHALFAOUI
- Tabakalı Zeminlerdeki Yüzeysel Temel Davranışının Nümerik ve Analitik Olarak İncelenmesi 125
Erdal UNCUOĞLU

TECHNICAL NOTE

- Farklı Oturmalar Nedeniyle Eğik Konuma Gelmiş Binanın Jet-Grout Yöntemiyle Doğrultulup Desteklenmesi 157
Sadık KÖSEOĞLU

Modeling of Asphalt Pavement Surface Temperature for Prevention of Icing on the Surface

Hüseyin AKBULUT¹
Lale ATILGAN GEVREK^{2*}
Murat AY³



ABSTRACT

Hydronic heating systems are emerging as one of the best methods, which are environmentally friendly, clean, and sustainable modern ice prevention methods, an alternative to traditional ice precautions in the pavements. In this present study, temperatures were measured on asphalt samples prepared using the hydronic heating system when the air temperature in situ fell below 0 °C. T (minute), the temperature of influent (°C), air temperature (°C), temperature of effluent (°C) and pavement mean temperature (°C) were measured for four different asphalt samples. The results of the measurements were then modeled separately for four samples (345×4=1380 data) by using multiple linear regression (MLR), multi-layer perceptron (MLP), and radial basis neural network (RBNN). The results were discussed as tables and graphs. The performances of the models were evaluated using the root mean square error (RMSE), mean absolute error (MAE), and determination coefficient (R²). According to the results, the RBNN models of four inputs had the best performance for each sample. The RBNN (4,0.6,9) model, which refers to 4-inputs, spread coefficient of 0.6 and hidden nodes of 9, of sample-3 with RMSE=0.76 °C and MAE=0.63 °C and R²=0.91 had the best performance among all models. In addition, it is thought that the models having low errors in this concept can be evaluated for early warning systems for the ice condition of the roads.

Keywords: Ice prevention, modeling of pavement temperature, traffic safety.

Note:

- This paper was received on November 29, 2022 and accepted for publication by the Editorial Board on October 13, 2023.
- Discussions on this paper will be accepted by May 31, 2024.
- <https://doi.org/10.18400/tjce.1211542>

1 Afyon Kocatepe University, Department of Civil Engineering, Afyonkarahisar, Türkiye
hakbulut@aku.edu.tr - <https://orcid.org/0000-0003-4504-4384>

2 Yozgat Bozok University, Department of Construction Technologies, Yozgat, Türkiye
lale.gevrek@bozok.edu.tr - <https://orcid.org/0000-0003-2015-9679>

3 Yozgat Bozok University, Department of Civil Engineering, Yozgat, Türkiye
murat.ay@bozok.edu.tr - <https://orcid.org/0000-0002-7222-7912>

* Corresponding author

1. INTRODUCTION

Snow and icing cause unsafe pavement surfaces for both pedestrians and motor vehicle traffic. At the same time, the chemicals used for defrosting or prevention both harm to the environment and create an economic burden to the countries [1, 2, 3, 4, 5, 6]. As another method for anti-icing on the pavements, hydronic heating systems have been used in many countries. This system circulates a heated fluid through a network of pipes placed under the pavement to melt the snow and ice in the pavement, and this liquid is a solution of salt and water or liquids such as oil and glycol [7]. The pipe network usually consists of systems laid in a crimped configuration. The material of the pipe is usually cross-linked or high-density polyethylene. Typical pipe ranges from 150 to 300 mm and depth from 50 to 75 mm. Nominal pipe diameters are usually between 18 and 25 mm. Various liquids such as saltwater, oils and glycol water are suitable as heat carrier fluids in hydronic heating systems. The heat source to be used for hydronic heating systems is an important choice [8]. Some sources such as boilers, electric heaters, groundwater, and ground source heat pumps can be used for such systems [9, 10]. Pipe materials used to convey hot water are metal or plastic. Steel, iron, and copper pipes have been widely used over the past years; however, these pipes are corroded easily. Therefore, plastic pipes are now more widely used, and the life span of such plastic pipes is more than 50 years [11, 12, 13, 14, 15].

The icing occurs as a result of frost, fog passing over a cold road surface, groundwater seepage or melting snow, and freezing with precipitation. In addition, when the snow height reaches approximately 5 cm, it is necessary to remove the snow from the road surface. If the necessary snow control is not achieved, the accumulated snow can become the compressed form under traffic loads and turn into an ice sheet. In addition, because bridges and viaducts are built independently from the soil, they are affected by icing much faster than other highway elements depending on the atmospheric conditions. These different road conditions are very critical and may cause heavy traffic accidents that may cause pecuniary loss and intangible damages [13, 16, 17, 18].

As it can be understood from these studies, it is very important to prevent or reduce icing on the road surface in real applications. From a theoretical point of view, some modeling studies have been implemented on hydronic heating systems and the normal pavements. For example, Chiasson et al. [19] examined a design and simulation tool to model the performance of a hydronic heating system. A sample application was simulated to demonstrate the feasibility of the heating system. Minhoto et al. [20] proposed that a three-dimensional finite element model was developed to calculate the temperature of a pavement located in northeast Portugal. Liu et al. [21] performed an experimental validation for the numerical model in an experimental setup to melt the snow on the road. The model can estimate snow, ice and water conditions of snowmelt on hydronic heated pavements. Liu et al. [22] defined a numerical model of a heated pavement and the snow melting processes occurring on its surface. A set of boundary conditions that allow the treatment of various surface and weather conditions associated with storm events were defined. Wang and Chen [23] investigated the mechanism of the critical free area ratio during snowmelt pavement and the factors affecting it, using fluids such as geothermal water and industrial wastewater. A simplified theoretical model is presented to explain the heat and mass transfer process on the coating. They found that the model was effective for predicting the critical free area ratio in the snowmelt process. Xu and Tan [24] developed a heat and mass-related model for

pavement snow melting systems using low-temperature heating fluids. They used this model to simulate the performance of hydronic heated pavement using the HVACSIM Plus program. Xu et al. [14] developed a two-dimensional heat and mass coupled model for hydronic heated pavements. The numerical algorithm can calculate the surface condition, temperature/moisture content in the coating profile. Mirzanamadi et al. [25] developed a two-dimensional numerical model to investigate how different design options affect the efficiency of hydronic heating coating systems. Meteorological data from the Östersund region of Sweden were used, and they found that the distance between pipes had a significant effect on reducing icing. Johnsson and Adl-Zarrabi [26] made a numerical model for designing low temperature (4-8°C) hydronic heated pavements. The model was validated with an experimental setup. They found that the developed model can be estimated with an RMSE<1.4 °C for surface temperatures and RMSE <0.4 °C for the effluent water temperature in the behavior of a hydronic heating system. In our study, the best estimation model (RBNN(4,0.6,9)) of the asphalt surface temperature gave RMSE=0.76 and MAE=0.63. Chen et al. [27] proposed a comprehensive review of existing models developed for predicting pavement temperature and discussed the effective variables in modeling of pavement temperature. Zeiada et al. [28] studied the effect of different design factors on asphalt pavement performance in cold regions by climate factors, such as temperature and precipitation. They determined the most significant design factors prevailing in cold climate conditions. Mirzanamadi et al. [29] examined the applicability of a hydronic heated pavement system for the creation of road surfaces that store solar energy and prevent icing in summer. A hybrid 3D numerical simulation model was used to analyze solar energy storage and anti-icing processes. Climate data were obtained in Östersund, Sweden. The proposed system could reduce the slippery time of road surfaces by up to 85%. Zhao et al. [30] implemented a hydronic snow melting system in Harbin, China. According to the experimental results, a two-dimensional model was developed. For the first time, the snow microstructure was considered in the model for the hydronic snow melting system. Three variables (buried pipe depth, buried pipe spacing, and supplied fluid temperature) were compared and analyzed to optimize the design of the hydronic snowmelt system in cold regions. They found that the snow can be cleared in about 4.5 hours (270 minutes). Marcelino et al. [31] designed a general approach for the development of pavement performance prediction models using machine learning techniques. Rigabadi et al. [32] developed the pavement temperature prediction models based on remote sensing data, multiple linear/non-linear regression and artificial neural network by using variables such as air temperature, solar radiation, wind speed, and humidity. Tabrizi et al. [33] developed a new model for hourly real-time forecasting of pavement temperatures. Zhao et al. [30] developed a temporary two-dimensional model to analyze the effects of three main variables to optimize the design of a hydronic snowmelt system. One of them is the inlet water temperature. In our study, it has also been revealed that the inlet water temperature is an important variable in the estimation of asphalt pavement temperature. Xu and Tan [24] emphasized that the ambient temperature and the heating fluid temperature are the two main factors in the snow melting performance.

The properties of the hydronic heating systems were tested both in the above-mentioned studies and in a thesis [15]. At this point, it was thought that these models obtained from the above-mentioned previous studies could be evaluated as an alternative to the systems that estimate and warn especially about icing on the roads. It is known that hydronic heating systems are expensive in terms of system cost. However, there may be systems that are

suitable to be built based on the cost-benefit analysis. It is known that the costly part in this type of systems is the heating source. The cost can be reduced by using geothermal energy from renewable resources as a heat source. Moreover, the performance of this modeling assumption can be proven theoretically, as mentioned in the above studies. At this point, the performance of the modeling results of the samples were tested by using both classical and innovative modeling methods for four asphalt samples under real outdoor conditions. Moreover, other aims and different aspects of this study from previous studies are: to assess the accuracy of the MLR, MLP and RBNN for estimation of pavement surface temperatures; to examine model's performances using four experimental samples (345×4=1380 data), and to present a support model to the early warning systems for icing on the roads.

2. EXPERIMENTAL MATERIAL AND DATA

The experiment results of four asphalt samples were used in the modeling. These samples were prepared to verify the samples' behaviors in the equivalent environmental conditions. Also, the four same samples were prepared to verify and compare the experiment's results. Metal molds in the form of 40x40x20 cm were prepared. After the four asphalt samples were prepared, they were brought to the laboratory. An electric combi boiler was used as a heat source for the water to circulate in the system, placed in the laboratory to simulate the geothermal energy. The capacity of the combi boiler was of 24 kW. 18 mm diameter pe-x pipes were used in the hydronic heating system. Pipes were placed at 15-cm spacing. Photos of the asphalt samples are shown in Figure 1.



Figure 1 - Preparation of asphalt samples with hydronic heating system

The pipe spacing used in the sample studies was determined in accordance with that in the literature. Mold dimensions were decided by considering the determined pipe spacing. A larger size was not considered due to difficulties in the manufacturing and transportation processes. The snow-covered sections was photographed shortly after the start of the heating as shown in the figure. After a certain period of time, there were no snow-covered areas. Ice melting time was not taken into account in the study. Because the system is being operated before the air temperature drops below zero (0) degree Celsius, ice formation is not foreseen.

Pe-x pipes are manufactured by crosslinking high density polyethylene molecules. Cross-links also increase the temperature and compressive strength of the material. Pe-x cross-linked polyethylene pipes can be used for applications where flexibility as well as long-term resistance to high temperature and pressure is required. The parts of the pipes in situ the laboratory were wrapped with insulation material. Similarly, when hot water was circulated in the hydronic system inside the asphalt samples, the four sides and the bottom of the asphalt samples were wrapped with insulation materials. It is thought that the use of hydronic heating system on asphalt pavement roads can prevent low-temperature cracks that will occur as a result of the reduction of tensile stresses occurring in the wear layer in the heated superstructure and thus contribute positively to the service life. The experimental setup in the laboratory is shown in Figure 2.



Figure 2- The experimental setups in the laboratory in below 0 °C



Figure 3 - Measurements of asphalt surface temperatures with thermocouples

During the datasets acquisition process, one data logger and eight thermocouples measuring temperature were used for the measurements of asphalt surface temperature, air temperature, and influent and effluent water temperatures. The measurements were made on four asphalt pavement samples with a hydronic heating system, using water inlets at 30-40 °C water temperatures for about 2-hour in real weather conditions. The measurements were taken

when the air temperature was below 0°C. To measure the surface temperature of the asphalt samples, four thermocouples were placed at the corner points and one thermocouple was placed at the midpoint of the asphalt surface (see Figure 3). At the same time, influent water temperature, effluent water temperature, and air temperature measurements were made with a thermocouple, as can be seen in Figure 3. The data was then stored into the personal computer.

In order to model the pavement, mean temperature (°C), the experimental variables, T (minute), the temperature of influent (°C), air temperature (°C) and temperature of effluent (°C), were used in the analysis. Before starting the analysis, the Pearson correlation test, which reveals the relationship between independent variable/variables and dependent variable, was performed. The test results were analyzed at the two-tailed hypothesis test and the significance level of 0.01 (1%). In this context, Table 1 shows the correlations of each independent variable with the dependent variable for all raw data (345×4=1380) of four samples. According to Table 1, the correlation coefficients (r) between time (minute), the temperature of influent, temperature of effluent and the pavement mean temperature were calculated as +0.799, +0.081, and +0.086, respectively. Accordingly, it can be said that the time has a statistically significant and strong relationship with the pavement mean temperature, and it is also statistically significant with the temperature of the influent and the effluent. Although the correlations of the temperature of influent and temperature of effluent with the pavement mean temperature had low values, they were used in the models because they were statistically significant, as stated in Table 1. A statistically significant relationship between the air temperature and the pavement mean temperature was not observed, but the physical effects of the in-situ environment were considered in the models. In this case, the error values and graphs formed by adding the air temperature to the models were examined in detail below.

Table 1- Pearson correlations matrix of the measured variables in the experiments

Variable	Independent variables				Dependent variable
	Time (minute)	Temperature of influent (°C)	Temperature of effluent (°C)	Air temperature (°C)	Pavement mean temperature (°C)
Time(minute)	1	-0.144*	-0.156*	-0.004	+0.799*
Temperature of influent(°C)	-0.144*	1	0.868*	0.205*	+0.081*
Temperature of effluent(°C)	-0.156*	0.868*	1	0.137*	+0.086*
Air temperature(°C)	-0.004	0.205*	0.137*	1	+0.044
Pavement mean temperature(°C)	0.799*	0.081*	0.086*	0.044	1

*: Correlation is significant at the 0.01 (1%) significance level in the two-tailed hypothesis test. The relationship of other variables with the modelled variable (pavement mean temperature (°C)) is statistically significant except for air temperature.

Basic statistics of the four asphalt samples are presented in Table 2. The high variation coefficients of pavement mean temperature can be seen for four asphalt samples. T (minute), the temperature of influent (°C), air temperature (°C), and temperature of effluent (°C) had not high variation coefficients. Air temperatures for four asphalt samples had below 0 °C. The temperature of influent (°C), temperature of effluent (°C) and pavement mean

Table 2 - Basic statistics of the variables in the experiments

		Mean	Minimum value	Maximum value	Standard deviation	Skewness coefficient	Kurtosis coefficient	Variation coefficient
Sample-1, N=345	Time(minute)	57.00	0.00	114.00	33.24	0.00	-1.20	0.58
	Temperature of influent (°C)	36.71	26.60	58.10	4.92	1.67	3.96	0.13
	Air temperature (°C)	-7.50	-9.30	-5.00	0.73	-0.13	0.52	-0.10
	Temperature of effluent (°C)	33.33	23.30	51.50	4.57	1.16	2.52	0.14
	Pavement mean temperature (°C)	1.24	-7.22	6.56	3.44	-0.34	-0.59	2.79
Sample-2, N=345	Time(minute)	57.00	0.00	114.00	33.24	0.00	-1.20	0.58
	Temperature of influent (°C)	39.20	18.10	61.90	8.32	0.14	-0.69	0.21
	Air temperature (°C)	-6.61	-9.20	-2.20	1.45	0.12	-0.46	-0.22
	Temperature of effluent (°C)	33.28	14.70	50.50	5.26	0.65	0.47	0.16
	Pavement mean temperature (°C)	2.25	-7.58	10.12	4.14	-0.16	-0.44	1.84
Sample-3, N=345	Time(minute)	57.00	0.00	114.00	33.24	0.00	-1.20	0.58
	Temperature of influent (°C)	38.29	14.40	53.50	4.96	0.24	1.06	0.13
	Air temperature (°C)	-7.84	-10.10	-4.50	1.27	1.01	0.46	-0.16
	Temperature of effluent (°C)	32.50	12.30	50.90	4.17	0.72	2.86	0.13
	Pavement mean temperature (°C)	1.84	-8.08	7.94	3.65	-0.69	-0.05	1.98
Sample-4, N=345	Time(minute)	57.00	0.00	114.00	33.24	0.00	-1.20	0.58
	Temperature of influent (°C)	36.06	5.60	44.40	4.60	-0.57	4.13	0.13
	Air temperature (°C)	-10.75	-13.00	-6.80	1.39	0.53	0.07	-0.13
	Temperature of effluent (°C)	33.40	4.30	42.40	4.09	-0.71	6.02	0.12
	Pavement mean temperature (°C)	2.27	-10.32	11.46	4.60	-0.35	-0.14	2.02

temperature of four asphalt samples had high standard deviations. Although the variation coefficients of T (minute), the temperature of influent ($^{\circ}\text{C}$), air temperature ($^{\circ}\text{C}$), temperature of effluent ($^{\circ}\text{C}$) were low, it was observed that the variation coefficients of the pavement mean temperature were high in four asphalt samples. It can be said that the variables with these statistical properties for four asphalt samples behave similarly on the pavement mean temperature. At this point, it is possible to say that the time is an important factor in the change of variability intervals (maximum and minimum). It can be said that the pavement mean temperatures for the four asphalt samples had positive values in terms of time, and 114-minute for the system was a good performance in terms of heating of the asphalt. Moreover, the correlation of time with pavement mean temperature in Table 1 is the highest value of +0.799. According to this result, it can be said that heating time (T) has a high effect on the pavement mean temperatures.

3. METHODOLOGY

Artificial neural networks (ANNs) have been used in many applications in the literature. These methods generally estimate well and produce outputs near to the measured values. However, when these methods are run with limited data, it is possible that their estimation performance may decrease. For better estimations, the databases of the models should be constantly supported with new datasets. Also, finding meaningful outputs for complex systems with low errors, even with insufficient data, are very important in the decision-making stages of engineering projects. Therefore, modelling of pavement mean temperature ($^{\circ}\text{C}$) was done using the classical regression method with multi-layer perceptron (MLP) and radial basis neural network (RBNN) methods to find the best model having minimum error and maximum R^2 in this study. MATLAB codes written by us were used in all models, MLP and RBNN. Nonlinear methods were considered to define the best relationship amongst the variables. Moreover, normalization of the data was done between 0.2 - 0.8 in the codes, and the data were scaled to this range. Two important methods used in this study are briefly given in the following subsections [34].

3.1. Multi-Layer Perceptron (MLP)

This section presents the architecture of the network that is most commonly used with the backpropagation algorithm the multi-layer feedforward network. MLP is based on the present understanding of the biological nervous system. It is a massive parallel system composed of many processing elements connected by links of variable weights [35]. An elementary neuron with R inputs (T (minute), temperature of influent ($^{\circ}\text{C}$), air temperature ($^{\circ}\text{C}$), and temperature of effluent ($^{\circ}\text{C}$)) is shown in Figure 4. Each input is weighted with an appropriate w . The sum of the weighted inputs and the bias form the input to the transfer function f . Neurons can use any differentiable transfer function f to generate their output (the pavement mean temperature ($^{\circ}\text{C}$)). The initial assigned weights are progressively corrected during the training process. In this process, the outputs predicted by MLP are compared with known outputs, and errors are back-propagated (from right to left in Fig. 4) to determine the appropriate weight adjustments necessary to minimize errors. In this study, the Levenberg-Marquardt [36] algorithm was used for adjusting the MLP weights.

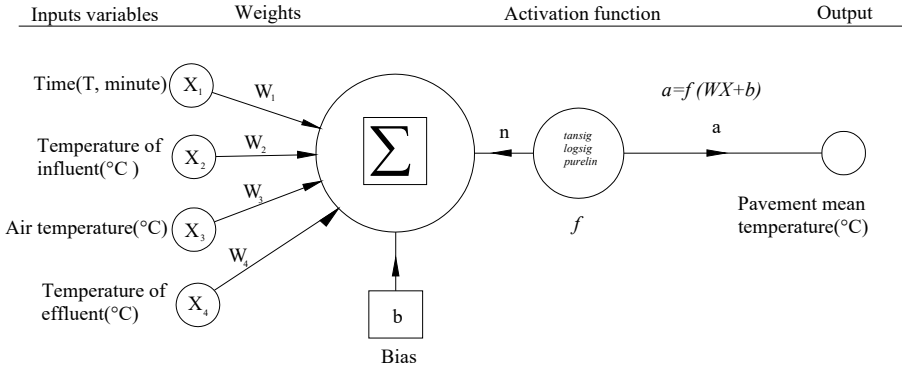


Figure 4 - Non-linear model of a neuron

In backpropagation, it is important to be able to calculate the derivatives of any transfer functions used. Each of the transfer functions above, *logsig*, *radbas*, *netinv*, *tansig* and *purelin*, can be called to calculate its derivative. The output of a neuron can be expressed as:

$$Output = f(n)$$

Where:

$$n = \sum_{j=1}^R w_j \cdot x_j + b; \quad x_1, x_2, x_3, \dots, x_R \quad (1)$$

$x_1, x_2, x_3, \dots, x_R$ are the input signals; w_1, w_2, \dots, w_R are the weights of the neurons; b is bias value; f is activation function, R is the number of the elements in the input vector. The *tansig*, *netinv*, *tansig*, *logsig*, *purelin* and *tribas* are the most commonly used activation functions in artificial neural networks.

3.2. Radial Basis Neural Network (RBNN)

RBNN was first introduced into the ANNs literature by Broomhead and Lowe [37]; Poggio and Girosi [38]. The RBNN has two layers whose output nodes form a linear combination of the basis functions. RBNN is also known as a localized receptive field network because the basis functions in the hidden layer produce a significant nonzero response to input stimulus only when the input falls within a small localized region of the input space. The relation between inputs and outputs is shown in Figure 5.

The RBNN has connection weights between the hidden layer and the output layer only. These weight values can be obtained by the linear least-squares method, which gives an important advantage for convergence. The Gaussian activation function is widely used as the radial basis function. The RBNN method does not perform parameter learning as in the MLP. It performs linear adjustment of the weights for the radial bases. This characteristic gives the

RBNN advantage of a very fast converging time without local minima because its error function is always convex. In this study, different numbers of hidden layer neurons are examined for the RBNN models with a simple trial-and-error method. Detailed information about RBNN theory can be obtained from Haykin.

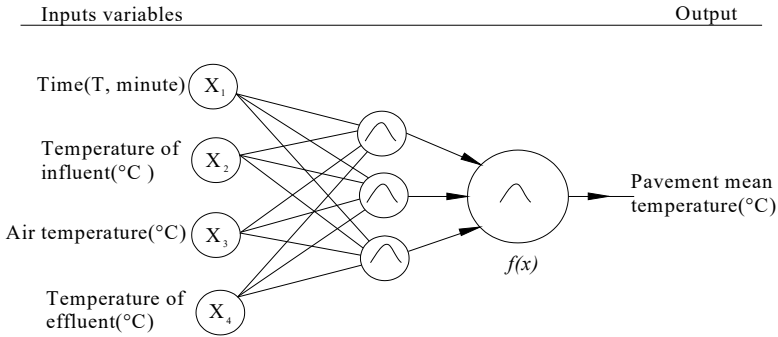


Figure 5 - Schematic diagram of RBNN architecture

4. DISCUSSIONS

To estimate pavement mean temperature, 345 experimental datasets for four samples were divided into two sets: training and testing. Approximately %70 (241) of data was randomly chosen for the training phase, %30 (104) of data was randomly chosen for the testing phase. Moreover, each sample having 345 experimental data was modeled differently and analyzed and compared, respectively, as table and graph. For the learning process for the MLP method, the inputs (T (minute), temperature of influent ($^{\circ}$ C), air temperature ($^{\circ}$ C) and temperature of effluent ($^{\circ}$ C)) and corresponding target vector (pavement mean temperature ($^{\circ}$ C)) were used to train the neural networks by applying Levenberg-Marquardt (LM) algorithm which is both fast and having the advantage in terms of gaining the time according to other training algorithms such as gradient descent and Bayesian regularization. Because the number of hidden units directly affected the performance of the network, many experimental investigations were conducted with the models. The number of intermediate layers from 1 to 20 was assayed for each model by looking at the minimum MSE values. In these analyses, one-hidden layer was enough for all models. It was found that the optimum number of hidden layers was one in all of the models for the MLP method. The stopped criteria for the training phase were $MSE=0.00001$ or the number of epochs of 100. The optimum transfer functions (*compet*, *logsig*, *purelin*, *netinv*, *tansig*, *radbas*, *softmax*, and *tribas*) for the MLP models were used for input and for output layers to find out the best model. Unlike the MLP, the RBNN has optimum spread; hidden node numbers are found by using a trial-error method. After the optimum spread coefficient and hidden nodes number are found, the main program is executed with these numbers. The MSE of the RBNN was taken as “0” for all of the models. Normalization of the data was done between 0.2 - 0.8 in the codes, and the data were scaled to this range. Formulas given by Eqs. 2-4 were used for the evaluation of the model’s performances in the study. The root mean square error (RMSE), mean absolute error (MAE), and determination coefficient (R^2) criteria are expressed as:

$$RMSE = \sqrt{\frac{1}{N} \sum_{j=1}^N (Y_{measured,j} - Y_{modeled,j})^2} \quad (2)$$

$$MAE = \frac{1}{N} \sum_{j=1}^N |Y_{measured,j} - Y_{modeled,j}| \quad (3)$$

$$R^2 = 1 - \frac{\sum_{j=1}^N [(Y)_{measured,j} - (Y)_{modeled,j}]^2}{\sum_{j=1}^N [(Y)_{measured,j} - (\bar{Y})_{mean\ measured}]^2} \quad (4)$$

Table 3 - RMSE, MAE and R² values of the MLR, MLP, and RBNN in training and testing phases for sample-1

Comb. No.	Inputs	Target (output)	Model and optimum transfer functions	Training (N=241)			Testing (N=104)		
				RMSE (°C)	MAE (°C)	R ²	RMSE (°C)	MAE (°C)	R ²
(1)	Time	Pavement mean temperature (°C)	MLR(1)	2.13	1.75	0.68	2.10	1.70	0.42
(2)	Time and temperature of influent	Pavement mean temperature (°C)	MLR(2)	2.07	1.71	0.70	1.95	1.65	0.56
(3)	Time, temperature of influent and air temperature	Pavement mean temperature (°C)	MLR(3)	2.06	1.69	0.70	2.01	1.69	0.54
(4)	Time, temperature of influent, air temperature and temperature of effluent	Pavement mean temperature (°C)	MLR(4)	1.94	1.56	0.74	1.95	1.62	0.60
(1)	Time	Pavement mean temperature (°C)	MLP(1,1,1), <i>netinv-purelin</i>	2.14	1.77	0.68	1.93	1.71	0.42
(2)	Time and temperature of influent	Pavement mean temperature (°C)	MLP(2,1,1), <i>netinv-purelin</i>	2.09	1.74	0.69	1.64	1.32	0.65
(3)	Time, temperature of influent and air temperature	Pavement mean temperature (°C)	MLP(3,1,1), <i>netinv-purelin</i>	2.10	1.73	0.69	1.68	1.37	0.64
(4)	Time, temperature of influent, air temperature and temperature of effluent	Pavement mean temperature (°C)	MLP(4,1,1), <i>netinv-purelin</i>	1.82	1.49	0.77	2.06	1.82	0.46
(1)	Time	Pavement mean temperature (°C)	RBNN(1,0.1,14)	2.39	1.98	0.76	3.09	2.49	0.32
(2)	Time and temperature of influent	Pavement mean temperature (°C)	RBNN(2,0.5,2)	1.65	1.35	0.80	1.62	1.21	0.66
(3)	Time, temperature of influent and air temperature	Pavement mean temperature (°C)	RBNN(3,0.7,3)	1.95	1.63	0.73	1.56	1.10	0.70
(4)	Time, temperature of influent, air temperature and temperature of effluent	Pavement mean temperature (°C)	RBNN(4,1.4,20)*	0.59	0.46	0.97	1.27	1.07	0.77

*indicates that the model has the best performance according to the RMSE and MAE.

Modeling of Asphalt Pavement Surface Temperature for Prevention of Icing on the Surface

Where N denotes the number of observations; Y indicates the modeled and measured pavement mean temperature, and \bar{Y} indicates the mean of pavement mean temperature. The results of the MLR method were examined by Gevrek [15]. In this present study, MLP and RBNN methods are used and compared with the results of the MLR method. Table 3 shows the results of MLR, MLP, and RBNN models and RMSE, MAE and R^2 values in the training and testing phases for sample-1. In this table, the RBNN model of four inputs has a better performance than the other models. The MLP models had similar performance with the MLR models according to RMSE, MAE, and R^2 criteria in the testing phase. The RBNN models in the testing phase gave better estimations than MLR and MLP models. It can be said that the temperature of effluent and the temperature of influent are effective variables in estimating pavement mean temperature ($^{\circ}\text{C}$).

Table 4 shows the results of MLR, MLP, and RBNN models and RMSE, MAE, and R^2 values in the training and testing phases for sample-2. In this table, the RBNN model of four inputs

Table 4- RMSE, MAE and R^2 values of the MLR, MLP, and RBNN in training and testing phase for sample-2

Comb. No.	Inputs	Target (output)	Model and optimum transfer function	Training (N=241)			Testing (N=104)		
				RMSE ($^{\circ}\text{C}$)	MAE ($^{\circ}\text{C}$)	R^2	RMSE ($^{\circ}\text{C}$)	MAE ($^{\circ}\text{C}$)	R^2
(1)	Time	Pavement mean temperature ($^{\circ}\text{C}$)	MLR(1)	2.15	1.69	0.77	2.29	1.79	0.47
(2)	Time and temperature of influent	Pavement mean temperature ($^{\circ}\text{C}$)	MLR(2)	1.98	1.61	0.80	1.72	1.40	0.71
(3)	Time, temperature of influent and air temperature	Pavement mean temperature ($^{\circ}\text{C}$)	MLR(3)	1.97	1.60	0.81	1.71	1.37	0.72
(4)	Time, temperature of influent, air temperature and temperature of effluent	Pavement mean temperature ($^{\circ}\text{C}$)	MLR(4)	1.96	1.61	0.81	1.73	1.37	0.71
(1)	Time	Pavement mean temperature ($^{\circ}\text{C}$)	MLP(1,1,1), <i>netinv-purelin</i>	2.18	1.72	0.76	2.59	2.28	0.47
(2)	Time and temperature of influent	Pavement mean temperature ($^{\circ}\text{C}$)	MLP(2,1,1), <i>netinv-purelin</i>	2	1.64	0.80	2.10	1.71	0.72
(3)	Time, temperature of influent and air temperature	Pavement mean temperature ($^{\circ}\text{C}$)	MLP(3,1,1), <i>netinv-purelin</i>	2.01	1.65	0.79	2.07	1.71	0.76
(4)	Time, temperature of influent, air temperature and temperature of effluent	Pavement mean temperature ($^{\circ}\text{C}$)	MLP(4,1,1), <i>tansig-purelin</i>	1.81	1.47	0.83	2.34	1.98	0.55
(1)	Time	Pavement mean temperature ($^{\circ}\text{C}$)	RBNN(1,0,2,1)	3.6	2.91	0.36	2.52	2.23	0.34
(2)	Time and temperature of influent	Pavement mean temperature ($^{\circ}\text{C}$)	RBNN(2,0,4,5)	1.19	0.95	0.93	1.74	1.42	0.80
(3)	Time, temperature of influent and air temperature	Pavement mean temperature ($^{\circ}\text{C}$)	RBNN(3,1,8)	0.98	0.75	0.95	1.54	1.21	0.86
(4)	Time, temperature of influent, air temperature and temperature of effluent	Pavement mean temperature ($^{\circ}\text{C}$)	RBNN(4,0,8,7)*	0.82	0.65	0.97	1.06	0.86	0.94

* indicates that the model has the best performance according to the RMSE and MAE.

had better performance than the other models. MLP models had similar performance with the MLR models according to RMSE, MAE, and R^2 criteria in the testing phase. The RBNN models in the testing phase gave better estimations than MLR and MLP models. It can be said that the temperature of effluent and the temperature of influent are effective variables in estimating pavement mean temperature ($^{\circ}\text{C}$).

Table 5 shows the results of MLR, MLP, and RBNN models and RMSE, MAE, and R^2 values in the training and testing phases for sample-3. In this table, the RBNN model of four inputs

Table 5- RMSE, MAE and R^2 values of the MLR, MLP, and RBNN in training and testing phase for sample-3

Comb. No.	Inputs	Target (output)	Model and optimum transfer function	Training (N=241)			Testing (N=104)		
				RMSE ($^{\circ}\text{C}$)	MAE ($^{\circ}\text{C}$)	R^2	RMSE ($^{\circ}\text{C}$)	MAE ($^{\circ}\text{C}$)	R^2
(1)	Time	Pavement mean temperature ($^{\circ}\text{C}$)	MLR(1)	2.19	1.77	0.71	1.89	1.71	0.52
(2)	Time and temperature of influent	Pavement mean temperature ($^{\circ}\text{C}$)	MLR(2)	2.18	1.77	0.71	1.89	1.71	0.52
(3)	Time, temperature of influent and air temperature	Pavement mean temperature ($^{\circ}\text{C}$)	MLR(3)	2.09	1.59	0.73	1.77	1.54	0.57
(4)	Time, temperature of influent, air temperature and temperature of effluent	Pavement mean temperature ($^{\circ}\text{C}$)	MLR(4)	1.90	1.41	0.78	1.67	1.34	0.74
(1)	Time	Pavement mean temperature ($^{\circ}\text{C}$)	MLP(1,1,1), <i>logsig-purelin</i>	2.18	1.78	0.71	1.74	1.20	0.53
(2)	Time and temperature of influent	Pavement mean temperature ($^{\circ}\text{C}$)	MLP(2,1,1), <i>logsig-purelin</i>	1.63	1.36	0.84	1.80	1.25	0.49
(3)	Time, temperature of influent and air temperature	Pavement mean temperature ($^{\circ}\text{C}$)	MLP(3,1,1), <i>netiv-purelin</i>	2.15	1.64	0.72	2.01	1.52	0.53
(4)	Time, temperature of influent, air temperature and temperature of effluent	Pavement mean temperature ($^{\circ}\text{C}$)	MLP(4,1,1), <i>logsig-purelin</i>	1.71	1.24	0.86	1.71	1.24	0.58
(1)	Time	Pavement mean temperature ($^{\circ}\text{C}$)	RBNN(1,0.1,3)	2.3	1.85	0.68	2.12	1.71	0.42
(2)	Time and temperature of influent	Pavement mean temperature ($^{\circ}\text{C}$)	RBNN(2,0.8,3)	1.64	1.36	0.83	1.64	1.35	0.48
(3)	Time, temperature of influent and air temperature	Pavement mean temperature ($^{\circ}\text{C}$)	RBNN(3,1,8)	1.99	1.61	0.76	1.56	1.27	0.55
(4)	Time, temperature of influent, air temperature and temperature of fluent	Pavement mean temperature ($^{\circ}\text{C}$)	RBNN(4,0.6,9)*	0.54	0.42	0.98	0.76	0.63	0.91

* indicates that the model has the best performance according to the RMSE and MAE.

had better performance than the other models. MLP models had similar performance with the MLR models according to RMSE, MAE, and R^2 criteria in the testing phase. RBNN models in the testing phase gave better estimations than MLR and MLP models. It can be said that the temperature of effluent and the temperature of influent are effective variables in estimating pavement mean temperature ($^{\circ}\text{C}$).

Table 6 shows the results of MLR, MLP, and RBNN models and RMSE, MAE, and R^2 values in the training and testing phases for sample-4. In this table, the RBNN model of four inputs had better performance than the other models. The MLP models were similar performance with the MLR models according to RMSE, MAE, and R^2 criteria in the testing phase. The RBNN models in testing phase gave better estimations than MLR and MLP models. It can be said that the temperature of effluent and temperature of influent are effective variables in estimating pavement mean temperature ($^{\circ}\text{C}$).

Table 6- RMSE, MAE and R^2 values of the MLR, MLP, and RBNN in training and testing phase for sample-4

Comb. No.	Inputs	Target (output)	Model and optimum transfer function	Training (N=241)			Testing (N=104)		
				RMSE ($^{\circ}\text{C}$)	MAE ($^{\circ}\text{C}$)	R^2	RMSE ($^{\circ}\text{C}$)	MAE ($^{\circ}\text{C}$)	R^2
(1)	Time	Pavement mean temperature ($^{\circ}\text{C}$)	MLR(1)	2.84	2.37	0.67	3.11	2.81	0.29
(2)	Time and temperature of influent	Pavement mean temperature ($^{\circ}\text{C}$)	MLR(2)	2.58	2.16	0.73	2.65	2.48	0.53
(3)	Time, temperature of influent and air temperature	Pavement mean temperature ($^{\circ}\text{C}$)	MLR(3)	2.46	1.98	0.75	2.58	2.35	0.54
(4)	Time, temperature of influent, air temperature and temperature of effluent	Pavement mean temperature ($^{\circ}\text{C}$)	MLR(4)	1.99	1.58	0.84	1.88	1.73	0.78
(1)	Time	Pavement mean temperature ($^{\circ}\text{C}$)	MLP(1,1,1), <i>tribas-purelin</i>	2.62	2.05	0.72	3.21	2.24	0.26
(2)	Time and temperature of influent	Pavement mean temperature ($^{\circ}\text{C}$)	MLP(2,1,1), <i>netinv-purelin</i>	2.60	2.16	0.72	2.01	1.79	0.67
(3)	Time, temperature of influent and air temperature	Pavement mean temperature ($^{\circ}\text{C}$)	MLP(3,1,1), <i>netinv-purelin</i>	2.51	2.04	0.74	1.97	1.62	0.65
(4)	Time, temperature of influent, air temperature and temperature of effluent	Pavement mean temperature ($^{\circ}\text{C}$)	MLP(4,1,1), <i>netinv-purelin</i>	1.87	1.45	0.86	2.51	1.94	0.72
(1)	Time	Pavement mean temperature ($^{\circ}\text{C}$)	RBNN(1,0,1,14)	2.39	1.98	0.77	3.09	2.49	0.32
(2)	Time and temperature of influent	Pavement mean temperature ($^{\circ}\text{C}$)	RBNN(2,0,9,3)	2.10	1.70	0.82	1.66	1.45	0.79
(3)	Time, temperature of influent and air temperature	Pavement mean temperature ($^{\circ}\text{C}$)	RBNN(3,1,7,18)	0.83	0.62	0.97	1.42	1.19	0.83
(4)	Time, temperature of influent, air temperature and temperature of effluent	Pavement mean temperature ($^{\circ}\text{C}$)	RBNN(4,1.5,8)*	1.28	0.96	0.93	1.07	0.86	0.91

* indicates that the model has the best performance according to the RMSE and MAE.

Table 7 shows the comparison of the best models for all samples in the testing phase. In this table, the RBNN models with four inputs had the best performance for each sample. RBNN(4,0.6,9) model, which is 4-inputs, spread coefficient of 0.6 and hidden nodes of 9 of sample-3, had the best performance among all models. When the other models were examined, it can be said that the RMSE and MAE error values were close to each other. It can also be said that the results of the models gave similar results in all four experimental samples. In general, the longer the T (heating time) is, the more other variables affect the pavement surface temperature. For example, the temperature of influent and temperature of effluent were effective variables in the models because they decreased the RMSE and MAE values of the models. According to the MAE values, it was seen that the error values were close to each other. The difference between the maximum MAE (1.07) and minimum MAE (0.63) was found to be $1.07 - 0.63 = 0.44$ °C, which is quite low value for 104 data in the testing phase.

Table 7- Comparison of the best models for all samples in testing phase (N=104)

Inputs	Target (output)	The number of the inputs in the models	Samples	Model	RMSE (°C)	MAE (°C)	R ²
Time, temperature of influent, air temperature and temperature of effluent	Pavement mean temperature (°C)	4	Sample-1	RBNN(4,1.4,20)	1.27	1.07	0.77
Time, temperature of influent, air temperature and temperature of effluent	Pavement mean temperature (°C)	4	Sample-2	RBNN(4,0.8,7)	1.06	0.86	0.94
Time, temperature of influent, air temperature and temperature of effluent	Pavement mean temperature (°C)	4	Sample-3	RBNN(4,0.6,9)*	0.76	0.63	0.91
Time, temperature of influent, air temperature and temperature of effluent	Pavement mean temperature (°C)	4	Sample-4	RBNN(4,1.5,8)	1.07	0.86	0.91

* indicates that the model has the best performance according to the RMSE and MAE.

The best models, (a)RBNN(4,1.4,20), (b)RBNN(4,0.8,7), (c)RBNN(4,0.6,9) and (d)RBNN(4,1.5,8) in Figure 6, are graphically compared in the form of time series according to the results of the testing phase. Scatter plots are also given in Figure 6 in which the measured pavement mean temperature in the x-axis and the modeled pavement mean temperature in the y-axis are depicted. It can be seen from Table 7 and the figures that the

Modeling of Asphalt Pavement Surface Temperature for Prevention of Icing on the Surface

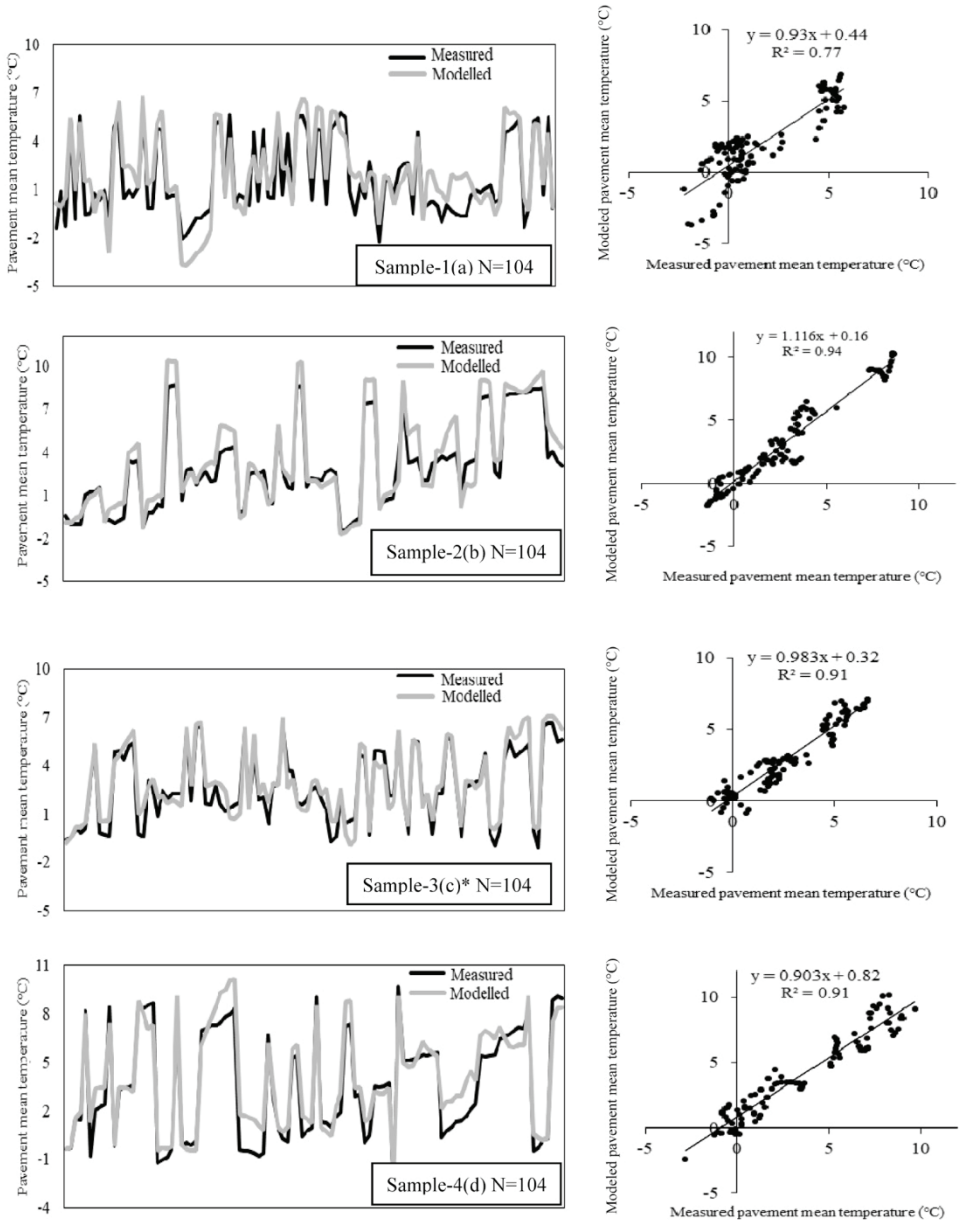


Figure 6 -The measured and modeled pavement mean temperature for the best models Sample-1(a) RBNN(4,1.4,20), Sample-2(b) RBNN(4,0.8,7), Sample-3(c) RBNN(4,0.6,9)* and Sample-4(d) RBNN(4,1.5,8) in the testing phase (N=104)

best model is RBNN(4,0.6,9) according to the evaluation criteria. Looking at the model results of four experimental examples, the methods generally have similar performance in terms of modeling of pavement mean temperature. In the four experimental examples, it was seen that the MLR models gave slightly better results than the MLP models in the testing phases. The RBNN method also gave similar results, which were the best models in four experimental examples. In this context, it can also be stated that the four asphalt samples behave similarly in the models in terms of experimental and modeling consistency.

5. CONCLUSIONS

After usability of the hydronic heating systems in snow and icing control in the pavements was investigated in Gevrek [15], the pavement mean temperature was modeled by using MLR, MLP, and RBNN methods. In this context, the performances of the models were evaluated using the model performance criteria of RMSE, MAE, and R^2 . In view of the results obtained, the following conclusions can be drawn:

1. Preventing snow and ice on the surface of hydronic asphalt pavement could make a significant contribution to reducing traffic accidents and environmental damages and increases the highway capacity in extreme weather conditions.
2. Thermal stress-induced shrinkage of asphalt pavement layers, which is one of the important deterioration forms in winter can be reduced by using hydronic heating systems.
3. Traditional road maintenance costs, such as salting and snow removal, which might damage the structure could be reduced by using hydronic heating systems. At the same time, these systems can positively contribute to the highway pavement life cycle.
4. Considering the benefit/cost ratios and project design-construction works of hydronic heating systems, it can be said that these systems are significantly cost effective in terms of investment costs in order to maintain their engineering properties in future projections.
5. It was generally seen that the MLR models gave slightly better results than the MLP models in the testing phases for the four experimental examples.
6. The RBNN models with four inputs had the best performance for each asphalt sample. The RBNN (4,0.6,9) model of sample-3 with RMSE=0.76 °C and MAE=0.63 °C and $R^2=0.91$ for 104 testing data had the best performance among all models. According to these results, it can be said that the statistically obtained models can be used in early icing warning systems, and can contribute to rapid decision-making processes.
7. Considering the model results of four experimental examples, it can be said that the methods generally have similar performance in terms of modeling of pavement mean temperature. In this context, the four asphalt samples behaved similarly in the models in terms of experimental and modeling consistency.
8. In terms of significant impact on these laboratory samples, this system could be tested and modeled on a larger scale in real in-situ conditions. However, it was thought that starting from this point as the first study it would inform us in terms of guiding our studies in the future.

9. It is recommended that some further analyses should be made using other artificial intelligence applications to find better estimates for the asphalt pavement surface temperature.

10. In the study, it was determined that the correlation coefficient increased significantly with the inclusion of the inlet water temperature in the model. As a result, it can be concluded that the inlet water temperature should be increased in order to increase the asphalt surface temperature. It has been shown that 40°C water can be a sufficient temperature for such systems to be used for snow and ice prevention purposes [39]. It can be made energy efficient by making use of waste heat sources from electricity and residential heating from renewable sources such as geothermal sources, where high temperatures are not needed.

Symbols

MAE	Mean absolute error
MLR	Multiple linear regression
MLP	Multi-layer perceptron
RBNN	Radial basis neural network
RMSE	Root mean square error
R²	Determination coefficient
r	Correlation coefficient
T	Time

Acknowledgements

We sincerely thank editor and anonymous reviewers for their valuable constructive comments and suggestions for this study. We also thank ÖZDEMİR Construction, Tourism and Energy Company in Turkey; and Ferdi GEVREK (Instructor at Yozgat Bozok University) who helped us during the experimental studies.

Disclosure statement

No potential conflict of interest was reported by the authors.

Funding

We would like to thank Afyon Kocatepe University, Scientific Research Projects Coordination Unit for supporting this study with the project number 18.FENBİL.41.

References

- [1] Fay, L., Volkening, K., Gallaway, C., Shi, X., Performance and Impacts of Current Deicing and Anti-Icing Products: User Perspective versus Experimental Data. Presented at 87th Annual Meeting of the Transportation Research Board, Washington DC., 08-1382, 2008.
- [2] Houssain, SMK., Optimum De-Icing and Anti-Icing for Snow and Ice Control of Parking Lots and Sidewalks. PhD thesis in Civil Engineering. The University of Waterloo, 186, Canada, 2014.
- [3] Adl-Zarrabi, B., Mirzanamadi, R., Jhonsson, J., Hydronic Pavement Heating for Sustainable Ice-free Roads. *Transportation Research Procedia*, 14, 704-713, 2016.
- [4] Akbulut, H., Woodside, AR., Traffic Safety and Unprotected Road Users in Low and Middle Income Countries. *Journal of Innovations in Civil Engineering and Technology*, 1(1), 1-9, 2019.
- [5] Blomqvist, S. Amiri, S. Rohdin, P. Ödlund, L., Analyzing the Performance and Control of a Hydronic Pavement System in a District Heating Network. *Energies*, 12(11), 2078, 2019.
- [6] Feng, J., Yin, G., Thermal Analyses and Responses of Bridge Deck Hydronic Snow Melting System. *Advances in Civil Engineering*. 8172494, 14p, 2019.
- [7] ASHRAE, Handbook of HVAC Applications, American Society of Heating, Refrigerating and Air-Conditioning Engineers, Inc, Atlanta, GA, 2003.
- [8] Ho, I-H., Li, S., Abudureyimu, S., Alternative Hydronic Pavement Heating System Using Deep Direct Use of Geothermal Hot Water. *Cold Regions Science and Technology*, 160, 194-208, 2019.
- [9] Liu X., Spitler J.D., A Simulation Tool for the Hydronic Bridge Snow Melting System, 12th International Road Weather Conference, 2003.
- [10] Anand, P., Nahvi, A., Ceylan, H., Pyrialakou, V.D., Gkritza, K., Gopalakrishnan, K., Kim, S., Taylor, PC., Energy and Financial Viability of Hydronic Heated Pavement Systems, National Technical Information Services (NTIS), Springfield, Virginia 22161, No. DOT/FAA/TC17/47, 2007.
- [11] Lund, JW., Pavement Snow Melting. *Geo-Heat Center Quarterly Bulletin*, 21(2), 12-19, 2000.
- [12] Fujimoto, A., Tokunaga, RA., Kiriishi, M., Kawabata, Y., Takahashi Ishida, T., Fukuhara, T., A road surface freezing model using heat, water and salt balance and its validation by field experiments. *Cold Reg. Sci. Technol.*, 106-107, 01-10, 2014.
- [13] Akbulut, H., Gürer, C., Gevrek, L., Highway Pavement Surface Icing and Traffic Safety. *International Journal of Scientific Engineering Research*, 9(8), 6-9, 2018.
- [14] Xu, H., Wang, D., Tan, Y., Zhou, J., Oeser, M., Investigation of design alternatives for hydronic snow melting pavement systems in China. *Journal of Cleaner Production*, 170, 1413-1422, 2018.

- [15] Gevrek Atılgan, L., Modeling of Anti-Icing Systems with Geothermal Energy in Highway Pavements. Afyon Kocatepe University, Graduate School of Natural and Applied Sciences, PhD Thesis, Turkey, 2021.
- [16] Gustafson, K., Icing Conditions on Different Pavement Structures. Transportation Research Record 860. Nr 84, ISSN 0347-6049, 1983.
- [17] Xiao, J., Kulakowski, BT., El-Gindy, M., Prediction of Risk of Wet-Pavement Accidents: Fuzzy Logic Model. Transportation Research Record, 1717(1), 2000.
- [18] Eugster, WJ., Road and Bridge Heating Using Geothermal Energy Overview and Examples. Proceedings European Geothermal Congress, Unterhaching, Germany, 30 May-1 June, 2007.
- [19] Chiasson, AD., Spitler, JD., Rees, SJ., Smith, MD., A model for simulating the performance of a pavement heating system as a supplemental heat rejecter with closed-loop ground-source heat pump systems. Journal of Solar Energy Engineering, 122(4), 183-191, 2000.
- [20] Minhoto, MJC., Pais, JC., Pereira, PAA., Picado-Santos, LG., Predicting asphalt pavement temperature with a three-dimensional finite element method. Transp. Res. Rec., 1919(1), 96-110, 2005.
- [21] Liu, X., Rees SJ., Spitler, JD., Modeling snow melting on heated pavement surfaces. Part I: Model development. App Therm Eng, 27, 1115-1124, 2007a.
- [22] Liu, X., Rees SJ., Spitler, JD., Modeling snow melting on heated pavement surfaces, Part II: Experimental validation. App Therm Eng, 27, 1125-1131, 2007b.
- [23] Wang, H., Chen, Z., Study of critical free-area ratio during the snow-melting process on pavement using low-temperature heating fluids. Energy Conversion and Management, 50(1), 157-165, 2009.
- [24] Xu, H., Tan, Y., Modeling and Operation Strategy of Pavement Snow Melting Systems Utilizing Low-Temperature Heating Fluids. Energy, 80, 666-676, 2015.
- [25] Mirzanamadi, R., Hagentoft, CE., Johansson, P., Johnsson, J., Anti-icing of Road Surfaces Using Hydronic Heating Pavement with Low Temperature. Cold Regions Science and Technology, 145, 106-118, 2018.
- [26] Jhonsson, J., Adl-Zarrabi, B., Modeling the thermal performance of low temperature hydronic heated pavements. Cold Regions Science and Technology, 161, 81-90, 2019.
- [27] Chen, J., Wang, H., Xie, P., Pavement temperature prediction: theoretical models and critical affecting factors. Applied Thermal Engineering, 158, 113755, 2019.
- [28] Zeiada, W., Hamad, K., Omar, M., Underwood, BS., Khalil, MA., Karzad, AS., Investigation and modelling of asphalt pavement performance in cold regions. International Journal of Pavement Engineering, 20(8), 986-997, 2019.
- [29] Mirzanamadi, R., Hagentoft, CE., Johansson, P., Coupling a Hydronic Heating Pavement to a Horizontal Ground Heat Exchanger for harvesting solar energy and heating road surfaces. Renewable Energy, 147(Part 1), 447-463, 2020.

- [30] Zhao, W., Su, W., Li, L., Zhang, Y., Li, B., Optimization design of the road unit in a hydronic snow melting system with porous snow. *Journal of Thermal Analysis and Calorimetry*, 141, 1509-1517, 2020.
- [31] Marcelino, P., Antunes, MDL., Fortunato, E., Gomes, MC., Machine learning approach for pavement performance prediction. *International Journal of Pavement Engineering*, 22(3), 341354, 2021.
- [32] Rigabadi, A., Herozi, MRZ., Rezagholilou, A., An attempt for development of pavements temperature prediction models based on remote sensing data and artificial neural network. *International J of Pavement Engineering*, 23(9), 2912-2921, 2021.
- [33] Tabrizi, SE., Xiao, K., Thè, JVG., Saad, M., Farghaly, H., Yang, SX., Gharabaghi, B., Hourly road pavement surface temperature forecasting using deep learning models. *Journal of Hydrology*, 603, Part A, 126877, 2021.
- [34] Ay, M., Kisi, Ö., Modelling of chemical oxygen demand by using ANNs, ANFIS and k-means clustering techniques. *Journal of Hydrology*, 511, 279-289, 2014.
- [35] Haykin, S., *Neural networks: A comprehensive foundation*. 2nd Ed., Prentice-Hall, Upper Saddle River, NJ., 1998.
- [36] Marquardt, D., An algorithm for least squares estimation of nonlinear parameters. *J. Soc. Ind. Appl. Maths.*, 11(2), 431-441, 1963.
- [37] Broomhead, D., Lowe, D., Multivariable functional interpolation and adaptive networks. *Complex Syst.*, 2(6), 321-355, 1988.
- [38] Poggio, T., Girosi, F., Regularization algorithms for learning that are equivalent to multilayer networks. *Science*, 247(4945), 978-982, 1990.
- [39] Wang, H., Zhao, J., Chen, Z., Experimental Investigation of Ice and Snow Melting Process on Pavement Utilizing Geothermal Tail Water. *Energy Conversion and Management*, 49, 1538-1546, 2008.

Application of Endurance Time Method in Seismic Assessment of RC Frames Designed by Direct Displacement-Based Procedure

Nisar Ahmad KARIMZADA¹
Amir SHIRKHANI²
Engin AKTAŞ^{3*}



ABSTRACT

This paper addresses the Direct Displacement-Based Design (DDBD) approach of multi-story RC frame structures consistent with changes to design criteria between Turkish earthquake codes of TSC-2007 and TBEC-2018. The corresponding response modification factor (R) of structures designed based on the DDBD approach is also estimated in this research. The design base shear forces of both codes are compared considering different R factors and also with that of the DDBD approach. The results showed that the DDBD approach, as per TBEC-2018, provides RC frame structures with higher R values compared to the similar approach in accordance with TSC-2007. The Endurance Time (ET) method is a time history-based procedure for seismic assessment of structures under intensifying dynamic excitations aided to judge their performance at various intensity levels. Since, up to now, the ET method has not been considered to evaluate the performance of the structures designed by the DDBD approach, this paper addresses this issue. The ET performance curves of RC frames show that structures designed by the DDBD approach in accordance with TBEC-2018 exhibit higher Interstory Drift Ratios (IDRs) values than TSC-2007 at various hazard levels.

Keywords: Direct displacement-based design, endurance time method, endurance time excitation function, interstory drift ratio, performance curve, pushover analysis, response modification factor.

Note:

- This paper was received on January 20, 2023 and accepted for publication by the Editorial Board on October 13, 2023.
- Discussions on this paper will be accepted by May 31, 2024.

• <https://doi.org/10.18400/tjce.1239730>

1 İzmir Institute of Technology, Department of Civil Engineering, İzmir, Türkiye
nissarahmadkarimzada3@gmail.com - <https://orcid.org/0000-0002-0915-5397>

2 University of Tabriz, Department of Structural Engineering, Tabriz, Iran
shirkhani@tabrizu.ac.ir - <https://orcid.org/0000-0003-2532-2906>

3 İzmir Institute of Technology, Department of Civil Engineering, İzmir, Türkiye
enginaktas@iyte.edu.tr - <https://orcid.org/0000-0002-5706-2101>

* Corresponding author

1. INTRODUCTION

Structures should be designed in such a way that they can resist different types of static and dynamic loads applied to them. The design of structures to such loads is guided through standards and codes. One of the dynamic loads is due to earthquakes, which poses a challenge for a structural engineer to design a structure to perform safely against. Traditional Seismic Design Codes (TSDCs) used for such purposes have been developed for several years based on Force-Based Design (FBD) and some linear elastic concepts. Furthermore, the Life Safety (LS) performance level under the design earthquake (10% probability of exceedance in 50 years) has been considered in such codes. Most of the TSDCs do not address the inelastic response of the structures directly in the design stage and thus cannot effectively deal with the damage due to structural, nonstructural, and content systems [1]. However, there are some modern codes that consider the inelastic response of the structures directly in the design stage. In addition, no clear information regarding economic losses and downtime is provided in the TSDCs [2]. The Performance-Based Seismic Design (PBSD) approach is a fairly new paradigm for the seismic assessment and retrofitting of existing structures and seismic design of new structures, which has attracted the attention of researchers for around the last two decades. It is a considerably reliable approach, and it promises to produce structures with a more realistic understanding of the risk of casualties, occupancy interruption, and economic losses which could occur as a result of future earthquakes [2]. The structure designed using the PBSD approach is expected to achieve the specific performance objectives selected prior to design, given certain hazard levels. Furthermore, it deals with the outcome of the structure rather than prescribing how it is to be built, and the ultimate goal is used as a starting point for the design purpose. In addition, it is capable of reducing the life cycle cost of the structure under a specific earthquake hazard level. It is also able to give more detailed information about the performance of structural, nonstructural, and content systems.

Different methods could be used in the PBSD framework, such as the N2 method, capacity spectrum method, Direct Displacement-Based Design (DDBD) method, etc. A performance objective is the combination of a performance level and a hazard level. Performance level can be determined by damage states of structural and nonstructural and content systems [3]. In this study, the DDBD approach is adopted since displacement has a direct relation with damage states of the structural and nonstructural components [4]. The Displacement-Based Design (DBD) procedure appeared in the 1990s for the design of structures, which drew the attention of the researchers. As a consequence, different DBD methodologies were developed. Major research devoted to this methodology are Chopra and Goel [5], Moehle [6], Panagiotakos and Fardis [7], Priestley and Kowalsky [8] for RC structures, and Medhekar and Kennedy [9, 10] for steel structures. Among the DBD methodologies, the most widely used one is the DDBD approach, first introduced by Priestley [11]. A critical review was provided by Sullivan et al. [12] into different DBD approaches, and a comparison between the DDBD approach and other DBD methodologies has been reported. A textbook by Priestley et al. [13] covers comprehensively the DDBD approach for seismic design of RC, steel, and timber buildings as well as buildings with isolation and supplemental damping devices. Besides, a model code DBD12 by Sullivan et al. [14] has also gained wide acceptance.

Remarkable studies have been conducted to develop the DDBD approach for different structural systems, such as RC structures, steel structures, masonry and timber structures,

bridges, and structures equipped with seismic isolation systems. Pettinga and Priestley [15] investigated the dynamic behavior of reinforced concrete tube frames designed with the DDBD approach. They proposed some modifications considering the higher mode's effects, specifically for buildings taller than 10 stories. Sullivan et al. [16] developed the DDBD procedure for RC dual-wall frame structures. The applicability of the DDBD approach for near-fault areas was investigated by Moghim and Saadatpour [17]. The suitability of the DDBD approach for the seismic design of precast concrete structures is conducted by Belleri [18] regarding the effect of the foundation flexibility, beam-to-column, and foundation-to-column connections. Sullivan and Lago [19] proposed a new methodology for DDBD of moment-resisting frames with viscous dampers. Malekpour and Dashti [20] investigated the DDBD approach for different RC structural systems, including moment-resisting, dual wall-frame and dual steel-braced systems.

Furthermore, using the elastoplastic single degree of freedom (SDOF) systems, the P-delta effect is investigated extensively for both DDBD and FBD approaches by Pourali et al. [21]. Seismic performance evaluation of low and medium-rise concentrically braced frames, designed using the DDBD approach, is carried out by Sahoo and Prakash [22]. Yan and Gong [23] developed a displacement profile expression for the DDBD method of regular RC frame structures. Giannakouras and Zeris [24] used the DDBD approach for the seismic design of RC frames with setback irregularity accounting for local ductility associated with global behavior. Kumbhar et al. [25] used six distinct DDBD approaches developed by various researchers for the design of low-, medium-, and high-rise RC frame buildings and compared their seismic performance. Malla and Wijeyewickrema [26] developed the DDBD approach for the coupled walls with steel shear link coupling beams using inelastic displacement spectra. Papagiannopoulos et al. [27] presented numerical examples of the eccentrically and concentrically braced steel frames to explain the DDBD approach and its advantages. Sharma et al. [28] investigated the inelastic behavior of low and mid-rise RC buildings designed by FBD and DDBD. Mohebbi et al. [29] extended the DDBD approach for the isolated structures equipped with viscous dampers and assessed the seismic performance of the structures for near and far-field earthquakes. Kalapodis et al. [30] improved the DDBD approach for three types of plane steel frames, namely moment-resisting frames, steel concentrically braced frames, and buckling-restrained braced frames.

The Endurance Time (ET) method initially introduced by Estekanchi et al. [31] is a rather fast incremental-based dynamic time history analysis in which structures experience intensifying dynamic excitations. The response of the structure is predicted by this method considering the relationship between Intensity Measures (IMs) and Engineering Demand Parameters (EDPs)[32]. The EDPs characterize the structural response, whereas IMs characterize the ground shaking intensity at different seismic hazard levels. In this method, structural response for a continuous range of IMs is provided by a single Nonlinear Time History Analysis (NTHA); however, traditional NTHA provides the structural response at a single IM level. In fact, the ET method represents the structural response at various IM levels using the least number (commonly three) of NTHA [32], which is conventionally provided by Incremental Dynamic Analysis (IDA). Several studies have been conducted on the ET method in recent years [33–39], and the validity of ET results has been confirmed by comparing them with the results of NTHA [40–45]. These research works compared the results of NTHA under 7 or 22 Ground Motion (GM) records with the ET method results under three simulated Endurance Time Excitation Functions (ETEFs) records. They showed

that the results of the ET method were sufficiently close to the results of the NTHA under GM records.

The Turkish Building Earthquake Code 2018 (TBEC-2018) replaced the previous code, the Turkish Seismic Code 2007 (TSC-2007), in 2019. Compared to TSC-2007 [46], significant changes have been made in TBEC-2018 [47], similar to ASCE 7-16 and comprising new design approaches. In this paper, an adaptive approach for the DDBD is presented with respect to the changes to Turkish seismic design criteria, for RC frame buildings. To this end, multi-story RC frame structures are considered here and designed based on the DDBD approach in compliance with both mentioned seismic design codes. For the detailed design purpose, i.e., flexural and shear design of columns and beams, TS500 Turkish Standards [48] is used together with the procedure given by Ersoy et al. [49]. Capacity design principles are applied to obtain a structure with the desired beam sway mechanism, i.e., a structure with strong-column weak-beam, in which plastic hinges form in beams rather than in columns.

This research generally pursues the following objectives: (i) First, designing multi-story RC frame structures using the DDBD approach in accordance with TSC-2007 and TBEC-2018 and comparing their results. (ii) Second, obtaining base shear forces for the selected RC frames using TSC-2007 and TBEC-2018 through the Equivalent Lateral Force (ELF) method for different response modification factors. A comparison between the base shear forces obtained based on TSC-2007 and TBEC-2018 is also made. These base shear forces are also compared to those obtained through the DDBD approach. (iii) Third, since estimating the response modification factors of the structures based on the DDBD approach has been less considered in the previous studies, this issue is also addressed in this paper. Hence, the actual response modification factors for each frame designed using the DDBD approach in accordance with TSC-2007 and TBEC-2018 are estimated, and their results are compared. To this end, nonlinear static pushover analyses are performed on the structures. (iv) Since up to now the ET method has not been used to assess the behavior of the structures designed by the DDBD approach, it is also considered here. To consider the impact of ground motion duration on the structural responses, the fourth generation of ETEFs [32, 40] is used in this study, which is including the cumulative absolute velocity (CAV) in its generation process.

2. SEISMIC DESIGN CODES USED IN THIS STUDY

Türkiye is located in a seismically active region. The North Anatolian Fault (NAF) and the East Anatolian Fault are two active faults that are responsible for many major earthquakes in Türkiye. The earthquake design code for buildings was published for the first time in Türkiye in 1940 after the Erzincan earthquake occurred in 1939, with a magnitude of 7.9 [50]. The earthquake code was then revised and improved several times due to the design deficiencies observed during the construction phase and also concerning technological and social development in society [51].

2.1. Difference of Criteria of Seismic Design Codes Used in This Study

After the Gölcük earthquake in 1999 with a magnitude of 7.4, TSC-2007 was published in 2007. A new chapter is included in TSC-2007 for the assessment and rehabilitation of the existing buildings. Furthermore, linear and nonlinear methods are considered in this

regulation. The last version of the earthquake code for buildings in Türkiye was published in March 2018, “Turkish Building Earthquake Code (TBEC-2018)”. This version has many changes with respect to TSC-2007, most of which are similar to ASCE 7-16 [51, 52]. Some of these changes are made in site classes, importance factors, occupancy category, period calculation, overstrength factor, response modification factor, or behavior factor [52].

One of the most important differences between these codes is the calculation of the elastic acceleration response spectrum used in this study. One of the required parameters for calculating the elastic response spectrum in TSC-2007 is the effective ground acceleration coefficient (A_0), which depends on the seismic zone. Seismic zones are divided into 4 different zones in TSC-2007, Zone 1 with the highest seismicity and Zone 4 with the lowest seismicity. However, in TBEC-2018, seismic hazard maps are used instead of seismic zones, from which mapped values of Maximum Considered Earthquake (MCE_R) spectral response acceleration parameters at one second (S_1) and at the short period (S_S) are obtained. Moreover, spectrum characteristic periods (T_A and T_B) are the other parameters required for calculating the elastic acceleration response spectrum, which depends on the local site class in TSC-2007. In contrast, these values are obtained using the provided equations in TBEC-2018, which depends on S_1 and S_S . For more detailed information about obtaining the elastic acceleration response spectrum, the reader is referred to TSC-2007 and TBEC-2018.

3. DIRECT DISPLACEMENT-BASED SEISMIC DESIGN APPROACH

Priestley and Kowalsky [8] proposed the DDBD approach for the design of RC structures. It is based on the PBSD method, and it is a simple design procedure widely accepted by researchers [20]. While FBD utilizes the acceleration response spectrum to calculate the global base shear for the structure, the DDBD approach utilizes the displacement response spectrum to estimate the global base shear; further, the maximum inelastic deformation of the structure is considered. Figure 1 is adopted from Priestley and Kowalsky [8], which provides the fundamentals of the DDBD approach. From Figure 1, it is evident that a Multi Degree of Freedom (MDOF) system is presented by an equivalent Single Degree of Freedom (SDOF) system. The equivalent SDOF system involves effective height (H_e) and effective mass (m_e), Figure 1(a). The maximum displacement of the SDOF system is presented with effective stiffness (K_{eff}), Figure 1(b), and equivalent viscous damping (ξ_{eq}), Figure 1(c). As can be seen that the effective stiffness of SDOF systems is significantly lower than the initial stiffness of the structure, which in turn gives lower base shear force [8]. The reason is that the SDOF system presents the MDOF system at the maximum inelastic response [53].

The first step in the procedure of the DDBD approach is to choose a performance level that corresponds to a specific ground motion hazard. Since damage is directly related to displacement, the IDR is selected. Then, using this ratio, target design displacement, and ductility demand are obtained. The ductility demand is used to obtain the equivalent viscous damping (ξ_{eq}); refer to Figure 1(c). The equivalent viscous damping is used to reduce the elastic design displacement response spectrum (elastic design displacement response spectrum is obtained for a 5% damping ratio). Finally, the effective period is obtained from

the reduced design displacement response spectrum, which can be used then to obtain the effective stiffness and base shear forces, respectively.

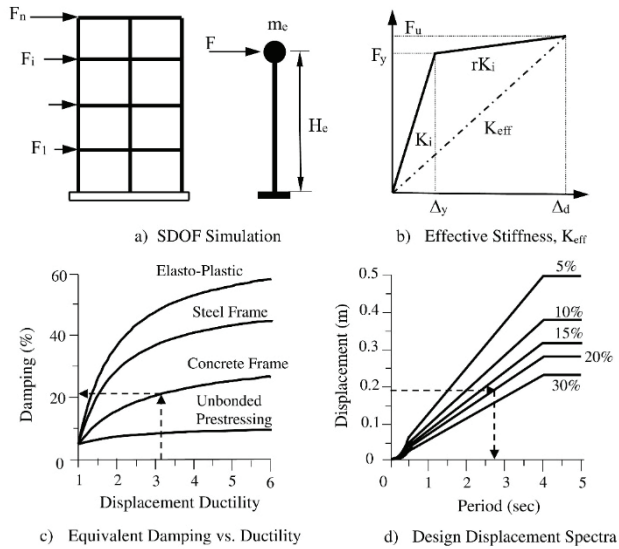


Figure 1 - Fundamentals of the DDBD approach [8].

A simple framework for the DDBD procedure is given in Figure 2. It starts with the selection of target displacement and ends with the determination of base shear force.

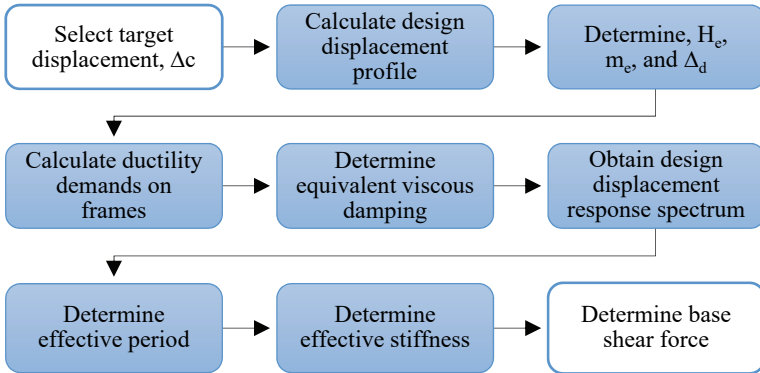


Figure 2 - Framework of the DDBD approach.

After selecting the drift ratio, target displacement (Δ_C) is obtained, and this value is used to obtain the design story displacement (Δ_i). To this end, the normalized inelastic mode shape (δ_i) should be found as follows [8]:

$$\delta_i = \frac{H_i}{H_n} \quad \text{for } n \leq 4 \quad (1)$$

$$\delta_i = \frac{4}{3} \left(\frac{H_i}{H_n} \right) \left(1 - \frac{H_i}{4H_n} \right) \quad \text{for } n > 4 \quad (2)$$

In these equations, H_i is the story height from the ground/foundation level, H_n is the total height of the frame, and n is the number of stories. In addition, these equations have been shown to be sufficient for the design purpose by Pettinga [54]. It has been shown that the design displacement profile obtained using these two equations reasonably matches the displacement profile obtained from the time history analysis [13, 54]. The design displacement at the top of each story, Δ_i can be calculated as follows:

$$\Delta_i = \omega_\theta \delta_i \frac{\Delta_c}{\delta_c} \quad (3)$$

where δ_c and Δ_c are the inelastic mode shape and design displacement of the critical story (the story with the largest drift ratio), respectively. ω_θ is the drift reduction factor to take into account the higher mode effects. It will have negligible effects for the number of stories less or equal to 10 ($n \leq 10$), and it can be obtained as follows [55]:

$$\omega_\theta = 1.15 - 0.0034H_n \leq 1.0 \quad (4)$$

Target design displacement (Δ_c) is obtained as follows:

$$\Delta_c = \theta_d H_c \quad (5)$$

where H_c and θ_d the height of the critical story from the ground/foundation level and IDR, chosen as performance level for a specific ground motion intensity.

Once the design displacement profile is obtained, then it is used to obtain the design displacement (Δ_d) effective mass (m_e) and effective height (H_e) of the equivalent SDOF system. The following equations are used for each of them.

$$\Delta_d = \sum_{i=1}^n (m_i \Delta_i^2) / \sum_{i=1}^n (m_i \Delta_i) \quad (6)$$

$$m_e = \frac{\sum_{i=1}^n (m_i \Delta_i)}{\Delta_d} \quad (7)$$

$$H_e = \sum_{i=1}^n (m_i \Delta_i H_i) / \sum_{i=1}^n (m_i \Delta_i) \quad (8)$$

where, m_i and Δ_i are the mass and displacement of the i^{th} story, respectively.

Equivalent damping for the SDOF system can be obtained through the following equation [13]:

$$\xi_{eq} = 0.05 + 0.565 \left(\frac{\mu - 1}{\mu \pi} \right) \quad (9)$$

The first term of the above equation is the 5% elastic viscous damping and the second term is the hysteretic damping, and μ is the design displacement ductility factor, and it is equal to:

$$\mu = \frac{\Delta_d}{\Delta_y} \quad (10)$$

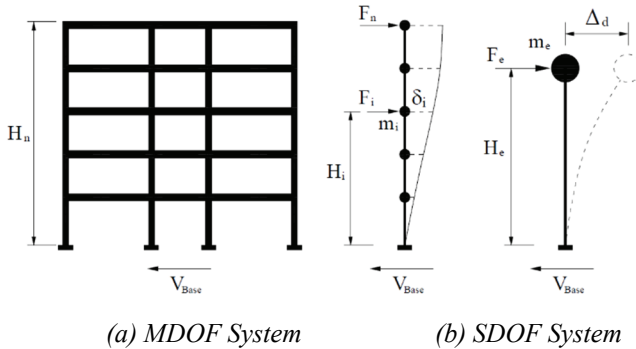


Figure 3 - Simplified model of MDOF system represented by SDOF system [55].

In this equation, Δ_y is the yield displacement of the equivalent SDOF system. For RC frame buildings with three bays (refer to Figure 3), it can be obtained using the following equation [13]

$$\Delta_y = \frac{2M_1 \theta_{y_1} + M_2 \theta_{y_2}}{2M_1 + M_2} H_e \quad (11)$$

where M_1 and M_2 are the moment contribution to the total overturning moment from outer and inner bays respectively. θ_{y_i} is the yield drift, and it is equal to:

$$\theta_{y_i} = 0.5\varepsilon_y \frac{L_{b_i}}{h_{b_i}} \quad (12)$$

In this equation, ε_y is the yield strain, which is the ratio of expected yield strength (f_{ye}) of the reinforcement over its modulus of elasticity (E_s), L_{b_i} is the length of the i^{th} bay and h_{b_i} is the depth of the beam of the i^{th} bay. It should be noted that Priestley et al. [56] recommended that f_{ye} should be taken 10% larger than characteristic yield strength (i.e. $f_{ye} = 1.1f_y$). Furthermore, in Equation (11), the values for M_1 and M_2 are not required; instead, only the ratio of them is needed. This ratio can be arbitrarily chosen, however, for the case study, since the depth of the beams is kept constant for all three bays, and it is assumed that the moment capacity of the inner and outer frames are equal, so according to the recommendation of Priestley et al. [56] this ratio is equal to:

$$\frac{M_1}{M_2} = 1 \Rightarrow M_1 = M_2 \quad (13)$$

Using this value, Equation (11) results in the following simple form:

$$\Delta_y = \frac{2\theta_{y_1} + \theta_{y_2}}{3} H_e \quad (14)$$

The design displacement response spectrum for the desired damping ($S_{D_{\xi}}$) rather than 5% elastic damping, can be obtained using the following equation [56]:

$$S_{D_{\xi}} = S_{D_{e,5}} \left(\frac{0.10}{0.05 + \xi_{eq}} \right)^{0.5} \quad (15)$$

In this equation $S_{D_{e,5}}$ is the design displacement response spectrum for 5% damping, which is equal to:

$$S_{D_{e,5}} = S_{ae}(T) \frac{T^2}{4\pi^2} \quad (16)$$

where $S_{ae}(T)$ is the elastic design acceleration response spectrum, which could be obtained by using TSC-2007 and TBEC-2018 separately. Since in the DDBD approach, displacement response spectrum is used, there must be a constant maximum displacement after reaching a specific value for the effective period, called the corner period. There is nothing mentioned about the corner period in TSC-2007, while in TBEC-2018, it is given as T_L and it is equal to 6 seconds; therefore, for TSC-2007, it is also assumed to be 6 sec. One of the reasons for

using a large period as a corner period is to adjust the design displacement spectrum to be useful for the higher value of the effective period resulting from the lower effective stiffness of the SDOF system [8]. Here, only the resultant elastic acceleration response spectrum for 5% damping has been shown in Figure 4 with design displacement response spectra for different damping values for both TSC-2007 and TBEC-2018.

From Figure 4, it can be concluded that the values for the design displacement response spectrum for TBEC-2018 are significantly smaller than the ones obtained for TSC-2007. Response spectra for TBEC-2018 are shown up to 6.5 sec, which is an arbitrary value, and the constant region for the displacement can be noticed clearly. On the other hand, for TSC-2007, it is shown up to 6 sec since, using equations provided in TSC-2007 it is not possible to obtain the constant displacement region.

Once such response spectra for the design displacement are obtained, then using design displacement (Δ_d) in the design displacement response spectrum for equivalent damping of the given figure, the corresponding effective period can be read as shown in Figure 4.

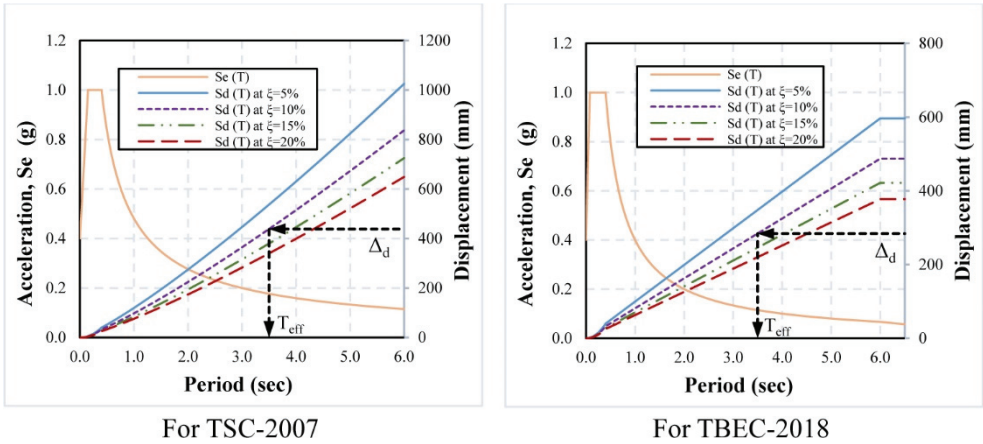


Figure 4 - Elastic acceleration (S_e) and design displacement (S_d) response spectra for different damping values.

$$\Delta_d \Rightarrow T_{eff}$$

Finally, the effective period is used to obtain effective stiffness and total base shear force as follows, respectively.

$$K_{eff} = \frac{4\pi^2}{T_{eff}^2} m_e \tag{17}$$

$$V_{Base} = K_{eff} \Delta_d \tag{18}$$

The total base shear force is then distributed up the height of the building, and lateral forces at the top of each floor are obtained using the following equation, provided by both TSC-2007 and TBEC-2018.

$$F_i = (V_{Base} - \Delta F_N) \frac{m_i H_i}{\sum_{i=1}^n m_i H_i} \quad (19)$$

where m_i is the mass of the i^{th} story. ΔF_N is the additional equivalent seismic load, acting at the top of the N^{th} floor, and it is equal to:

$$\Delta F_N = 0.0075N V_{Base} \quad (20)$$

Here, N is the total number of stories of the building (see Figure 5).

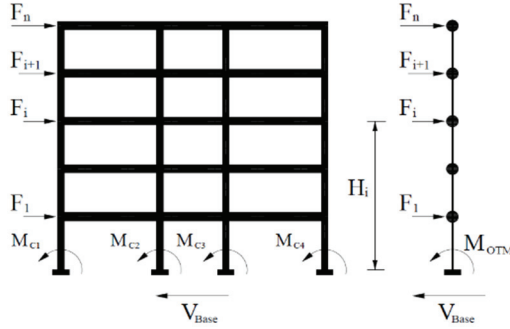


Figure 5 - Story forces and total overturning moment (M_{OTM}) [13].

The stability index (θ_Δ) is calculated by Equation (21) to see if P-Delta effects are required to be considered in the analysis. According to model code DBD12 [14], the stability index shall not exceed 0.3. If $0.1 \leq \theta_\Delta \leq 0.30$, P-Delta effects should be considered. If $\theta_\Delta > 0.30$, then the structure must be made stiffer and the calculations should be revised. Furthermore, if $\theta_\Delta < 0.1$, then there is no need to consider P-Delta effects. The base shear force is amplified (if $0.1 \leq \theta_\Delta \leq 0.30$ and will be calculated by Equation (22) [13, 55].

$$\theta_\Delta = \frac{P\Delta_{max}}{M_D} \quad (21)$$

$$V_{Base} = K_{eff} \Delta_d + C \frac{P\Delta_d}{H_e} \quad (22)$$

where M_D and Δ_{max} are total overturning moment (M_{OTM}) at the base of the structure and design displacement of the equivalent SDOF system obtained by using Equation (6), respectively [55]. P is the axial force due to gravity loads, C is a constant, and for reinforced concrete structures, $C=0.5$ is used.

$$M_{OTM} = \sum_{i=1}^n F_i H_i \quad (23)$$

Once the base shear force is distributed up the height of the building using Equation (19), then it is easy to find the story shear forces. Two different methods of structural analysis under lateral forces vector are given by Priestley et al. [13] in the DDBD approach for the determination of moment capacities at plastic hinge locations. The first one is the analysis of the frame under lateral forces based on the relative stiffness of the members, and the second one is based on the equilibrium consideration of the nodes. Here, the latter is being considered. In this method, to find the shear forces in the columns at each story, the inner columns are assumed to take twice the shear forces compared to the outer columns. To avoid the soft story mechanism of the first story, the contra flexure height for columns of the first story is considered at 0.6 of the height of that story ($0.6H_1$) from the base of the column [13]. For further discussions about how to find the internal forces in columns and beams and for discussions about capacity design principles, the reader is referred to Priestley et al. [13].

4. EVALUATION OF RESPONSE MODIFICATION FACTOR (R)

The TSDCs are based on the FBD approach and some linear elastic techniques. In most of these codes, the nonlinear behavior of structures is not considered directly in the design process; instead, their nonlinear behavior is considered by means of the response modification factor (R), which reduces the demand due to design earthquake [4, 57]. Since the design earthquake is a rare event that a structure may experience in its life cycle, to have an economical design, the structures are allowed to go under inelastic deformation and dissipate induced energy by inelastic deformation due to the design earthquake, so TSDCs handle that by R factors and properly designed seismic details. In seismic design codes, specific R factors are used for specific types of structures. R factor is the ratio of the maximum elastic base shear force (V_e) of a structure obtained through elastic analysis to its maximum inelastic base shear force (V_u) obtained through inelastic analysis. R factor could be evaluated for a designed structure, for which alternative formulations are proposed in the literature. The following equation widely used in research works, such as [58–65], is used in this study.

$$R = R_{\Omega} R_{\mu} \quad (24)$$

In this equation, R_{Ω} is the overstrength factor and R_{μ} is the ductility factor, given as follows:

$$R_{\Omega} = \frac{V_y}{V_d} \quad (25)$$

$$R_{\mu} = \left(\frac{\mu - 1}{\Phi} \right) + 1 \quad (26)$$

$$\mu = \frac{u_{max}}{u_y} \quad (27)$$

$$\Phi = 1 + \frac{1}{10T - \mu T} - \frac{1}{2T} e^{-1.5(\ln T - 0.6)^2} \quad (28)$$

where V_y is the base shear force at the yield point (Figure 6) which cannot be less than the design base shear force (V_d), u_{max} is the maximum top displacement of the structure that it can go for, and u_y is the displacement at the yield strength of the structure, μ is global ductility ratio, Equation (27), and Φ is the factor which depends on soil condition, and for rock type soil it can be calculated through Equation (28), T is the fundamental period of the structure. Equations (26) and (28) are suggested by Miranda and Bertero [66]. The concept of the response modification factor is illustrated in Figure 6 (in the figure $\Delta_y = u_y$ and $\Delta_u = u_{max}$).

For evaluation of the R-value, the capacity curve, obtained through pushover analysis of the structure, is approximated by a bilinear curve to obtain a clear yield point (which corresponds to V_y Figure 7). Different methods exist for this purpose. One of the methods used in this study is called the equal-energy method, which assumes that the areas enclosed by the pushover curve above and below the bilinear curve are equal ($Area_1 \cong Area_2$).

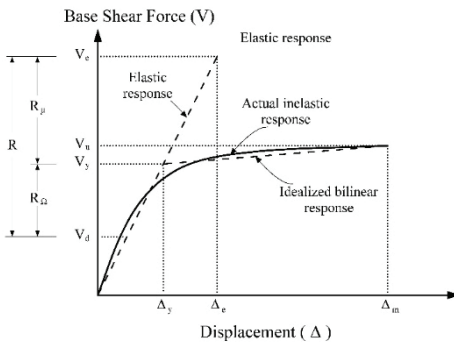


Figure 6 - Base shear force vs roof displacement relationship [58].

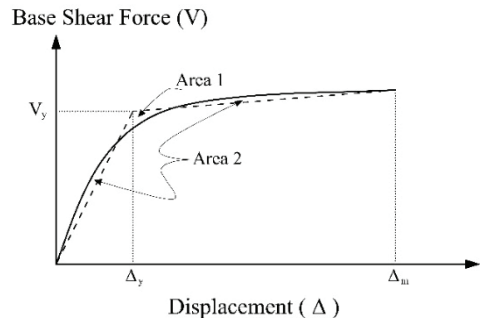


Figure 7 - Bilinear approximation of the capacity curve [67].

5. ENDURANCE TIME METHOD

A hypothetical shaking-table test could be used to explain the concept of the Endurance Time (ET) method. As shown in Figure 8, the structures are located on shaking-table and loaded with an intensifying artificial dynamic excitation. The aim is to determine the relative performance of the three structures under dynamic excitation [32].

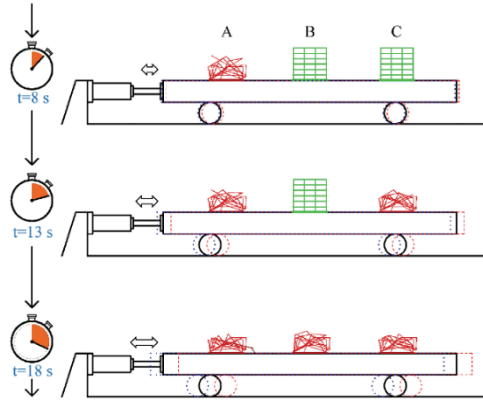


Figure 8 - Hypothetical shaking-table test [32].

The response of the structures is tracked during the hypothetical shaking-table test. The behavior of the structures shifts gradually from linear elastic behavior to nonlinear inelastic behavior, experiencing some damage states, and finally, collapse will occur as the amplitude of the ET excitation increases with time. The results of the hypothetical shaking-table test are given in terms of the ET curves, which show the relation between ET and EDPs, e.g., maximum IDR. The main advantage of the ET method over the conventional NTHA procedure utilizing ground motions is that the computational time for analysis is reduced significantly [68]. It is worth mentioning that the actual EDPs and final design, obtained using the ET method, should be verified by conducting more precise procedures, e.g., IDA and cloud analysis methods [69, 70].

In contrast to the typical time history analysis, which uses real Ground Motion (GMs) or artificially generated motions, the ET method utilizes the ETEFs, which are the main component of the ET method, and thus directly affects the results. The ETEFs are acceleration functions for which the intensity increases with time, and from zero to each time corresponds to a specific seismic hazard level. They are created such that to induce suitable responses in structures as compared to GMs [40]. In this study, the ETA40lc series of ETEFs are used that are generated by Mashayekhi et al. (2018) [40] using the FEMAP695 far-field record set (22 real GM records). For the simulation of this series of ETEFs, the consistency of the ground motion duration has been included directly in the generation process. This is because structural responses could be influenced by ground motion duration significantly [71–74]. In addition, since the ETA40lc series of ETEFs follows an exponentially intensifying profile that is consistent in cumulative absolute velocity (CAV) when compared to conventional GM scaling to match desired intensity. Some research works showed that the

CAV could also be used as an alternative for the Arias Intensity (AI) [75–77] to evaluate the motion duration’s effect on structural response [78]. To this end, the CAV has been included in the generation process of the ETA40lc series, and it has been selected as an IM to reflect the impact of duration [40]. The target acceleration response spectrum of the ETEFs can be defined as follows:

$$S_{ac}(t, T) = g(t) \times S_a^{\text{target}}(T) \tag{29}$$

where, $S_a^{\text{target}}(T)$ is GMs target acceleration spectrum as the average acceleration response spectrum of GMs. The records of the ETA40lc series have been optimized to fit the average acceleration spectrum, average displacement spectrum, and average CAV of the first components of the FEMAP695 far-field GM set. These GMs are recorded on soft rock, stiff sites, and shallow crustal sites. Site-to-sources distances are at least 10 km, and the magnitudes of the events are larger than 6.5. The peak ground velocity of each individual record is used for normalization while generating the ETA40lc series. To this end, Mashayekhi et al. (2018) [40] used the procedure of the FEMAP695 [79] in their study. Because of inherent differences in magnitude, source type, and site condition, there is unwarranted variability between records; thus, normalization is used considering peak ground velocity to eliminate them while retaining inherent aleatory variability for anticipating seismic response assessment [42, 79]. In Figure 9, $S_a^{\text{target}}(T)$ related to these GMs are shown. $g(t)$ is the intensifying profile which controls the shape of increasing acceleration spectra in time [40].

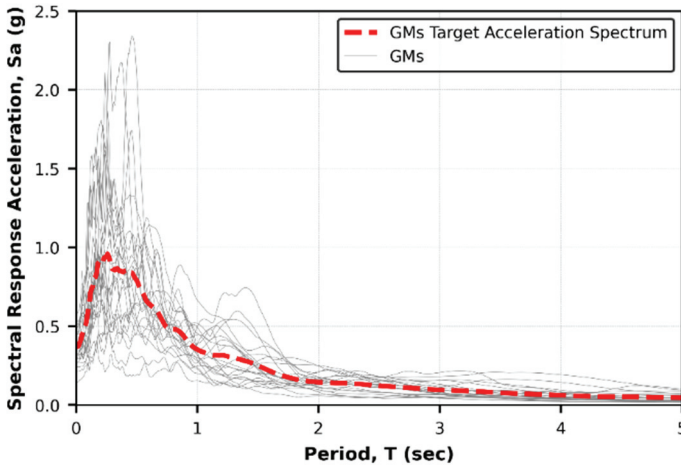


Figure 9 - Target acceleration spectrum of first components of FEMAP695 far-field GM set

Figure 10 shows the ETA40lc01 accelerogram and the comparison of its acceleration response spectra at different times of excitation with target response spectra. Three excitation functions of the ETA40lc series are used in this study to reduce the effects of random scatter

in the results, as recommended in research work by Estekanchi et al. [80]. The target times of these excitation functions are calculated in such a way that first, the GMs target acceleration spectrum is placed above the code spectrum in the range of $0.2T$ to $1.5T$ (T is the fundamental period of the structure), and second, the average acceleration response spectrum of ETA40lc01-03 is matched with the scaled GMs target acceleration spectrum in the same interval of $0.2T$ to $1.5T$. The variation of the corresponding hazard return period with the target time in ET analysis and structural period in this study is shown in Figure 11.

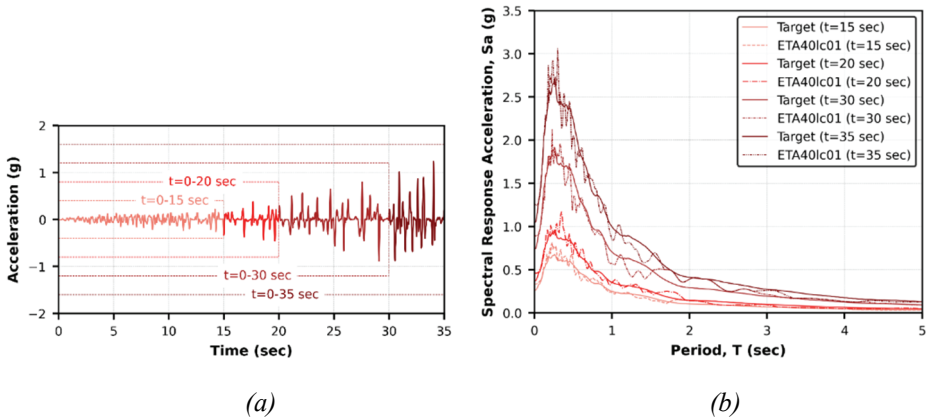


Figure 10 - (a) ETA40lc01 accelerogram, (b) Acceleration response spectra at different times of excitation.

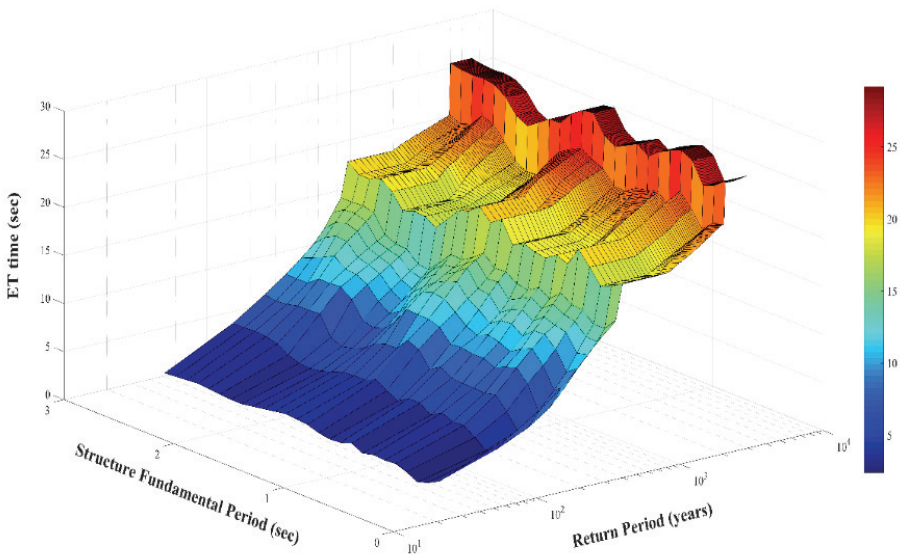


Figure 11 - Return period vs. target time in ET analysis and structural period.

6. STRUCTURAL DESIGN

6.1. Seismic Design Codes

Four special moment-resisting RC frames are selected to demonstrate the DDBD approach. They are related to commercial office buildings, similar in terms of the plan, while different in terms of the number of stories (three-, five-, eight-, and 12- story buildings). It is assumed that the structures are located in Düzce province, in the north of Türkiye. The necessary parameters for estimating the acceleration response spectrum for TBEC-2018 were obtained, such as S_S and S_1 . Since the location is close to the North Anatolian fault, which is an active fault, according to TSC-2007, seismic zone 1 with $A_0 = 0.4$ is chosen. The site class used in this study is Z1 according to TSC-2007, which corresponds to ZB given by TBEC-2018 [52]. The compressive strength of the concrete used here is 25 MPa, and the elasticity modulus of the concrete is assumed to be equal to 3.1×10^4 MPa. The yield strength of the steel reinforcement is taken as 420 MPa, and its modulus of elasticity is equal to 2×10^5 MPa. The selected frames in each case have the highest gravitational loads on them (i.e., the gravity load is maximum on the chosen frame in each case), and each has three bays, the outer bays of the frames are larger than the inner bay. Cross-sectional sizes for each frame are provided in Table 1. Elevation of frames with their vertical and horizontal dimensions is given in Figure 12.

6.2. DDBD Approach

The DDBD approach is applied to the frames in compliance with TSC-2007 and TBEC-2018, and base shear forces are obtained. The detailed design for the given frames with specified cross-sectional sizes is carried out only for the base shear forces obtained through the DDBD in compliance with TSC-2007. Since the base shear forces obtained through the DDBD as per TBEC-2018 are much smaller, cross-sectional sizes are changed for the frames, and the DDBD in accordance with TBEC-2018 has been applied once again, and the base shear forces are obtained. In this case, cross-sectional sizes are given in Table 2, and it should be noted that for detailed design, TSC-2007 and TBEC-2018, together with TS-500, are used. Then, the R factor is evaluated for each frame designed in both cases from the results obtained through nonlinear static pushover analysis.

Table 1 - Designed sections for the studied RC frames

Frame	Story-Level	Member Size		
		Beams	Exterior Columns	Interior Columns
3-Story	1-3	35x50 cm	40x40 cm	40x40 cm
5-Story	1-3	35x60 cm	50x50 cm	50x50 cm
	4-5	35x60 cm	45x45 cm	45x45 cm
8-Story	1-5	35x60 cm	60x60 cm	60x60 cm
	6-8	35x60 cm	50x50 cm	50x50 cm
12-Story	1-8	35x60 cm	70x70 cm	70x70 cm
	9-12	35x60 cm	60x60 cm	60x60 cm

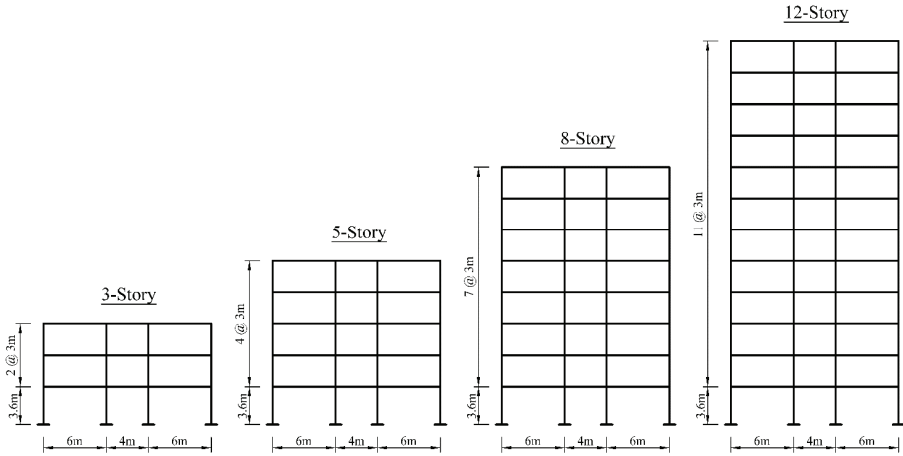


Figure 12 - Elevation of frames with their vertical and horizontal dimensions.

6.3. Discussion of the Results

The results obtained for the DDBD approach in accordance with both TSC-2007 and TBEC-2018, for some important parameters, are tabulated in Table 3 for the same frames, i.e., having the same cross-sectional sizes for columns and beams in both cases. From Table 3, it can be seen that up to equivalent damping, the results are the same in both cases, while after that, since TSC-2007 and TBEC-2018 are involved, the results are different. The ductility demands of the frames are slightly changing with respect to the height of the frames in both cases. The design displacement ductility (μ) is slightly reducing with the increase in the number of stories (in the case of three-story, since the depth of the beams is 50cm while in other cases it is 60cm; thus, the μ is smaller than the one for five and eight-story frames) in both cases. A similar conclusion can be made regarding equivalent damping. For frames with the same cross-sectional sizes of the beams, the stiffness of the frames is reducing significantly with the increasing number of stories. Stability indices, in the case of DDBD in accordance with TSC-2007 are slightly changing, while in accordance with TBEC-2018 the changes are significant. Finally, the changes in base shear forces obtained for frames through the DDBD approach in accordance with TSC-2007 are significant compared to the ones obtained for frames in accordance with TBEC-2018.

Tables 3-5 show the base shear forces obtained through the DDBD in compliance with TSC-2007 and TBEC-2018 and the ones obtained through TSC-2007 and TBEC-2018 by the ELF method for different R factors, respectively. These results are also shown in Figure 13. It should be noted that while modeling frames, the beams are assumed to be axially rigid members. From Table 4 and Figure 13a, it can be concluded that for the three-story frame, the base shear force obtained through the DDBD as per TSC-2007 is slightly smaller than the one obtained for the same frame through TSC-2007 by the ELF method for $R=4$. On the other hand, for the remaining frames, the DDBD approach estimates higher values of the base shear forces compared to the ones obtained for the same frames through TSC-2007 by the ELF method for $R=4$.

Table 2 - Re-designed sections for the studied RC frames through TBEC-2018

Frame	Story-Level	Member Size		
		Beams	Exterior Columns	Interior Columns
3-Story	1-3	25x50 cm	35x35 cm	35x35 cm
5-Story	1-5	30x50 cm	40x40 cm	40x40 cm
8-Story	1-8	30x50 cm	50x50 cm	50x50 cm
12-Story	1-8	30x50 cm	55x55 cm	55x55 cm
	8-12	30x50 cm	30x50 cm	30x50 cm

Table 3 - Initial design values of frames obtained through DDBD approach.

	According to TSC-2007				According to TBEC-2018			
	3-Story	5-Story	8-Story	12-Story	3-Story	5-Story	8-Story	12-Story
Drift Limit, θ_d (%)	2	2	2	2	2	2	2	2
Design Displacement, Δ_d (mm)	145.08	185.39	278.28	403.41	145.08	185.39	278.28	403.41
Effective height, H_e (m)	7.25	10.86	16.57	24.24	7.25	10.86	16.57	24.24
Effective Mass, m_e (ton)	163.17	293.40	473.37	731.85	163.17	293.40	473.37	731.85
Yield Displacement, Δ_y (mm)	89.37	111.54	170.11	248.82	89.37	111.54	170.11	248.82
Design Displacement Ductility, μ	1.62	1.66	1.64	1.62	1.62	1.66	1.64	1.62
Equivalent Damping, ξ_{eff} (%)	11.91	12.16	11.99	11.89	11.91	12.16	11.99	11.89
Effective Period, T_{eff} (sec)	1.464	1.807	2.525	3.432	1.898	2.444	3.649	5.275
Effective Stiffness, K_{eff} (kN/m)	3005.26	3546.03	2932.09	2453.20	1788.48	1939.77	1403.22	1038.36
Base Shear Force, V_{Base} (kN)	436.00	657.41	815.94	989.65	259.47	359.62	390.49	418.88
Stability Index, θ_{Δ}	0.09	0.09	0.12	0.15	0.16	0.17	0.25	0.32
Final Base Shear Forces, V_{Base} (kN)	436.00	657.41	868.01	1070.82	280.22	391.39	442.56	491.32

However, a different conclusion can be made about the results obtained for base shear forces for the frames through the DDBD in compliance with TBEC-2018 and the ones obtained for the same frames through TBEC-2018 by the ELF method. As it is evident from Table 5 and Figure 13, the base shear force obtained for the three-story frame through the DDBD in accordance with TBEC-2018 is very close to the value obtained through TBEC-2018 by the ELF method for $R=7$, while for the remaining frames base shear forces obtained through the DDBD in accordance with TBEC-2018 are close enough to the ones obtained through TBEC-2018 by the ELF method for $R=6$.

Another conclusion could be made regarding the results obtained through the TSC-2007 and TBEC-2018 by the ELF method. As can be seen from Tables 4 and 5, for the frames with the lower number of stories, both TSC-2007 and TBEC-2018 give close results; however, by increasing the number of stories, the differences in the results are significantly increasing. One of the reasons for such difference is due to the design displacement response spectra, which could be obtained from acceleration response spectra provided in both TSC-2007 and TBEC-2018.

As can be seen from Figure 4, the design displacement response spectrum for TSC-2007 is significantly larger than the one for TBEC-2018 for the same damping ratio and identical effective period. For example, for 5% damping at 6sec for TSC-2007, the design displacement is equal to around 1050 mm, while for TBEC-2018, it is equal to around 600 mm.

Table 4 - Base shear forces (kN) obtained through DDBD approach and ELF method based on TSC-2007

Number of Stories	DDBD	TSC-2007 by ELF method				
		R=4	R=5	R=6	R=7	R=8
3	436.00	457.27	365.81	304.85	261.30	228.63
5	657.41	620.28	496.23	413.52	354.45	310.14
8	868.01	770.87	616.70	513.92	440.50	385.44
12	1070.82	915.64	732.51	610.43	523.22	457.82

Table 5 - Base shear forces (kN) obtained through DDBD approach and ELF method based on TBEC-2018.

Number of Stories	DDBD	TBEC-2018 by ELF method				
		R=4	R=5	R=6	R=7	R=8
3	280.22	462.34	372.35	311.68	268.01	235.08
5	391.39	577.70	462.16	385.13	330.11	288.85
8	442.56	666.85	533.48	444.56	381.06	333.42
12	491.32	737.55	590.04	491.70	421.45	368.77

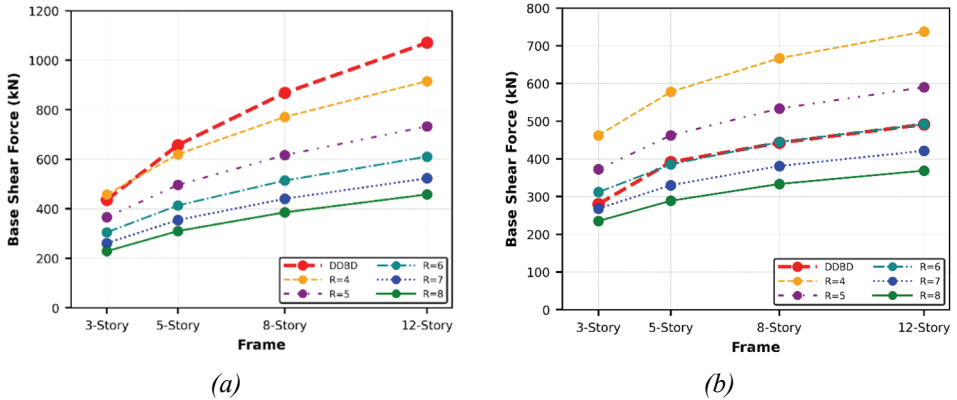


Figure 13 - Comparison of base shear forces obtained through DDBD approach and ELF method based on: (a) TSC-2007 and (b) TBEC-2018.

As mentioned earlier that, the base shear forces obtained for the frames through the DDBD in accordance with TBEC-2018 were very small (see Tables 4 and 5); therefore, cross-sectional dimensions for columns and beams are reduced. The DDBD approach in compliance with TBEC-2018, is once again applied on frames with smaller cross-sectional dimensions for columns and beams, and the base shear forces are obtained. The results of some important parameters are shown in Table 6. Note that for the 12-story frame, according to TBEC-2018, the stability index has exceeded the limit $\theta_{\Delta} = 0.32 > 0.30$ (see Table 3).

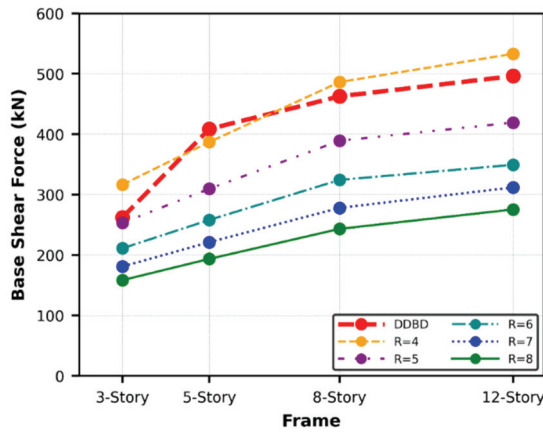


Figure 14 - Comparison of base shear forces obtained through DDBD approach and ELF method based on TBEC-2018 for the re-designed frames.

However, from equation (21), it is evident that the gravity loads also affect the stability index; thus, by reducing the gravity loads, the stability index may be reduced. With the reduction in

the cross-sectional dimensions, the gravity load is also reduced, which results reduction in the stability index (see Table 6, $\theta_{\Delta} = 0.28 < 0.30$). In addition, the same frames are analyzed through TBEC-2018 by the ELF method for different values of R , and the base shear forces are obtained. The results are tabulated in Table 7 together with the base shear forces obtained through the DDBD in compliance with TBEC-2018 and shown in Figure 14.

Table 6 - Initial design values of frames obtained through the DDBD approach for the re-designed frames.

	DDBD Results According to TBEC-2018			
	3-Story	5-Story	8-Story	12-Story
Drift Limit, θ_d (%)	2	2	2	2
Design Displacement, Δ_d (mm)	144.96	185.54	279.34	405.77
Effective height, H_e (m)	7.25	10.87	16.64	24.40
Effective Mass, m_e (ton)	154.01	270.43	438.37	648.51
Yield Displacement, Δ_y (mm)	89.30	133.96	205.02	300.65
Design Displacement Ductility, μ	1.62	1.39	1.36	1.35
Equivalent Damping, ξ_{eff} (%)	11.91	10.00	9.78	9.66
Effective Period, T_{eff} (sec)	1.897	2.286	3.417	4.943
Effective Stiffness, K_{eff} (kN/m)	1689.66	2042.54	1482.04	1047.83
Base Shear Force, V_{Base} (kN)	244.94	378.98	413.99	425.18
Stability Index, θ_{Δ}	0.14	0.15	0.22	0.28
Final Base Shear Forces, V_{Base} (kN)	262.20	408.53	462.54	496.25

Table 7 - Base shear forces (kN) obtained through DDBD approach and ELF method based on TBEC-2018 for the re-designed frames.

Number of Stories	DDBD	TBEC-2018 by ELF method				
		R=4	R=5	R=6	R=7	R=8
3	262.20	316.58	253.26	211.05	180.90	158.29
5	408.53	386.95	309.56	257.97	221.12	193.48
8	462.54	486.32	389.06	324.21	277.90	243.16
12	496.25	532.99	419.19	349.33	311.88	275.35

From Table 7 and Figure 14, it can be concluded that the depth of the beams has a significant effect on design displacement ductility, and with the increase in the depth of the beam, the design displacement ductility increases (refer to Equations (10)-(14)). As a consequence, increase in effective period and reduction in base shear force could be witnessed.

7. ANALYSIS AND RESULTS

7.1. Pushover Analysis and Results

The frames are designed in detail for the base shear forces obtained through the DDBD in accordance with TSC-2007 and TBEC-2018 (provided in Tables 4 and 7) by using TS-500. The capacity design principle is used to obtain the beam sway mechanism (i.e., strong-column weak-beam mechanism). In nonlinear static pushover analysis, horizontal forces are distributed up the height of the frames as inverse triangular. In this section, the results of the nonlinear static pushover are presented.

Nonlinear static pushover analysis is performed on all frames in both cases, and the results for the sway mechanism and pushover curves are shown. The results of the beam sway mechanism shown in Figure 15 for the frames designed for the base shear forces obtained through the DDBD approach in accordance with TSC-2007 are satisfactory. The capacity curves for these frames along with the idealized bilinear curves, are shown in Figure 16. The results of the beam sway mechanism shown in Figure 17 for the frames designed for the base shear forces obtained through the DDBD approach in accordance with TBEC-2018 are also satisfactory. The capacity curves for these frames along with the idealized bilinear curves, are shown in Figure 18. From Figures 15-18, it can be observed that the initial objective of the design of the frames, which is LS performance level, is satisfied for all frames, even for higher values of base shear forces than the design base shear forces.

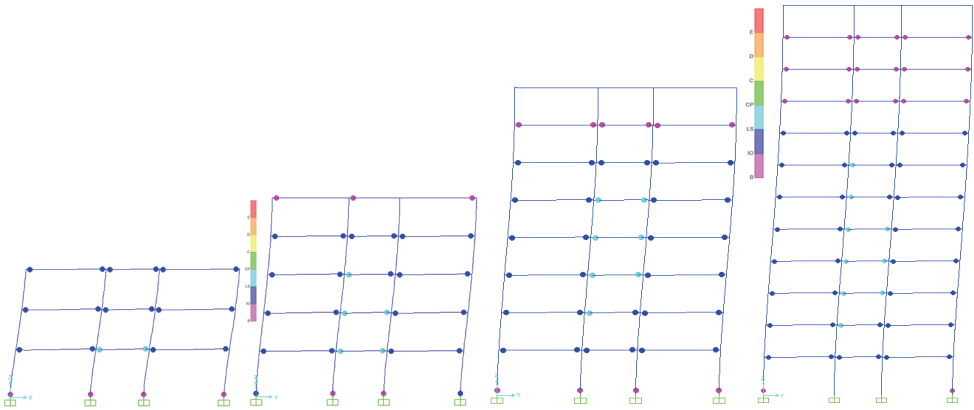


Figure 15 - Sway mechanisms obtained through pushover analysis for frames designed by DDBD in accordance with TSC-2007,

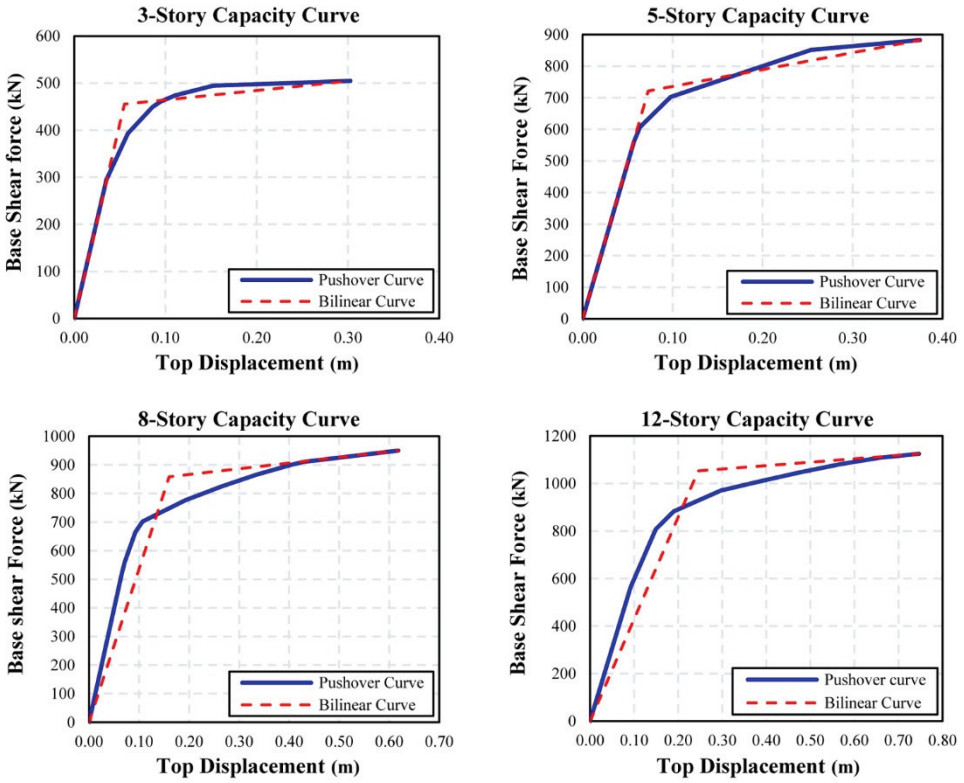


Figure 16 - Capacity curves obtained through pushover analysis for frames designed by DDBD in accordance with TSC-2007.

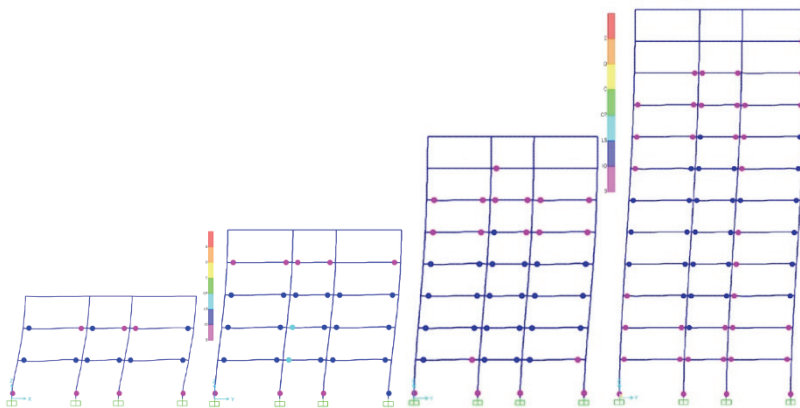


Figure 17 - Sway mechanisms obtained through pushover analysis for frames designed by DDBD in accordance with TBEC-2018.

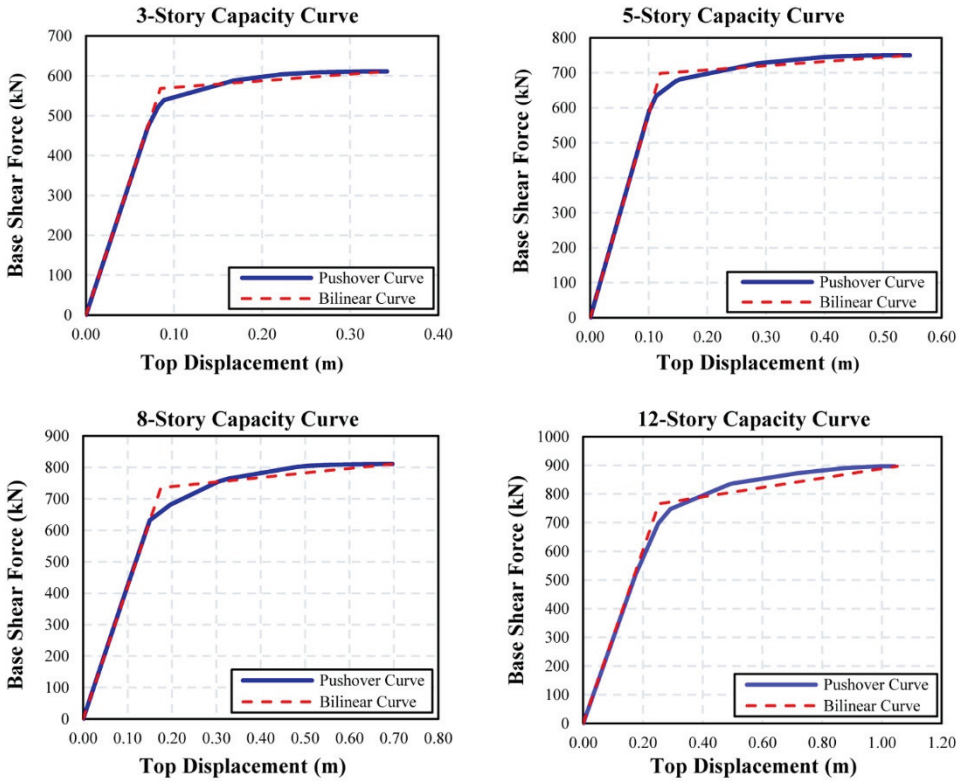


Figure 18 - Capacity curves obtained through pushover analysis for frames designed by DDBD in accordance with TBEC-2018.

The results for some of the important parameters together with the evaluated R values for the designed frames in both cases are tabulated in Table 8.

From the table, it can be observed that for the case in which frames are designed through the DDBD approach in accordance with TSC-2007, overstrength factors for all frames are around one. They are just above one for 3- and 5-story frames, while for the 8- and 12-story frames, they are exactly one. This is because the yield strength of the structure should not be less than the design strength of the structure; thus, the yield strength of the structure is kept at least equal to the design strength. However, for the case in which frames are designed through the DDBD approach based on TBEC-2018, overstrength factors for all frames are larger than one. In addition, generally, in both cases, the R values are reduced with an increase in the number of stories. Finally, from the table, it can be seen that RC frames designed using the DDBD approach based on TBEC-2018 provide higher R -value values than those designed using the DDBD approach based on TSC-2007. This is because of the overstrength factors, which for the cases designed through the DDBD approach with respect to TBEC-2018 are much larger than for the case of frames designed using the DDBD approach with respect to TSC-2007.

Table 8 - Evaluated values of R for designed frames with some important parameters.

Parameters	DDBD in Accordance with TSC-2007				DDBD in Accordance with TBEC-2018			
	3-Story	5-Story	8-Story	12-Story	3-Story	5-Story	8-Story	12-Story
V_d (kN)	436.00	657.41	858.83	1053.00	262.20	408.53	462.54	496.25
V_y (kN)	455.46	721.30	858.83	1053.00	568.20	698.14	735.46	765.72
V_u (kN)	504.61	882.99	950.15	1124.77	611.19	749.73	811.04	896.94
u_y (m)	0.0550	0.0728	0.1600	0.2455	0.0846	0.1197	0.1752	0.2533
u_{max} (m)	0.3027	0.3749	0.6180	0.7467	0.3418	0.5458	0.6970	1.0517
R_Ω	1.0446	1.0972	1.00	1.00	2.1670	1.7089	1.5901	1.5430
μ	5.5061	5.1486	3.8626	3.0415	4.0412	4.5595	3.9777	4.1523
T (sec)	0.7417	0.8783	1.2418	1.7741	0.8407	1.1357	1.6686	2.4758
Φ	1.0993	0.9786	0.8082	0.7995	0.9572	0.8470	0.8033	0.9027
R_μ	5.0989	5.2393	4.5417	3.5535	4.1771	5.2026	4.7067	4.4922
R	5.3265	5.7485	4.5417	3.5535	9.0518	8.8907	7.4839	6.9858

7.2. ET Analysis and Results

To compare the results obtained by the DDBD approach based on two Turkish seismic codes by dynamic analyses, the ET method is used due to its ability to decrease computational efforts and provide reasonable estimates of structural responses. To consider the impact of ground motion duration on the structural responses, the ETA40lc series of excitation functions are used for which the cumulative absolute velocity (CAV) has been included in its generation process. Three earthquake hazard levels having the probability of exceedance 50%, 10%, and 2% in 50 years with 72, 475, and 2475 years of return periods are considered.

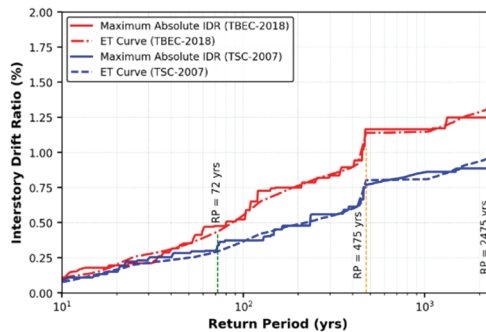


Figure 19 - Performance curve of 8-story RC frame designed by the DDBD approach in accordance with TSC-2007 and TBEC-2018.

According to the way previously stated, the target times of these excitation functions are also calculated for each frame corresponding to these hazard levels. The ET performance curve for eight-story frames is shown in Figure 19. Since the structures designed by the DDBD approach have different periods for TSC2007 and TBEC2018, the times are mapped to return periods. In this way, it becomes simpler to interpret the differences in the IDR results. As shown in the figure, TBEC-2018 exhibits higher IDRs values than TSC-2007 at various hazard levels. This confirms the results of pushover analysis as well.

The average values of maximum base shear forces of each frame at different hazard levels under ETA40lc01-03 are tabulated in Table 9 for the DDBD approach based on TSC-2007 and TBEC-2018. From the table, it can be concluded that as the number of stories increases, the base shear force is also increasing for all cases of hazard levels.

Table 9 - Average values of maximum base shear forces (kN) obtained from three ET analyses.

Number of Stories	TSC-2007			TBEC-2018		
	50%/50 yrs	10%/50 yrs	2%/50 yrs	50%/50 yrs	10%/50 yrs	2%/50 yrs
3	362.682	509.466	662.841	264.116	562.447	596.492
5	436.309	796.567	934.156	323.175	751.028	786.500
8	530.943	872.270	1161.959	335.760	835.601	935.933
12	544.646	1121.363	1477.376	380.879	878.117	1121.882

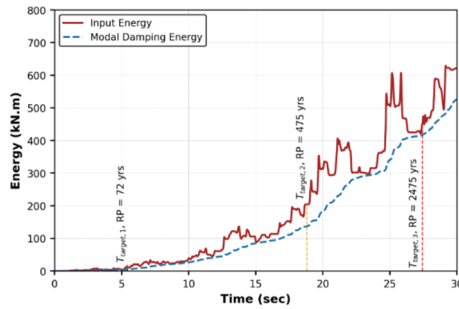
The average values of input energy and modal damping energy at target times corresponding to different hazard levels are tabulated in Table 10 and Table 11, respectively. Figure 20 shows the input and modal damping energies of the eight-story RC frame designed by the DDBD approach in accordance with TSC-2007 and TBEC-2018, obtained from ET analysis for the ETA40lc01 excitation function. In this figure, the target times for different hazard levels used in this study are also shown.

Table 10 - Average values of input energy (kN,m) at target times corresponding to different hazard levels

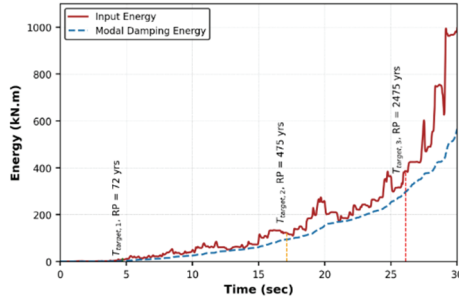
Number of Stories	TSC-2007			TBEC-2018		
	50%/50 yrs	10%/50 yrs	2%/50 yrs	50%/50 yrs	10%/50 yrs	2%/50 yrs
3	8.717	130.734	310.073	7.469	113.040	318.338
5	9.016	152.427	460.622	7.622	127.937	449.818
8	13.909	169.816	565.449	10.846	134.214	579.328
12	15.286	248.219	759.461	13.244	199.886	581.085

Table 11 - Average values of modal energy (kN.m) at target times corresponding to different hazard levels

Number of Stories	TSC-2007			TBEC-2018		
	50%/50 yrs	10%/50 yrs	2%/50 yrs	50%/50 yrs	10%/50 yrs	2%/50 yrs
3	5.742	94.345	277.810	4.094	74.787	256.388
5	5.936	119.810	406.166	4.298	96.019	344.250
8	7.719	132.585	477.114	4.436	104.832	373.628
12	8.071	172.255	582.258	6.853	98.679	252.792



(a)



(b)

Figure 20 - Input and modal damping energy for 8-story frame under ETA40lc01: TSC-2007 and (b) TBEC-2018.

In Figure 21, maximum IDRs resulting from ETA40lc01-03 excitation functions and their averages for frames designed by the DDBD approach in compliance with TSC-2007 are shown for three hazard levels used in this study. Whereas Figure 22 compares the results of average maximum IDRs for the frames designed by the DDBD approach based on TSC-2007 and TBEC-2018 for three hazard levels used in this study. From this figure, it is evident that in all cases, TBEC-2018 gives higher IDR values with respect to TSC-2007, except for the case of 3-story frame at lower hazard level with the return period of 72 years.

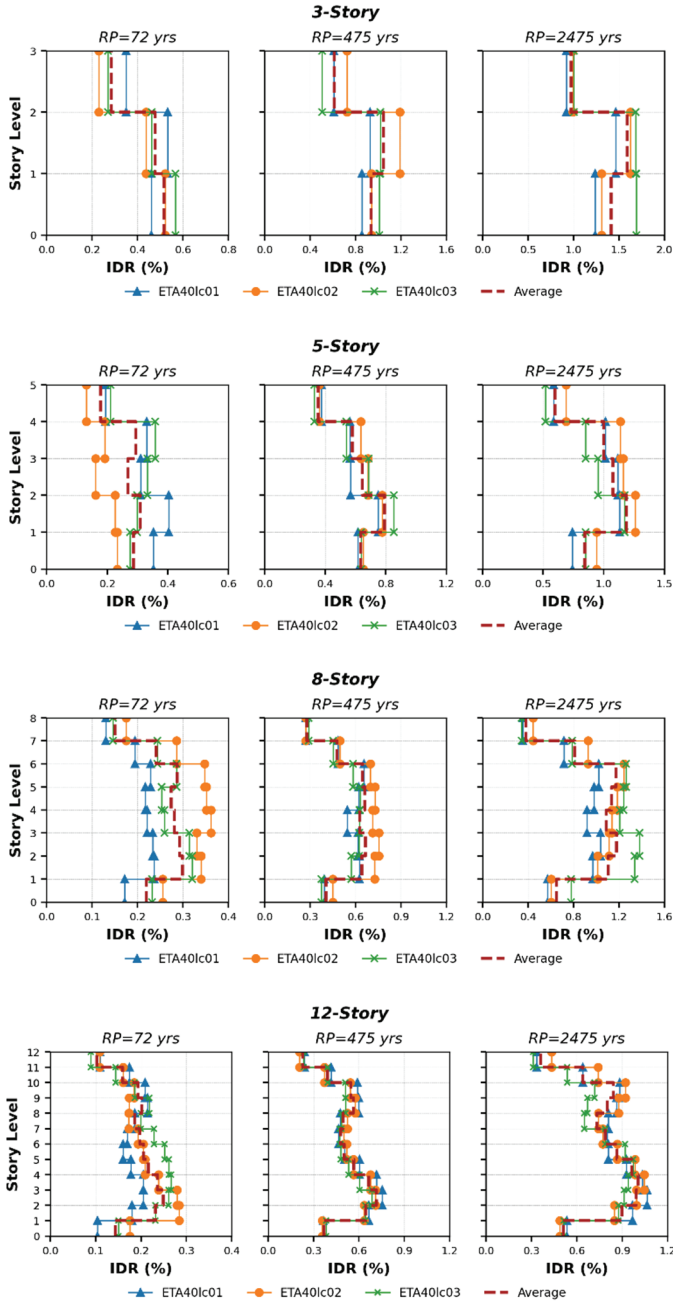


Figure 21 - IDR obtained through ET analysis for frames designed by DDBD in accordance with TSC-2007.

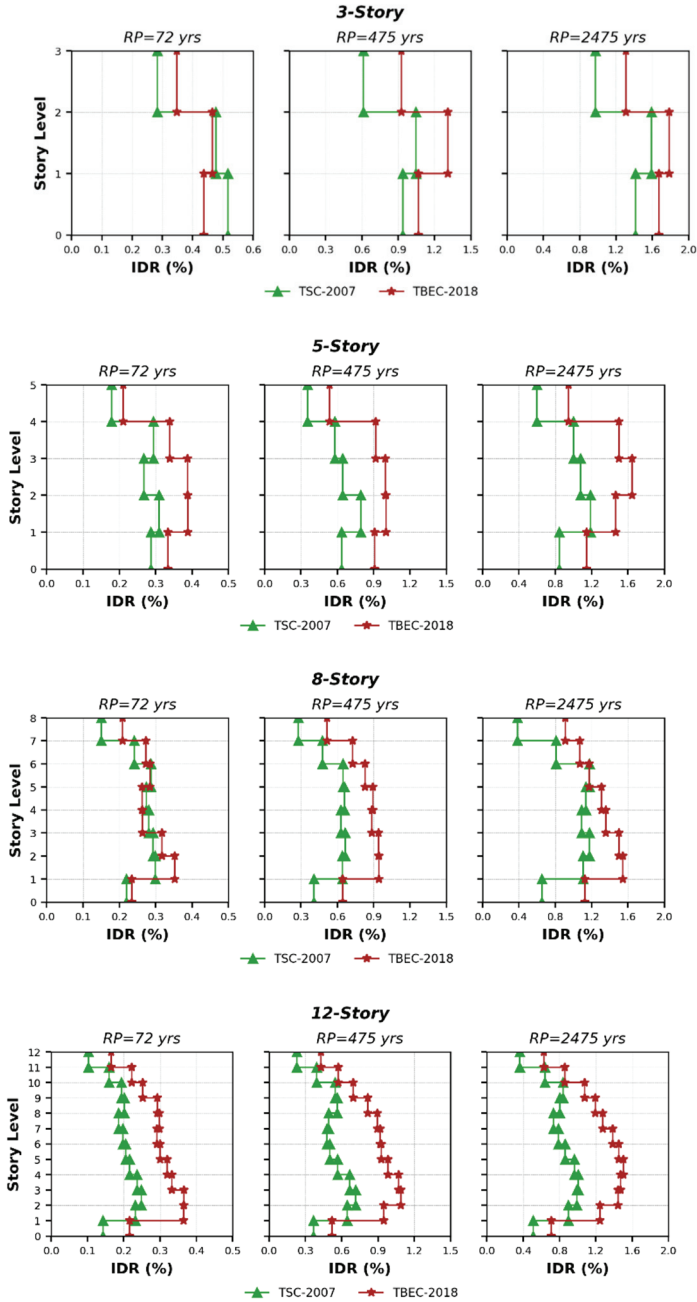


Figure 22 - Comparison of IDR obtained through ET analysis for frames designed by DDBD approach in accordance with TSC-2007 and TBEC-2018.

The difference percentage between maximum IDR, base shear force, input energy, and modal damping energy, obtained by the ET method between TSC-2007 and TBEC-2018, are tabulated in the following table.

Table 12 - Difference (%) of the results obtained by ET method between TSC-2007 and TBEC-2018

Number of Stories	Maximum IDR			Base Shear Force		
	50%/50 yrs	10%/50 yrs	2%/50 yrs	50%/50 yrs	10%/50 yrs	2%/50 yrs
3	10.47	22.37	11.55	31.45	9.89	10.54
5	22.92	23.45	32.42	29.79	5.89	17.16
8	16.50	34.55	26.83	45.04	4.29	21.55
12	38.23	41.15	39.79	35.39	24.33	27.35
	Input Energy			Modal Damping Energy		
3	15.42	14.52	2.63	33.52	23.13	8.02
5	16.76	17.47	2.37	32.02	22.05	16.50
8	24.74	23.42	2.42	54.02	23.38	24.33
12	14.31	21.57	26.61	16.31	54.31	78.91

8. SUMMARY AND CONCLUSIONS

In this paper, the DDBD approach, which is a performance-based design approach, has been applied to multi-story RC moment-resisting frames in accordance with the Turkish seismic design codes of TSC-2007 and TBEC-2018. The frames were also analyzed through TSC-2007 and TBEC-2018 by the ELF method, and the base shear forces were obtained. These base shear forces were compared with the ones obtained through the DDBD approach. The ET method is a time history-based procedure for seismic evaluation of structures under intensifying dynamic excitations aided to judge their performance at different intensity levels. Because of the ability of the ET method to diminish computational efforts and provide reasonable estimates of structural responses, it was also employed in this study to compare the results acquired by the DDBD approach on the basis of two Turkish seismic design codes.

The main findings of this research are summarized as follows:

- It was found that the DDBD approach in accordance with TSC-2007 gives higher base shear forces compared to the DDBD approach based on TBEC-2018 for frames with the same cross-sectional dimensions of the members.
- The analysis results obtained for the frames according to TSC-2007 and TBEC-2018 by the ELF method were also compared, and it was found that TBEC-2018 gives lower values of base shear forces compared to TSC-2007 for different values of R .

- After designing the frames, pushover analysis was implemented for performance assessment purposes. The beam-sway mechanism, i.e., the strong-column weak-beam concept, was satisfied for all frames in both cases.
- The results from pushover analysis also showed that frames designed through the DDBD approach in accordance with TSC-2007 give R values between 5.75 to 3.55, while the ones designed using the DDBD approach according to TBEC-2018 give R values between 6.99 to 9.05. It was also observed that with the increase in the number of stories, in general, the R values decrease in both cases.
- The ET performance curves of RC frames indicate that structures designed by the DDBD approach in accordance with TBEC-2018 exhibit higher IDRs values than TSC-2007 at various hazard levels.
- The ET analysis results showed that the DDBD approach, in accordance with TSC-2007, shows higher values for base shear force, input energy, and modal damping energy for all frames, compared to the DDBD approach as per TBEC-2018.
- The differences in the results between two Turkish seismic design codes obtained by the ET method were also calculated. It was observed that the differences in the results have various trends for the EDPs at three hazard levels used in this study.

References

- [1] Zou, X.K., Teng, J.G., De Lorenzis, L., Xia, S.H.: Optimal performance-based design of FRP jackets for seismic retrofit of reinforced concrete frames. *Compos. Part B Eng.* 38, 584–597 (2007). <https://doi.org/10.1016/j.compositesb.2006.07.016>
- [2] FEMA-445: Next-Generation Performance-Based Seismic Design Guidelines: Program Plan for New and Existing Buildings. Prepared for Federal Emergency Management Agency: Washington, DC, USA by Applied Technology Council, August 2006 (2006)
- [3] FEMA-P-58-1: Seismic performance assessment of buildings: Volume 1 – Methodology. , USA (2018)
- [4] Kalapodis, N.A., Papagiannopoulos, G.A., Beskos, D.E.: A comparison of three performance-based seismic design methods for plane steel braced frames. *Earthq. Struct.* 18, 27–44 (2020). <https://doi.org/10.12989/eas.2020.18.1.027>
- [5] Chopra, A.K., Goel, R.K.: Direct displacement-based design: Use of inelastic vs. Elastic design spectra. *Earthq. Spectra.* 17, 47–64 (2001). <https://doi.org/10.1193/1.1586166>
- [6] Moehle, J.P.: Displacement-Based Design of RC Structures Subjected to Earthquakes. *Earthq. Spectra.* 8, 403–428 (1992). <https://doi.org/10.1193/1.1585688>
- [7] Panagiotakos, T.B., Fardis, M.N.: A displacement-based seismic design procedure for RC buildings and comparison with EC8. *Earthq. Eng. Struct. Dyn.* 30, 1439–1462 (2001). <https://doi.org/10.1002/eqe.71>

- [8] Priestley, M.J.N., Kowalsky, M.J.: Direct Displacement-Based Seismic Design of Concrete Buildings. *Bull. New Zeal. Soc. Earthq. Eng.* 33, 421–444 (2000). <https://doi.org/10.5459/bnzsee.33.4.421-444>
- [9] Medhekar, M.S., Kennedy, D.J.L.: Displacement-based seismic design of buildings - application. *Eng. Struct.* 22, 210–221 (2000). [https://doi.org/10.1016/S0141-0296\(98\)00093-5](https://doi.org/10.1016/S0141-0296(98)00093-5)
- [10] Medhekar, M.S., Kennedy, D.J.L.: Displacement-based seismic design of buildings - theory. *Eng. Struct.* 22, 201–209 (2000). [https://doi.org/10.1016/S0141-0296\(98\)00092-3](https://doi.org/10.1016/S0141-0296(98)00092-3)
- [11] Priestley, M.J.N.: Myths and Fallacies in Earthquake Engineering - Conflicts between Design and Reality. *Bull. New Zeal. Soc. Earthq. Eng.* 26, 329–341 (1993)
- [12] Sullivan, T.J., Calvi, G.M., Priestley, M.J.N., Kowalsky, M.J.: The limitations and performances of different displacement based design methods. *J. Earthq. Eng.* 7, 201–241 (2003). <https://doi.org/10.1080/13632460309350478>
- [13] Priestley, M.J.N., Calvi, G.M., Kowalsky, M.J.: *Displacement-Based Seismic Design of Structures*. Pavia, ITALY, IUSS PRESS. ISBN: 978-88-6198-000-6 (2007)
- [14] Sullivan, T.J., Priestley, M.J.N., Calvi, G.M. eds: *A Model Code for the Seismic Design of Structures*. IUSS press Pavia, Italy, Pavia, ITALY (2012)
- [15] Pettinga, J.D., Priestley, M.J.N.: Dynamic behaviour of reinforced concrete frames designed with direct displacement-based design. *J. Earthq. Eng.* 9, 309–330 (2005). <https://doi.org/10.1142/S1363246905002419>
- [16] Sullivan, T.J., Priestley, M.J.N., Calvi, G.M.: Direct displacement-based design of frame-wall structures. *J. Earthq. Eng.* 10, 91–124 (2006). <https://doi.org/10.1080/13632460609350630>
- [17] Moghim, F., Saadatpour, M.M.: The applicability of Direct Displacement-Based Design in designing concrete buildings located in near-fault regions. In: *The 14th World Conference on Earthquake Engineering*. 12-17 October (2008)
- [18] Belleri, A.: *Displacement Based Design for Precast Concrete Structures*. Presented at the (2009)
- [19] Sullivan, T.J., Lago, A.: Towards a simplified Direct DBD procedure for the seismic design of moment resisting frames with viscous dampers. *Eng. Struct.* 35, 140–148 (2012). <https://doi.org/10.1016/j.engstruct.2011.11.010>
- [20] Malekpour, S., Dashti, F.: Application of the Direct Displacement Based Design Methodology for Different Types of RC Structural Systems. *Int. J. Concr. Struct. Mater.* 7, 135–153 (2013). <https://doi.org/10.1007/s40069-013-0043-2>
- [21] Pourali, N., Khosravi, H., Dehestani, M.: An investigation of P-delta effect in conventional seismic design and direct displacement-based design using elasto-plastic SDOF systems. *Bull. Earthq. Eng.* 17, 313–336 (2019). <https://doi.org/10.1007/s10518-018-0460-3>
- [22] Sahoo, D.R., Prakash, A.: Seismic behavior of concentrically braced frames designed using direct displacement-based method. *Int. J. Steel Struct.* 19, 96–109 (2019). <https://doi.org/10.1007/s13296-018-0092-0>

- [23] Yan, L., Gong, J.: Development of displacement profiles for direct displacement based seismic design of regular reinforced concrete frame structures. *Eng. Struct.* 190, 223–237 (2019). <https://doi.org/10.1016/j.engstruct.2019.04.015>
- [24] Giannakouras, P., Zeris, C.: Seismic performance of irregular RC frames designed according to the DDBD approach. *Eng. Struct.* 182, 427–445 (2019). <https://doi.org/10.1016/j.engstruct.2018.12.058>
- [25] Kumbhar, O.G., Kumar, R., Noroozinejad Farsangi, E.: Investigating the efficiency of DDBD approaches for RC buildings. *Structures.* 27, 1501–1520 (2020). <https://doi.org/10.1016/j.istruc.2020.07.015>
- [26] Malla, N., Wijeyewickrema, A.C.: Direct displacement-based design of coupled walls with steel shear link coupling beams. *Structures.* 34, 2746–2764 (2021). <https://doi.org/10.1016/j.istruc.2021.09.004>
- [27] Papagiannopoulos, G.A., Hatzigeorgiou, G.D., Beskos, D.E.: Direct Displacement-Based Design. (2021)
- [28] Sharma, A., Tripathi, R.K., Bhat, G.: Direct-displacement and force-based seismic assessment of RC frame structures. *J. Build. Pathol. Rehabil.* 7, (2022). <https://doi.org/10.1007/s41024-021-00160-z>
- [29] Mohebbi, M., Noruzvand, M., Dadkhah, H., Shakeri, K.: Direct displacement-based design approach for isolated structures equipped with supplemental fluid viscous damper. *J. Build. Eng.* 45, (2022). <https://doi.org/10.1016/j.jobe.2021.103684>
- [30] Kalapodis, N.A., Muho, E. V., Beskos, D.E.: Seismic design of plane steel MRFS, EBFS and BRBFS by improved direct displacement-based design method. *Soil Dyn. Earthq. Eng.* 153, 107111 (2022). <https://doi.org/10.1016/j.soildyn.2021.107111>
- [31] Estekanchi, H.E., Vafai, A., Sadegh, A.M.: Endurance time method for seismic analysis and design of structures. *Sci. Iran.* 11, 361–370 (2004)
- [32] Estekanchi, H.E., Mashayekhi, M., Vafai, H., Ahmadi, G., Mirfarhadi, S.A., Harati, M.: A state-of-knowledge review on the endurance time method. *Structures.* 27, 2288–2299 (2020). <https://doi.org/10.1016/j.istruc.2020.07.062>
- [33] Estekanchi, H.E., Harati, M., Mashayekhi, M.R.: An investigation on the interaction of moment-resisting frames and shear walls in RC dual systems using endurance time method. *Struct. Des. Tall Spec. Build.* 27, 1–16 (2018). <https://doi.org/10.1002/tal.1489>
- [34] Mashayekhi, M., Harati, M., Estekanchi, H.E.: Development of an alternative PSO-based algorithm for simulation of endurance time excitation functions. *Eng. Reports.* 1, 1–15 (2019). <https://doi.org/10.1002/eng2.12048>
- [35] Mashayekhi, M., Estekanchi, H.E., Vafai, H.: Simulation of Endurance Time Excitations via Wavelet Transform. *Iran. J. Sci. Technol. - Trans. Civ. Eng.* 43, 429–443 (2019). <https://doi.org/10.1007/s40996-018-0208-y>
- [36] Shirkhani, A., Farahmand Azar, B., Charkhtab Basim, M.: Optimum slip load of T-shaped friction dampers in steel frames by endurance time method. *Proc. Inst. Civ. Eng. Struct. Build.* 173, 746–760 (2020). <https://doi.org/10.1680/jstbu.18.00169>

- [37] Shirkhani, A., Farahmand Azar, B., Charkhtab Basim, M.: Evaluation of efficiency index of friction energy dissipation devices using endurance time method. *Numer. Methods Civ. Eng.* 5, 12–20 (2020). <https://doi.org/10.52547/nmce.5.2.12>
- [38] Hariri-Ardebili, M.A., Sattar, S., Estekanchi, H.E.: Performance-based seismic assessment of steel frames using endurance time analysis. *Eng. Struct.* 69, 216–234 (2014). <https://doi.org/10.1016/j.engstruct.2014.03.019>
- [39] Amouzegar, H., Riahi, H.T.: Seismic assessment of concrete frames by endurance time method. *Proc. Inst. Civ. Eng. Struct. Build.* 168, 578–592 (2015). <https://doi.org/10.1680/stbu1400042>
- [40] Mashayekhi, M., Estekanchi, H.E., Vafai, A., Mirfarhadi, S.A.: Simulation of Cumulative Absolute Velocity Consistent Endurance Time Excitations. *J. Earthq. Eng.* 25, 892–917 (2018). <https://doi.org/10.1080/13632469.2018.1540371>
- [41] Shirkhani, A., Mualla, I.H., Shabakhty, N., Mousavi, S.R.: Behavior of steel frames with rotational friction dampers by endurance time method. *J. Constr. Steel Res.* 107, 211–222 (2015). <https://doi.org/10.1016/j.jcsr.2015.01.016>
- [42] Mashayekhi, M., Estekanchi, H.E., Vafai, H., Mirfarhadi, S.A.: Development of hysteretic energy compatible endurance time excitations and its application. *Eng. Struct.* 177, 753–769 (2018). <https://doi.org/10.1016/j.engstruct.2018.09.089>
- [43] Basim, M.C., Estekanchi, H.E.: Application of endurance time method in performance-based optimum design of structures. *Struct. Saf.* 56, 52–67 (2015). <https://doi.org/10.1016/j.strusafe.2015.05.005>
- [44] Riahi, H.T., Estekanchi, H.E.: Seismic assessment of steel frames with the endurance time method. *J. Constr. Steel Res.* 66, 780–792 (2010). <https://doi.org/10.1016/j.jcsr.2009.12.001>
- [45] Shirkhani, A., Farahmand Azar, B., Charkhtab Basim, M.: Seismic loss assessment of steel structures equipped with rotational friction dampers subjected to intensifying dynamic excitations. *Eng. Struct.* 238, 112233 (2021). <https://doi.org/10.1016/j.engstruct.2021.112233>
- [46] TSC: Turkish Seismic Design Code : Specification for Structures to be Built in Disaster Areas. Ministry of Public Works and Settlement Government of Republic of Turkiye (2007)
- [47] TBEC: Turkish Building Earthquake Code. The Disaster and Emergency Management Authority (AFAD), Ankara , Turkiye. (2018)
- [48] TS-500: Requirements for Design and Construction of Reinforced Concrete Structures. English version, publication NO.2003/1. Turkish Standards Institute, Ankara Turkiye. (2000)
- [49] Ersoy, U., Özcebe, G., Tankut, T.: Reinforce Concrete. METU Press. ISBN:978-605-4362-17-2, Middle East Technical University (METU), Ankara, Turkiye (2013)
- [50] Soyuluk, A., Harmankaya, Z.Y.: The History of Development in Turkish Seismic Design Codes. *Int. J. Civ. Environ. Eng.* 12, 25–29 (2012)
- [51] Atmaca, N., Atmaca, A., Kılçık, S.: Comparison of 2018 and 2007 Turkish Earthquake Regulations. *Int. J. Energy Eng. Sci.* 4, 19–25 (2019)

- [52] Aksoylu, C., Mobark, A., Arslan, M.H., Erkan, I.H.: A comparative study on ASCE 7-16, TBEC-2018 and TEC-2007 for reinforced concrete buildings. *Rev. la Constr.* 19, 282–305 (2020). <https://doi.org/10.7764/RDLC.19.2.282>
- [53] Džaki, D., Kraus, I., Mori, D.: Direct Displacement Based Design of Regular Concrete Frames in Compliance With Eurocode 8. 19, 973–982 (2012)
- [54] Pettinga, J.D.: *Dynamic Behaviour of Reinforced Concrete Frames Designed with Direct Displacement-Based Design*, (2005)
- [55] Massena, B., Bento, R., Degée, H.: Direct displacement based design of a RC frame – Case of study. (2010)
- [56] Priestley, M.J.N., Calvi, G.M., Kowalsky, M.J.: Direct Displacement-Based Seismic Design of Structures. In: NZSEE Conference. , New Zealand, 2007 (2007)
- [57] Habibi, A., Gholami, R., Izadpanah, M.: Behavior factor of vertically irregular RCMRFs based on incremental dynamic analysis. *Earthq. Struct.* 16, 655–664 (2019). <https://doi.org/10.12989/eas.2019.16.6.655>
- [58] Fayed, M.N., Nasr, N.E., Saleh, M., Ahmed, G.M.: Seismic Response Modification factors for Multi-Story R.C buildings having Flat Slab System. *IOSR J. Mech. Civ. Eng.* 17, 1–14 (2020). <https://doi.org/10.9790/1684-1701050114>
- [59] Hussein, M.M., Gamal, M., Attia, W.A.: Seismic response modification factor for RC-frames with non-uniform dimensions. *Cogent Eng.* 8, (2021). <https://doi.org/10.1080/23311916.2021.1923363>
- [60] Mahmoudi, M., Zaree, M.: Evaluating response modification factors of concentrically braced steel frames. *J. Constr. Steel Res.* 66, 1196–1204 (2010). <https://doi.org/10.1016/j.jcsr.2010.04.004>
- [61] Mohamed, A.E., Attia, W.A., El-Degwy, W.M.: Seismic Response Modification Factor of Reinforced Concrete Frames Based on Pushover Analysis. *J. Archit. Environ. Struct. Eng. Res.* 2, 2–10 (2019). <https://doi.org/10.30564/jaeser.v2i2.818>
- [62] Mwafy, A.M., Elnashai, A.S.: Calibration of force reduction factors of RC buildings. *J. Earthq. Eng.* 6, 239–273 (2002). <https://doi.org/10.1080/13632460209350416>
- [63] Zahrai, S.M., Khorraminejad, A., Sedaghati, P.: Response modification factors of concrete bridges with different bearing conditions. *Earthq. Struct.* 16, 185–196 (2019). <https://doi.org/10.12989/eas.2019.16.2.185>
- [64] Pérez, J.C.V., Loachamín, M.A.C.: Calibration of the response reduction factors used in Ecuador for steel SMRF. *Bull. Int. Inst. Seismol. Earthq. Eng.* 52, 22–37 (2018)
- [65] Sadeghi, A., Abdollahzadeh, G., Rajabnejad, H., Naseri, S.A.: Numerical analysis method for evaluating response modification factor for steel structures equipped with friction dampers. *Asian J. Civ. Eng.* 22, 313–330 (2021). <https://doi.org/10.1007/s42107-020-00315-2>
- [66] Miranda, E., Bertero, V. V.: Evaluation of Strength Reduction Factors for Earthquake-Resistant Design. *Earthq. Spectra.* 10, 357–379 (1994). <https://doi.org/10.1193/1.1585778>
- [67] ATC-19: Structural Response Modification Factors. Applied Technology Council, 555 Twin Dolphin Drive, Suite 550, Redwood City, California. (1995)

- [68] Estekanchi, H.E., Vafai, A., Riahi, H.T.: Endurance Time Method: From ideation to Application. In: US-Iran Seismic Workshop. bl 205–218 (2009)
- [69] Vamvatsikos, D., Allin Cornell, C.: Incremental dynamic analysis. *Earthq. Eng. Struct. Dyn.* 31, 491–514 (2002). <https://doi.org/10.1002/eqe.141>
- [70] Azarbakht, A., Dolsek, M.: Prediction of the median IDA curve by employing a limited number of ground motion records. *Earthq. Eng. Struct. Dyn.* 36, 2401–2421 (2007). <https://doi.org/DOI: 10.1002/eqe.740> Prediction
- [71] Mashayekhi, M., Harati, M., Ashoori Barmchi, M., Estekanchi, H.E.: Introducing a response-based duration metric and its correlation with structural damages. *Bull. Earthq. Eng.* 17, 5987–6008 (2019). <https://doi.org/10.1007/s10518-019-00716-y>
- [72] Hancock, J., Bommer, J.J.: Using spectral matched records to explore the influence of strong-motion duration on inelastic structural response. *Soil Dyn. Earthq. Eng.* 27, 291–299 (2007). <https://doi.org/10.1016/j.soildyn.2006.09.004>
- [73] Harati, M., Mashayekhi, M., Ashoori Barmchi, M., Estekanchi, H.: Influence of Ground Motion Duration on the Structural Response at Multiple Seismic Intensity Levels. *Numer. Methods Civ. Eng.* 3, 10–23 (2019). <https://doi.org/10.29252/nmce.3.4.10>
- [74] Mashayekhi, M., Harati, M., Darzi, A., Estekanchi, H.E.: Incorporation of strong motion duration in incremental-based seismic assessments. *Eng. Struct.* 223, 111144 (2020). <https://doi.org/10.1016/j.engstruct.2020.111144>
- [75] Cabanas, L., Benito, B., Herraiz, M.: An Approach To the Measurement of the Potential Structural Damage of Earthquake Ground Motions. *Earthq. Eng. Struct. Dyn.* 26, 79–92 (1997). [https://doi.org/10.1002/\(SICI\)1096-9845\(199701\)26:1<79::AID-EQE624>3.0.CO;2-Y](https://doi.org/10.1002/(SICI)1096-9845(199701)26:1<79::AID-EQE624>3.0.CO;2-Y)
- [76] Reed, J.W., Kassawara, R.P.: A criterion for determining exceedance of the operating basis earthquake. *Nucl. Eng. Des.* 123, 387–396 (1990). [https://doi.org/10.1016/0029-5493\(90\)90259-Z](https://doi.org/10.1016/0029-5493(90)90259-Z)
- [77] Campbell, K.W., Bozorgnia, Y.: A comparison of ground motion prediction equations for arias intensity and cumulative absolute velocity developed using a consistent database and functional form. *Earthq. Spectra.* 28, 931–941 (2012). <https://doi.org/10.1193/1.4000067>
- [78] Harati, M., Mashayekhi, M., Estekanchi, H.E.: Correlation of ground motion duration with its intensity metrics: A simulation based approach. *J. Soft Comput. Civ. Eng.* 4, 17–39 (2020). <https://doi.org/10.22115/SCCE.2020.227576.1207>
- [79] FEMA-P695: Quantification of building seismic performance factors. Federal Emergency Management Agency, Washington, DC (2009)
- [80] Estekanchi, H.E., Valamanesh, V., Vafai, A.: Application of Endurance Time method in linear seismic analysis. *Eng. Struct.* 29, 2551–2562 (2007). <https://doi.org/10.1016/j.engstruct.2007.01.009>

Appendix

The reinforcement details are provided in the following figures for the elements of all structures.

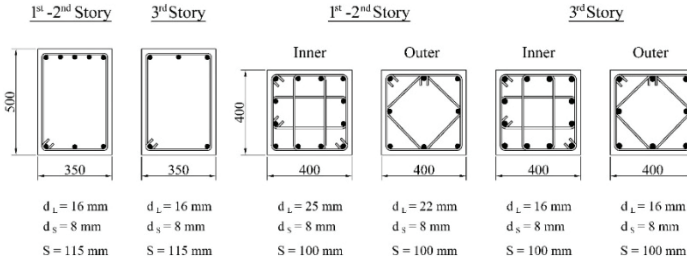


Figure A.1 - Cross-sections of columns and beams for 3-Story structure designed using the DDBD approach in accordance with TSC-2007.

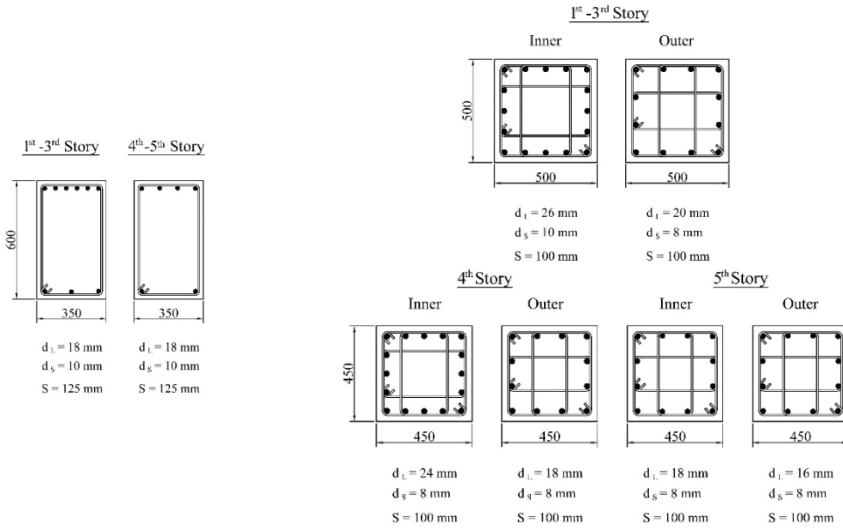


Figure A.2 - Cross-sections of columns and beams for 5-Story structure designed using the DDBD approach in accordance with TSC-2007.

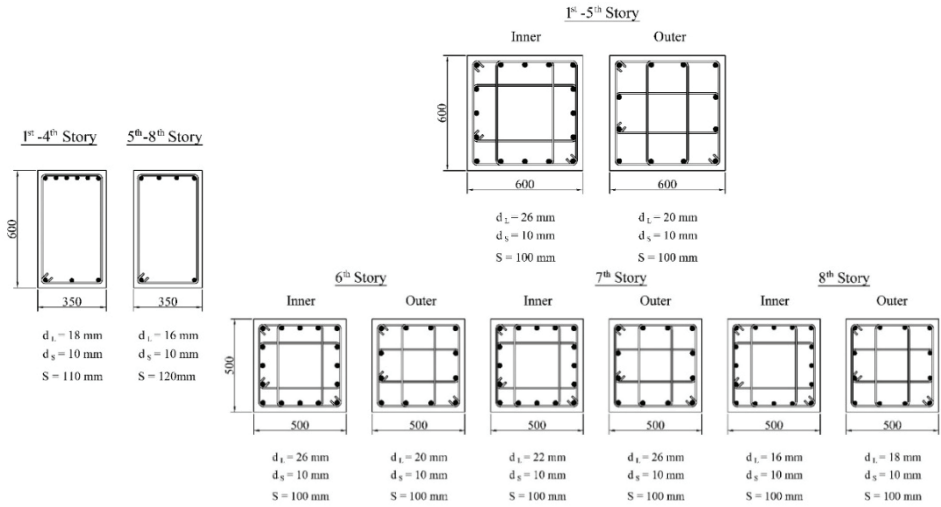


Figure A.3 - Cross-sections of columns and beams for 8-Story structure designed using the DDBD approach in accordance with TSC-2007.

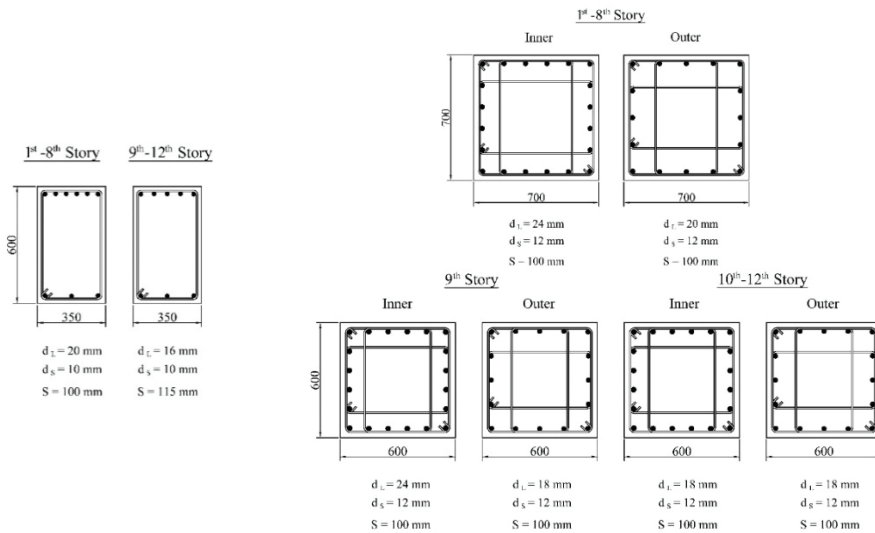


Figure A.4 - Cross-sections of columns and beams for 12-Story structure designed using the DDBD approach in accordance with TSC-2007.

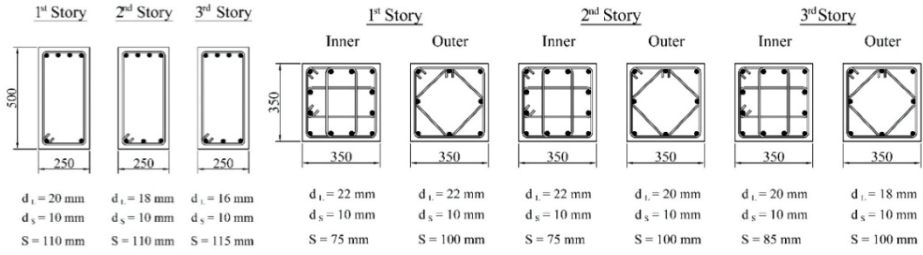


Figure A.5 - Cross-sections of columns and beams for 3-Story structure designed using the DDBD approach in accordance with TBEC-2018.

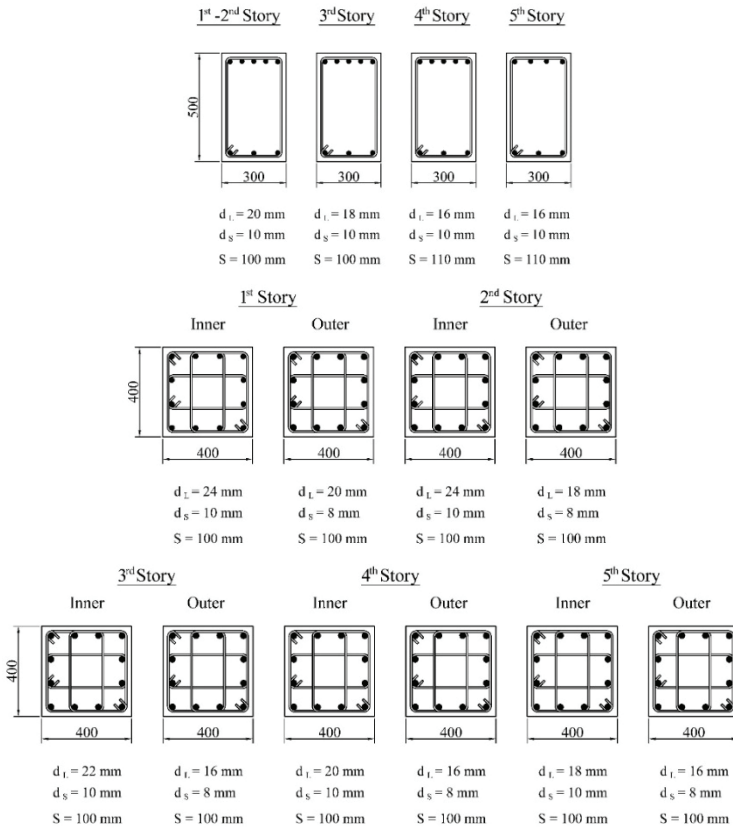


Figure A.6 - Cross-sections of columns and beams for 3-Story structure designed using the DDBD approach in accordance with TBEC-2018.

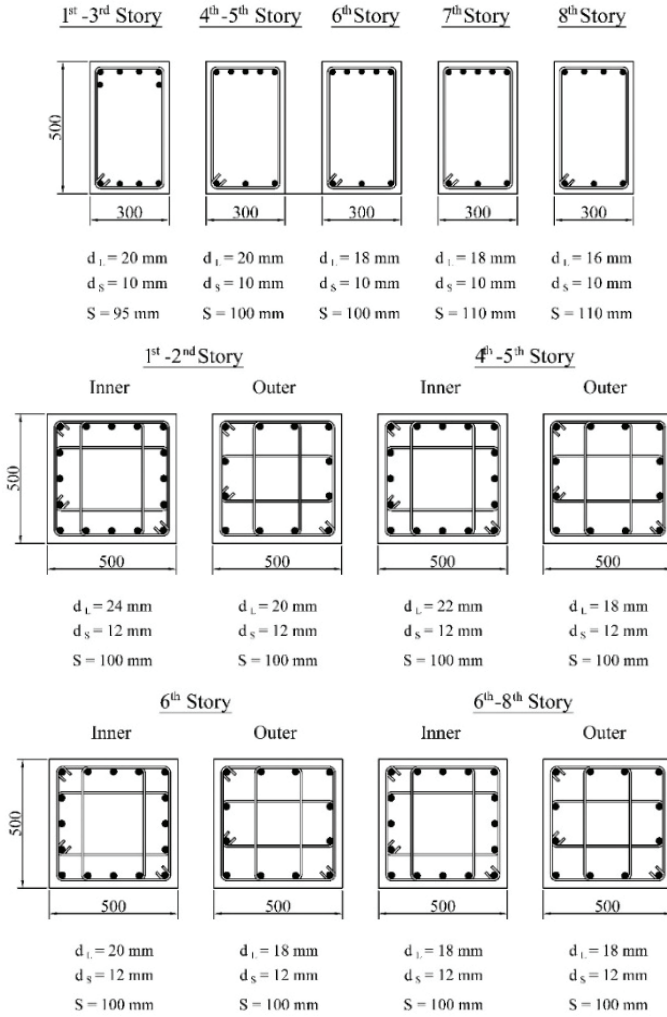


Figure A.7 - Cross-sections of columns and beams for 8-Story structure designed using the DDBD approach in accordance with TBEC-2018.

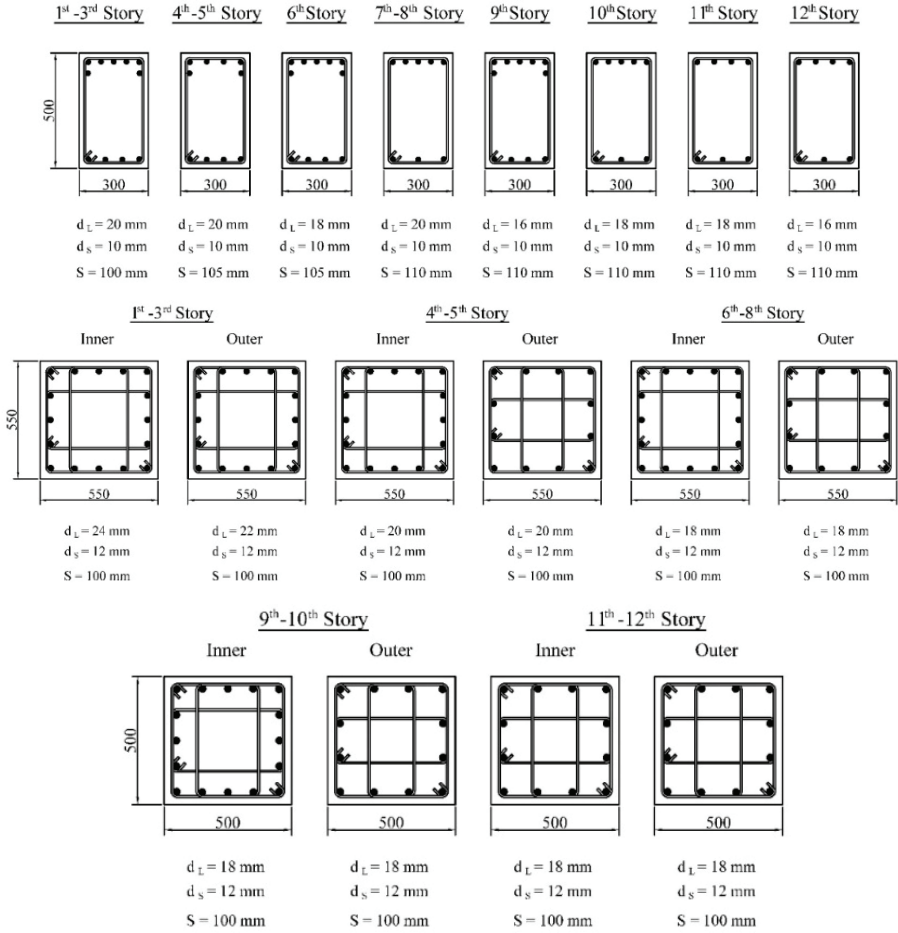


Figure A.8 - Cross-sections of columns and beams for 12-Story structure designed using the DDBD approach in accordance with TBEC-2018.

From Cut-in to Qanats - Ancient Groundwater Extraction Techniques

Hartmut WITTENBERG¹
Hafzullah AKSOY^{2,*}



ABSTRACT

Where a hillside stratified aquifer intersects the earth surface, springs and seepings from the surface are observed. Cutting into this zone, thus opening it by digging, allows to increase and capture water outflow. As a matter of principle this classical method for water extraction without pumping, which is still found in hilly rural regions today, was already used 3600 years ago by the Hittites to fill the ponds of their capital Hattuša in Central Anatolia. The today sedimented reservoirs were dug downhill of groundwater bearing zones. Rising in winter, groundwater discharged into the ponds through alongside cuts. The Hittites avoided the risks of strongly varying surface flows by opening near-surface groundwater and stratum aquifers. Although hydraulic investigation based on in-situ measurement of groundwater level supports the short-term efficiency of the ponds in supplying water to the ancient city, at the long-term, the decline of the Empire was probably triggered by severe droughts expanded over years. This seems plausible as severe droughts are still being experienced. For a higher and more reliable water yield, the further development went from 'cutting' in to 'penetrating' into the aquifer with tunnel-like drain conduits which collected the water and conveyed it to settlements and irrigation schemes. The improved water extraction system, named qanats, appeared in Eastern Anatolia and Persia about 500 years after the abandon of Hattuša. An example of a qanat system in western Iran is presented in this study with less emphasis compared to the cut-in yet representative enough to demonstrate its role in supplying water sustainably. We conclude that the ancient time thinking is the same as that of modern engineering, and the ancient time hydraulic works are fundamental for today's civil structures.

Keywords: Cut-in, qanats, groundwater extraction, Hattuša, Hittites, Persians.

Note:

- This paper was received on February 8, 2023 and accepted for publication by the Editorial Board on October 13, 2023.
- Discussions on this paper will be accepted by May 31, 2024.
- <https://doi.org/10.18400/tjce.1247836>

1 Leuphana University of Lüneburg, Institute of Ecology, Lüneburg, Germany
wittenberg@leuphana.de - <https://orcid.org/0000-0001-6467-1194>

2 Istanbul Technical University, Department of Civil Engineering, İstanbul, Türkiye
haksoy@itu.edu.tr - <https://orcid.org/0000-0001-5807-5660>

* Corresponding author

1. INTRODUCTION

With increasing concern on the global climate change and the local asymmetrical balance between water demand and supply, drought remained one of the unsolved problems of hydrological extremes [1]. This is the fundamental reason for the bloomed interest about the drought not only to better understand its technical context at local, regional or larger scales, and to develop methodologies [2-6] but also to link the drought with its social aspects due to the direct impact on economy, ecology and society [7-8]. As it is for today, the drought has affected on the society in the ancient time. Its effect has been such strong that several well-known civilizations including the Mayas [9-11], the Hittites [12-13], and civilizations along the ancient Silk Road [14] have collapsed because of its consequences reducing the agricultural yield, causing famine and destabilizing the food security.

Drought is related to deficit in water resources through a cause-effect link. Any deficit in water makes the resources unsustainable and thus unreliable. To combat water deficit as a result of unsustainable water availability because of either the usual within-year seasonality or the over-year variability during prolonged dry periods with severe droughts, water is collected in natural or human-made small scale ponds or large-scale dam reservoirs. This has been practiced in the ancient time as well in a much less modern fashion than today. The Hittites, an ancient civilization in Central Anatolia, Turkey, have practiced these by building dam to collect water in reservoirs. A simpler technology they have practiced is the so-called 'cut-in' the groundwater aquifer, which is the issue we present in this study. In the absence of modern machinery technology in the ancient time, stored water has been conveyed to lower altitude points where water is demanded by using the gravity through open channels or underground pipes. For arid regions where surface water resources are lacking, qanats, another technology, that convey water from the groundwater aquifer through underground galleries excavated for long distances have been used.

In this study, we look at these two ancient water extraction techniques; the 'cut-in' and 'qanats', the latter is being more engineered than the former. The 'qanat' technology has been well documented in the literature, while the 'cut-in' technology itself and its transition (or better we say its evolution) from the water-storing 'cut-in' to the water-conveying 'qanats' has not been well demonstrated. Thus, we pay an attention to this evolution with less emphasis on qanats through examples from Central Anatolia in Turkey and Western Iran.

2. THE HITTITE'S CUT-IN WATER COLLECTION SYSTEM

Among many ancient civilizations, the Hittites who settled in the Hattuša (Hattusha) region in Central Anatolia, Turkey (Figure 1) have left remarkable remains of water works [15]. Hattuša is in the western part of the Kızılırmak River basin at approximately 40°N and 34.6°E. The area of the ruined city rises from about 950 m above sea level in the north to 1250 m in the south. The mean annual temperature is between 8 and 9°C, with great seasonal variation. Mean annual precipitation is around 500 mm, significantly smaller than the potential annual evapotranspiration of about 1000 mm caused by the high solar radiation. The deficit of 500 mm occurs in the period from April to November and leads to high water losses and intermitting the surface runoff. The discharge of the small creek, Budaközü, which flows in the valley east below the ruined city to the north, fluctuates at the gauging station 15-166 Boğazkale of State Hydraulic Works (Devlet Su İşleri) of Turkey between more than

25 m³/s (400 l s⁻¹ km⁻²) at snow melting season and less than 20 l/s (0.32 l s⁻¹ km⁻²) in the dry summer.

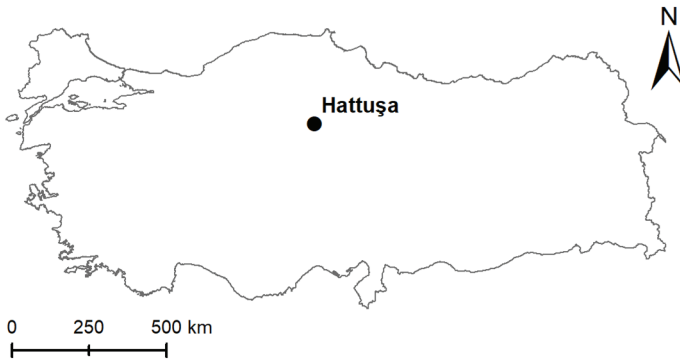


Figure 1 - Location of the Hittites' capital city Hattuşa (Hattusha) in Central Anatolia, Turkey.

The excavations and investigations in the archaeological site yielded extensive knowledge about construction techniques, history, culture and social structure of the Hittites and life in their capital Hattuşa (Figure 2). However, the issue of the city water supply received less attention, apart from the discovery of some cisterns, water basins and springs. There are remains of dams, irrigation canals, and water collection structures from the Hittite period in Central Anatolia dating back to the second millennium BC [16]. Many thousands of people lived and worked on the steeply sloping terrain of today's ruined city, whose households, gardens, livestock, workshops, and places of worship had to be supplied with water and protected from fire. Targeted water management was necessary for this, especially in view of the hot and dry summers.

In 1989, larger, completely sedimented water reservoirs were discovered in the upper city and excavations were carried out on them, initially at the two eastern ponds with a capacity of approximately 36,000 m³, and from the year 2000 at the complex of the five southern ponds (total volume 20,000 m³) (see map in Figure 3 from [17]). When P. Neve uncovered East Pond 1 (Ostteich 1), found by himself, he considered it to be a cultic facility, a "sacred pond". However, the size of the reservoir and several Hittite hydraulic structures that were documented in the following period suggested that the ponds played an essential role in the water supply. Therefore, the issue was investigated from the hydraulic engineering perspective [18].

In the region, numerous artesian wells and cattle troughs indicate abundant groundwater resources while at the same time, rivers and streams fall dry. There are also various spring horizons on the slope of the ruined city and south of it, which presumably fed the ponds 1 and 2 in the central upper town (Figure 3), as well as some fountains in the urban area. In modern times, the city of Boğazkale, located directly to the north below Hattuşa, is supplied with drinking water from the hillside springs, some of which are located within the ruins. The wells are still in use today.



Figure 2 - Remains and ruins of the lower city of Hattusa.

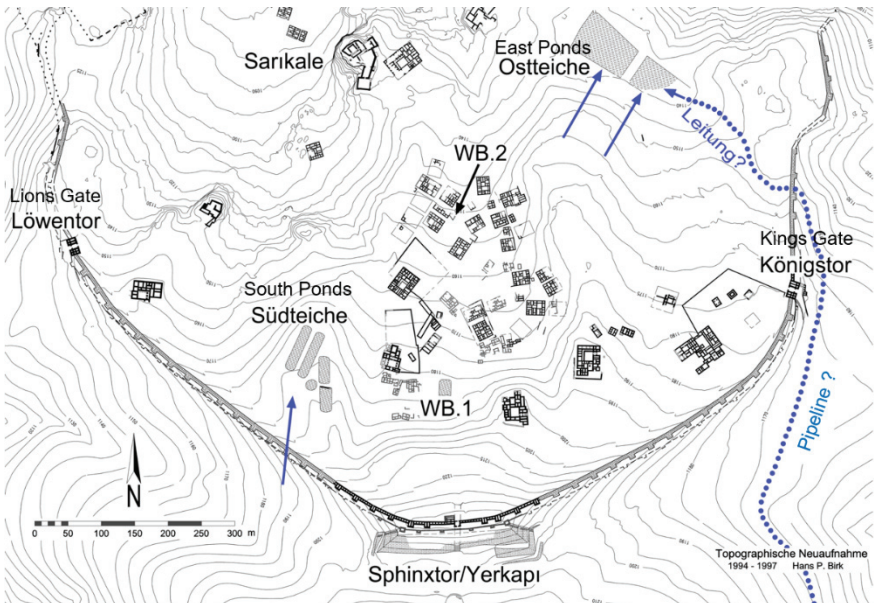


Figure 3 - Topographic map of the upper city of Hattusa with East and South ponds [17] as revised by J. Seeher in 2023. The blue dotted line with question marks shows the approximate routing of the initially assumed pipeline, the blue arrows indicate the seepage directions of groundwater into the ponds.

3. FROM CUT-IN TO QANATS

We easily understand that after the climatic catastrophe and its impacts on civilization, antique engineers looked for methods for a higher and more reliable water supply. After the ‘cutting-in’ water-bearing layers, it was logical to expect more water by ‘penetrating’ the layer through a gallery called qanats (from Arabic canal) as a follow-up technology. Qanat systems were operating 500 years later in Eastern Anatolia [19] and then or simultaneously in Persia for which an example from western Iran is given in this study. It is likely that the new technology spread from the then empire of Urartu. Some scholars report that the qanat technology might have been developed independently in various regions of the Middle East, Mediterranean and North Africa [20]. However, it is generally agreed that qanats were developed somewhere between the northwest of today’s Iran, southern Azerbaijan and Armenia, and eastern Turkey [21], and spread to the Mediterranean, North Africa and Europe through cultural exchange, conquests, resettlement, migration and wars; to South America through colonization; and to Afghanistan, Pakistan, China and Japan through trade routes, particularly the Silk Road [22-25]. For China, while one theory says that the shaft/tunnel construction technology was used by ancient Chinese, thus it was a local innovation developed by indigenous people, it is more convincing that this technology was imported to China along the ancient Silk Road [26].

Despite the uncertainties about the time and place of the origin, it is mostly agreed that settlements as old as of 1000 BC relied on the qanat system for irrigation, meaning that the qanat technology is at least 3000 years old [27]. Some discoveries in central Iran date even back to 2000~3000 BC; e.g., the Gonabad qanat system in Iran of 2700 BC is recognized as the oldest in the World, still used for irrigation of Saffron farmlands [28]. Many existing qanat systems have stopped flowing by the effect of droughts as in the example from Afghanistan [29] while some may, at the same time, be flooded after the human-made intervention as in the example from the Bouda Oasis in Algeria [30]. With the rise in the awareness and demand for sustainable development and resilience against the nowadays climate change, the ancient-time qanat technology gained popularity among the modern-time researchers and practitioners. Among many, for instance, the ancient qanat systems in Iran [31], Syria [32], Cyprus [33], Algeria [34], China [35], and Afghanistan [36] were studied.

We see that qanats are mostly built where there is no permanent and reliable surface water available. When surface water resources are scarce or groundwater is preferred as the main water resource, qanats could particularly be useful. They prevent evaporation from water flowing under the surface without being in direct contact with the heat. Thus, they were practiced mostly in arid and semi-arid parts of the Earth where one of the sustainable water resources is groundwater. It should also be emphasized that the qanat system is not simply a set of vertical wells connected to a sloping conduit. It is made of a complex networks of water distribution with connections between qanats to ensure water supply to each owner [37].

4. RESEARCH HYPOTHESIS

In a first stage of the field inspection and sighting of documents, the earlier assumption of adduction of water through pipes or canals from outside the city of Hattuša (hypothetical route dotted in Figure 3) could be practically ruled out due to water management, strategic and topographical considerations, especially since no remains of such a pipeline were found. In contrast, the perennial pasture fountains on the slope (Figure 4) indicate layers carrying

groundwater. Figure 5 shows a schematic section in south-north direction through the area of the ruined city and the eastern ponds, considering the topographical and hydrogeological conditions. Geologically, the area is characterized by ophiolitic series. The percolating precipitation is dammed up on impermeable or low permeable layers of serpentine, loam, or clay. The resulting groundwater drains down on these layers and emerges through springs or wells situated where the impermeable layer meets the ground surface.



Figure 4 - Pasture fountain on the slope.

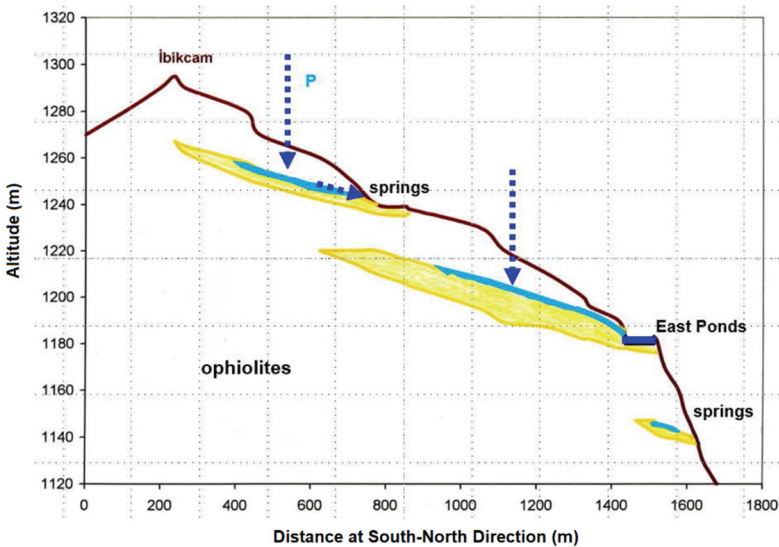


Figure 5 - Schematic topographical and geological section of the East Ponds. Infiltrating precipitation is retained and distributed by impermeable clay layers feeding springs.

The following hypothesis was defined: As the nowadays herders who build simple troughs at out seeping spots for their animals, the Hittite engineers were aware of the water bearing layer (Figure 5). Instead by a spot opening, however, they opened it by a longer cut for a higher yield. A reservoir (pond) dug into the impermeable layer below the cut collected and stored the discharging groundwater.

5. HYDRAULICS AND HYDROLOGY

5.1. Characteristics of Rockfill Dam and Principal Mechanism of Filling the Ponds - Hydraulics

On the valley side, the eastern ponds were enclosed by approximately 1.5 m high rockfill dam, which, like modern rockfill dams, were equipped with a sealing core made of clay with a foundation in a spur ditch (Figure 6). The mountain-side southern bank of the pond was also sealed. Figure 6 shows a cross-section through the spur ditch that was deepened into the impermeable layer and filled with clay. Remains of an overflow channel can also be seen in the archaeological site. This was apparently a spillway, an indispensable structure even on today's dams. With a usable volume of approximately 24,000 m³ the East Ponds could support thousands of inhabitants and store essential volumes for firefighting, livestock watering, gardens, crafts and ritual purposes.

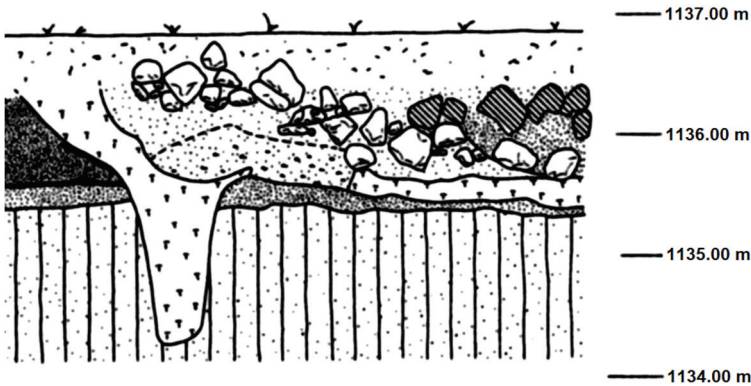


Figure 6 - Cross-section of the rockfill dam through the spur ditch [38].

Following the idea in the hypothesis, in autumn 2009, boreholes were sunk directly above the ponds in the Hattuša archaeological site and groundwater level measuring points were set up to collect data. The recordings of the groundwater level confirmed the working hypothesis. In the wetter winter half of the year, the groundwater rises and pours out of the cuts into the ponds. For this purpose, the groundwater level had to exceed a minimum height (threshold level), which required sufficient precipitation for the formation of new groundwater. Figure 7 shows the weekly measured groundwater level from 2009 to 2011 and the replenishment processes at the hillside edge of East Pond 1. In these years with normal annual precipitation, the threshold groundwater level was exceeded for many weeks allowing that the ponds would have been filled sustainably.

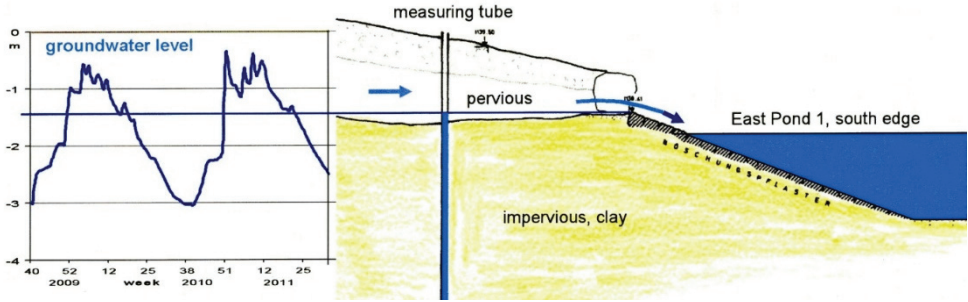


Figure 7 - Measured groundwater level in 2009 – 2011 (left), East Pond 1 and inflow principle (right)

5.2. Temporal Variation - Hydrology

While the hypothesis and the principal mechanisms of filling the ponds of Hattusa by cutting in groundwater bearing hillsides are confirmed by the measurements, the quantification and determination of the temporal distribution of these inflows need further evaluations. In the following, a hydrogeological approach is proposed which is based on the performed drillings as well as some assumptions and estimations. It is explained how the ponds are filled based on in-situ measurements of groundwater level.

The approach is applied for the example of East Pond 1 (Osteich 1). Available topographical maps (e.g., Figure 3) show that the land surface slopes by about 10% from the south towards the southern cut edge of the pond where the filling was to be expected (Figure 7). The same slope is assumed for the approaching groundwater surface; several smaller seeps and wells are backing this assumption. Particularly valuable for the method was the existence of a modern well in the vicinity uphill of the East ponds. This perennial fountain named K r Ahmet Pınarı (Blind Ahmet Spring) has a trough for livestock watering and is fed via a perforated tube from the same aquifer as the East Ponds were. In addition to the groundwater levels at the installed measuring tubes at the ponds, the outflow of the fountain was measured every week since September 2009 by counting the seconds to fill a 10-liter bucket.

When in winter due to precipitation, the groundwater rose above the threshold level, the inflow to the pond came out of the same subsurface reservoir as the fountain outflow. In a simplified view, during each time step of 7 days, a water volume with a rectangular cross section of about 90 m length (length of the cut-in, thus the southern edge of the pond) and its measured height of groundwater level minus threshold height is passing the cut-in. The reservoir consists of pervious material (see Figure 7), gravel, sand silt etc. for which a hydraulic conductivity of $k_f \approx 1 \times 10^{-3}$ m/s was assumed. The percentage of effective pore volume (n_{eff}) of the total volume can be estimated by [39]

$$n_{eff} = 0.462 + 0.045 \ln(k_f) \quad (1)$$

Thus, in the present case, $n_{eff} = 15\%$. Following the slope, the water stored in the pores will move towards the pond. Since groundwater flow is considered as laminar, the Darcy equation can be used to estimate flow velocity (v_f):

$$v_f = k_f I \quad (2)$$

where I is slope of the groundwater surface. For $I = 0.1$ and $k_f = 0.001$ m/s, $v_f = 0.0001$ m/s is obtained. With this velocity, groundwater of a flow travel length $f_i \approx 60$ m flows out at the cut-in line during one time step of 7 days. At a height above the threshold (e.g. $h = 0.5$ m), a water volume of about 400 m^3 , typically observed at 20 measurements in a year (weeks of groundwater level above threshold), a volume of around 8000 m^3 would pour out into the pond. With a basis area of $90 \text{ m} \times 50 \text{ m} = 4500 \text{ m}^2$, this would correspond to a filling depth of 1.8 m in the pond.

However, it is important to consider that the inflows into the pond are not directly represented by the measured groundwater levels above the threshold. These values indicate the grade of filling of the aquifer or the recharge of this reservoir. The outflows of groundwater storage ($Q_{storage}$) above the threshold (1.5 m) determined as lined out above are the inflows into the pond. Since the flows into the pond are originating of the same aquifer as those of the nearby fountain, it is expected that their temporal pattern, their response to the variation of groundwater levels will be very similar, except the volumes.

For verification, we applied the linear reservoir algorithm to calculate inflow (Q_i) and outflow (Q_o). The linear reservoir algorithm assumes that at any time the outflow Q_o is proportional to storage volume S , thus:

$$S = kQ_o \quad (3)$$

The flow recession is described by an exponential equation. Since the algorithm corresponds to the Darcy law (laminar flow), its application on groundwater processes is reasonable. Continuity equation is:

$$S_t = S_{t-1} + (\overline{Q_i} - \overline{Q_o})\Delta t \quad (4)$$

in which $\overline{Q_i}$ and $\overline{Q_o}$ are inflow and outflow discharges, respectively, averaged over time interval Δt . Equation 4 can be numerically solved to compute outflow at the current time by using outflow at the previous time and inflows at the current and previous time steps, as:

$$Q_o, t = \frac{(Q_i, t + Q_i, t-1) 0.5 \Delta t + Q_o, t-1 (k - 0.5 \Delta t)}{k + 0.5 \Delta t} \quad (5)$$

The calibration of the recession coefficient k which has the dimension of time is based on the recession curve analysis; k is the reciprocal value of the slope of the logarithmic recession curves. Figure 8 shows the calibration using the recession of the fountain flows from 31 May to 5 October 2012. As the slope is 0.0503, the reciprocal is $1/0.0503 \approx 20$ and with weekly (7-day) time interval of the measurements, k becomes 140 days.

The computed outflows of the aquifer and inflows into the pond are shown in Figure 9 together with the fountain outflow. For an easier visual comparison, the fountain outflow was extrapolated to $Q_{storage}$ at East Pond 1 from 2010 to 2015, by multiplying with the ratio between the volumes of groundwater storage and the fountain, $\text{Vol}_{storage} / \text{Vol}_{fountain}$, for every year. Figure 9 shows also the time series of groundwater storage ($Q_{storage}$). The inflow

volumes and their temporal patterns are now clearly seen. It shows the retention effect and the characteristics of flows having passed a reservoir: attenuation of flows, retardation, with the typical indication that the peak of the outflow hydrograph is positioned on the recession limb of inflow. The coefficient of determination between $Q_{fountain}$ and the computed outflow into the pond $Q_{reservoir}$ is $R^2 = 0.9$.

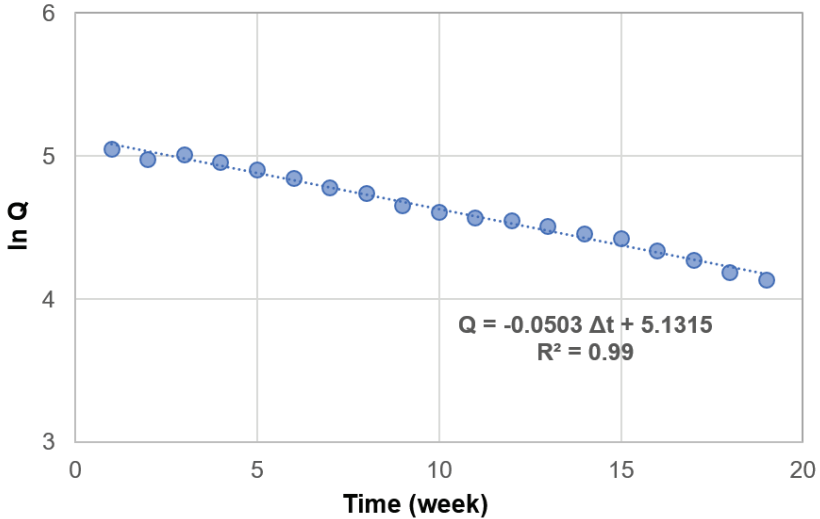


Figure 8 - Calibration of recession constant k for the fountain flow ($Q_{fountain}$) measured weekly between 31 May 2011 and 5 October 2011.

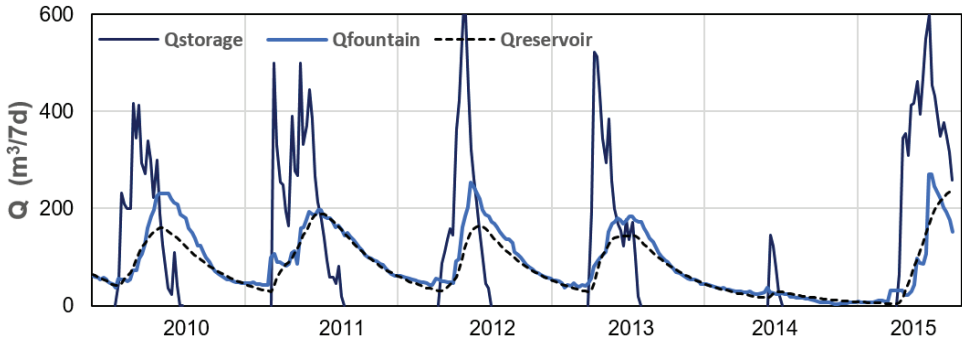


Figure 9 - Infiltration inflows to aquifer of East Pond 1 (fluctuating line with sharp peaks) based on measured groundwater storage level, fountain outflow extrapolated (round solid line), outflow into the pond computed by linear reservoir routing (round dashed line). Note the dry year 2014.

6. QANATS IN SUFI VILLAGE, NORTHWEST IRAN

A still functioning example was selected from Sufi Village located near Maku in West Azerbaijan province, Northwest Iran (Figure 10). The Sufi River crosses the center of the village and drains its area of 45 km². It is 14.65 km long with 5.75% slope. Mean elevation of the drainage area is 2008 m above sea level and concentration time is 2 hours. The climate of the region can be considered as semi-arid cold with mean annual temperature of 15°C and 295 mm annual precipitation. The village is home of three qanats named Amir, Dirsak and Choupan Goli. As reported [40], the qanat system has an average outflow between 4.0 l/s and 13.2 l/s.

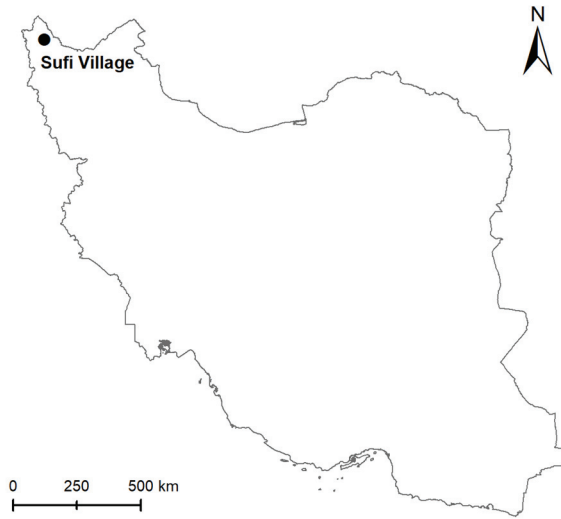


Figure 10 - Location of Sufi Village near Maku in West Azerbaijan province, Northwest Iran.

The Sufi Village qanat system was improved with the so-called underground or submerged sand dam constructed in the Sufi River. This is a technical term used for a structure to store water of an intermittent river within the sand and gravel of the riverbed. It is apt for riverbeds of bedrock or in other impervious material filled with gravel and sand. A wall of about 1-m width is built of rubble concrete or masonry in a trench across the river up to the gravel surface level (Figure 11). Stepwise the trench is refilled with gravel supporting the wall against horizontal forces. The wall is blocking the gravel zone of the river. In the rainy season, flow which would otherwise go downstream is retained filling the interstices of the gravel behind the wall. The storage volume, depending on the porosity, can make up to 50% of the gravel volume. The stored water is protected against evaporation and pollution and can be obtained by wells or conveyed to a downstream water intake system through an orifice attached to the wall as an underneath bottom outlet. The stored water is of high value in dry seasons particularly. The Sufi River case is detailed below as an example combined with the qanat system.

The underground dam in the Sufi River is used to retain and store water infiltrating during flows in the pores of the sediment upstream (Figure 12). The sediment is composed of sand or natural gravel allowing easy transmission of water. Water is discharged to the existing qanat channel (conduit) by an orifice attached to the wall as an underground bottom outlet of the submerged dam and reservoir. It is then conveyed by the qanat channel to lower areas. The qanat system reaches downstream for about 100 m to capture further smaller occasional drain water volumes.



Figure 11 - Sand dam, schematic; left: longitudinal section, gravel upstream of wall storing water retained from a flood, right: cross-section, sight on the wall without gravel.



Figure 12 - View from the crest of the underground dam in Sufi River (Photo by B Vaheddoost).

For a quantitative assessment, reported discharge measurements [40] from the seventh month (Mehr) of the Jalali year 1382 (starting from 23 September of the Gregorian year 2003) to the twelfth month (Isfand) of the Jalali year 1386 (ending in 20 March of the Gregorian year 2008) were used (Figure 13). Sudden rise is visible in the first month (Ferwerdin) of the Jalali year 1386 in the Amir qanat after the upstream underground dam was completed.

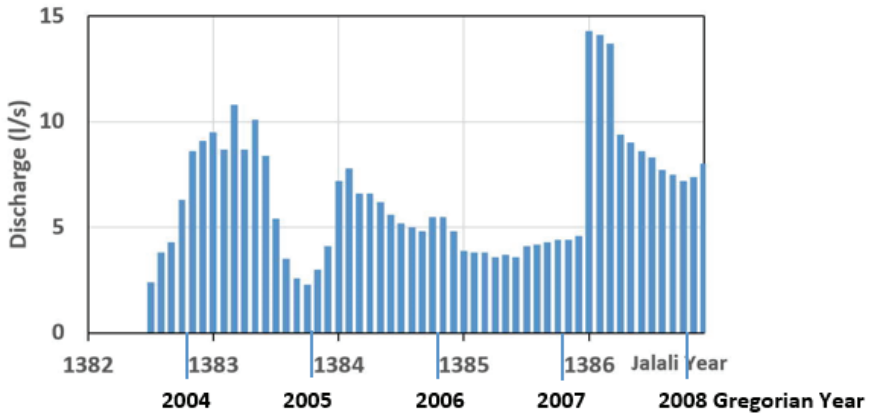


Figure 13 - Monthly mean discharge at the Amir qanat with a sudden rise in the first month of the Jalali year 1386 (March in the Gregorian year 2007) after construction of the underground dam (Data from [40])

7. AN INSIGHT FROM ENGINEERING POINTS OF VIEW

7.1. Drought and the Decline of the Hittite Empire

The decline and abandonment of Hattuša began around 1200 BC. During this period, famines due to low rainfall in the Greater Region are historically documented. At the time of Pharaoh Merenptah (1213-1204 BC) the Egyptians delivered grain to the Hittites to cope with a famine that had occurred there [41]. A series of ‘dry years’ in 1198-1196 BC with little precipitation, which showed the character of prolonged droughts, not only led to the failure of the grain harvests, but also prevented the supply of water in the ponds and thus initiated the abandonment of the city [12].

The dry year 2013-2014 with its measured values gave the opportunity to understand such a situation. In 2013, the Çorum meteorological station of Turkish State Meteorological Service (Devlet Meteoroloji İşleri) recorded the lowest annual precipitation of the time series 1929-2018 with just over half of the mean annual precipitation. This is a dry year with severe drought being effective in Turkey [42-43]. The dry year has a statistical return interval of around 90 years. The correspondingly low groundwater recharge brought the water level in the east ponds only for a short period of time above the threshold level while, in the south ponds, it remained below the measurement range. The southern ponds would not have been filled, the eastern ponds only slightly. Figure 14 shows the groundwater level below the terrain level of the two measurement points and above the annual precipitation. The dry phase and the recovery in 2015 are evident. The southern ponds were taken out of service earlier, probably due to unreliable filling. A longer series of years with little precipitation will also have restricted the function of the eastern ponds and contributed to the decline of the empire.

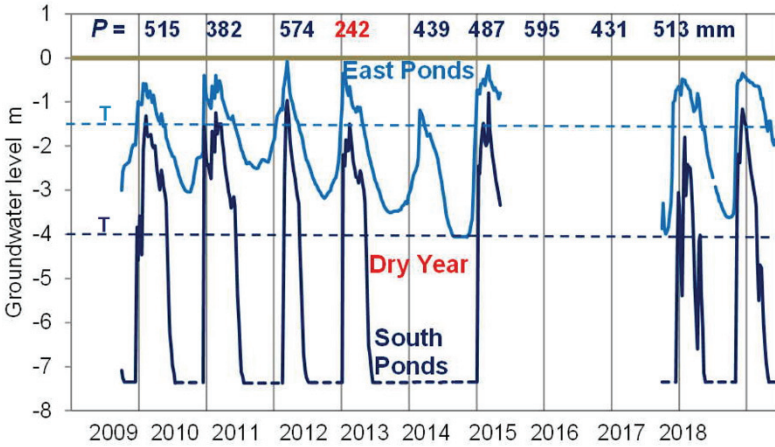


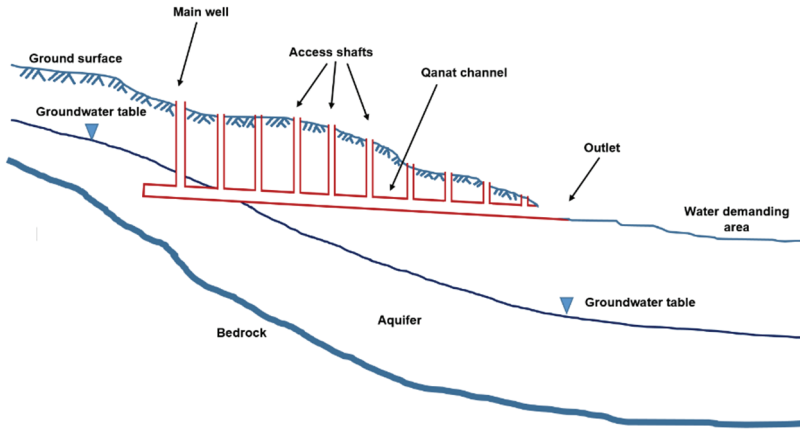
Figure 14 - Measured groundwater levels in 2009 – 2018, South and East Ponds, with annual precipitation P (Çorum) and threshold levels T, above which groundwater could discharge into the ponds. The data gap 2015-2017 was simply caused by loss of the hand-written data sheets of this period.

7.2. Hydraulic Engineering about Qanats

Qanat technology is understood as a further development of the ‘cut-in’ method described above for extracting ground and strata water. Instead of simply opening up the aquifer where it meets the ground surface, a 1- to 2-m diameter tunnel is driven into the aquifer. Well-like vertical shafts are dug at regular intervals, first for removing the excavated material, then for maintenance and ventilation (Figure 15a). Craftsmen who excavated the qanat were called *Muqanni* in Farsi (the qanat-diggers). Stabilized by rough rubble masonry to withstand collapse, the gallery (Figure 15b-c) receives water draining from the aquifer and transports it by gravity to the outlet. The gallery typically follows the slope of the ground surface or aquifer, but other slopes can be used where appropriate. Structurally, qanats are resistant to natural or human-made disasters; e.g. earthquakes, floods or wars. In spite of the old background, there are still qanats actively in use.

This evidences that the way of thinking and the engineering approach of the ancient water supply systems was evidently similar, if not the same, as today's engineering practice. With machinery and much better-established theories it is possible to replicate the ancient water systems in hydraulic engineering for sustainable water resources development projects, for groundwater particularly. The modern water chambers and well rooms are based on the principle of opening water-bearing layers, as used for the qanats.

The discharge rate of qanats is traditionally determined by volumetric flow measurements at the downstream outlets, while modern systems are now available. The physics behind the technology is almost the same as the classical drainage systems, that water is discharged naturally by gravity given by the hydraulic gradient and the soil conductivity of the aquifer and the cut surface area. In the qanat, it is the slope of the channel (the almost horizontal conduit) transporting the outflow.



(a)



(b)



(c)

Figure 15 - (a) A typical longitudinal view of qanat showing main elements of the system, (b) top entrance of vertical access shafts on the ground surface, (c) qanat channel (Fogara at Adrar, Grand Western Erg, Algeria, year 1965, Photos by H Wittenberg).

8. CONCLUDING REMARKS TO THE ANCIENT TECHNOLOGICAL HERITAGE

In the case of the ponds, as well as of other Hittite reservoirs, such as that of Alacahöyük (~1250 BC), the risks of strongly fluctuating and often violent surface inflows were avoided by opening near-surface groundwater and strata aquifers. The technology improved the water supply and the prerequisites for the development of Hattuša into the capital of a great empire. After this success by ‘cutting-in’ water-bearing layers on the slope, it was only logical to achieve even better results by ‘penetrating’.

The ‘cut-in’ technology can be regarded as a preliminary stage of the qanat systems, in which tunnel-like drainage conduits allowed the extraction of larger groundwater flows throughout the year in a more sustainable way. Qanats, as an ancient invention, are appropriate for supplying water in arid and semi-arid regions as they are little affected by the fluctuation of surface waters and prevent groundwater overuse.

Spring captures and well rooms of today are also based on the principle of opening water-bearing layers. An engineering points of view insight shows the non-machinery human-powered or gravity-oriented ancient simple techniques have been fundamentals for today’s machinery-powered complex technology. The way of thinking and the approach of the

builders of antiquity were evidently quite the same as those of today's engineers, even without machines and theoretical foundations. Their works were fundamental for today's methods. Qanats can still be considered among appropriate water supply methods in arid and semi-arid areas despite the availability of modern equipments such as pumps allowing the withdrawal of higher discharges from deeper groundwater levels.

Perhaps it is more important to emphasize that the qanat technology has contributed to civilizations by helping the settlements; e.g., villages, to form and supported cooperation among water users by sharing the available water for their demand. The qanats might have better overcome deficit in surface water during drought, and thus might have prevented or delayed the collapse of the Empire if they would have been known by the Hittites.

Symbols

I	: Slope of groundwater surface
k	: Recession constant (day)
k_f	: Hydraulic conductivity (m/s)
n_{eff}	: Effective pore volume (%)
Qi	: Inflow discharge (m ³ /s)
Qo	: Outflow discharge (m ³ /s)
S	: Groundwater storage (m ³)
t	: Time (week)
v_f	: Flow velocity (m/s)
Δt	: Time interval (week)

Acknowledgements

Boreholes above the ponds in Hattuşa were dug and groundwater measuring points were set up in autumn 2009 with funds from the GRH Foundation (Gisela and Reinhold Häcker Foundation, Österingen, Germany) and with the approval of the antiquity's authority of Turkey. Without falling into clichés, archaeologists and engineers have different professional approaches. Cooperating however, the specific skills may add up and the human and professional gain will compensate occasional frictions. The authors, both civil engineers, thank the Hattuşa excavation director, Prof. Dr. Andreas Schachner, for the opportunity, suggestion, exchange and cooperation. The measuring assistant of the German Archaeological Institute, Mr. Murat Can, is expressly thanked for his commitment and reliability. We thank also Assoc. Prof. Dr. Babak Vaheddoost of Bursa Technical University, Turkey, for his help in the qanat-related part of this study, and Assoc. Prof. Dr. Ebru Eris of Ege University, Turkey, for her help in the graphic- and figure-related issues. Groundwater levels in Hattusa were owned by Deutsches Archäologisches Institut (German Archaeological Institute) in Istanbul, Turkey. These data can be made available by the first author based on reasonable requests. Precipitation data in Çorum can be acquired from Turkish State Meteorological Service. Discharges at the Amir qanat were obtained from a published report as referenced in this paper.

References

- [1] Blöschl G, Bierkens MFP, Chambel A, Cudennec C, Destouni G, Fiori A, Kirchner JW, McDonnell JJ, Savenije HHG, Sivapalan M, Stumpp C, Toth E, Volpi E, Carr G, Lupton C, Salinas J, Szeles B, Viglione A, Aksoy H, Allen ST, Amin A, Andreassian V, Arheimer B, Aryal SK, Baker V, Bardsley E, Barendrecht MH, Bartosova A, Batelaan O, Berghuijs, WR, Beven K, Blume T, Bogaard T, de Amorim PB, Boettcher ME, Boulet G, Breinl K, Brilly M, Brocca L, Buytaert W, Castellarin A, Castelletti A, Chen X, Chen Y, Chen Y, Chiffard P, Claps P, Clark MP, Collins AL, Croke B, Dathe A, David PC, de Barros FPJ, de Rooij G, Di Baldassarre G, Driscoll JM, Duethmann D, Dwivedi R, Eris E, Farmer WH, Feiccabrino J, Ferguson G, Ferrari E, Ferraris S, Fersch B, Finger D, Foglia L, Fowler K, Gartsman B, Gascoin S, Gaume E, Gelfan A, Geris J, Gharari S, Gleeson T, Glendell M, Bevacqua AG, Gonzalez-Dugo MP, Grimaldi S, Gupta AB, Guse B, Han D, Hannah D, Harpold A, Haun S, Heal K, Helfricht K, Herrnegger M, Hipsey M, Hlavacikova H, Hohmann C, Holko L, Hopkinson C, Hrachowitz M, Illangasekare TH, Inam A, Innocente C, Istanbuloglu E, Jarihani B, Kalantari Z, Kalvans A, Khanal S, Khatami S, Kiesel J, Kirkby M, Knoben W, Kochanek K, Kohnova S, Kolechkina A, Krause S, Kreamer D, Kreibich H, Kunstmann H, Lange H, Liberato MLR, Lindquist E, Link T, Liu J, Loucks D, Luce C, Mahe G, Makarieva O, Malard J, Mashtayeva S, Maskey S, Mas-Pla J, Mavrova-Guirguinova M, Mazzoleni M, Mernild S, Misstear BD, Montanari A, Mueller-Thomy H, Nabizadeh A, Nardi F, Neale C, Nesterova N, Nurtaev B, Odongo VO, Panda S, Pande S, Pang Z, Papacharalampous G, Perrin C, Pfister L, Pimentel R, Polo MJ, Post D, Prieto C, Ramos M-H, Renner M, Reynolds JE, Ridolfi E, Rigon R, Riva M, Robertson DE, Rosso R, Roy T, Sa JHM, Salvadori G, Sandells M, Schaeffli B, Schumann A, Scolobig A, Seibert J, Servat E, Shafiei M, Sharma A, Sidibe M, Sidle RC, Skaugen T, Smith H, Spiessl SM, Stein L, Steinsland I, Strasser U, Su B, Szolgay J, Tarboton D, Tauro F, Thirel G, Tian F, Tong R, Tussupova K, Tyralis H, Uijlenhoet R, van Beek R, van der Ent RJ, van der Ploeg M, Van Loon AF, van Meerveld I, van Nooijen R, van Oel PR, Vidal J-P, von Freyberg J, Vorogushyn S, Wachniew P, Wade AJ, Ward P, Westerberg IK, White C, Wood EF, Woods R, Xu Z, Yilmaz KK, Zhang Y (2019) Twenty-three unsolved problems in hydrology (UPH) - a community perspective, *Hydrological Sciences Journal*, 64(10), 1141-1158. doi: 10.1080/02626667.2019.1620507
- [2] Bulut B, Yilmaz MT (2016) Türkiye'deki 2007 ve 2013 yılı kuraklıklarının NOAH hidrolojik modeli ile incelenmesi. *Teknik Dergi*, 7619-7634, Yazı 463.
- [3] Cavus Y, Aksoy H (2020) Critical drought severity/intensity-duration-frequency curves based on precipitation deficit. *Journal of Hydrology*, 584 (7), 124312. doi: 10.1016/j.jhydrol.2019.124312
- [4] Dikbas F, Bacanlı UG (2021) Detecting drought variability by using two-dimensional correlation analysis. *Teknik Dergi*, 10947-10965, Paper 619. <https://doi.org/10.18400/tekderg.559195>

- [5] Aksoy H, Cetin M, Eris E, Burgan HI, Cavus Y, Yildirim I, Sivapalan M (2021) Critical drought intensity-duration-frequency curves based on total probability theorem-coupled frequency analysis. *Hydrological Sciences Journal*, 66 (8), 1337-1358. doi:10.1080/02626667.2021.1934473
- [6] Cavus Y, Stahl K, Aksoy H (2023) Drought intensity-duration-frequency curves based on deficit in precipitation and streamflow for water resources management, *Hydrology and Earth System Science*, 27, 3427-3445. doi:10.5194/hess-27-3427-2023.
- [7] Kreibich H, Van Loon AF, Schröter K, Ward PJ, Mazzoleni M, Sairam N, Abeshu GW, Agafonova S, AghaKouchak A, Aksoy H, Alvarez-Garreton C, Aznar B, Balkhi L, Barendrecht MH, Biancamaria S, Bos-Burginger L, Bradley C, Budiyo Y, Buytaert W, Capewell L, Carlson H, Cavus Y, Couasnon A, Coxon G, Daliakopoulos I, De Ruiter MC, Delus C, Erfurt M, Esposito G, François D, Frappart F, Freer J, Frolova N, Gain AK, Grillakis M, Grima JO, Guzmán DA, Huning LS, Ionita M, Kharlamov M, Khoi DN, Kieboom N, Kireeva M, Koutroulis A, Lavado-Casimiro W, Li H-Y, Llasat MC, Macdonald D, Mård J, Mathew-Richards H, McKenzie A, Mejia A, Mendiondo EM, Mens M, Mobini S, Mohor GS, Nagavciuc V, Ngo-Duc T, Nguyen HTT, Nhi PTT, Petrucci O, Nguyen HQ, Quintana-Seguí P, Razavi S, Ridolfi E, Riegel J, Sadik MS, Savelli E, Sazonov A, Sharma S, Sørensen J, Souza FAA, Stahl K, Steinhausen M, Stoelzle M, Szalińska W, Tang Q, Tian F, Tokarczyk T, Tovar C, Tran TVT, Van Huijgevoort MHJ, Van Vliet MTH, Vorogushyn S, Wagener T, Wang Y, Wendt DE, Wickham E, Yang L, Zambrano-Bigiarini M, Blöschl G, Di Baldassarre G (2022) The challenge of unprecedented floods and droughts in risk management. *Nature* 608, 80–86. <https://doi.org/10.1038/s41586-022-04917-5>
- [8] Kreibich H, Schröter K, Di Baldassarre G, Van Loon AF, Mazzoleni M, Abeshu GW, Agafonova S, AghaKouchak A, Aksoy H, Alvarez-Garreton C, Aznar B, Balkhi L, Barendrecht MH, Biancamaria S, Bos-Burginger L, Bradley C, Budiyo Y, Buytaert W, Capewell L, Carlson H, Cavus Y, Couasnon A, Coxon G, Daliakopoulos I, de Ruiter MC, Delus C, Erfurt M, Esposito G, François D, Frappart F, Freer J, Frolova N, Gain AK, Grillakis M, Grima JO, Guzmán DA, Huning LS, Ionita M, Kharlamov M, Khoi DN, Kieboom N, Kireeva M, Koutroulis A, Lavado-Casimiro W, Li H-Y, LLasat MC, Macdonald D, Mård J, Mathew-Richards H, McKenzie A, Mejia A, Mendiondo EM, Mens M, Mobini S, Mohor GS, Nagavciuc V, Ngo-Duc T, Nguyen HTT, Nhi PTT, Petrucci O, Quan NH, Quintana-Seguí P, Razavi S, Ridolfi E, Riegel J, Sadik MS, Sairam N, Savelli E, Sazonov A, Sharma S, Sørensen J, Souza FAA, Stahl K, Steinhausen M, Stoelzle M, Szalińska W, Tang Q, Tian F, Tokarczyk T, Tovar C, Tran TVT, van Huijgevoort MHJ, van Vliet MTH, Vorogushyn S, Wagener T, Wang Y, Wendt DE, Wickham E, Yang L, Zambrano-Bigiarini M, Ward PJ (2023) Panta Rhei benchmark dataset: socio-hydrological data of paired events of floods and droughts. *Earth Syst. Sci. Data*, 15, 2009–2023. <https://doi.org/10.5194/essd-15-2009-2023>
- [9] Peterson LC, Haug GH (2005) Climate and the collapse of Maya civilization: a series of multi-year droughts helped to doom an ancient culture. *American Scientists*, 93, 322-329.

- [10] Evans NP, Bauska TK, Gazquez-Sanchez F, Brenner M, Curtis JH, Hodell DA (2018) Quantification of drought during the collapse of the classic Maya civilization. *Science* 361: 498-501. <https://doi.org/10.1126/science.aas9871>
- [11] Kennett DJ, Masson M, Lope CP, Serafin S, George RJ, Spencer TC, Hoggarth JA, Culleton BJ, Harper TK, Prufer KM, Milbrath S, Russell BW, González EU, McCool WC, Aquino VV, Paris EH, Curtis JH, Marwan N, Zhang M, Asmerom Y, Polyak VJ, Carolin SA, James DH, Mason AJ, Henderson GM, Brenner M, Baldini JUL, Breitenbach SFM, Hodell DA (2022) Drought-induced civil conflict among the ancient Maya. *Nat Commun* 13, 3911. <https://doi.org/10.1038/s41467-022-31522-x>
- [12] Manning SW, Kocik C, Lorentzen B, Sparks JP (2023) Severe multi-year drought coincident with Hittite collapse around 1198–1196 BC. *Nature* 614: 719-724. <https://doi.org/10.1038/s41586-022-05693-y>
- [13] Durusu-Tanriover M (2023) Signs of climate crisis as an ancient empire unraveled. *Nature* 614: 625-626
- [14] Li, Z., Chen, Y., Wang, Y. Li W (2016) Drought promoted the disappearance of civilizations along the ancient Silk Road. *Environ Earth Sci* 75, 1116 (2016). <https://doi.org/10.1007/s12665-016-5925-6>
- [15] Ozis U (1987) Ancient water works in Anatolia. *International Journal of Water Resources Development* 3(1):55-62. <https://doi.org/10.1080/07900628708722333>
- [16] Wittenberg H (2014) Groundwater use in the Hittite capital Hattuşa 1600 BC. In C. Ohlig (ed.), *Schriften DWhG*, 21:139-147.
- [17] Seeher, J (2001), *Die Ausgrabungen in Boğazköy-Hattuşa 2000*. *Archäologischer Anzeiger* 2001, Heft 3, 340-362.
- [18] Wittenberg H, Schachner A (2013) The Ponds of Hattuşa – Early Groundwater Management in the Hittite Kingdom. *Water Science and Technology: Water Supply*, 13(3):692-697, 2013.
- [19] Laessøe J (1951) The irrigation system at Ulhu, 8th century B.C. *J Cuneiform Studies* 5:21-32.
- [20] Vaughan CS (2021, February 08) Qanat. *World History Encyclopedia*. Retrieved from <https://www.worldhistory.org/qanat/>
- [21] Kobori I (1973) Some notes on diffusion of qanat. *Orient* 9:43-66.
- [22] Goldsmith E (1968) The qanats of Iran. *SciAm* 218(4):94–105. <https://doi.org/10.1038/scientificamerican0468-94>
- [23] Wilson A (2008) *Hydraulic Engineering and Water Supply*. In Oleson, John Peter (ed.). *Handbook of Engineering and Technology in the Classical World* (PDF). New York: Oxford University Press. pp. 290–293. ISBN 978-0-19-973485-6
- [24] Nikravesh M, Ardakanian R, Alemohammad SH (2009) Institutional capacity development of water resources management in Iran. *Capacity development for improved water management*, 159.

- [25] Manuel M, Lightfoot D, Fattahi M (2018) The sustainability of ancient water control techniques in Iran: an overview. *Water Hist* 10:13–30. <https://doi.org/10.1007/s12685-017-0200-7>
- [26] Hu WJ, Zhang JB, Liu YQ (2012) The qanats of Xinjiang: historical development, characteristics and modern implications for environmental protection. *Journal of Arid Land* 4(2):211-220. <https://doi.org/10.3724/SP.J.1227.2012.00211>
- [27] Hussain I, Abu-Rizaiza OS, Habib MA, Ashfaq M (2008) Revitalizing a traditional dryland water supply system: the karezes in Afghanistan, Iran, Pakistan and the Kingdom of Saudi Arabia. *Water Int* 33(3):333-349. <https://doi.org/10.1080/02508060802255890>
- [28] FAO (Food and Agriculture Organization) (2021). Qanat-based Saffron Farming System in Gonabad, Iran. <https://www.fao.org/giahs/giahsaroundtheworld/designated-sites/asia-and-the-pacific/qanat-based-saffron-farming-system-in-gonabad/ru/> Accessed October 2021
- [29] Macpherson GL, Johnson WC, Liu H (2017) Viability of karezes (ancient water supply systems in Afghanistan) in a changing world. *Appl Water Sci* 7:1689–1710. <https://doi.org/10.1007/s13201-015-0336-5>
- [30] Boutadara Y, Remini B, Benmamar S (2018) The foggaras of Bouda (Algeria): from drought to flood. *Appl Water Sci* 8:162. <https://doi.org/10.1007/s13201-018-0822-7>
- [31] Beaumont P (1971) Qanat systems in Iran. *Hydrol Sci J* 16(1):39-50. <https://doi.org/10.1080/02626667109493031>
- [32] Lightfoot DR (1996a) Syrian qanat Romani: history, ecology, abandonment. *J Arid Environ* 33(3):321-336. <https://doi.org/10.1006/jare.1996.0068>
- [33] Endreny TA (2008) Estimating recharge rates for qanat-based water supply in Northern Cyprus: a case study using remotely sensed and in-situ data. *Urban Water J* 5(2):161-171. <https://doi.org/10.1080/15730620701754202>
- [34] Remini B, Achour B (2013) The qanat of the greatest western Erg. *Journal of American Water Works Association*, 105(5):104-107.
- [35] Luo L, Wang X, Guo H, Liu C, Liu J, Li L, Du X, Qian G (2014) Automated extraction of the archaeological tops of qanat shafts from VHR imagery in google earth. *Remote Sens* 6(12):11956-11976. <https://doi.org/10.3390/rs61211956>
- [36] Goes BJM, Parajuli UN, Haq M, Wardlaw RB (2017) Karez (qanat) irrigation in the Helmand River Basin, Afghanistan: a vanishing indigenous legacy. *Hydrogeol J* 25(2):269-286. <https://doi.org/10.1007/s10040-016-1490-z>
- [37] Remini B, Achour B, Albergel J (2015) The qanat of Algerian Sahara: an evolutionary hydraulic system. *Appl Water Sci* 5:359-366. <https://doi.org/10.1007/s13201-014-0195-5>
- [38] Neve P (1991). Die Ausgrabungen in Boğazköy-Ḫattuša. *Archäologischer Anzeiger* 1991/3, 299–348.

- [39] Marotz G (1968) Technische Grundlagen einer Wasserspeicherung im natürlichen Untergrund. Verlag Wasser und Boden, 228 p.
- [40] Jafari Bari M, Gohari, E, Jafari Z, Amiri JS (2008) Final report: Investigation of the use of underground dams in the water resources management of Qanats. Case of study: Sufi-Maku Flood plain Qanats. Ministry of Agriculture, Institute of Soil protection and watershed management. Project No. 82-0500402000-08.
- [41] Zwickel W (2007) Regen, Dürre, Hungersnöte. Die Erforschung des Klimas in Palästina in den letzten 10.000 Jahren, Welt und Umwelt der Bibel 46:2-7.
- [42] Cavus Y, Aksoy H (2019) Spatial drought characterization for Seyhan River basin in the Mediterranean region of Turkey. *Water*, 11 (7), 1331. <https://doi:10.3390/w11071331>
- [43] Cavus Y, Stahl K, Aksoy H (2022) Revisiting major dry periods by rolling time series analysis for human-water relevance in drought. *Water Resour Manag* 36:2725-2739. <https://doi.org/10.1007/s11269-022-03171-8>

A Quantitative Investigation on the Effects of Flexure-Dominated Reinforced Concrete Column Characteristics on the Dissipated Energy

Ziya MÜDERRISOĞLU^{1*}

Ahmet Anıl DINDAR²

Ali BOZER³

Hasan ÖZKAYNAK⁴

Ahmet GÜLLÜ⁵

Bilal GÜNGÖR⁶

Furkan ÇALIM⁷

Serkan HASANOĞLU⁸



ABSTRACT

This paper presents the effects of fundamental member and loading parameters on total dissipated energy capacity of RC columns in a quantitative way by using an experimental database. Specifically, concrete compressive strength, yield strength of reinforcing bars; shear span-to-depth ratio, reinforcement ratios; peak drift ratio, and axial load ratio, are considered as influencing factors. Pearson's correlation coefficients are utilized as dependency indicators to construct a correlation matrix where the effect of each factor on

Note:

- This paper was received on March 28, 2023 and accepted for publication by the Editorial Board on October 13, 2023.
- Discussions on this paper will be accepted by May 31, 2024.
- <https://doi.org/10.18400/tjce.1272125>

1 Istanbul Beykent University, Department of Civil Engineering, Istanbul, Türkiye
ziyamuderrisoglu@beykent.edu.tr - <https://orcid.org/0000-0003-1220-8047>

2 Gebze Technical University, Department of Civil Engineering, Kocaeli, Türkiye
adindar@gtu.edu.tr - <https://orcid.org/0000-0003-3168-8322>

3 Eskişehir Technical University, Department of Civil Engineering, Eskişehir, Türkiye
alibozer@eskisehir.edu.tr - <https://orcid.org/0000-0002-3632-2605>

4 Istanbul Beykent University, Department of Civil Engineering, Istanbul, Türkiye
hasanozkaynak@beykent.edu.tr - <https://orcid.org/0000-0003-2880-7669>

5 Texas State University, Ingram School of Engineering, Texas, USA
ahmetgullu@txstate.edu - <https://orcid.org/0000-0001-6678-9372>

6 Gebze Technical University, Department of Civil Engineering, Kocaeli, Türkiye
bgungor@gtu.edu.tr - <https://orcid.org/0000-0001-6749-2706>

7 Istanbul Technical University, Faculty of Civil Engineering, Istanbul, Türkiye
calimf@itu.edu.tr - <https://orcid.org/0000-0001-8365-9553>

8 University School for Advanced Studies IUSS, Pavia, Italy
serkan.hasanoglu@iusspavia.it - <https://orcid.org/0000-0002-7018-0479>

* Corresponding author

dissipated energy level is quantified. Results show that the effective factors among selected features are peak drift ratio, transverse reinforcement volumetric ratios of a member, and yield strength of rebars whereas the heaviest influencing factors are the first two.

Keywords: Energy-based design, dissipated energy capacity, reinforced concrete columns, correlation levels.

1. INTRODUCTION

The fundamental structural design principle in earthquake engineering is to avoid failure of structural members and partial or total collapse of structural system. In other words, dissipating the earthquake-induced input energy without jeopardizing member integrity and structural stability is a key issue in seismic design. This is commonly achieved by maintaining adequate strength and ductility on material, section, and structural levels. Both the conventional seismic design procedures (i.e., force-based, and displacement-based), and recently developing design approach namely energy-based seismic design of structures, recommend the designers to avoid brittle or low-ductile behavior of components due to high compression forces; shear failure in members and connections; inadequate reinforcement development, splicing and development length. Once these actions are avoided, stable hysteresis loops, thus effective energy dissipation, through inelastic cyclic responses is achieved.

The inelastic cyclic response of structural members plays a crucial role in accumulation of deformations in a structure. When fundamental seismic design recommendations are improperly applied to a structural element, it can lead to misleading outcomes. This can result in the accumulation of damage throughout the structure, primarily caused by insufficient levels of total energy dissipation in individual structural members.

The energy dissipation capacity of the structural members is evaluated as calculating the area enclosed by the force-displacement hysteresis achieved during the cyclic loading. Specifically, the area under the force-displacement response is known as the dissipated energy. Examples of experiment-based loading procedure and corresponding component response are represented in Figures 1a and 1b, respectively [1].

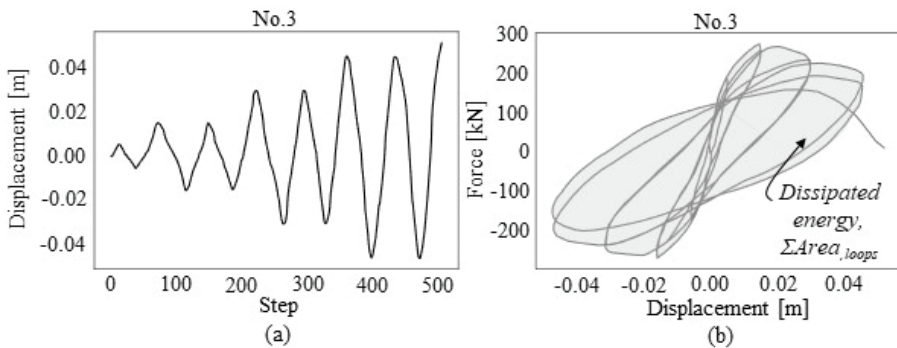


Figure 1 - (a) Experimental loading protocol, (b) obtained force-displacement hysteresis for No.3 specimen of Gill [1]

The prediction of component-based energy dissipation and deformation capacity has been studied by several researchers in the past years. Poljanšek et al. [2] presented the effects of fundamental input parameters on the hysteretic energy dissipation and deformation capacity of RC columns in terms of several normalized forms of energy quantities. They concluded that the hysteretic energy capacity is mostly affected by the reinforcement ratio and axial load level variations. Acun and Sucuoğlu [3] investigated the effect of failure modes, ductility, and material characteristics of RC columns on the energy dissipation capacity. For this purpose, test units were subjected to cyclic displacements having varying amplitudes. Deteriorations were observed in dissipated energy levels with constant-amplitude cycle numbers. Rodrigues et al. [4] performed an experimental study to assess the energy dissipation characteristics and to estimate the equivalent damping ratio of RC columns under biaxial bending effects via full-scale testing. Significant variations in dissipated energy capacity were observed due to the level of axial loading. Vu et al. [5] investigated the effects of variability in axial loads on the hysteresis characteristics of RC short columns. Results showed that the hysteresis loops become more unsymmetrical depending on the variations in axial load. Yang et al. [6] performed an experimental study to reveal the effects of the corrosion of rebars on hysteresis behavior. Critical thresholds for the maximum corrosion level and numerical dilation crack widths were proposed. Based on component-based investigations detailed as above, recently proposed seismic design methodologies are being developed to implement the energy-based design principles for RC type structures [7].

Due to the limitations in the number of specimens that can be tested, researchers may also refer to the existing experimental databases [8-10]. Very often, these databases are compiled based on specimen and reinforcement details, test loading protocols and types. Then, the compiled datasets are either used to investigate the correlations between the feature and target quantities or to propose empirical equations for predicting the target parameter [11-12]. Finally, relevant research studies may be a good basis for defining the hysteresis rules in scope of analytical processes [13-16].

The attention on the energy-based seismic design is increasing, however, determination of the energy capacity of structural members and joints is still a developing topic. To the authors' knowledge, even here are numerous efforts on predicting the energy dissipation capacities that will contribute to the improved design of structural members [17-20], very limited or none of them deals with predicting the effects of parameters on energy dissipation capacities in a quantitative way. Hence, the rationale of this study is to associate the section and loading characteristics with the dissipated energy levels of members and thus to release crucial impact on energy capacity of RC columns. Moreover, a fore-knowledge of influencing factors may lead the designers to more efficient solutions and may provide a basis for future seismic code provisions focusing on the energy-based design concept. Specifically, the correlations are revealed in a quantitative way with the compilation of a dataset. For this purpose, the compiled dataset is described first, and the statistical properties are given. Then, the methods to be used for correlation-based investigations are explained. Following the discussions for the correlation and dependency levels between the features and target capacity parameter, selected test unit characteristics are further investigated. In this paper, the target dataset is fundamentally focused on flexure-dominated rectangular RC column type members to represent new code compliant structures. In the study, a wide feature parameter set, (i.e., concrete compressive strength, yield strength of rebars, shear span-to-depth ratio, longitudinal rebar ratio -as the ratio between the area of longitudinal rebars and the member

cross-sectional area- and transverse reinforcement volumetric ratios -as the ratio between the volume of transverse reinforcement spaced as the interval and the core area times spacing between transverse reinforcement-, peak drift ratio, and axial load ratio) were considered. The effect of shear deformations on the shape of hysteresis loops are not considered within the scope of this work but based on this premise, further investigations will be implemented into different database contents by taking into account the proposed procedure.

2. MATERIAL AND METHODOLOGY

Details of compiled test unit database and methods that are used to investigate the dependency levels between the selected features and energy capacity parameters are explained in this section.

2.1. RC Column Test Unit Database

Open access databases provide a basis for analytical studies including metadata and the responses of past experiments in the literature as verification results. The database used in this study is extracted from DesignSafe database [9] that includes RC column test units having rectangular type cross-sections that are subjected to flexural effects. In this study, the authors emphasized the importance of assembling a dataset that accurately reflects the scope of their research. They compiled RC column information from existing databases, specifically focusing on rectangular cross sections subjected to flexural effects. However, they discovered that approximately 37% of the dataset (24 out of 65 specimens) had almost identical metadata characteristics obtained from a single reference. The presence of a large number of data representing similar characteristics may introduce a bias in the results, therefore these data were eliminated. Moreover, it was also observed that the remaining limited data basically represent the commonly considered member characteristics in existing buildings. Selected criteria are given in Table 1. Here, the axial load ratio refers to the ratio between the axial load acting on a member during the test and the cross-sectional area, and the material strengths are considered as nominal values reported for a test unit. After filtering the compiled dataset by taking into account the criteria, the 41 test units subjected to static reversed cyclic loadings is set for the analysis.

Table 1 - Selection criteria and limitations for the compiled dataset

Feature	Limitation
Compressive strength of concrete, f_c [MPa]	≤ 45
Yield strength of longitudinal rebar, f_{yl} [MPa]	≤ 500
Yield strength of transverse rebar, f_{yt} [MPa]	≤ 500
Shear span-to-depth ratio, a/d	≥ 3
Axial load ratio, ρ_{axial}	Between 0.15 and 0.40

Identified critical properties which predominantly influence hysteretic behavior thus energy dissipation, and their respective relative frequencies within the dataset are given in Figure 2. Moreover, the statistical parameters for selected features are provided in Table 2.

Table 2 - Statistical parameters of the selected features and target response

Parameter/ Indicator	f_c [MPa]	f_{yl} [MPa]	f_{yt} [MPa]	a/d [-]	ρ_l [-]	ρ_t [-]	Δ_{max} [-]	ρ_{axial} [-]	E_{cd} [kNm]
Minimum	17.6	330.9	254.9	3.28	0.0101	0.0016	0.018	0.15	2.94
Maximum	44.0	496.9	475.9	8.9	0.0382	0.0300	0.102	0.39	597.93
Median	27.1	439.9	391.9	4.1	0.0194	0.0148	0.051	0.22	66.42
Mean	29.1	433.4	395.7	4.6	0.0208	0.0149	0.053	0.23	154.29
Skew	1.08	-0.67	-0.30	1.64	1.08	0.21	0.22	0.63	1.34

ρ_l : Longitudinal rebar ratio, ρ_t : Transverse rebar volumetric ratio, Δ_{max} : Peak drift ratio, E_{cd} : Total dissipated energy

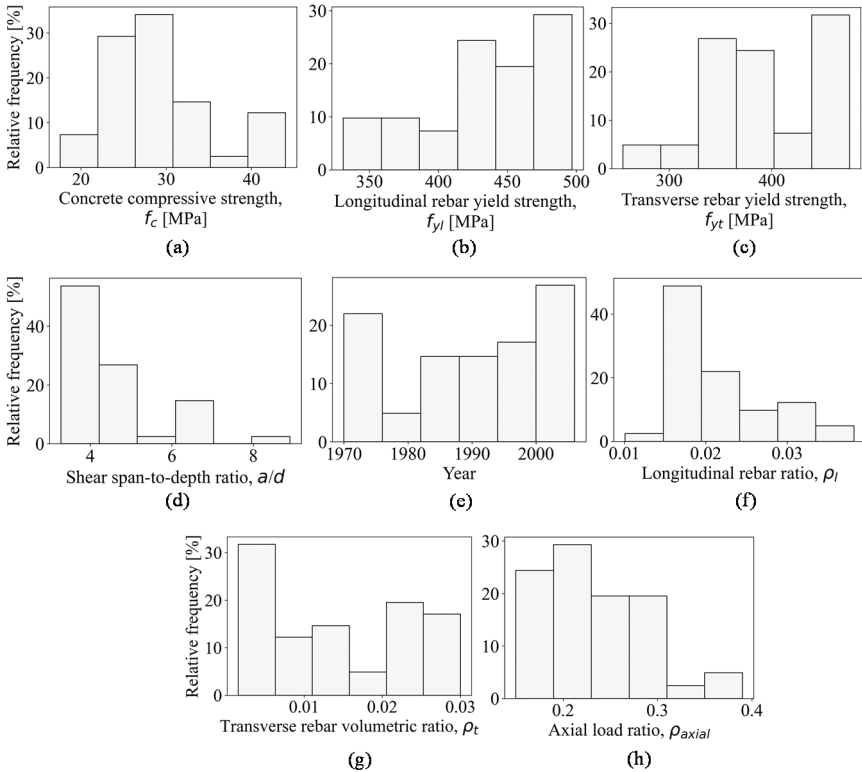


Figure 2 - Relative frequency distributions of fundamental properties for a selected dataset: (a) f_c , (b) f_{yl} , (c) f_{yt} , (d) a/d , (e) test year, (f) ρ_l , (g) ρ_t , (h) ρ_{axial} .

The cumulative energy dissipation and corresponding total dissipated energy capacities of selected test units are represented in Figure 3. The total energy dissipation capacity of the columns is determined as the area enclosed by the base shear and top displacement hysteresis derived through the entire experiment. In Figure 3a, development of the cumulative energy dissipation through the increasing steps for each specimen is illustrated whereas the total energy dissipation capacities of the specimens are given in Figure 3b. Numerical values of the input features of the test units considered in this study are provided in Appendix/Table A.1.

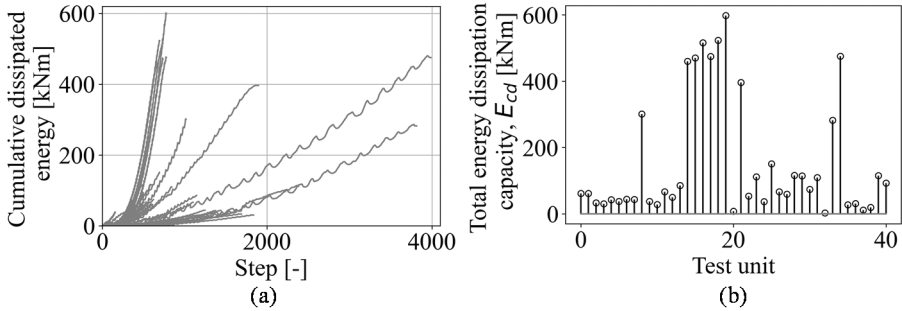


Figure 3 - Variabilities on the dissipated energy levels of selected test units: (a) cumulative energy dissipations, (b) total energy dissipation capacities

Based on a compilation of the dataset, the correlations between the selected features and the target total energy dissipation capacities are investigated next by considering a statistical approach (i.e., using the Pearson's correlation coefficient [21]).

2.2. Dependency of the Dissipated Energy Capacity on Selected Features

The dissipated energy is used to quantitatively represent the cumulative damage level since the seismic energy is the enclosed area by force-displacement relation of each column. Thereby, correlation of the damage on the columns with a scalar quantity, i.e., energy, is possible.

Here, the minimum and the maximum dissipated energies were obtained as 2.94 kNm and 597.93 kNm, respectively. The variation of energy capacities is directly related to several factors, including the sectional/geometrical, material, and mechanical properties of test units, as well as the loading path characteristics. Previous research [2,11] has shown that selected parameters have a significant impact on the dissipated energy capacity. However, there are additional parameters, such as peak drift ratio and yield strength of rebars, that are directly implemented to enhance the features for a more comprehensive analysis.

In the current study, the dependency level of dissipated energy capacity on selected features is investigated by using the correlation between the input and target parameters. For this purpose, the Pearson's correlation coefficients are considered as dependency indicators. Following equation is implemented to predict the level of correlation:

$$\rho_{F,T} = \frac{\sigma_{FT}}{\sigma_F \sigma_T} \quad (1)$$

Here, σ_{FT} is the covariance between the selected feature and the target response, and σ_F and σ_T denote for the standard deviations of feature and target data, respectively. Here, the implemented parametric correlation approach enables user to measure the level of linear dependence between two variables based on distribution characteristics.

3. STATISTICAL INVESTIGATION

Predicted correlation levels are presented as heatmaps by utilizing the Python [22,23] software. In Figure 4, the correlations between the selected feature set and the energy capacity levels are presented. In this matrix, the boundary levels of +1, 0, and -1 of a correlation matrix typically represent the complete positive, no correlation, and complete negative correlation levels, respectively. Here, the complete positive correlation case basically corresponds to a directly proportional relationship between the selected feature and the target parameter (i.e., as target parameter increases the feature level also increases by the exactly same percentage). An exactly opposite relationship between two variables is observed in case of a complete negative correlation. It is observed from the figure that, loading characteristics (i.e., axial load ratio and peak drift ratio) and transverse rebar properties have considerable effects on the dissipated energy. Specifically, the peak drift ratio and the transverse reinforcement contribute the total dissipated energy capacity, mostly (i.e., as moderate positive correlation levels of 0.60, approximately). However, it should be noted that this case is especially valid for well-confined (i.e., by considering the maximum reinforcement ratio recommendations available in codes and standards) sections. The correlation between the concrete material characteristics and the energy capacity is lower compared to those correlation levels of other features. Here, it should be noted that only 4 out of 41 total test specimens' concrete compressive strength levels are not considered as normal strength concrete (e.g., 20 MPa < f_c < 40 MPa). A comprehensive comparison for the effect of normal and high-strength concrete RC columns concluded that the total energy dissipation capacity of normal strength concrete is higher than that of the capacity of high strength concrete because of the brittle nature of high strength concrete. This can be attributed to the fact that the inverse relationship between strength and the ductility level of material affects the dissipated energy levels [2].

The levels of individual correlations are summarized in Figure 5. The results show that, the total dissipated energy capacity is mostly influenced by the peak drift ratio. The total dissipation capacity increases with an increasing peak drift ratio. This indicates that although strength degradation due to high level damage state occurs, members still dissipate energy which might be called residual capacity. On the other hand, an opposite trend is valid for the axial load level. Figure 5 shows that, for test specimens subjected to lower axial load levels have higher energy capacity. The total energy dissipation capacity decreases due to high axial stress levels owing to the specimens' lateral deformation is limited under the effects of high axial loads. Comparison over the material characteristics reveals that, rebar yield strength positively influences dissipated energy capacity of the member. Based on ductile design principle, it is also observed that high dissipated energy capacities are obtained for heavily reinforced test specimens (i.e., a positive correlation level of 0.53) and well-confined sections. As the dataset selected in this study includes flexure-dominated RC column type

test units, the minimum threshold for shear span-to-depth ratios is limited by 3. Due to this limitation, an increment trend in energy capacity is observed for decreasing values of shear span-to-depth ratios (i.e., a negative correlation level of -0.3). This inverse proportionality trend for other case (i.e., for $a/d < 3$ RC columns) was recommended in previous studies [2]

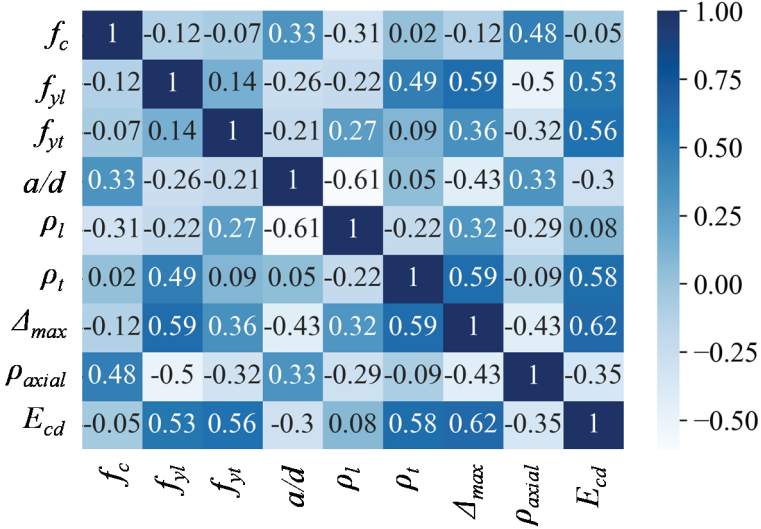


Figure 4 - Correlation matrix for input features and the dissipated energy level

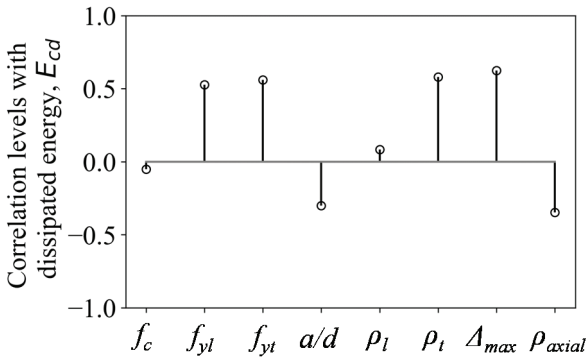


Figure 5 - Correlation with dissipated energy levels obtained for input features

The pairwise regression plots with 95% of confidence intervals for a single feature (i.e., peak drift ratio) having the highest positive correlation with the dissipated energy capacity, and for the opposite case such as axial load ratio that shows a considerable negative correlation with the target parameter, are given in Figures 6a and 6b, respectively. Moreover, additional partial figures given at top and right of the figure of interest represent the approximate feature distribution and tendency characteristics.

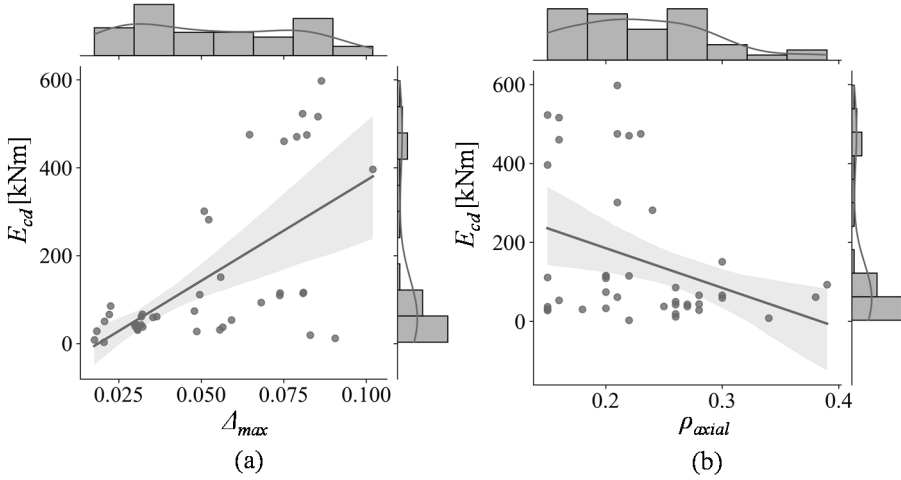


Figure 6 - Pairwise regression between: (a) Δ_{max} - E_{cd} , (b) ρ_{axial} - E_{cd} .

In order to compare the energy dissipation characteristics of RC column test units having the minimum (i.e., UM_205 [24]) and the maximum (i.e., C3-3 [25]) energy capacities in a dataset, the total dissipated energy, $E_{cd,L}$ normalized by the maximum strength, F_{max} and the shear span a is given as follows:

$$E_{cd,L} = \frac{E_{cd}}{F_{max} \times a} \quad (2)$$

General properties and loading histories of the test units UM_205 and C3-3 are provided in Table 3 and Figures 7a and 7b.

Table 3 - General properties of test units

ID	Year	Δ_{max}	ρ_t	ρ_{axial}	a/d	f_{yt} [MPa]
UM_205	1970	0.021	0.003	0.22	3.3	324.1
C3-3	2000	0.086	0.006	0.21	4	459.4

Regarding the general characteristics provided in Table 3, the fundamental differences between test specimens are mainly based on the transverse rebar amount, its material quality, and peak displacement properties. The normalized energy dissipation capacities are compared by considering the elastic (1), pre-capping (2), and post-capping (3) regions (Figures 8a and 8b). While the hysteretic curves of the specimens were given by solid lines, the envelope of the hysteresis loops are given by dashed lines in the figures.

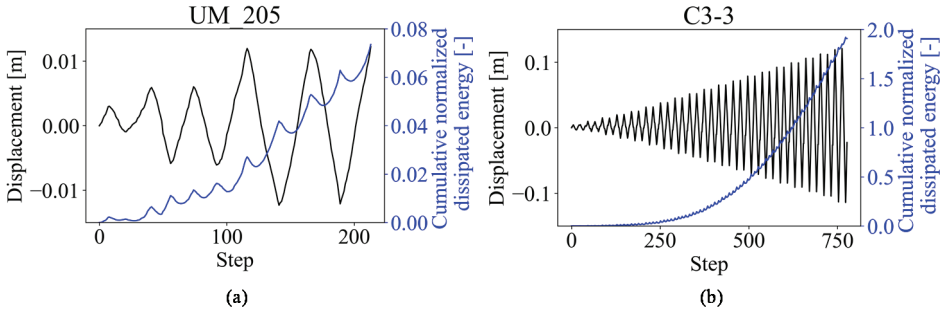


Figure 7 - Loading histories of test specimens: (a) UM_205, (b) C3-3

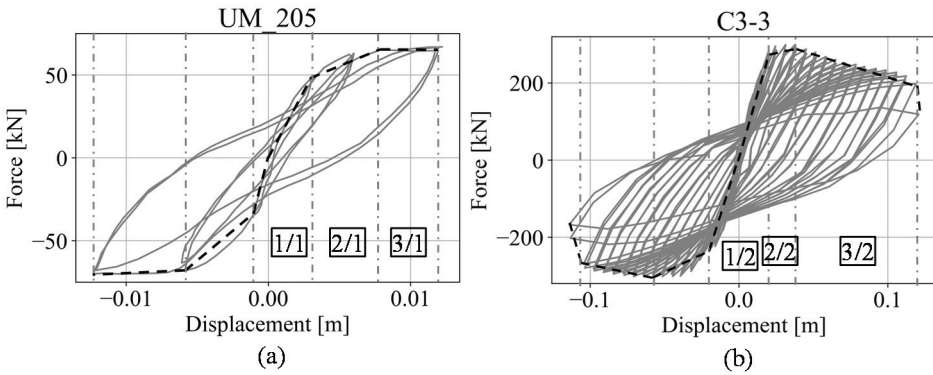


Figure 8 - Force-displacement history and envelopes for test specimens:(a) UM_205, (b) C3-3

The preliminary results indicate that, the highest amount of energy is dissipated at post-capping regions for UM-205 and C3-3 test units (i.e., 69.4% and 88.7% of total dissipated energy, respectively). Moreover, it is seen that in the post-capping region, normalized dissipated energy graph has a steeper slope for the C3-3 test unit (Figure 9). This is attributed to both the strong level of correlated features (Table 3), and the large number of cycles captured during the loading stages for C3-3 test specimen. Further clarification can be achieved by investigating the related issue.

The correlation levels are also investigated by using the normalized capacity for the entire data set. Similar observations with the total energy dissipation capacity-based results, are obtained for the selected indicator (Figure 10a). Moreover, to compare the calculated correlation levels via total and normalized dissipated energy levels, the relative differences between the two approaches are compared (Figure 10b). Here, the positive relative differences indicate an increment in predicted correlation level by implementing the normalized energy capacity parameters in dependency-based investigations. Specifically, even similar trends are obtained for both approaches, the correlation level between the high-

correlated features and the target capacity may be also increased (i.e., correlation level for transverse reinforcement ratio is 0.58 to 0.71 from approximately moderate to strong positive correlation).

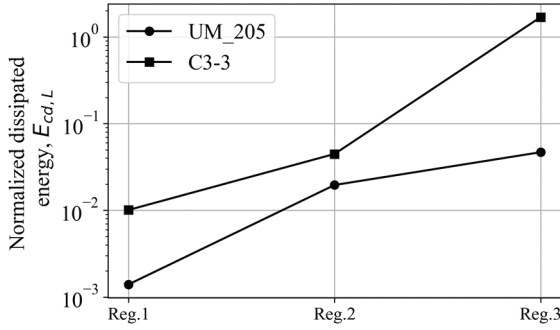


Figure 9 - Comparison of normalized dissipated energy capacities

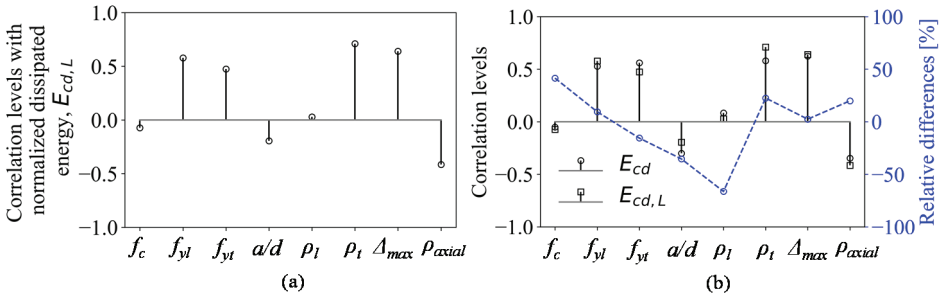


Figure 10 - (a) Correlation levels obtained for input features using the normalized capacity parameter, (b) Comparison between two capacity indicators

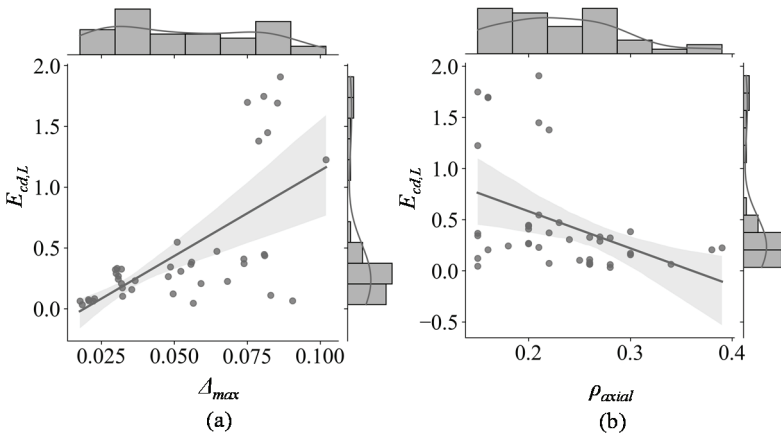


Figure 11 - Pairwise regression between: (a) $\Delta_{max} - E_{cd,L}$, (b) $\rho_{axial} - E_{cd,L}$.

Finally, to compare the input feature-based results between the total dissipated energy and the normalized parameter evaluated through Equation 2, the pairwise regression plots for peak drift ratio and the axial load ratio are given in Figures 11a and 11b, respectively. Similar to the overall regression trends captured for total dissipated energy capacities, the positive and negative correlations are also observed for selected input features.

4. DISCUSSION AND CONCLUSION

A quantitative investigation of the effects of flexure-dominated RC column properties on the total energy dissipation capacity is presented and discussed in this paper. For this purpose, a dataset including 41 RC column test units is compiled from the existing comprehensive databases. Correlations between the selected fundamental member and loading-base features and the dissipated energy capacity parameter are represented using the commonly used statistical approaches. Results of the study are summarized below:

- The degree of dependency of the energy capacity on critical features is obtained numerically. For this purpose, a considerable number of a parameter set (i.e., 8 parameters) is considered. Peak drift ratios and the axial load levels are found to have the highest positive and negative correlations, respectively.
- For flexure-dominated RC columns, a negative correlation is obtained between the shear span-to-depth ratio and the dissipated energy capacity parameter which indicates that shear-domination has negative affect on the member response.
- Higher energy dissipation capacity levels are obtained for well-confined members. It is found that this is directly proportional to the volumetric ratio of transverse reinforcement.
- It is observed that the minimum concrete strength and longitudinal rebar ratio have a marginal effect on the dissipated energy capacity.
- In order to consider the possible effects of dispersions due to member-wise characteristics, the correlation levels are also calculated via normalized dissipated energy capacity parameter. Similar trends in dependencies are also obtained for the actual and normalized capacity levels.

As energy-based seismic design of structures gains popularity, the metadata including a detailed experimental information of existing test specimens compiled using the available databases in the literature may be a good starting point for future analytical studies. Moreover, correlation levels evaluated in the current study are believed to have a contribution to future seismic codes that include the fundamentals of energy-based design procedures by taking into account the effectiveness levels of structural member related features in a statistical way. In other words, the outcomes of this study are essential for use in implicit equations, which may aim to estimate the energy dissipation capacity of structural elements and the proposed methodology could be extended to determine the energy dissipation capacity of dual systems and/or moment resisting frame systems containing beam, shear wall and column elements. Additionally, the study provides insights into the critical features that affect the energy dissipation capacity of these members, which can be considered in the design process. The outcomes can be used to calibrate current design standards and practices for assessing the seismic performance of buildings with configuration irregularities in terms

of providing quantitative triggers and related design requirements that can be used to improve the seismic performance of buildings.

Acknowledgment

This work has been funded and supported by the Scientific and Technological Research Council of Türkiye, (TÜBİTAK, Turkish Research Foundation), Project ID: 121M713. This support is greatly acknowledged.

References

- [1] Gill, W.D., Ductility of Rectangular Reinforced Concrete Columns with Axial Load. University of Canterbury, Department of Civil Engineering, Master of Engineering, 1979.
- [2] Poljanšek, K., Peruš, I., Fajfar, P., Hysteretic Energy Dissipation Capacity and the Cyclic to Monotonic Drift Ratio for Rectangular RC columns in Flexure. *Earthquake Engineering & Structural Dynamics*, 38(7), 2009.
- [3] Acun, B., Sucuoğlu, H., Energy Dissipation Capacity of Reinforced Concrete Columns under Cyclic Displacements. *ACI Structural Journal*, 109(4), 2012.
- [4] Rodrigues, H., Furtado, A., Arêde, A., Behavior of Rectangular Reinforced-Concrete Columns Under Biaxial Cyclic Loading and Variable Axial Loads. *Journal of Structural Engineering*, 142(1), 04015085, 2016.
- [5] Vu, N.S., Li, B., Tran, C.T.N., Seismic Behavior of Reinforced Concrete Short Columns Subjected to Varying Axial Load. *ACI Structural Journal*, 119(6), 2022.
- [6] Yang, S. Y., Song, X. B., Jia, H. X., Chen, X., Liu, X. L., Experimental Research on Hysteretic Behaviors of Corroded Reinforced Concrete Columns with Different Maximum Amounts of Corrosion of Rebar. *Construction and Building Materials*, 121, 2016.
- [7] Yalçın, C., Dindar, A. A., Yüksel, E., Özkaynak, H., Büyüköztürk, O., Seismic Design of RC Frame Structures based on Energy-Balance Method. *Engineering Structures*, 237, 112220, 2021.
- [8] Browning, J.A., Pujol, S., Eigenmann, R., Ramirez, J.A., NEEShub Databases. *Concrete International*, <https://datacenterhub.org/resources/databases>, 2013 (Accessed: 01.10.2021).
- [9] Rathje, E., Dawson, C. Padgett, J.E., Pinelli, J.-P., Stanzione, D., Adair, A., Arduino, P., Brandenburg, S.J., Cockerill, T., Dey, C., Esteva, M., Haan, Jr., F.L., Hanlon, M., Kareem, A., Lowes, L., Mock, S., Mosqueda, G., DesignSafe: A New Cyberinfrastructure for Natural Hazards Engineering. *ASCE Natural Hazards Review*, 18(3), 2017.
- [10] Berry, M., Parrish, M., Eberhard, M., PEER structural performance database user's manual (version 1.0). University of California, Berkeley, 2004.

- [11] Haselton, C.B., Assessing Seismic Collapse Safety of Modern Reinforced Concrete Moment Frame Buildings, Stanford University, Doctoral Dissertation, 2006.
- [12] Liu, Z., Wang, Y., Cao, Z., Chen, Y., Hu, Y., Seismic Energy Dissipation Under Variable Amplitude Loading for Rectangular RC Members in Flexure. *Earthquake Engineering & Structural Dynamics*, 47(4), 2018.
- [13] Ibarra, L. F., Medina, R. A., Krawinkler, H., Hysteretic Models that Incorporate Strength and Stiffness Deterioration. *Earthquake Engineering & Structural Dynamics*, 34(12), 2005.
- [14] Di Domenico, M., Ricci, P., Verderame, G. M., Empirical Calibration of Hysteretic Parameters for Modelling the Seismic Response of Reinforced Concrete Columns with Plain Bars. *Engineering Structures*, 237, 112120, 2021.
- [15] Rodas, P. T., Zareian, F., Kanvinde, A., Hysteretic Model for Exposed Column–Base Connections. *Journal of Structural Engineering*, 142(12), 04016137, 2016.
- [16] Horton, T. A., Hajirasouliha, I., Davison, B., Ozdemir, Z., Accurate Prediction of Cyclic Hysteresis Behaviour of RBS Connections Using Deep Learning Neural Networks. *Engineering Structures*, 247, 113156, 2021.
- [17] Rayjada, S. P., Raghunandan, M., Ghosh, J., Machine Learning-Based RC Beam-Column Model Parameter Estimation and Uncertainty Quantification for Seismic Fragility Assessment. *Engineering Structures*, 278, 2023.
- [18] Luo, H., Paal, S. G., Machine Learning–Based Backbone Curve Model of Reinforced Concrete Columns Subjected to Cyclic Loading Reversals. *Journal of Computing in Civil Engineering*, 32(5), 2018.
- [19] Akbaş, B., Jay, Shen, Depreme Dayanıklı Yapı Tasarımı ve Enerji Kavramı. *Teknik Dergi*, 14(67), 2003.
- [20] Merter, O., Bozdağ, Ö., Düzgün, M., Energy-based Design of Steel Structures According to the Predefined Interstory Drift Ratio, *Teknik Dergi*, 23(115), 1573-1593, 2012.
- [21] Pearson, K., Notes on the history of correlation. *Biometrika*, 13(1), 25-45, 1920.
- [22] Van Rosum, G., Drake, F.L., Python 3 reference manual, CreateSpace, 2009.
- [23] Waskom, M.L., Seaborn: Statistical Data Visualization. *Journal of Open Source Software*, 6(60), 2021.
- [24] Umemura H., Endo, T., Report by Umemura Lab, Tokyo University, 1970.
- [25] Mo, Y. L., Wang, S. J., Seismic Behavior of RC Columns with Various Tie Configurations. *Journal of Structural Engineering*, 126(10), 1122-1130, 2000.
- [26] Atalay, M. B., Penzien, J., The Seismic Behavior of Critical Regions of Reinforced Concrete Components as Influenced by Moment, Shear and Axial Force. Berkeley, CA, USA: Earthquake Engineering Research Center, University of California, 1975.

- [27] Harries, K. A., Ricles, J. R., Pessiki, S., Sause, R., Seismic Retrofit of Lap Splices in Nonductile Square Columns Using Carbon Fiber-Reinforced Jackets. *ACI Structural Journal*, 103(6), 874, 2006.
- [28] Lynn, A. C., Moehle, J. P., Mahin, S. A., Holmes, W. T., Seismic Evaluation of Existing Reinforced Concrete Building Columns. *Earthquake Spectra*, 12(4), 715-739, 1996.
- [29] Nosh, K., Stanton, J., MacRae, G., Retrofit of Rectangular Reinforced Concrete Columns Using Tonen Forca Tow Sheet Carbon Fiber Wrapping. Report No. SGEM, 96-2, 1996.
- [30] Saatcioglu, M., Ozcebe, G., Response of Reinforced Concrete Columns to Simulated Seismic Loading. *Structural Journal*, 86(1), 3-12, 1989.
- [31] Sezen, H., Moehle, J. P., Seismic Behavior of Shear-Critical Reinforced Concrete Building Columns. In *Seventh US National Conference on Earthquake Engineering*, Earthquake Engineering Research Institute, Boston, MA, 2002.
- [32] Soesianawati, M. T., Limited Ductility Design of Reinforced Concrete Columns, 1986.
- [33] Tanaka, H., Park, R., Effect of Lateral Confining Reinforcement on the Ductile Behavior of Reinforced Concrete Columns [Report 90-2]. Department of Civil Engineering, University of Canterbury, 1990.
- [34] Wehbe, N., Saiidi, M.S., Sanders, D., Confinement of Rectangular Bridge Columns for Moderate Seismic Areas. National Center for Earthquake Engineering Research, 1998.
- [35] Wight, J. K., Sozen, M. A., Shear Strength Decay in Reinforced Concrete Columns Subjected to Large Deflection Reversals. *Structural Research Series No. 403*. Civil Engineering Studies. Urbana-Champaign (IL): University of Illinois, 1973.
- [36] Yoshimura, M. Y., Ultimate Limit State of RC Columns. The Second U.S.- Japan Workshop on Performance-Based Earthquake Engineering Methodology, 2000.
- [37] Zahn, F. A., Priestley, M.J.N., Design of Reinforced Concrete Bridge Columns for Strength and Ductility. Christchurch, New Zealand, University of Canterbury, 1986.

A Quantitative Investigation on the Effects of Flexure-Dominated Reinforced Concrete Column Characteristics on the Dissipated Energy

APPENDIX

Table A.1 - Input features and total energy dissipation capacities of the test units considered in this study

ID	Unit	Ref.	$b \times h^{**}$ [m]	H^* [m]	ρ_{axial} [-]	f_c [MPa]	f_{jt} [MPa]	f_{yt} [MPa]	a/d [-]	ρ_l [-]	ρ_t [-]	E_{cd} [kNm]
1	No.3	[1]	0.40x0.40	1.60	0.38	23.6	426.9	320.0	4.50	0.0151	0.0280	61.46
2	No.4	[1]	0.40x0.40	1.60	0.21	25.0	426.9	280.0	4.45	0.0151	0.0220	61.47
3	No.5S1	[26]	0.31x0.31	1.68	0.20	29.4	428.9	391.9	6.64	0.0163	0.0150	33.33
4	No.6S1	[26]	0.31x0.31	1.68	0.18	31.8	428.9	391.9	6.64	0.0163	0.0090	30.53
5	No.9	[26]	0.31x0.31	1.68	0.26	33.3	362.9	391.9	6.64	0.0163	0.0150	42.82
6	No.10	[26]	0.31x0.31	1.68	0.27	32.4	362.9	391.9	6.64	0.0163	0.0090	37.96
7	No.11	[26]	0.31x0.31	1.68	0.28	31.0	362.9	372.9	6.64	0.0163	0.0150	44.02
8	No.12	[26]	0.31x0.31	1.68	0.27	31.8	362.9	372.9	6.64	0.0163	0.0090	43.29
9	NC1	[26]	0.46x0.46	1.37	0.21	39.3	438.9	453.9	3.49	0.0194	0.0220	301.15
10	L0	[27]	0.46x0.46	2.40	0.25	24.6	459.9	437.8	5.88	0.0148	0.0020	37.64
11	2CMH18	[28]	0.46x0.46	2.95	0.28	25.5	330.9	399.8	3.71	0.0194	0.0016	28.45
12	3SMD12	[28]	0.46x0.46	2.95	0.28	25.5	330.9	399.9	3.74	0.0303	0.0041	66.42
13	3CMH18	[28]	0.46x0.46	2.95	0.26	27.6	330.9	399.8	3.74	0.0304	0.0016	50.33
14	3CMD12	[28]	0.46x0.46	2.95	0.26	27.6	330.9	399.8	3.74	0.0304	0.0042	85.68
15	C1-2	[25]	0.40x0.40	1.40	0.16	26.7	496.9	459.4	4.00	0.0214	0.0300	460.46
16	C1-3	[25]	0.40x0.40	1.40	0.22	26.1	496.9	459.4	4.00	0.0214	0.0300	470.45
17	C2-2	[25]	0.40x0.40	1.40	0.16	27.1	496.9	459.4	4.00	0.0214	0.0300	516.26
18	C2-3	[25]	0.40x0.40	1.40	0.21	26.8	496.9	459.4	4.00	0.0214	0.0300	475.05
19	C3-2	[25]	0.40x0.40	1.40	0.15	27.5	496.9	459.4	4.00	0.0214	0.0300	523.20
20	C3-3	[25]	0.40x0.40	1.40	0.21	26.9	496.9	459.4	4.00	0.0214	0.0300	597.93
21	No.1	[29]	0.28x0.28	2.13	0.34	40.6	406.9	350.9	8.90	0.0101	0.0218	8.15
22	U4	[30]	0.35x0.35	1.00	0.15	32.0	437.9	469.9	3.28	0.0331	0.0250	396.52
23	U2	[30]	0.35x0.35	1.00	0.16	30.2	452.9	469.9	3.28	0.0321	0.0069	53.62
24	Specimen_1	[31]	0.46x0.46	2.95	0.15	21.1	434.3	475.9	3.76	0.0248	0.0020	111.65
25	Specimen_4	[31]	0.46x0.46	2.95	0.15	21.8	434.3	475.9	3.76	0.0248	0.0020	37.35
26	No.2	[32]	0.40x0.40	1.60	0.30	44.0	445.9	359.9	4.31	0.0151	0.0120	151.02
27	No.3	[32]	0.40x0.40	1.60	0.30	44.0	445.9	363.9	4.30	0.0151	0.0080	66.57
28	No.4	[32]	0.40x0.40	1.60	0.30	40.0	445.9	254.9	4.29	0.0151	0.0060	59.70
29	No1	[33]	0.40x0.40	1.60	0.20	25.6	473.9	332.9	4.73	0.0157	0.0250	116.28
30	No2	[33]	0.40x0.40	1.60	0.20	25.6	473.9	332.9	4.73	0.0157	0.0250	114.47
31	No3	[33]	0.40x0.40	1.60	0.20	25.6	473.9	332.9	4.73	0.0157	0.0250	74.14
32	No4	[33]	0.40x0.40	1.60	0.20	25.6	473.9	332.9	4.73	0.0157	0.0250	109.45
33	UM_205	[24]	0.20x0.20	0.60	0.22	17.6	462.0	324.1	3.33	0.0199	0.0061	2.94
34	A2	[34]	0.38x0.61	2.34	0.24	27.2	447.9	427.9	4.12	0.0222	0.0040	282.08
35	B2	[34]	0.38x0.61	2.34	0.23	28.1	447.9	427.9	4.10	0.0222	0.0050	475.25
36	WI_40_048E	[35]	0.15x0.31	0.88	0.15	26.1	495.9	344.9	3.45	0.0245	0.0048	27.76
37	WI_40_048W	[35]	0.15x0.31	0.88	0.15	26.1	495.9	344.9	3.45	0.0245	0.0048	31.35
38	FS0	[36]	0.30x0.30	0.90	0.26	27.0	386.9	354.9	3.53	0.0382	0.0148	11.92
39	FS1	[36]	0.30x0.30	0.90	0.26	27.0	386.9	354.9	3.53	0.0382	0.0148	19.33
40	No.7	[37]	0.40x0.40	1.60	0.22	28.3	439.9	465.9	4.34	0.0151	0.0160	115.26
41	No.8	[37]	0.40x0.40	1.60	0.39	40.1	439.9	465.9	4.34	0.0151	0.0200	93.18

* H : Height of test unit; b, h : Column cross-sectional dimensions along and perpendicular to loading, respectively.

Corrosion Rate-Based Adjustment of Plastic Hinge Parameters of Corroded RC Elements

Mustapha BENREDOUANE¹
Nouredine BOURAHLA^{2*}
Anouar GHODBANE³
Hala KHALFAOUI⁴



ABSTRACT

In line with the trend towards predictive seismic codes adopting the performance-based design method, this paper presents an integrated protocol to determine the degraded hysteresis parameters of corroded RC hinges based on relationships developed for this purpose together with a calibration procedure using the random-mutation hill-climbing algorithm. The adjustment procedure is integrated into the material library of the OpenSees software and used to perform nonlinear dynamic analyses to investigate the seismic performance of a typical bridge with affected piers at different corrosion levels. In practice the proposed procedure permits to assess the seismic performance of existing or new structures for a given corrosion rate distribution.

Keywords: Hysteresis degradation parameters, reinforcement corrosion, nonlinear dynamic analysis, corroded RC bridge pier.

1. INTRODUCTION

Corrosion of steel reinforcement, alkali-silica reaction, freeze-thaw damage, and sulfate attack are some of the age-related degradation mechanisms for RC structures. Among these mechanisms, the corrosion of steel has been identified as the most widespread and predominant mechanism responsible for the deterioration of RC structures [1,2]. Extensive

Note:

- This paper was received on December 6, 2022 and accepted for publication by the Editorial Board on October 20, 2023.
- Discussions on this paper will be accepted by May 31, 2024.
- <https://doi.org/10.18400/tjce.1214088>

1 National School of Public Works, LTPITE Laboratory, Algiers, Algeria
m.benredouane@enstp.edu.dz - <https://orcid.org/0000-0003-3680-8258>

2 National Polytechnic School, Civil Engineering Department, Algiers, Algeria
Nouredine.bourahla@g.enp.edu.dz - <https://orcid.org/0000-0002-1377-5943>

3 National Polytechnic School, Civil Engineering Department, Algiers, Algeria
anouar.ghodbane@g.enp.edu.dz - <https://orcid.org/0009-0008-8832-2544>

4 National Polytechnic School, Civil Engineering Department, Algiers, Algeria
hala.khalfaoui@g.enp.edu.dz - <https://orcid.org/0009-0003-1364-6636>

* Corresponding author

research work has contributed to elucidate many aspects related to the corrosion of steel reinforcement. At a fundamental level, the initiation and propagation of corrosion in steel reinforcement, which has been addressed in many research programs documented in the literature [3,4] constitutes an essential issue for the service life assessment of RC structures subjected to corrosion [5,6].

Of particular interest is the effect of corrosion on the performance of structures in seismic-prone zones [7-11]. Akiyama and Frangopol [12] proposed a framework to integrate the corrosion effect in terms of airborne chloride hazard probability in the assessment of the seismic performance of bridge piers. Similarly, Choe et al. [13] evaluated seismic fragility curves based on a probabilistic model of chloride-induced corrosion. Following the trend in the generalization of seismic fragility analysis as a corrosion time-dependent concept, Hu et al. [14] proposed a framework and applied it to determine the seismic damage of an aging four-span continuous RC bridge. Using a different approach, Domaneschi et al. [15] investigated the coupling of corrosion and earthquake action on bridge piers to predict the early collapse under such conditions.

It is clear that these frameworks help predict life service and potential damage to structures under seismic threats. Nonetheless, there is a pressing need for the precise assessment of existing deteriorated structures for rehabilitation or other purposes. To fulfil this demand, several experimental studies [16-18] and numerical techniques have been developed to provide practical assessment modeling tools [19,20].

Owing to the complexity and variability of the corrosion phenomena affecting the steel reinforcement of structural elements subjected to seismic loading, it is essential to provide transparent and explicit practical methods that express the relationships between a factor characterizing the corrosion level of a structural element that can be measured in situ or predicted by a time-dependent approach and the numerical model parameters that control the structural deterioration.

In this study, the modified peak-oriented model proposed by Ibarra-Medina-Krawinkler (MODIMK) [21] was chosen as a reference hysteresis model and corrected to account for changes in the properties and deterioration parameters using relationships developed for this purpose. These relationships link the mechanical properties and degradation parameters of the hysteresis loop to the corrosion-level factor. They were integrated into the existing hysteresis model within the material library of the OpenSees software [22].

The proposed model was calibrated using available experimental data for five RC columns with different levels of reinforcement corrosion. Taking advantage of the explicit model, nonlinear dynamic analysis was performed to investigate the performance of a typical RC bridge with piers having different levels of corrosion.

2. MODELING APPROACH OF A CORRODED PLASTIC HINGE

The approach used in this paper is based on the integration of the effect of aging due to the corrosion of reinforcement into a hysteresis model of a plastic hinge of a RC element. The modified Ibarra-Medina-Krawinkler (MODIMK) Peak-Oriented model takes into account six different mechanisms of deterioration: Basic strength deterioration, post-yielding, post-capping, unloading stiffness, reloading stiffness, and pinching. The model is ideal for the

management of degradation phenomena, henceforth, it is adopted to incorporate the deteriorating effect of the corrosion of the reinforcement.

The MODIMK model requires the specification of 23 parameters, where seven parameters at least are calibrated using experimental data.

Further to the initial calibration of the model parameters [21], subsequent studies have been carried out in order to provide explicit and simplified equations to predict the model parameters. Haselton et al. [23] proposed a calibration procedure based on 255 RC column tests and developed a set of equations that can be used to calculate the parameters necessary for the development of the complete "backbone" curve and establish a hysteresis degradation rate knowing only some of the physical and geometric characteristics of a reinforced concrete section. The equations of the parameters which potentially can be affected by the steel reinforcement corrosion are used in this study to calculate the initial rigidity K_e , the plastic rotations capacity (θ_p), the post capping rotation capacity (θ_{pc}) and the post-yield hardening stiffness characterized by the ratio of the maximum moment capacity and the yield moment capacity (M_c/M_y).

The yield moments (M_{y+} and M_{y-}) are estimated using the formulae given by Panagiotakos et al. [24]. However, the cyclic degradation parameters ($\lambda_A, \lambda_K, \lambda_S, \lambda_C$) and their exponents (C_A, C_K, C_S, C_C), will be estimated by a calibration procedure using experimental hysteresis loops available in the literature.

3. HYSTERESIS LOOP PARAMETERS FOR A CORROSION LEVEL (CL)

The degradation of RC structures by corrosion is a very complex phenomenon and involves multiple effects. The visual aspects of the degradations are mainly corrosion-spots, cracks in the vicinity of the rebars, spalling and even the splitting of the concrete cover. The effect on the structural capacity of a RC element, particularly on the dynamic potential expressed in terms of the hysteresis loop parameters, is illustrated in Fig 1.

As mentioned before, the 'MODIMK' model is controlled by several parameters associated with the geometric and mechanical properties of the RC element. Thus, in the first instance, a corrosion level (CL) is defined to characterize the deteriorated RC element and used to determine the altered geometric and mechanical characteristics of the model.

These functions are implemented in the OpenSees and used to simulate series of experimental tests of columns degraded by accelerated (artificial) corrosion at increasing levels. A calibration process is performed to match the numerical and experimental hysteresis loops in order to determine the best fit of the deterioration parameters (λ_i and c_i) for different corrosion rates Fig. 2.

3.1. Characterization of the Corrosion in Existing Elements and Structures

Precise assessment of existing structures subjected to corrosion depends on the accuracy of the evaluation of the degree and locations of the corrosion on the structural elements which are needed to fine-tune the hysteresis parameters at potential plastic hinges. Although, measuring the corrosion rate is difficult, numerous methods exist in the literature for researchers and engineers to evaluate and appreciate the degree of corrosion of existing structures.

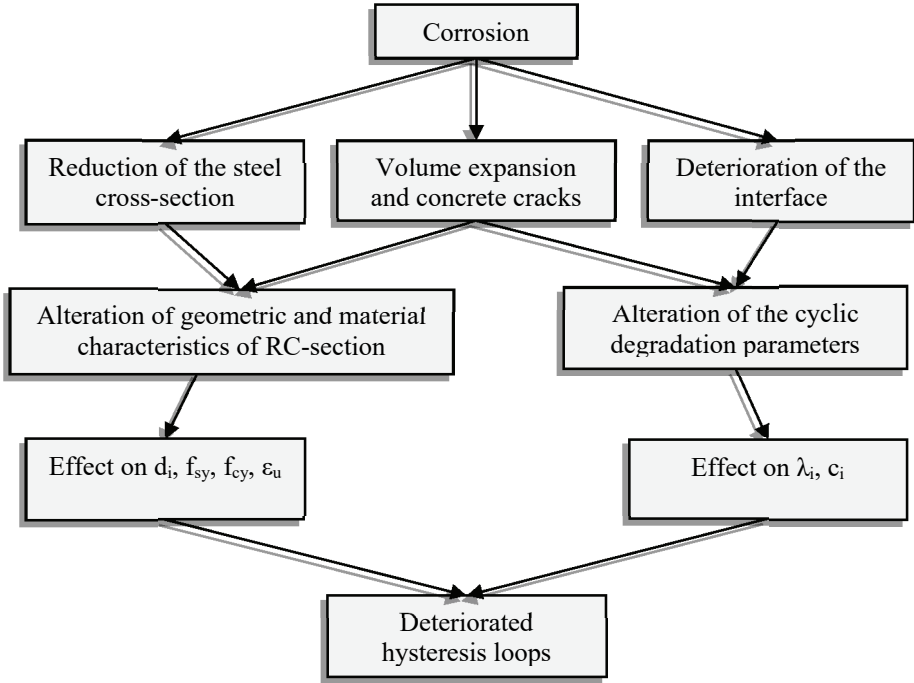


Figure 1 - Effect of the corrosion of reinforcement on the hysteresis loop

In this research work, the corrosion level, CL , is the factor used to characterize structural damage related to aging. It is defined as the average mass loss of rebar.

$$CL = \frac{\Delta w}{w} \times 100 \% \quad (1)$$

- Δw is the mean mass loss of corroded rebars.
- w is the mass of the original rebars.

If the corrosion is homogeneous, over an average surface of the rebar, the level of corrosion can be expressed in terms of corroded and uncorroded cross sections A_c and A_i respectively or in terms of corroded and uncorroded diameters d_c and d_i as follows:

$$CL = \frac{(A_i - A_c)}{A_i} \times 100 \quad (2)$$

$$CL = \left[1 - \frac{A_c}{A_i} \right] \times 100 \quad (3)$$

$$CL = \left[1 - \left(\frac{d_c}{d_i} \right)^2 \right] \times 100 \quad (4)$$

In practice, the corrosion level can be obtained by measurement of the residual diameter d_c or by means of techniques that correlate the width of external cracks with the reduction of the cross-section of the reinforcement bar [25-28].

Other techniques based upon direct measurement of the corrosion current density (i_{corr}), using the linear polarization resistance LPR method or indirect predictions method using non-destructive resistivity measurements [29], are suitable to predict the corrosion current density in a specific location of a structural element at a period of time during its life service.

The conversion of the current density i_{corr} to a corrosion level CL can be obtained using one of the formulae available in the literature such as the expression proposed by Du et al. [30]:

$$CL = 0.046 \frac{i_{corr}}{d_i} t \times 100 \tag{5}$$

Where

d_i : Nominal diameter of the non-corroded rebar in (mm);

i_{corr} : Corrosion current density in ($\mu\text{A}/\text{cm}^2$);

t : Time in years since the initiation of the corrosion.

Figure 2 illustrates the procedure to correct the hysteresis properties of a corroded plastic hinge. A hybrid approach is used in the proposed framework incorporating two methods:

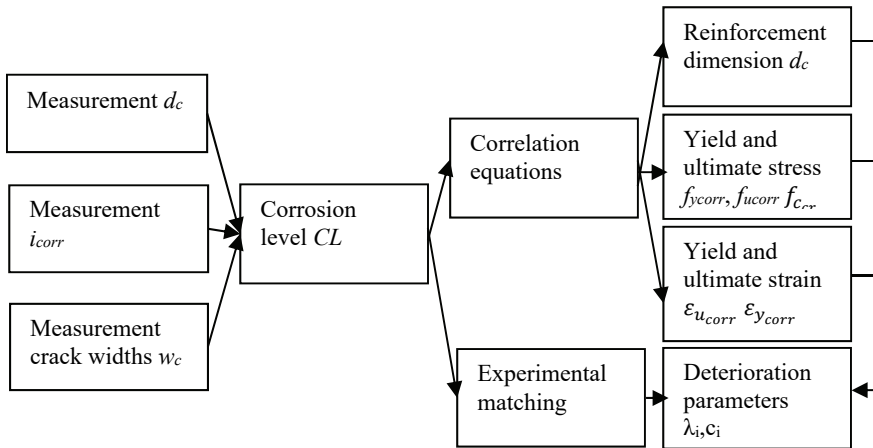


Figure 2 - Corrosion correction of the hysteresis loop parameters

Explicit Method: This method explicitly considers the impact of corrosion on the geometry and material properties of a particular section (hinge) through correlation functions, taking into account the corrosion level (CL).

Implicit Method: The implicit method compensates for the effects of corrosion that cannot be explicitly or directly accounted for in the current study. This includes factors such as stress-strain incompatibility or the loss of bond between reinforcement and concrete. The

implicit method involves either calibrating the degradation parameters or employing a correction factor (interpolation) for the yield moment using a data-based approach.

By combining these explicit and implicit techniques, the proposed framework aims to comprehensively consider the influence of corrosion on the structural behavior, accounting for both known and unidentified corrosion-related effects.

3.2. Corrosion Effect on the Cross Section of the Rebar

Homogeneous corrosion affects the cross-section with more or less uniform loss over the perimeter of reinforcing bars. Localized (or pitting) corrosion, however, concentrates over small areas of the reinforcement. The residual cross-section as reported by several experimental research tests is no longer round with variation in circumference along the bar because of the pitting penetration [31]. Considering Eq. 3, the mean cross-section of the corroded bar (A_c) can be expressed in terms of the degree of corrosion as:

$$A_c = A_i(1 - 0.01CL) \quad (6)$$

All other parameters of the plastic hinge depending on the steel reinforcement sections can be derived from the above relationship.

3.3. Yield and Ultimate Strength and Strain Reduction Due to Corrosion

Numerous studies have been conducted on the stress-strain relationship and the residual strength and ductility capacities of corroded steel reinforcing bars. Within the scope of the present framework, the drop in yield strength and the ultimate strain of the corroded steel reinforcements can be estimated using the formulae proposed by Du et al. [32]:

$$f_{y_{corr}} = f_{y_0}(1 - 0.005CL) \quad (7)$$

$$\varepsilon_{u_{corr}} = \varepsilon_{u_0}(1 - 0.05CL) \quad (8)$$

The altered yield strain, ultimate strength and elastic modulus for uniform corrosion:

$$\varepsilon_{y_{corr}} = \varepsilon_{y_0}(1 - 0.0124CL) \quad (9)$$

$$f_{u_{corr}} = f_{u_0}(1 - 0.0107CL) \quad (10)$$

$$E_{corr} = E_0(1 - 0.0075CL) \quad (11)$$

And for pitting corrosion:

$$\varepsilon_{y_{corr}} = \varepsilon_{y_0}(1 - 0.0198CL) \quad (12)$$

$$f_{u_{corr}} = f_{u_0}(1 - 0.0157CL) \quad (13)$$

$$E_{corr} = E_0(1 - 0.0115CL) \quad (14)$$

3.4. Cracking of Concrete Effect

Cracking of concrete due to corrosion results in a loss of concrete integrity, which reduces the ultimate load capacity of the concrete element [33] and decreases the bond strength [34] which will be accounted for later by the hysteresis degradation parameters calibration. A model proposed by Coronelli and Gambarova, [35] can be used to partially account for the effect of cracked concrete cover on the compression strength. In this model, the reduced compression strength can be determined from:

$$f_{c_{cr}} = \frac{f_c}{1+0.1\frac{\varepsilon_1}{\varepsilon_{c0}}} \quad (15)$$

ε_{c0} is the strain of non-cracked concrete corresponding to compression strength f_c . ε_1 is the average tensile strain of the cracked concrete, which can be calculated as follows:

$$\varepsilon_1 = \frac{n_{bars}w_{cr}}{b_0} \quad (16)$$

Where, b_0 is the width of the element section before cracking, n_{bars} is the number of corroded bars in the cracked concrete width b_0 and w_{cr} is the full width of the crack caused by corroded longitudinal reinforcement and can be calculated as follows:

$$w_{cr} = 2\pi(v_{rs} - 1)P_x \quad (17)$$

$$P_x = 0.0115i_{corr}t \quad (18)$$

P_x , the attack penetration factor, is the average value of corrosion penetration which is the reduction of the bar diameter in (mm), the time t in (years) since the initiation of corrosion and i_{corr} is the corrosion current in ($\mu A/cm^2$). v_{rs} is the volume ratio between the specific volume of a corrosion product and the specific volume of iron, which is taken equal to 2 for steel [36].

By virtue of the above formula and for a given corrosion level CL, the parameters of the MODIMK model are automatically calculated using functions elaborated in Tcl language and implemented into the material library of the OpenSees software.

4. CALIBRATION OF THE DETERIORATING PARAMETERS OF THE HYSTERESIS MODEL

The experimental results of cyclic testing of five columns having different corrosion rates [37] have been used in this study to calibrate the corroded deterioration factors of MODIMK hysteresis model. For this purpose, the specimens are modeled using an elastic element connected to a zero-length element that serves as a plastic hinge to represent the nonlinear behavior of the element. Translational DOFs are constrained to one end of the elastic element through the "equal DOF" command. The specimen geometry and the corresponding numerical model are shown in Fig. 3.

Table 1 - Modified hysteresis parameters

CL(%)	My ⁺ (KN.m)	My ⁻ (KN.m)	Ke(KN.m)	θ_{pc}^+ (rad) θ_{pc}^- (rad)
0	58.68	58.68	14466.6	0.054
5.1	58.33	58.33	14478.4	0.054
8.3	58.13	58.13	14485.8	0.054
13.25	57.60	57.60	14505.7	0.053
16.8	51.54	51.54	14505.7	0.053

4.2. Calibration Procedure of the Cyclic Degradation Parameters for Different Corrosion Levels

As mentioned before, the effect of the reinforcement corrosion on the geometrical and mechanical characteristics of the RC elements have been explicitly considered using correlation functions. However, there are additional effects of the corrosion level that have not been explicitly accounted for. These effects will be compensated for through a calibration procedure to match the rate of degradation under cyclic loading. The MODIMK hysteresis model provides four degradation parameters $\lambda_A, \lambda_K, \lambda_S, \lambda_C$ and their exponents C_A, C_K, C_S, C_C to control the deterioration of the loading strength, post capping strength, the loading, and unloading stiffness, respectively. A calibration procedure based on random-mutation hill-climbing (RMHC) algorithm is used to fine-tune the values of these parameters for different levels of corrosion. This optimization technique is believed to be suitable for this case because local optimum values are sought [38]. The starting values of the parameters p_i ($i=1$ to 8) corresponding to $\lambda_A, \lambda_K, \lambda_S, \lambda_C, C_A, C_K, C_S, C_C$ respectively are chosen within the intervals of variation and then iteratively the algorithm progresses to find a better solution by making an incremental change starting from the initial solution.

The degradation parameters λ_i have an appreciable effect for values equal to 10 or smaller. A zero value is assigned to deactivate the degradation effect. The variation range of the exponential factors C_i vary from 1.0 for constant rate of deterioration to 2.0 for slow down rate of deterioration at initial cycles and increased rate of deterioration in subsequent cycles [21,39].

Therefore, in the hill-climbing algorithm, the ranges of variation of the degradation parameters are taken in the intervals [0. 10.] for λ_i ($p_{i=1}$ to 4) and [1.0 2.0] for C_i ($p_{i=5}$ to 8). Both ranges have been normalized with respect to their relative maximal and minimal values (boundaries of the intervals) and subdivided into $Np=100$ increments each.

The algorithm keeps improving the solution by making incremental changes $\Delta p_{i,k}$ until it converges to an optimal solution or it stops for a given limit of iterations. The objective function aims to follow as closely as possible the experimental (reference) force-displacement hysteresis loops. In addition to the strength and stiffness cyclic variations, it reflects the energy dissipated by the RC specimen at the plastic hinge. For N digitalized experimental and numerical pairs $(F_{exp,i}, \theta_i), (F_{mod,i}, \theta_i)$ respectively, corresponding to a corrosion level (test), the algorithm minimizes the relative error given for each iteration k by:

$$e_k = \sqrt{\sum_{i=1}^N \left(\frac{F_{mod,i} - F_{exp,i}}{F_{exp,i}} \right)^2} \quad (19)$$

With an acceptance criterion:

$$\frac{e_{k+1} - e_k}{e_k} < e_l \quad (20)$$

An error $e_k = 1\%$ is considered precise enough to terminate the optimization process or a limit of 200 iterations. It should be noted also that the acceptance criterion e_l for an adjustment has been given a positive value to avoid a premature convergence of the objective function towards local minima [38].

The cyclic degradation parameters and their exponents (λ_i and c_i) for specimen with increasing levels of corrosion obtained from the calibration with the experimental tests are given in Table 2. It should be noted that the effect of individual deterioration parameters can compensate each other's, therefore the calibration process is not firmly robust.

Table 2 - Calibrated cyclic degradation parameters

CL (%)	λ_C	λ_A	λ_K	λ_S	C_C	C_A	C_K	C_S
0	1	1	1	1	1	1	1	1
5.1	6.8	0.3	0.3	0.4	1.02	1.06	1.01	1.01
8.3	7.3	0.4	0.1	0.6	1.13	1.04	1.20	1.24
13.25	7.1	0.4	0.2	0.7	1.12	1.31	1.40	1.51
16.8	7.0	0.5	0.1	0.7	1.10	1.16	1.21	1.46

Representative hysteresis loops of the specimens before reaching the ultimate state are given in Fig. 4. The maximum number of loading cycles varies from 14 cycles for specimens ZZ-1 to 12 cycles for specimen ZZ-5. The number of loading cycles decreases with increasing degrees of corrosion.

Default values of the degradation parameters for 0% corrosion where all degradation parameters are set to unity as given in Table 2, were used for specimen ZZ-1 which resulted in large discrepancies between the numerical and experimental curves. Calibration of the degradation parameters were made for corroded specimens and gave an acceptable approximation except for ZZ-5 sample where the last maximum lateral load dropped sharply compared to the previous ones ZZ-3 and ZZ-4. This can be attributed to buckling of longitudinal reinforcement because of the transverse reinforcement corrosion that has not been accounted for explicitly. Therefore, for specimen ZZ-5 with 16.8% corrosion, the yield moment has been adjusted using a correction coefficient of the moment $\alpha = 0.85$. If additional data becomes available, it is possible to further calibrate the value of the correction factor α specifically for higher levels of corrosion.

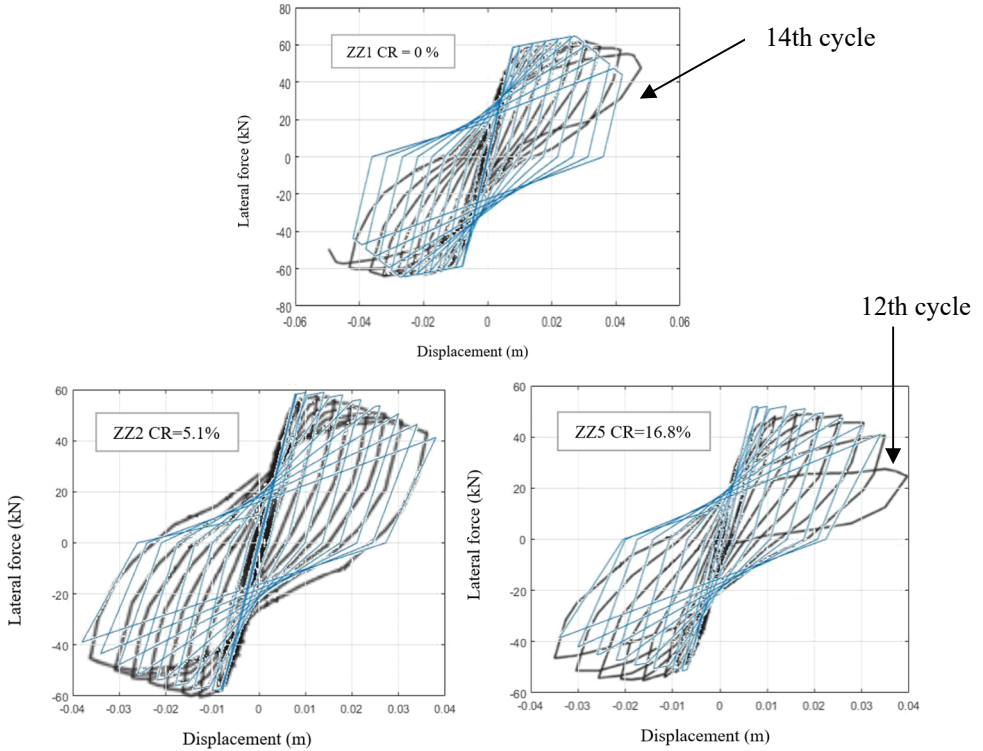


Figure 4 - Experimental and numerical hysteresis loops for samples with corrosion levels: 0% for ZZ-1, 5.1% for ZZ-2 and 16.8% for ZZ-5 [37]

5. NONLINEAR DYNAMIC PERFORMANCE OF A BRIDGE WITH CORRODED PIERS

This section is dedicated to the evaluation of the effect of the corrosion of the steel reinforcement on the seismic response of a typical full scale bridge structure.

5.1. Description of the Bridge Structure

The choice of the structure was dictated by the availability of data for the calculation of the parameters governing the constitutive law and the availability of some results of previous work [40] for comparison and validation of the model. The chosen structure is a regular straight bridge consisting of a deck resting on six prefabricated NEBT 1600 (New England Bulb Tee) prestressed girders supported by a three-column pier system. The deck consists of two continuous spans of 36 m long and 13 m wide (Fig. 5).

The columns are constituted of rectangular cross-section of 1.2 m deep and 0.6 m wide. The design was carried out according to the requirements of the Canadian Bridge Code CSA-S6

[41]. The columns extend into the foundation and the pier cap for a distance of 0.5 m. The height of the columns and the pier cap are 6 m and 1m, respectively, bringing the total height of the frame to 7 m.

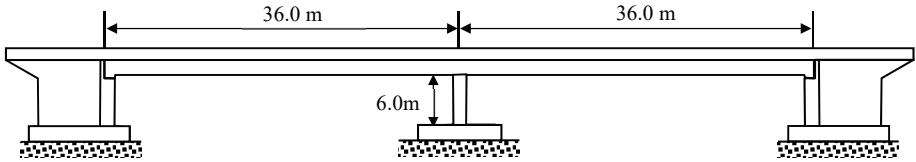


Figure 5 - Longitudinal elevation and dimensions of the studied bridge

5.2. OpenSees Model

The deck is segmented into two linear elastic column-beam elements. The piers are also modeled as column-beam elements adopting linear elastic behavior with zero-length springs (plastic hinges) added at the ends idealizing the nonlinear behavior in the plastic hinges. The pier cap was taken very rigid to allow the plastic hinge to develop properly at the foot and head of the piers.

The geometry of the model is composed of 7 elastic beam elements and 6 nonlinear zero-length hinges using uniaxial Ibarra-Medina-Krawinkler "peak oriented" material. The degrees of freedom of translation and rotation in two directions of the hinges are linked to the element nodes via the "equal DOF" command (Fig. 6).

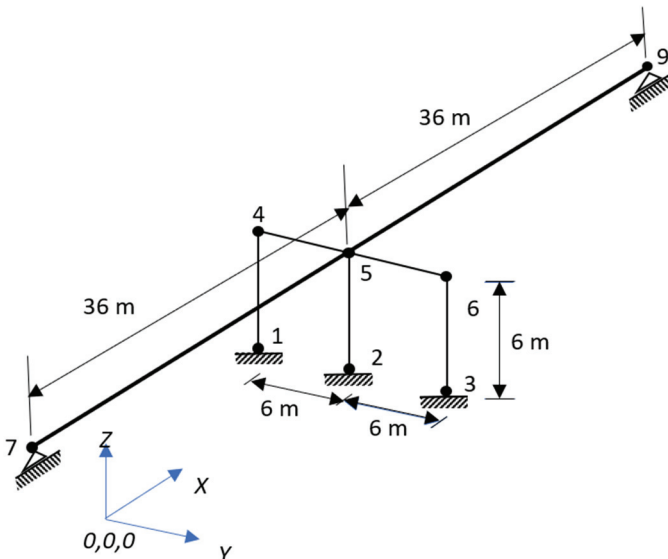


Figure 6 - OpenSees model of a typical bridge with plastic hinges (MODIMK)

It is assumed that the corrosion degradation is uniform, meaning that the level of corrosion is identical for all hinges during the same analysis and it varies from 0% (undamaged structure) to a corrosion rate of 20%.

The hysteresis parameters depending on the geometric and material properties of the steel reinforcement and concrete are computed for sound and corroded sections for corrosion rates of 0% and 20% using the correction factors of Eqs.5-18. The degradation parameters of MODIMK model have been calibrated for a corrosion degree varying from 0% to 16.80%. Due to a lack of experimental data above this level, the performance analysis is limited to 20% of corrosion rate. The cyclic degradation parameters in the MODIMK model and their exponents have been extrapolated by curve fitting the results of the calibration phase up to 20% (Table 3).

Table 3 - Cyclic degradation parameters and their exponents

CL (%)	λ_C	λ_A	λ_K	λ_S	C_C	C_A	C_K	C_S
20	7.12	0.65	0.42	0.95	1.10	1.11	1.27	1.29

The yield moment M_y is corrected using the same value $\alpha = 0.85$.

5.3. Seismic Loading and Nonlinear Dynamic Analysis

A dataset composed of four records of horizontal components of real earthquakes, and two artificial accelerograms are selected to best cover the RPA99 seismic code spectrum [42] and applied as a representative seismic loading of a high seismic zone. The artificial accelerograms are generated using ‘seismoArtif’ software [43]. The main characteristics of the selected acceleration time histories are given in Table 4. and Fig. 7 shows the mean response spectra of the six accelerograms closely covering the target site spectrum.

Table 4 - Characteristics of the accelerograms

Accelerograms	PGA(g)	Field	Duration (s)
Manjil	0.515	Far	52.0
Northridge	0.568	Near	38.0
Dar El Beida	0.341	Far	55.3
Friuli	0.531	Near	36.3
Artif 1	0.618	Far	20.0
Artif 2	0.599	Near	11

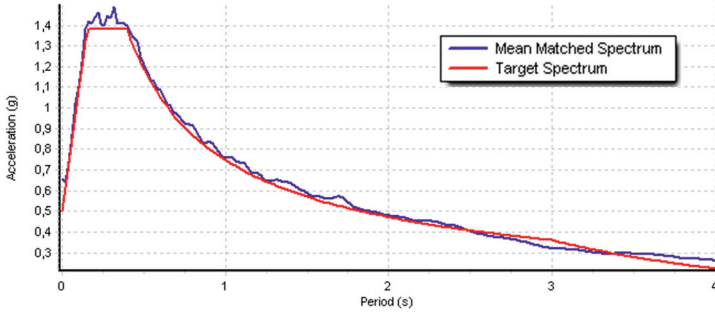


Figure 7 - The target seismic code spectrum and the mean spectrum of the different accelerograms

The performance of the structure is evaluated in terms of the structural responses of the hysteresis loops, the maximum lateral displacements and the dissipated energy.

5.4. Effect of the Corrosion Level on the Displacement Response Under Different Earthquake Ground Motions

Representative displacement time histories of the bridge deck along the longitudinal direction under the far-field Artifi1 earthquake and the near-field Friuli earthquake are shown in Figs. 8 and 9. The effect of the corrosion is more pronounced under Artifi1 accelerogram and the

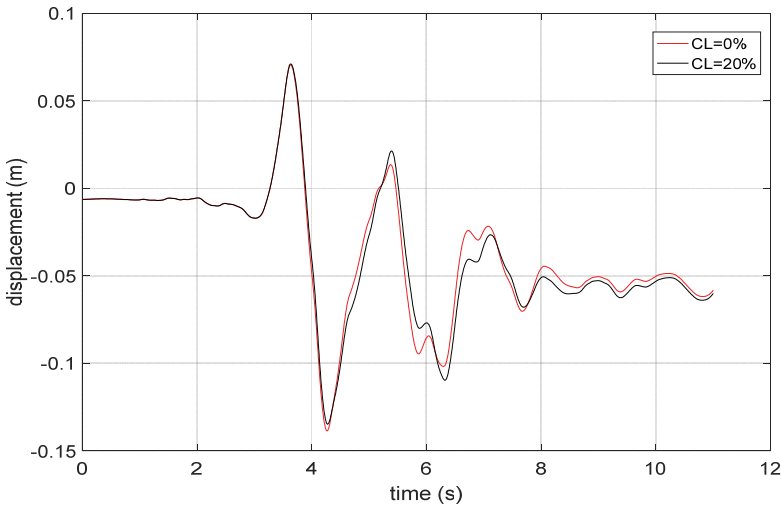


Figure 8 - Lateral displacement responses under Friuli

peak displacement increases with increasing CL. Permanent deformation, which is an important indicator of damage, is observed at the end of the action effects. This residual displacement is highly dependent on the loading conditions. For a 20% corrosion level, it reaches 1.64 times the displacement of the uncorroded model under the far-field Artifl earthquake. However, it remains almost the same under the near-field Friuli earthquake.

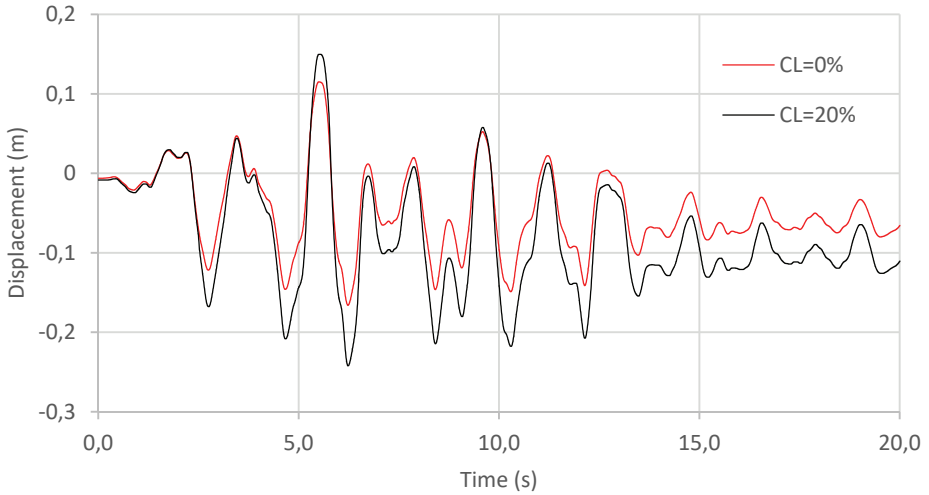


Figure 9 - Lateral displacement responses under Artifl

The hysteresis loops of the different plastic hinges are more regular for far-field accelerograms compared to near-field accelerograms as represented by the results of the Friuli and Artifl accelerograms in Fig. 10. Deteriorations of strength, stiffness and pinching are more noticeable in corroded hinges.

The corrosion effect is more pronounced for severe ground acceleration. Table 5 shows the percentage increase in displacements and plastic rotations for increasing ground acceleration intensity (Artifl) scales.

Where:

$$\Delta D_{max} = \frac{(D_{CL} - D_{CL0})}{(D_{CL0})} \times 100\% \quad (21)$$

$$\Delta \theta_{max} = \frac{(\theta_{CL} - \theta_{CL0})}{(\theta_{CL0})} \times 100\% \quad (22)$$

With:

D_{CL} et θ_{CL} displacement and plastic rotation corresponding to corrosion rate CL;

D_{CL0} et θ_{CL0} displacement and plastic rotation corresponding to CL=0.

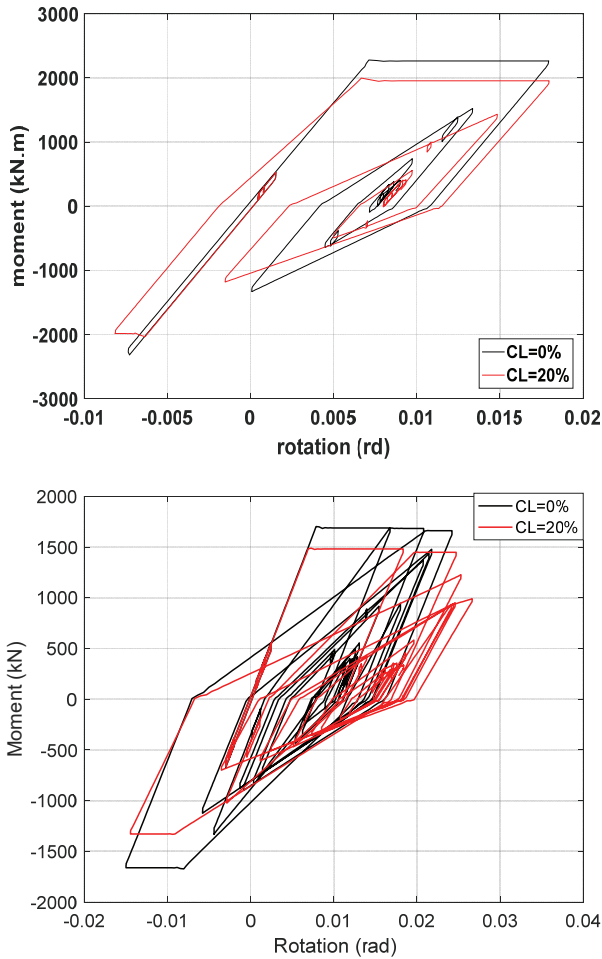


Figure 10 - Hysteresis loop responses under Friuli and Artifl accelerograms

Table 5 - Displacements and plastic rotations for increasing loading intensity at different corrosion levels

CL	Scale = 1.0		Scale = 1.5		Scale = 2.0	
	ΔD_{max}	$\Delta \theta_{max}$	ΔD_{max}	$\Delta \theta_{max}$	ΔD_{max}	$\Delta \theta_{max}$
20%	0	3.76	2.25	11.9	15.08	23.63

5.5. Effect of the Corrosion Level on the Hysteresis Energy Dissipation Capacity

Figure 11 shows the dissipated energy curve under Artifl accelerogram for 0% and 20% corrosion level. It can be noticed that the dissipation energy decreases with increasing CL

which has been also reported in the literature [44]. This trend is not perceived under Friuli accelerogram (Fig. 12), where the energies for the different corrosion levels are comparable. The energy dissipated at CL = 20% is slightly higher than CL=0%. This can be attributed to the fact that the strength and stiffness degradations are compensated by an early yielding and larger plastic rotations.

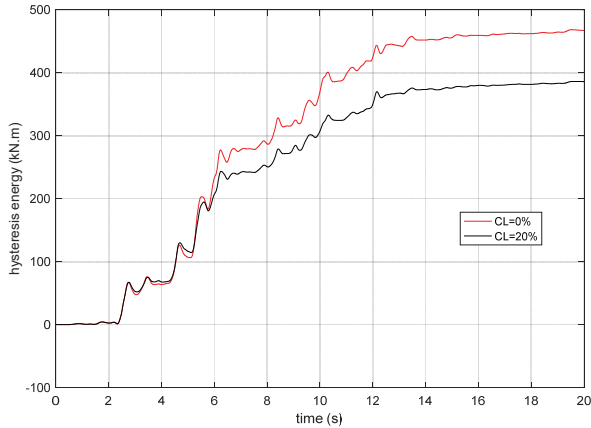


Figure 11 - Energy dissipated under Artificial earthquake

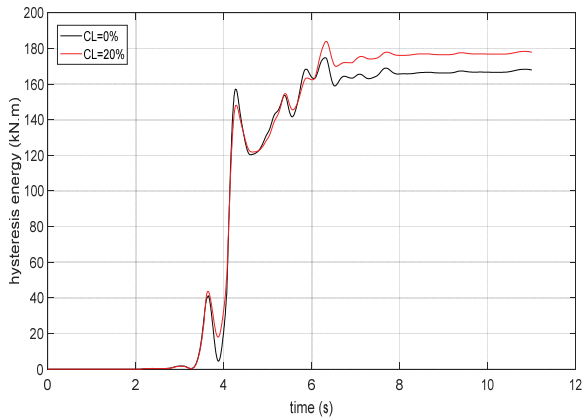


Figure 12 - Energy dissipated under Friuli earthquake

6. CONCLUSION

A major durability concern for RC infrastructures in aggressive environment is steel reinforcement corrosion. The trend of seismic codes towards new predictive generations suggests explicit quantifications of degradation parameters to be integrated into nonlinear dynamic analyses in the design phase or for structural assessment of existing buildings.

A framework for the application of a corrosion dependent geometric and material properties together with degradation hysteresis parameters of a RC element section has been put in place. For this purpose, a corrosion level indicator that can be obtained from in-situ measurements or predicted by a time-dependent approach is used to adjust the geometric and material properties of a corroded RC section. The adjustment functions are implemented into the material library of the OpenSees software to automatically calculate the parameters of the MODIMK model. The cyclic degradation parameters and their exponents (λ_i and c_i) are fine-tuned using a random-mutation Hill-Climbing (RMHC) algorithm for a range of corrosion levels corresponding to available experimental data. It should be noted that the yield moment, in addition to the geometric and material properties alteration, needs to be reduced by an extrapolated factor α to account for transverse reinforcement corrosion and other effects that have not been compensated for explicitly.

To investigate the effect of the corrosion on the seismic behavior of structures, a typical full scale two spans bridge model having three piers with increasing uniform corrosion levels has been studied under several earthquake ground accelerations. The performance of the bridge has been evaluated using lateral displacements, plastic rotations and hysteresis energy dissipation audit. The results showed that the effect of corrosion highly dependent on the intensity and type of earthquake ground motions. Within the limit of the considered seismic loading, the permanent displacement (taken as an indicator of damage) reached 1.64 times for a corrosion level of 20%. The general trend is that the corroded piers are less dissipative, however in some cases where the dissipated hysteresis energy was comparable for the corroded and saline structure, the plastic hinges at the ends of the corroded piers undergo excessive plastic rotations.

Although, the proposed protocol can be used for practical issues where seismic performance prediction or structural assessment are sought for design or existing structures, further work and research are required to complete and improve the robustness of the calibration process for full scale specimen with higher corrosion levels.

Acknowledgements

The financial support of the Ministry of higher education MESRS in Algeria (Grant CNEPRU J0400420140001) for conducting this study is greatly acknowledged.

References

- [1] Li W., Xu C., Ho S.C., Wang B., Song G., Monitoring concrete deterioration due to reinforcement corrosion by integrating acoustic emission and FBG strain measurements. *Sensors*. 2017;17(3):657. <https://doi.org/10.3390/s17030657>
- [2] Bertolini L., Elsener B., Pedefferri P., Redaelli E., Polder R., Corrosion of steel in concrete: Prevention, diagnosis, repair (2nd ed.); Weinheim, Germany: Wiley VCH; 2013.
- [3] Andrade C., Propagation of reinforcement corrosion: principles, testing and modelling, *Mater Struct*. 2019; 52:2, <https://doi.org/10.1617/s11527-018-1301-1>

- [4] François R., Laurens S., Deby F., Steel corrosion in reinforced concrete, Editor(s): Raoul François, Stéphane Laurens, Fabrice Deby, Corrosion and its consequences for reinforced concrete structures, Elsevier, 2018; 1-41, ISBN 9781785482342, <https://doi.org/10.1016/B978-1-78548-234-2.50001-9>
- [5] Bertolini L., Steel corrosion and service life of reinforced concrete structures, *Struct Infrastruct Eng.* 4:2, 123-137, <http://dx.10.1080/15732470601155490>
- [6] Şengül, Ö. (2011). Probabilistic Design for the Durability of Reinforced Concrete Structural Elements Exposed to Chloride Containing Environments . *Teknik Dergi* , 22 (110) , 1461-1475, <https://dergipark.org.tr/en/pub/tekderg/issue/12749/155174>
- [7] Andisheh K., Scott A., Palermo A., Seismic behavior of corroded RC bridges: Review and research gaps, *Int J Corros.* 2016, Article ID 3075184, <http://dx.doi.org/10.1155/2016/3075184>.
- [8] Inci P., Goksu C., Ilki A., Kumbasar N., Effects of reinforcement corrosion on the performance of RC frame buildings subjected to seismic actions. *Journal of Performance of Constructed Facilities*, 27(6), 683–696. doi:10.1061/(ASCE)cf.1943-5509.0000378
- [9] Nataraj S., Hogan L., Scott A., Ingham J., Simplified Mechanics-Based Approach for the Seismic Assessment of Corroded Reinforced Concrete Structures *J Struct Eng.*, 2022, 148(3), 04021296, doi:10.1061/(ASCE)ST.1943-541X.0003265.
- [10] Opabola E. A., Residual seismic capacity of beam-column components with corroded reinforcement, *Constr. Build. Mat.* 332 (2022) 127269, <https://doi.org/10.1016/j.conbuildmat.2022.127269>
- [11] Bourahla N., Taфраout S., Attar A., Nonlinear dynamic response of aging degraded reinforced concrete structures under earthquake loading, *Proceedings of the 14th European Conference on Earthquake Engineering*, Ohrid Macedonia 2010, paper 537.
- [12] Akiyama M., Frangopol D.M., Long-term seismic performance of RC structures in an aggressive environment: emphasis on bridge piers, *Struct Infrastruct Eng.* 2014;10:7, 865-879, doi: 10.1080/15732479.2012.7612
- [13] Choe D.E., Gardoni P., Rosowsky D., Haukaas T., Seismic fragility estimates for reinforced concrete bridges subject to corrosion. *Struct. Saf.*, 2009;31(4), 275-283. doi:10.1016/j.strusafe.2008.10.001
- [14] Hu S., Wang Z., Guo Y., Xiao G., Life-cycle seismic fragility assessment of existing RC bridges subject to chloride-induced corrosion in marine environment. *Adv Civ Eng.* 2021, Article ID 9640521, 18 pages, <https://doi.org/10.1155/2021/964052>
- [15] Domaneschi M., De Gaetano A., Casas J.R., Cimellaro G.P., Deteriorated seismic capacity assessment of reinforced concrete bridge piers in corrosive environment. *Struct Concr.* 2020;1–16. <https://doi.org/10.1002/suco.202000106>
- [16] Naderpour H., Ghasemi-Meydansar F., Haji M., Experimental study on the behavior of RC beams with artificially corroded bars, *Structures*, Volume 43, 2022, pp1932-1944, <https://doi.org/10.1016/j.istruc.2022.07.005>.

- [17] Goksu C. and Ilki A., Seismic behavior of reinforced concrete columns with corroded deformed reinforcing Bars, *ACI Structural Journal* 113 (5) 2016: 1053-1064, DOI:10.14359/51689030
- [18] Meda A., Mostosi S., Rinaldi Z., Riva P., Experimental evaluation of the corrosion influence on the cyclic behaviour of RC columns. *Eng Struct*, 2014; 76: 112 – 123. doi:10.1016/j.engstruct.2014.06.043
- [19] Kim T.H., Seismic performance assessment of deteriorated two-span reinforced concrete bridges. *Int J Concr Struct Mater* 2022; 16:4 <https://doi.org/10.1186/s40069-022-00498->
- [20] Scattarreggia N., Qiao T., Malomo D., Earthquake response modeling of corroded reinforced concrete hollow-section piers via simplified fiber-based FE analysis. *Sustain* 2021; 13, 9342. <https://doi.org/10.3390/su13169342>
- [21] Ibarra L.F., Medina R.A., Krawinkler H., Hysteretic models that incorporate strength and stiffness deterioration, *Earthq Eng Struct Dyn*, 2005; 34(12), 1489-1511. <https://doi.org/10.1002/eqe.495>
- [22] McKenna F., OpenSees: A Framework for earthquake engineering simulation, *Comput Sci Eng*. 2011; 13(4), 58-66, doi:10.1109/MCSE.2011.66.
- [23] Haselton C.B., Liel A.B., Lange S.T., Deierlein G.G., Beam-column element model calibrated for predicting flexural response leading to global collapse of RC frame buildings, PEER Report 2007/03, PEER Center, University of California, Berkeley, 2008.
- [24] Panagiotakos T.B., Fardis M.N., Deformations of reinforced concrete at yielding and ultimate, *ACI Struct J*, 2001; 98(2), 135-147.
- [25] Özyurt N., Söylev T. A., Özturan T., Pehlivan A.O., Niş A., Corrosion and chloride diffusivity of reinforced concrete cracked under sustained flexure. *Teknik Dergi* 31 2020: 10315-10337
- [26] Bezuidenhout S.R., Van Zijl G.P.A.G., Corrosion propagation in cracked reinforced concrete, toward determining residual service life. *Struct Concr.* 2019;1–11. <https://doi.org/10.1002/suco.201800275>
- [27] Bossio A., Lignola G.P., Fabbrocino F., Monetta T., Prota A., Bellucci F., Manfredi G., Nondestructive assessment of corrosion of reinforcing bars through surface concrete cracks, *struct concr*, 2017;18(1), 104-117. <https://doi.org/10.1002/suco.201600034>.
- [28] Khan I., François R., Castel A., Prediction of reinforcement corrosion using corrosion induced cracks width in corroded reinforced concrete beams. *Cem. Concr. Res.* 2014, 56, 84–96. <https://doi.org/10.1016/j.cemconres.2013.11.006>
- [29] Nikoo M., Sadowski Ł., Nikoo M., Prediction of the corrosion current density in reinforced concrete using a self-organizing feature map. *Coatings* 2017; 7, 160. <https://doi.org/10.3390/coatings7100160>
- [30] Du Y.G., Clark L.A., Chan A.H.C., Effect of corrosion on ductility of reinforcing bars. *Mag Concr Res.* 2005; 57(7), 407-419. doi:10.1680/macr.2005.57.7.407

- [31] González J.A., Andrade C., Alonso C., Feliu S., Comparison of rates of general corrosion and maximum pitting penetration on concrete embedded steel reinforcement. *Cem. Concr. Res.* 1995; 25(2), 257–264. doi:10.1016/0008-8846(95)00006-2
- [32] Du Y.G., Clark L.A., Chan A.H.C., Residual capacity of corroded reinforcing bars, 2005, *Mag Concr Res.* 57(3), 135-147. doi:10.1680/macr.2005.57.3.135
- [33] Tapan M., Aboutaha R.S., Effect of steel corrosion and loss of concrete cover on strength of deteriorated RC columns, *Constr. Build. Mat.* 25 (2011) 2596–2603, doi:10.1016/j.conbuildmat.2010.12.003
- [34] Apostolopoulos C., Koulouris K.F., Apostolopoulos A.C., Correlation of surface cracks of concrete due to corrosion and bond strength (between steel bar and concrete), *Advances in Civil Engineering*, vol. 2019, Article ID 3438743. <https://doi.org/10.1155/2019/3438743>
- [35] Coronelli D., Gambarova P., Structural assessment of corroded reinforced concrete beams: Modeling guidelines. *J Struct Eng.* 2004;130(8), 1214–1224. doi:10.1061/(asce)0733-9445(2004)130:8(1214).
- [36] Poursaei A., Corrosion of steel in concrete structures, 1st Edition, Woodhead Publishing, ISBN - 13:9781782423812.
- [37] Yang S.Y., Song X.B., Jia H.X., Chen X., Liu X.L., Experimental research on hysteretic behaviors of corroded reinforced concrete columns with different maximum amounts of corrosion of rebar. *Construct Build Mater*, 2016; 121, 319–327. doi:10.1016/j.conbuildmat.2016.06.002
- [38] Taborda D.M.G., Zdravkovic L., Application of a Hill-Climbing technique to the formulation of a new cyclic nonlinear elastic constitutive model. *Comput Geotech.* 2012; 43, 80–91. doi:10.1016/j.compgeo.2012.02.001
- [39] Ibarra L., Krawinkler H., Global collapse of frame structures under seismic excitations. Blume Center TR 152, Stanford University; 2003.
- [40] Khaled A., Tremblay R., Massicotte B., Combination rule for the prediction of the seismic demand on columns of regular bridges under bidirectional earthquake components. *Can J Civ Eng.* 2011 38(6), 698–709. doi:10.1139/111-031
- [41] Canadian Standard Association (CSA). CSA-S6: Canadian Highway Bridge Design Code. Rexdale, ON, 2006.
- [42] RPA99 version 2003, Algerian Seismic Regulations, DTR BC 2.48, Earthquake Engineering National Research Centre, Algiers, 9961-923-13-8, 2004.
- [43] Seismosoft 2020, SeismoArtif – A computer program for generation of artificial accelerograms. Available from URL: www.seismosoft.com accessed 12-03-2021.
- [44] Celik A., Yalciner H., Kumbasaroglu A., Turan A.I., An experimental study on seismic performance levels of highly corroded reinforced concrete columns. *Struct Concr.* 2021;1–19. <https://doi.org/10.1002/suco.202100065>

Tabakalı Zeminlerdeki Yüzeysel Temel Davranışının Nümerik ve Analitik Olarak İncelenmesi

Erdal UNCUOĞLU^{1*}



ÖZ

Arazide yapılmış tam ölçekli yükleme deney sonuçları kullanılarak doğrulanmış ve kalibre edilmiş bir sonlu elemanlar modeli oluşturulmuştur. Temel boyutunun, kum zeminin başlangıç gerilme durumu ve gerilme geçmişinin, üstte yer alan kum tabakası kalınlığının ve altta yer alan kil tabakasının drenajsız kayma mukavemetinin tabakalı zeminlerdeki kare temellerin taşıma kapasitesi ve oturma davranışları üzerindeki etkileri gerçekleştirilen bir seri üç boyutlu sonlu elemanlar analizi ile araştırılmıştır. Sonlu eleman analizleri sonucu bulunan taşıma gücü değerleri zımbalama kesme yöntemi ile hesaplanan taşıma gücü değerleri ile karşılaştırılmış ve bunun yanı sıra K_s katsayısı değerlerinin H/B oranına ve λ_s ' e bağlı değişimi incelenmiştir.

Anahtar Kelimeler: Tabakalı zeminler, taşıma gücü, sonlu elemanlar yöntemi.

ABSTRACT

The Numerical and Analytical Investigation of Shallow Foundation Behaviour on Layered Soils

A validated and calibrated finite element model has been generated using the results of the full-scale loading tests performed in the field. The affects of the footing size, initial stress state and stress history of sand layer, the thickness of upper sand layer and the undrained shear strength of lower clay layer on the bearing capacity and settlement behaviours of square footings on layered soils have been investigated by performing a series of three-dimensional finite element analyses. The bearing capacity values obtained from finite element analyses have been compared to the bearing capacity values calculated by punching shear method. Also, the variation of K_s coefficient depending on the H/B ratio and λ_s has been investigated.

Keywords: Layered soils, bearing capacity, finite element method.

Not: Bu yazı

- Yayın Kurulu'na 3 Mart 2023 günü ulaşmıştır. 24 Ekim 2023 günü yayımlanmak üzere kabul edilmiştir.
- 31 Mayıs 2024 gününe kadar tartışmaya açıktır.

• <https://doi.org/10.18400/tjce.1259495>

1 Erciyes Üniversitesi, İnşaat Mühendisliği Bölümü, Kayseri, Türkiye
erdalu@erciyes.edu.tr - <https://orcid.org/0000-0002-6122-9066>

* Sorumlu yazar

1. GİRİŞ

Yüzeysel temelerde nihai taşıma kapasitesinin göçme mekanizmaları tarafından belirlendiği yaygın olarak bilinmektedir. Geleneksel taşıma gücü teorilerinde [1-4] zeminin homojen olduğu kabul edilmektedir. Tabakalı zemin profillerinde ise, tabakaların rijitliği ve mukavemet özellikleri birbirinden farklı olduğundan nihai taşıma kapasitesi tek tabakalı homojen bir zemin gibi değerlendirilemez. Tabakalı zeminlerde nihai taşıma kapasitesi, göçme mekanizmasının tamamı ile içinde yer aldığı yeterli kalınlıkta bir üst tabaka bulunmadığı sürece altta yer alan tabakanın özelliklerine de bağlıdır. Bu nedenle; geleneksel taşıma gücü teorileri, homojen zeminlerde başarılı taşıma gücü tahminleri yaparken zemin özelliklerinin derinlikle değiştiği durumlarda, genellikle, uygulanamazlar.

Kontrollü sıkıştırılmış dolgular, genellikle, kum ve çakıl karışımı granüler malzemeden oluşmakta ve herhangi bir yüklemeye koşulunda drenajlı davranış sergilemektedir. Yumuşak kil zemin üzerine nispeten ağır olmayan bir yapı inşa edileceğinde veya otoyol yapımlarında yumuşak kil zeminlerle karşılaşıldığında, bu zeminler üzerinde oluşturulacak sağlam bir granüler tabaka ile temel zemini taşıma kapasitesinde ve oturma özelliğinde iyileştirme sağlanabilir. Böylelikle; yapay olarak, kil tabakası üzerinde yer alan kum zeminden oluşan tabakalı bir zemin profili elde edilmiş olur. Yumuşak zemin tabakalarının bulunduğu sahalarda ağır iş makineleri için güvenli çalışma ortamları sağlamak amacı ile yumuşak kil tabakası üzerinde sıkıştırılmış granüler malzeme ile geçici çalışma platformları oluşturulmaktadır. Açık deniz mühendislik uygulamalarında kullanılan jack-up temeller, genellikle, yumuşak deniz kili üzerinde yer alan kum tabakaları üzerine inşa edilmektedir. Sayılan bu örnekler zayıf kohezyonlu zeminler üzerinde yer alan nispeten ince sıkı granüler zemin tabakası içeren tabakalı zeminlerin taşıma kapasitesi ve davranışlarının tahmin edilmesinin pratikte yaygın olarak karşılaşılan önemli bir problem olduğunu göstermektedir. Problemin karmaşıklığı nedeni ile temel-zemin etkileşiminin kapsamlı bir şekilde anlaşıldığı kesin bir analitik taşıma gücü modeli de günümüzde hala mevcut değildir. Geoteknik mühendisleri, tabakalı zeminlere oturan yüzeysel temellerin taşıma gücünü tahmin etmek için ya limit denge yöntemine dayalı yarı-deneysel taşıma gücü modellerini ya da sayısal analiz yöntemlerini kullanmaktadır.

Pratikte, kil tabakası üzerinde yer alan kum tabakasına oturan rijit bir yüzeysel temelin nihai taşıma kapasitesi, genellikle, limit denge yöntemine dayalı yarı-deneysel taşıma gücü modelleri kullanılarak tahmin edilir. Çözüm, genel olarak, temel tabanı ve kil tabakası yüzeyi arasında yer alan hayali bir kum bloğun temel ile birlikte aşağı doğru itildiği, kum tabakasında zımbalama ve kil tabakasında da bir genel kayma göçmesi olduğu kabul edilen basitleştirilmiş bir göçme mekanizması ve kuvvet dengesine dayanmaktadır. Kum bloğun tabanındaki düşey efektif gerilme, kil tabakasının yüzeyine oturan rijit pürüzlü bir temelin taşıma kapasitesine eşit olarak alınır. Kum bloğa etkileyen kuvvetlerin dengesinden yola çıkılarak nihai taşıma kapasitesi hesaplanır. Bu yöntemler; yapılan kabuller, kum bloğun kenar yüzeyleri boyunca oluşan kayma direncinin taşıma gücüne katkısı ve kullanılan deneysel katsayılarından kaynaklı belirsizlikler nedeni ile birbirinden çok farklı taşıma gücü değerleri üretebilmektedir. Bu konuda en iyi bilinen taşıma gücü modellerinden biri Meyerhof [5], Hanna ve Meyerhof [6] ve Hanna [7] tarafından önerilmiş olan Zımbalama Kesme Yöntemidir. Bu yöntemde; kum tabakası boyunca yükün yayılma açısı olan α_p , $0'$ a eşit olarak alınır. Kum bloğun kenar yüzeyleri boyunca oluşan kayma direnci, zımbalama kesme katsayısı K_s kullanılarak hesaba katılmaktadır. K_s katsayısı, kum ve kil tabakalarının

taşıma kapasiteleri arasındaki oranın (q_2/q_1) ve kumun içsel sürtünme açısının (ϕ_1) bir fonksiyonu olarak grafiklerden elde edilmektedir. Ancak; tasarım grafiğinde tanımlanmış değerlerin dışındaki değerler için interpolasyon ya da ekstrapolasyon yapma zorunluluğu vardır. Ayrıca; sınırlı bir malzeme özelliği aralığı için geçerli olan K_s katsayısının kullanımı tahmin edilen taşıma gücü değerleri üzerinde belirsizlikler oluşturmaktadır. Limit denge yöntemine dayalı taşıma gücü yöntemleri malzeme özelliklerinin sınırlı aralıkta olduğu laboratuvar model deneylerine ait sonuçların yorumlanması ile geliştirilmiştir. Deneysel olarak test edilen aralığın dışındaki temel geometrilerine ve zemin özelliklerine uygulanabileceği genel olarak kabul edilmesine rağmen göçme mekanizmalarının söz konusu uygulamaya aralıkları için ne kadar geçerli olabileceği konusunda şüpheler bulunmaktadır. Deformasyon oluşumunun dikkate alınmadığı bu yöntemlerde tahmin edilen taşıma gücü değerinin hangi deplasman değerinde elde edildiği, yük-oturma eğrisinin nasıl geliştiği, tabakaların rölatif mukavemetleri ve geometrik koşulların göçme mekanizmasını nasıl değiştireceği bilinmemektedir. Uygulamada karşılaşılabilecek geniş aralıktaki malzeme özellikleri ve farklı temel geometrileri için tabakalı zeminlerin davranışını dikkate alan, temel-zemin etkileşiminin kapsamlı bir şekilde anlaşıldığı bir taşıma gücü modeli günümüzde henüz mevcut değildir.

Sonlu elemanlar yöntemi (FEM) kullanılarak yapılan analizlerde problem geometrisi bir bütün olarak değerlendirilmektedir. Üstteki tabaka kalınlığı, kumun sıkılığı, kilin kayma mukavemeti, yer altı su seviyesi, yükleme koşulları, malzeme modelleri, sonlu elemanlar ağı vb. faktörlere bağlı olarak ortaya çıkan deformasyon davranışı ile göçme durumuna gelmektedir. Bununla birlikte; tabakaların deformasyon karakterlerinin farklı olması, altta yer alan kilin mukavemetine de bağlı olarak, kum tabakasında mobilize hale gelen içsel sürtünme açısı değerini ve taşıma gücünü etkileyecektir. Bu nedenle belirli bir göçme mekanizması yoktur.

Yüzeysel temellerin taşıma gücü konusunda yakın zamanda yapılmış çalışmaların çoğunluğu tabakalı zeminlerdeki taşıma gücünün tahmin edilmesine odaklanmıştır [8-16]. Bu çalışmalarda; limit denge yöntemine dayalı analitik çözümler, farklı nümerik yöntemler (FEM, FELA, RPFEM vb.), istatistiksel analiz yöntemleri ve yapay zeka teknikleri kullanılarak tabakalı zeminlerde taşıma gücünün tahmin edilmesinde kullanılan limit denge yöntemine dayalı, yarı-deneysel geleneksel taşıma gücü modellerinin modifiye edilmesi, basitleştirilmiş göçme mekanizmalarının iyileştirilmesi ve modellerdeki belirsizliklerin giderilmesi amaçlanmıştır.

Bu çalışmada; göçme mekanizmalarının oluşumu ve yük-oturma davranışları, temel boyutu, başlangıç gerilme durumu, tabakalanma koşulları gibi farklı parametrelerin tabakalı zeminlerin taşıma gücü ve deformasyon davranışları üzerindeki etkileri araştırılmıştır. Takip edilen adımlar aşağıda özetlenmiştir.

- Briaud ve Gibbens [17] tarafından kum zemine oturan prototip boyutlardaki kare tekil temeller üzerinde yapılmış yükleme deneyleri sonlu elemanlar yöntemi kullanılarak modellenmiş ve analiz edilmiştir. Bu şekilde, çalışma kapsamında araştırılacak parametreler için analizlerde kullanılmak üzere doğrulanmış ve kalibre edilmiş bir sonlu eleman modeli oluşturulmuştur.
- Üstte yer alan kum tabakası kalınlığının (H), kilin drenajsız kayma mukavemetinin (c_u), temel genişliğinin (B) ve kum zeminin başlangıç gerilme koşullarının tabakalı zeminlere

oturan yüzeysel temellerin taşıma gücü ve oturma davranışları üzerindeki etkilerinin araştırılması amacı ile farklı H/B oranlarında (H/B=0.25, 0.50, 0.75, 1.00, 1.50, 2.00, 2.50 ve 3.00), farklı c_u değerlerinde (10 kPa, 20 kPa, 40 kPa ve 60 kPa), farklı temel genişliklerinde (B=1.0, 2.0 ve 3.0 m) ve farklı sükunetteki toprak basıncı katsayısı değerlerinde ($K_0 = 0.4, 0.7$ ve 1.0) analizler gerçekleştirilmiştir.

- Zımbalama kesme yönteminde K_s katsayısı, q_2/q_1 ve ϕ_1 ' e bağlı olarak tanımlanmakta, H/B oranı ve şekil katsayısı λ_s ' den bağımsız olarak, sadece, kil tabakasının drenajsız kayma mukavemeti ve temel boyutu ile değişmektedir. Yapılan FEM analizleri ile K_s katsayısı değerlerinin H/B oranına ve λ_s ' e bağlı değişimi araştırılmıştır.
- Tabakalı davranışın H ve c_u ' ya bağlı olarak hangi durumlarda son bulduğu, limit denge yaklaşımına dayalı yöntemlerde yapılan tabakalı durum kabulünün doğruluğu, yumuşak kil zeminlerde iyileştirme amacı ile yapılan granüler dolgularda temel boyutu ve minimum üst tabaka kalınlığı ilişkisi, yükleme büyüklüğüne bağlı olarak taşıma gücünde ve oturma miktarında meydana gelen değişimler değerlendirilmiştir. Elde edilen sonuçlar ile pratikteki uygulamalara yönelik öneriler sunulmaya çalışılmıştır.

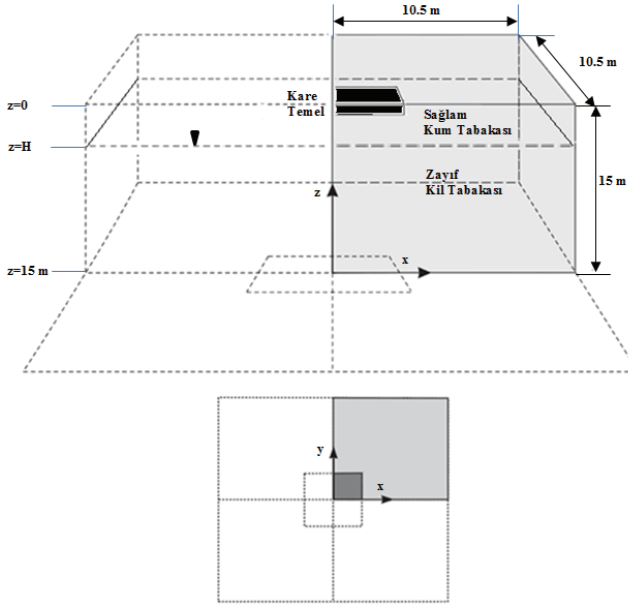
Çalışma, gerek araştırdığı parametreler gerekse de taşıma gücü ve deformasyon davranışlarının değerlendirilmesine yönelik elde ettiği sonuçlar ile literatüre yeni katkılar sağlayabilecektir.

2. PROBLEMİN TANIMI

Bu çalışmada, Çizim 1' de gösterildiği gibi kalın ve zayıf bir kil tabakası üzerinde yer alan rölatif olarak ince ve sağlam bir kum tabakasına oturan yüzeysel kare temellerin taşıma gücü ve oturma davranışları incelenmiştir. Hem kum tabakası hem de kil tabakasının homojen olduğu, kum tabakasının drenajlı kil tabakasının da drenajsız davranış sergilediği kabul edilmiştir. Tabakalı zemin profilinde yer alan kil tabakası zayıf tabaka olarak modellenmiştir. Bu nedenle, kil tabakasının drenajsız kayma mukavemeti değerleri seçilirken kilin kıvamının çok yumuşak, yumuşak, orta katı ve katı olduğu durumlar göz önüne alınmıştır. Bütün analizlerde, yer altı su seviyesinin kil tabakası yüzeyinde bulunduğu ve kil tabakasının suya doygun normal konsolide bir kil olduğu varsayılmıştır. Briaud ve Gibbens [17] tarafından yükleme deneylerinin yapıldığı sahada yer alan kum zemine ait endeks ve mukavemet özellikleri kullanılarak tabakalı zemin profilindeki sağlam kum tabakası modellenmiştir. Kum zeminde yapılan standart penetrasyon deneylerinde (SPT) ortalama darbe sayısı değeri $N_{30} = 20$ olarak elde edilmiş olup kum zemine ait boşluk oranları ile yapılan hesaplamalar sonucu da kum zeminin rölatif sıklığı $D_r = \%55$ olarak bulunmuştur. Analizlerde orta sıklıkta kum zemin normal konsolide olarak göz önüne alınmış olup yapılan parametrik çalışmalarda kum zeminin gerilme tarihçesinin tabakalı zeminlerin taşıma gücü ve oturma davranışına etkisi de değerlendirilmiştir.

Yük-oturma eğrilerinden nihai taşıma kapasitesinin tanımlanmasına yönelik literatürde farklı yaklaşımlar bulunmaktadır. Bunlardan biri de Briaud ve JeanJean [18] tarafından önerilmiş olan 0.1B yöntemidir. Bu yaklaşıma göre temel genişliğinin %10' u oturmaya neden olan yük değeri göçme yükü olarak kabul edilmektedir [4, 18-23]. Bu çalışmada nihai taşıma gücü, q_u , temel merkezi altında temel genişliğinin %10' u seviyesinde deplasmana neden olan taşıma gücü, $q_{u-s/B=0.1}$ değeri olarak tanımlanmıştır. Elde edilen sonuçların

karşılaştırılmasında temel merkezi altında elde edilen yük-oturma eğrileri kullanılmıştır. Farklı boyutlara sahip temeller üzerinde yapılan analizlerden elde edilen nihai taşıma gücü-oturma (q_u - s) davranışları karşılaştırıldığında bu sonuçlar üzerinde ölçek etkisinin var olduğu unutulmamalıdır. Bu nedenle iki tabakalı zemin profili üzerinde yer alan temellerin taşıma kapasitesi ve oturma davranışları değerlendirilirken elde edilen büyüklükler temel boyutu ile normalize edilmiştir. Taşıma gücü için $q_u/\gamma B$, oturma için s/B , kil zemininin drenajsız kayma mukavemeti için $c_u/\gamma B$ ve tabakalanma durumu için de H/B kavramları kullanılmıştır. Bu ifadelerde yer alan; q_u , B , H , c_u , γ ve s , sırası ile, ortalama nihai temel taban basıncı, temel genişliği, üstte yer alan kum tabakasının kalınlığı, altta yer alan kil tabakasının drenajsız kayma mukavemeti, kum zeminin birim hacim ağırlığı ve oturma miktarını temsil etmektedir. Kil tabakasının drenajsız davranış sergilediği kabul edildiğinden bulunan taşıma gücü değerleri, kil zeminin birim hacim ağırlığından bağımsızdır [24-26].



Çizim 1 - Problemin tanımı

3. SONLU ELEMANLAR İLE MODELLEME

Sonlu eleman analizleri ticari bir program olan Plaxis 3D 2012 programı kullanılarak gerçekleştirilmiştir. Sonlu eleman modelinin doğruluğu, literatürdeki tam ölçekli yüklemeye deneylerinin modellenmesi ve analizlerden elde edilen yük-oturma eğrilerinin deneysel yük-oturma eğrileri ile karşılaştırılması yoluyla ortaya konmuştur. Sonlu eleman analizlerinde kullanılacak model geometrinin sınırları, derinliği, analizlerin gerçekleştirileceği mesh yoğunluğu, yüklemeye tipi ve başlangıç gerilme durumunun oluşturulması gibi konular doğrulama analizleri sırasında göz önüne alınmıştır.

Briaud ve Gibbens [17] kum zemine oturan kare tekil temeller üzerinde yüklemeye deneyleri yaparak temel boyutunun taşıma kapasitesi ve oturma davranışı üzerindeki etkilerini

araştırmıştır. Yükleme deneyleri 1.0 x 1.0, 1.5 x 1.5, 2.5 x 2.5 ve 3.0 x 3.0 m boyutlarındaki kare tekil temeller üzerinde gerçekleştirilmiştir. Yükleme deneylerinde temel derinliği 0.76 m dir. Deneylerde, 150 mm oturmaya neden olan yük değeri göçme yükü olarak kabul edilmiştir. Yükleme deneylerinin yapıldığı sahada zemin profili, yüzeyden itibaren 11.0 m derinliğe kadar orta sıkı siltli kum tabakası ve devamında 33.0 m derinliğe kadar katı kil tabakasından oluşmaktadır. Yer altı su seviyesi zemin yüzeyinden itibaren -4.9 m derinliktedir. Zemin içerisindeki ince danelerde kuruma ve temellerin inşa edildiği kısımlarda yaklaşık 1.0 m kalınlığında örtü yükü kaldırılmış olduğundan kum zemin hafif aşırı konsolide olarak değerlendirilmiştir. Bu çalışma kapsamındaki sayısal analizlerde kum tabakası için Briaud ve Gibbens [17]' in deney yaptıkları kum zemine ait malzeme özellikleri kullanılmıştır.

Zeminlerin deformasyon özellikleri, efektif gerilme durumunun, zemin sıklığının, deformasyon seviyesinin ve gerilme-deformasyon geçişinin bir fonksiyonu durumundadır. Kum zeminlerin gerilme-deformasyon-dilatasyon davranışlarını kapsayan mekanik özellikleri çevre basıncı değişiminden önemli ölçüde etkilenmektedir. Gerçekten, zemin nonlinear davranır. Diğer bir ifade ile zemin rijitliği sabit olmayıp zemin kütledeki gerilme seviyesine bağlı olarak değişmektedir. Hardening Soil (HS) modelde zemin davranışı üç farklı zemin rijitlik modülü kullanılarak çok daha doğru bir şekilde modellenenmektedir. Bunun yanı sıra; HS model zemin rijitlik modüllerinin gerilme bağımlı durumunu da hesaba katmaktadır. Zeminin dilatasyon davranışı göz önüne alınmaktadır. Yenilme yüzeyi plastik deformasyonlardan dolayı genişleyebilir. HS Model gibi ileri malzeme modellerinde aşırı konsolidasyon oranı (OCR) ya da ön örtü yükü basıncı (POP) bilgileri kullanılarak zeminin gerilme geçmişi göz önüne alınabilmektedir [27-31]. HS modelde, içsel sürtünme açısı ve dilatasyon açısı arasındaki ayrımı dikkate alan bir plastik potansiyel fonksiyon ile birlikte çakışmayan akış kuralı (non-associated flow rule) kullanılır. Sayılan bu nedenlerden dolayı, kum zeminin drenajlı davranışının modellenmesinde HS model seçilmiştir. Sonlu eleman analizlerinde kullanılan kum zemine ait özellikler deney sahasında yapılmış arazi çalışmaları ile arazi ve laboratuvar deneylerine ait sonuçlar kullanılarak elde edilmiştir. Kum zeminin özellikleri Çizelge 1' de özetlenmiştir. Plaxis programında referans çevre basıncı $p_{ref.} = 100$ kN/m² olarak kullanılmaktadır. Gerçek rijitlik, küçük asal gerilme σ_3' e bağlıdır. HS modelde kullanılan rijitlik modülleri gerilme bağımlı olup gerilme bağımlılığın miktarı m üs değeri kullanılarak hesaba katılmaktadır. Birincil deviatorik yükleme sırasında oluşan plastik deformasyonları modellemek için kullanılan $E_{50}^{ref.}$ değeri üç eksenli basınç deneylerine ait sonuçlar kullanılarak referans çevre basıncı için elde edilen elastisite modülü değeridir. Yükün boşaltılması ve yeniden yüklenmesi durumundaki elastik davranışı modellemek için kullanılan $E_{ur}^{ref.}$ elastisite modülü birçok pratik uygulama için $E_{ur}^{ref.} = 3 \times E_{50}^{ref.}$ eşitliği ile elde edilebilir. $E_{oed.}^{ref.}$ elastisite modülü değeri birincil sıkışmadan kaynaklı plastik deformasyonları modellemek için kullanılmaktadır. Ödometre deney sonuçlarının bulunmadığı durumda $E_{oed.}^{ref.} = E_{50}^{ref.}$ olarak alınabilir. Zeminlerin çoğunluğunda göçme oranı, R_f , 0.75-1.00 aralığında değer almaktadır. Plaxis, R_f için ortalama 0.9 değerini kullanılmaktadır. HS modelde elastik bir parametre olarak kullanılan boşaltma-yeniden yükleme için poisson oranı, ν_{ur} , birçok zemin grubunda 0.2 olarak seçilebilir. Plaxis programında başlangıç gerilme durumu K_0 -procedure kullanılarak oluşturulmuştur. Modellemede, zeminin normal konsolide olduğu kabul edilmektedir. Bu nedenle $K_0^{nc} = 1 - \sin\phi'$ eşitliği ile başlangıç düşey ve yatay gerilmeleri ilişkilendirilir. Zeminin aşırı konsolide olduğu durumda OCR ya da POP değerlerinin kullanılarak K_0 katsayısının değerinin

düzenlenmesi gerekmektedir. İleri zemin modellerinde $K_{0-procedure}$ ile başlangıç gerilmelerinin oluşturulmasında K_0 değeri; K_0^{pc} , v_{ur} , OCR ve POP değerlerinden etkilenir ve otomatik olarak hesaplanır. Elde edilen K_0 değeri gerilme bağımlı bir değerdir. Normal konsolide bir zeminde başlangıç gerilme durumu için OCR=1 ve POP=0 dır. Yapılan doğrulama analizlerinde farklı POP değerleri için elde edilen yük-oturma eğrileri deneysel yük-oturma eğrileri ile karşılaştırılarak uygun POP değeri seçilmiş ve bu şekilde kum zeminin hafif aşırı konsolide hali dikkate alınmıştır [27-32]. Bununla birlikte, tabakalı zemin durumunda yapılan analizlerde hem kum zemin hem de kil zeminin normal konsolide oldukları kabul edilmiştir.

Dilatasyon açısının değeri laboratuvar deney sonuçları kullanılarak Bolton [33] tarafından önerilmiş olan aşağıdaki bağıntı ile tahmin edilmiştir.

$$I_R = I_D (10 - \ln p') - 1 \quad (1)$$

Bu eşitlikte yer alan I_R , I_D ve p' , sırası ile, rölatif dilatasyon indeksi, rölatif sıklık ve göçme anındaki ortalama efektif gerilme değeridir. Üç eksenli deformasyon durumunda $0 < I_R < 4$ için pik dilatasyon açısının değeri $\psi_{pik} = 3.75 I_R$ eşitliği ile elde edilebilir. HS modelde genleşme davranışı, genellikle, zemin kritik duruma ulaştığında son bulur. Dilatancy cut-off seçeneği kullanıldığında kum zeminin boşluk oranı maksimum boşluk oranı değerine ulaşınca mobilize dilatasyon açısının değeri de otomatik olarak sıfırlanacaktır.

Plaxis, drenajsız malzeme davranışının modellenmesi için Undrained (A), Undrained (B) ve Undrained (C) olmak üzere üç farklı seçenek sunmaktadır. Yumuşak zeminlerdeki projelerde efektif kayma mukavemeti parametreleri ile ilgili doğru ve güvenilir deney sonuçları bulunmamaktadır. Arazi ve laboratuvar deneyleri, çoğunlukla, drenajsız koşullardaki kayma mukavemeti parametrelerinin elde edilmesi için gerçekleştirilmektedir. Drenajsız kayma mukavemeti parametrelerinin deneysel değerlerini kullanarak efektif kayma mukavemeti parametrelerinin elde edilmesi ise son derece zordur. Deneysel olarak ölçülmüş drenajsız haldeki Young modülü Hooke kanunları ile efektif Young modülü değerine dönüştürülebilirken ileri malzeme modellerinde bu tarz bir dönüşüm mevcut değildir. Bu nedenlerden dolayı kil zeminin drenajsız davranışı Undrained (B) seçeneği ile Mohr-Coulomb (MC) malzeme modeli kullanılarak modellenmiştir. Undrained (B) seçeneğinde drenajsız kayma mukavemeti değeri giriş verisi olarak kullanıldığından kayma mukavemeti üzerinde direk kontrol sağlanabilmektedir. Bu seçenekte; kayma mukavemeti parametreleri $\phi = \phi_u$ ve $c = c_u$ olup efektif rijitlik parametreleri (Young modülü, E' ve Poisson oranı ν') kullanılarak drenajsız efektif gerilme analizi yapılabilmektedir. Kil zeminin elastik davranışı için $\nu' = 0.33$ değeri kullanılmış olup drenajsız Young modülü değeri de $E_u = 500 \times c_u$ eşitliği ile elde edilmiştir. Kil zemine ait deformasyon modülü ve drenajsız kayma mukavemeti parametrelerinin derinlik boyunca sabit olduğu kabul edilmiştir. Gerçekçi analiz sonuçları elde etmek için suyun bulk modülü zemin iskeletinin bulk modülüne göre yüksek olmalıdır. Bu koşul, $\nu' \leq 0.35$ alınarak sağlanabilir. Poulos ve Small [34], drenajsız yükleme durumunda elde edilen elastisite modülü değeri ile β düzeltme katsayısının çarpılarak drenajlı durumdaki elastisite modülü değerinin elde edilebileceğini belirtmişlerdir. Yumuşak kil ve katı kil zeminler için β katsayısı değerlerini, sırası ile, 0.4 ve 0.6 olarak önermişlerdir. Bu çalışmada kil zemine ait farklı kıvam durumlarının tamamında kullanılmak üzere β düzeltme katsayısı ortalama bir değer olarak 0.5 seçilmiştir.

$$E_s (\text{Drenajlı}) = \beta \times E_s (\text{Drenajsız}) \quad (2)$$

Fazla aşırı konsolide kil zeminler dışında, kil zeminlerde dilatasyon davranışı gözlenmez. Diğer bir ifade ile kil zeminlerde dilatasyon açısının değeri $\psi=0$ olarak kabul edilir [27, 32, 35-37]. Kil zeminin özellikleri Çizelge 2' de özetlenmiştir.

Çizelge 1 - Kum zemin için HS model parametreleri [17]

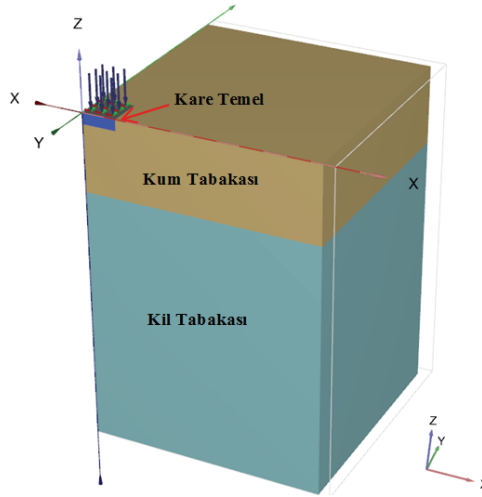
HS Model Parametreleri	Değer
Doğal Birim Hacim Ağırlık, γ_n (kN/m ³)	15.65
İçsel Sürtünme Açısı, ϕ (°)	36.40
Kohezyon, c (kN/m ²)	0.30
Dilatasyon (Genleşme) Açısı, ψ (°)	4.00
Üç Eksenli Yükleme Rijitliği, E_{50}^{ref} (kN/m ²)	14600
Üç Eksenli Boşaltma/Yeniden Yükleme Rijitliği, $E_{\text{ur}}^{\text{ref}}$ (kN/m ²)	43800
Ödometre Rijitliği, $E_{\text{oad}}^{\text{ref}}$ (kN/m ²)	14600
Boşaltma/Yeniden Yükleme Poisson Oranı, ν_{ur}	0.20
Referans Basınç, p^{ref} (kN/m ²)	100
Gerilme Bağımlı Rijitlik için Üs Değeri, m	0.50
Göçme Oranı, R_f	0.90
Normal Konsolide Zemin için Sükunetteki Yanal Toprak Basınç Katsayısı, K_0^{nc}	0.407
Sükunetteki Yanal Toprak Basınç Katsayısı, K_0	Automatic
Ön Örtü Yüğü Basıncı, POP (kN/m ²)	362.50
Aşırı Konsolidasyon Oranı, OCR	1

Çizelge 2 - Kil zeminin özellikleri

Parametreler	Değer
İçsel Sürtünme Açısı, ϕ' (°)	$\phi' = \phi_u = 0^\circ$
Birim Hacim Ağırlık, γ_{kil} (kN/m ³)	21.00
Dilatasyon (Genleşme) Açısı, ψ (°)	0
Poisson Oranı, ν'	0.33

Yapılan doğrulama analizlerinde temel, hem linear elastik davranış sergileyen non-porous hacim elemanı olarak hem de plate eleman kullanılarak modellenmiştir. Modellemelerde, temel kalınlığı deneysel çalışmalar ile uyumlu olarak 76 cm seçilmiştir. Analizlerde, temel elemanının çok rijit ve tam pürüzlü olduğu kabul edilmiştir. Ara yüzey davranışını temsil

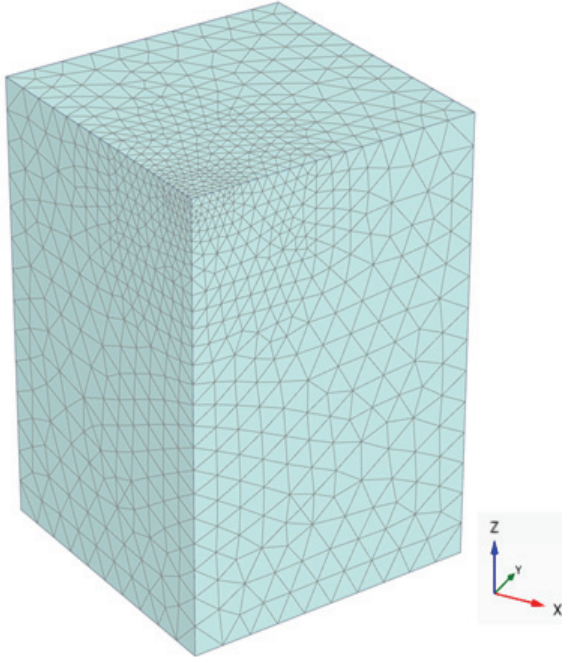
eden R_{inter} katsayısının değeri 1.0 olarak seçilmiştir. Bu durum; temel ve zemin hacim elemanları arasındaki sürtünmenin iki hacim elemanı arasında rölatif deplasman oluşumuna izin vermeyecek kadar büyük olduğu anlamına gelmektedir. Diğer bir ifade ile tam pürüzlülük hali $\phi_i = \phi$ bulunmaktadır. Temel elemanı için elastite modülü, poisson oranı ve birim hacim ağırlık değerleri, sırası ile, $E = 32 \times 10^6$ kN/m², 0.2 ve 24.0 kN/m³ olarak kullanılmıştır. Temelin hacim eleman olarak modellendiği analizlerde deneysel davranışı çok daha iyi temsil eden yük-oturma eğrileri elde edilmiştir. Yükleme iki farklı yolla gerçekleştirilmiştir. Birinci durumda, arazi yükleme deneylerinde olduğu gibi temele tekil bir yük uygulanmıştır. İkinci durumda ise temelin belirlenmiş bir deplasmanı yapması sağlanarak bu deplasmana karşılık gelen yük değeri elde edilmiştir. Tam pürüzlü hali temsil eden koşullarda yapılan her iki farklı yüklemeye de hemen hemen birbiri ile çakışan yük-oturma eğrileri elde edilmiştir. Kare tekil temel hem x hem de y yönünde var olan simetriden dolayı dörtte bir geometri ile modellenmiş olup, yük deneysel göçme yükünün 0.25 katı değerinde tekil yük olarak uygulanmıştır. Parametrik çalışmaların gerçekleştirildiği analizlerde temel kalınlığı $t=0.50$ m olarak seçilmiş olup yükleme, üniform yayılı basıncın temel alanı boyunca uygulanması ile gerçekleştirilmiştir. Model geometri için yatay sınır mesafeler temel kenarından itibaren her iki yönde (x ve y) 3B ve dikey sınır mesafe de temel tabanından itibaren 5B olarak seçilmiştir. Doğrulama analizleri için $B=3.0$ m genişlikteki kare tekil temel göz önüne alındığından çalışma alanı boyutları 10.5 m x 10.5 m x 15.0 m olarak oluşturulmuştur. Örnek bir sonlu elemanlar modeli Çizim 2' de gösterilmiştir. Çalışma kapsamında yapılan bütün analizlerde, seçilen sınır mesafelerin plastik göçme bölgeleri ve deplasman alanlarının oluşumunu etkilemeyecek yeterli uzaklıklarda yer aldığı görülmüştür. Plaxis, model geometri için sınır şartlarını otomatik olarak uygulamaktadır.



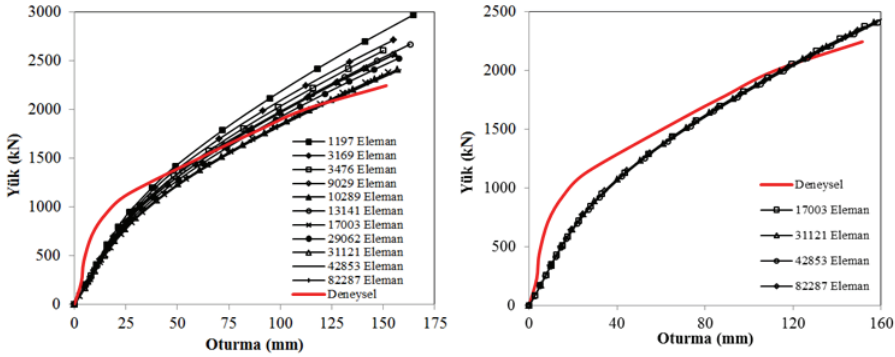
Çizim 2 - $B=3.0$ m genişlikteki kare temel için $H/B=1.0$ ve $c_u=10$ kPa durumdaki sonlu eleman modeli

Model geometride, gerilme ve deformasyon yoğunluğunun olduğu temel alanı ile temel kenarlarından ve temel tabanından itibaren farklı mesafelerde mesh sıklıkları artırılarak

farklı sonlu eleman sayılarında bir seri analiz yapılmıştır. Öncelikle seçilen bir mesh sıklığı için tüm model geometri sonlu elemanlara ayrılmıştır. Sonrasında, temel bölgesi seçilerek bu bölgedeki mesh sıklığı incelenmiştir. Daha sonra ise temel kenarlarından ve temel tabanından itibaren belirli mesafeleri kapsayan hacim elemanı için tekrar ağ inceltmesi yapılmıştır. Böylelikle; Çizim 3' den de görüldüğü gibi temel alanı boyunca en yoğun, temel kenarları ve temel tabanı altında belirli mesafelere kadar yoğun ve bu mesafeler dışında da daha az yoğun olan bir sonlu elemanlar ağı oluşturulmuştur. $B=3.0$ m genişlikteki kare tekil temel için farklı mesh yoğunluklarında yapılan analizlerden elde edilen yük-oturma eğrileri deneysel yük-oturma eğrileri ile karşılaştırılmıştır. Farklı mesh yoğunluklarında elde edilmiş olan yük-oturma eğrileri Çizim 4' de gösterilmiştir. Yapılan analizlerde sonlu eleman sayıları 1197 ile 82287 arasında değişiklik göstermiştir. Farklı başlangıç mesh sıklıkları ve farklı hacim elemanı boyutları ile yapılan denemeler sonrasında 17003 sonlu eleman, 25196 düğüm noktası ve 0.3119 m ortalama eleman boyutuna sahip sonlu elemanlar ağının oluşturulduğu yaklaşım analizlerde kullanılmak üzere seçilmiştir. Plaxis 3D programı model geometrinin sonlu elemanlara ayrılması işlemini zemindeki tabakalanmayı, yapısal elemanları, yükleme ve sınır koşullarını hesaba katarak otomatik olarak gerçekleştirmektedir. Üç boyutlu sonlu elemanlara ayırma işlemi için 10 düğümlü tetrahedral elemanlar kullanılmaktadır. Model geometride göz önüne alınan tabakalanma durumu, temel boyutu ve mesh inceltmesi yapılan bölgenin boyutlarına bağlı olarak sonlu eleman ve düğüm noktası sayılarında farklılıklar oluşsa da ortalama eleman boyutlarının farklı model geometriler için birbiri ile uyumlu oldukları görülmüştür.

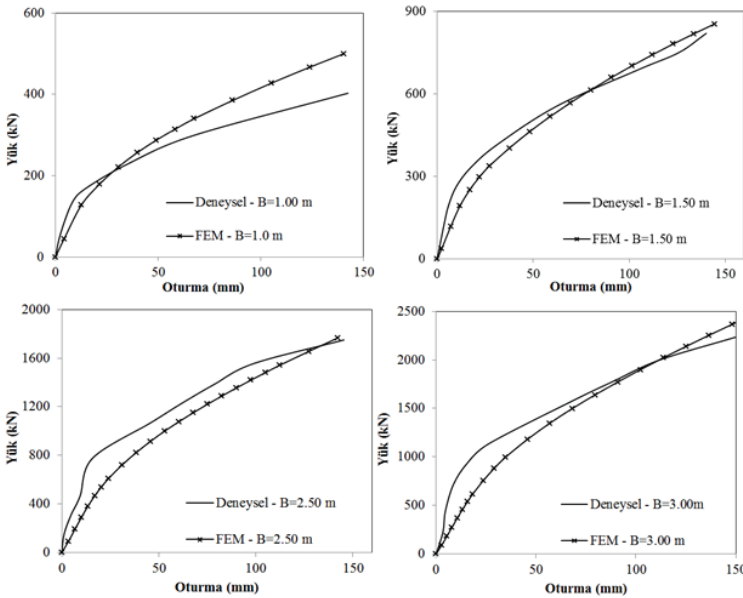


Çizim 3 - $B=3.0$ m genişlikteki kare temel için doğrulama analizi sonlu elemanlar ağı



a) Farklı ağ sıklıkları için elde edilen yük-oturma eğrileri b) Daha fazla iyileşmenin gözlenmediği ağ sıklıkları

Çizim 4 - Uygun ağ sıklığını tanımlamak için yapılan analizlerden elde edilen yük-oturma eğrilerinin deneysel yük-oturma eğrisi ile karşılaştırılması



Çizim 5 - Deneysel yük-oturma eğrilerinin analizler sonucu elde edilen yük-oturma eğrileri ile karşılaştırılması

Yapılan bu analizler sonucunda, Çizim 4' te de gösterildiği gibi, belirli bir mesh sıklığından sonra elde edilen yük-oturma eğrilerinde daha fazla bir iyileşme oluşmadığı ve eğrilerin birbirleri ile aynı olduğu görülmüştür. Aynı zamanda bu mesh yoğunluklarında elde edilmiş yük-oturma eğrileri deneysel yük-oturma eğrilerine en yakın davranışı ortaya koymuştur.

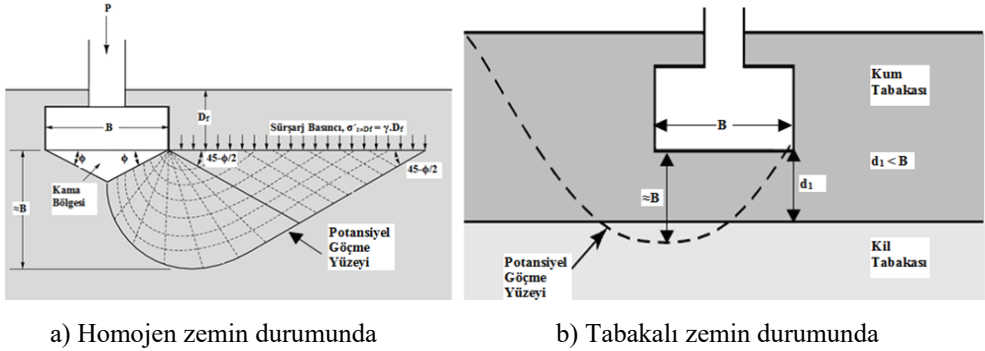
Bununla birlikte mesh sıklığının artması hesaplama zamanı üzerinde ciddi artışlara neden olmaktadır. Bu nedenle deneysel yük-oturma davranışına en yakın sonuçları veren ve hesaplama süresi açısından en elverişli olan mesh sıklığı seçilmiştir.

Yüklemeye deneylerindeki farklı boyuta sahip her bir temel için yüklemeye deneyleri ve sayısal analizlerden elde edilmiş yük-oturma eğrileri karşılaştırılmalı olarak Çizim 5’ de gösterilmiştir. Çizim 5’den görüldüğü gibi sonlu eleman analizlerinden elde edilmiş olan yük-oturma eğrileri deneysel yük-oturma eğrileri ile iyi bir uyum sergilemektedir.

4. BULGULAR VE TARTIŞMALAR

4.1. Üstte Yer Alan Kum Tabakası Kalınlığının (H/B) ve Altta Yer Alan Kil Zeminin Drenajsız Kayma Mukavemetinin (c_u) Etkisi

Tabakalı zeminlere oturan yüzeysel temellerin nihai taşıma kapasitesinin tahmin edilmesinde kullanılan geleneksel taşıma gücü yöntemlerinde, kum tabakası kalınlığının temel genişliğinden küçük olması durumunda, Çizim 6’ da gösterildiği gibi, yenilme yüzeyinin alttaki kil tabakasının içine doğru genişleyeceği ve göçme yüzeyi derinliği içerisinde yer alan tabakaların elde edilecek taşıma gücünü etkileyeceği kabulü yapılmaktadır. Bu nedenle; tabakalı zeminler üzerinde yer alan temellerin tasarımında zemindeki tabakalanma koşullarının hem geometrik açıdan hem de tabakaların rölatif mukavemetleri açısından göz önüne alınarak taşıma gücü ve deformasyon davranışları üzerindeki etkilerinin değerlendirilmesi önemlidir.

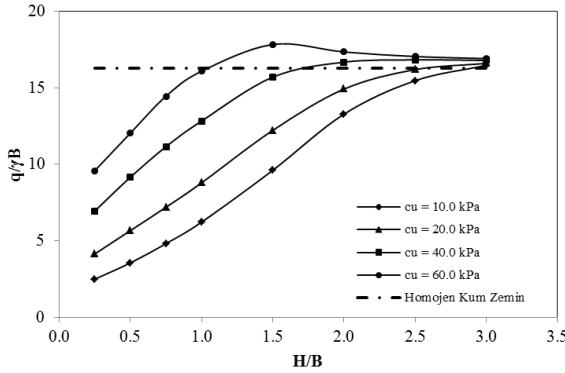


Çizim 6 - Homojen ve tabakalı zemin durumlarında potansiyel göçme yüzeyleri [38]

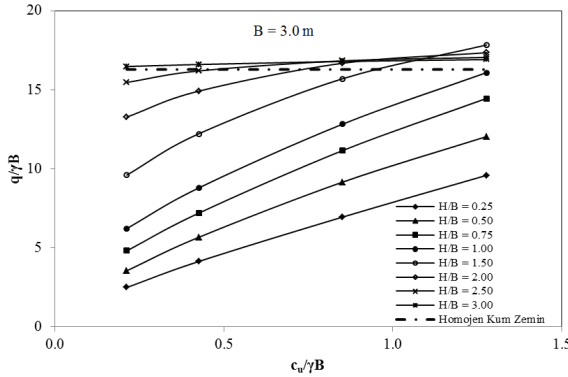
Altta yer alan zayıf kil tabakasının farklı drenajsız kayma mukavemeti değerleri için farklı üst tabaka kalınlıklarında $B=3.0$ m genişliğindeki kare temelde elde edilen boyutsuz taşıma gücü değerlerinin karşılaştırılması Çizim 7’ te gösterilmiştir. Limit denge yöntemine dayalı teorik taşıma gücü yöntemlerinde yapılan kabulün aksine tabakalı durumun hem alttaki kil tabakasının drenajsız kayma mukavemeti hem de üstte yer alan kum tabakasının kalınlığına bağlı olarak $H/B > 1.0$ durumunda da geçerli olduğu görülmektedir. Homojen kum zemindeki taşıma gücü, tabakalı durum için bir üst sınır olarak kabul edildiğinde $c_u=10.0$ kPa olduğu durumda $H/B=2.5-3.0$ için bu değere ulaşılırken $c_u=20.0, 40.0$ ve 60.0 kPa olduğu durumlarda, sırası ile, $H/B=2.5, H/B=1.5-2.0$ ve $H/B=1.0-1.5$ için ulaşılmıştır. Kil

tabakasının drenajsız kayma mukavemetindeki artış taşıma gücü değerini artırırken c_u ' nun artması ile birlikte daha küçük üst tabaka kalınlıklarında homojen kum zemin durumundaki taşıma gücüne ulaşılmaktadır.

Çizim 8' de gösterildiği gibi c_u ' nun artması ile birlikte bütün H/B oranlarında taşıma gücü değerleri artmaktadır. $H/B=3.0$ durumunda tabakalı durum söz konusu olmamakla birlikte alttaki kil tabakasının varlığı, özellikle $c_u > 10$ kPa için, tabakalı durumdaki taşıma gücünde homojen kum zemin durumundakine göre artışa neden olmaktadır. Üstteki tabaka kalınlığı sabit iken c_u ' nun artması $H/B=0.25, 0.50, 0.75$ ve 1.00 olan üst tabaka kalınlıklarında taşıma gücünde doğrusal bir artışa neden olmuştur. $H/B > 1.0$ durumunda göçme yüzeyinin daha büyük kısmı kum tabakası içerisinde geliştiğinden $c_u/\gamma B < 1.0$ değerlerinde homojen kum zemindeki taşıma gücü değerinin yakalandığı görülmüştür.



Çizim 7 - Farklı c_u değerleri için $H/B - q_u/\gamma B$ ilişkileri



Çizim 8 - Farklı H/B oranları için $c_u/\gamma B - q_u/\gamma B$ ilişkileri

s_i/S (%), herhangi bir derinlikteki oturmanın toplam oturmaya oranı olarak tanımlanmıştır. Çizelge 3' te kil tabakası yüzeyinde ölçülen oturmaların toplam oturmaya oranları verilmiştir. Çizelge 3' te verilen değerlere göre $c_u=10$ ve 20 kPa için tabakalanma etkisi $H/B > 2.50$ durumunda kalkarken $c_u=40$ ve 60 kPa için $H/B > 1.50$ durumunda kalkmaktadır.

Kil zeminin bütün drenajsız kayma mukavemeti değerleri için H/B oranının artması ile ilave boşluk suyu basıncı değerlerinde azalma meydana gelmiştir. Kum tabakası kalınlığının artması ile etki derinliği içerisindeki kil tabakası kalınlığı azalmakta, yer altı su seviyesinin zemin yüzeyinden itibaren derinliği artmakta ve kil tabakası yüzeyinde meydana gelen deplasman değerleri azalmaktadır. Diğer taraftan kil tabakasının mukavemetinin artması ile birlikte aynı H/B oranlarında elde edilen ilave boşluk suyu basıncı değerleri taşıma kapasitesindeki artışa bağlı olarak artmıştır. $c_u=10$ kPa için H/B=0.25 durumunda elde edilen ilave boşluk suyu basıncı değeri 356.10 kPa iken H/B=3.0 durumunda bu değer 19.71 kPa olarak elde edilmiştir. $c_u=20$ kPa için H/B=0.25 durumunda elde edilen ilave boşluk suyu basıncı değeri 682.80 kPa iken H/B=2.5 durumunda bu değer 45.64 kPa dır. $c_u=40$ kPa için H/B=0.25 durumunda elde edilen ilave boşluk suyu basıncı değeri 1190 kPa iken H/B=2.0 durumunda 78.83 kPa değeri elde edilmiştir. $c_u=60$ kPa için H/B=0.25 durumunda 1933 kPa olan ilave boşluk suyu basıncının değeri H/B=2.0 durumunda 44.48 kPa olarak elde edilmiştir.

Çizelge 3 - Farklı H/B ve farklı c_u değerleri için s_i/S (%) oranları

B = 3.00 m				
H/B	$c_u = 10$	$c_u = 20$	$c_u = 40$	$c_u = 60$
	kN/m ²	kN/m ²	kN/m ²	kN/m ²
	s_i / S (%)	s_i / S (%)	s_i / S (%)	s_i / S (%)
0.25	98.179	96.951	95.302	94.593
0.50	96.054	92.915	88.122	84.147
0.75	89.906	83.267	73.632	66.134
1.00	78.080	68.241	54.105	45.092
1.50	48.585	36.693	24.735	17.914
2.00	23.436	16.769	9.627	6.149
2.50	7.643	5.842	3.455	2.494
3.00	0.226	0.228	0.362	0.362

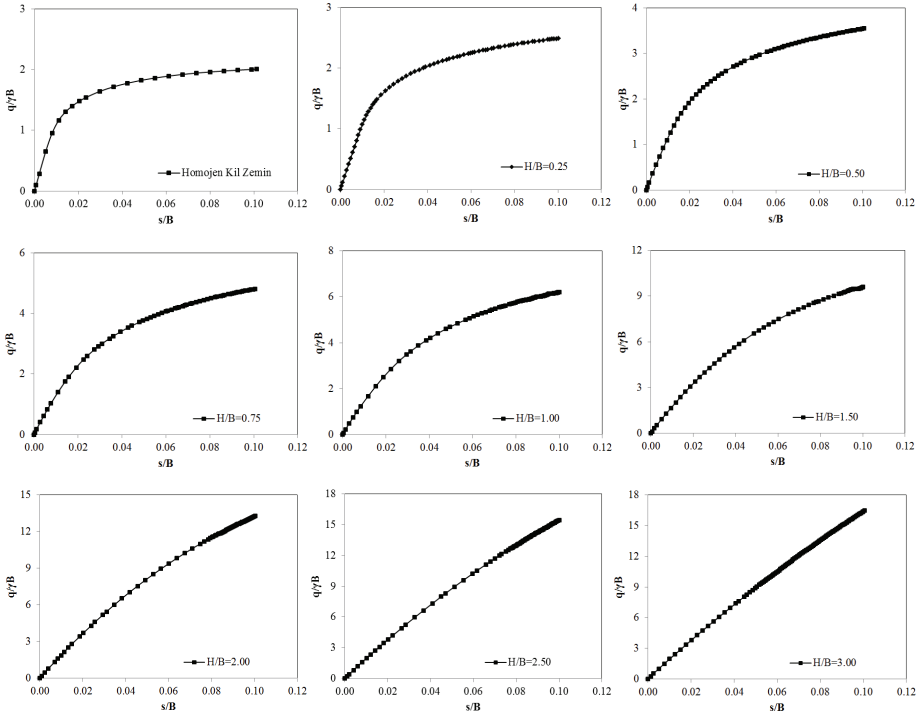
Uygulanan yük etkisinde derinlik boyunca meydana gelen oturmaların toplam oturmaya oranının %10' dan küçük olduğu durumda yük etkisinin ihmal edilebilir olduğu kabul edilmiştir. Çizelge 4' te gösterildiği gibi homojen kil zeminde durumunda etki derinliği temel tabanından itibaren 2B derinlikte son bulmakta ve bu derinlik içerisinde toplam oturmaların %94' ünden fazlası gerçekleşmektedir. Homojen kum zemin durumunda ise etki derinliği 2B-3B derinlikleri arasında son bulmaktadır. 2B-3B derinlikleri arasında gerçekleşen oturmaların toplam oturmaya oranı yaklaşık %10 dur. H/B=0.25 ve 0.50 için bütün c_u değerlerinde etki derinliği temel tabanından itibaren 2B dir. Bununla birlikte; H/B=0.75, 1.00, 1.50, 2.00 ve 2.50 için $c_u=10$ ve 20 kPa değerlerinde etki derinliği 2B-3B aralığında iken $c_u=40$ ve 60 kPa için 2B dir. H/B=0.25, 0.50, 0.75 ve 1.00 için temel tabanı ile B derinliği arasında meydana gelen oturmanın toplam oturmaya oranı sırası ile %63, %41, %27 ve %22 iken B-2B derinliği arasında bu değerler sırası ile %31, %48, %56 ve %57 olarak elde

Çizelge 4 - Temel tabanından itibaren B, 2B ve 3B derinliklerde gözlenen s_i/S oranları

B=3.00 m	c_u (kN/m ²)	10	20	40	60
	Derinlik	s_i/S (%)	s_i/S (%)	s_i/S (%)	s_i/S (%)
Homojen Kil	B	22.551	22.267	22.373	22.566
	2B	4.311	4.257	4.276	4.315
	3B	1.232	1.215	1.218	1.229
H/B = 0.25	B	36.785	27.898	20.497	16.063
	2B	6.521	4.659	3.306	2.56
	3B	1.810	1.243	0.893	0.701
H/B = 0.50	B	59.270	47.434	35.455	28.537
	2B	11.731	8.096	5.424	4.171
	3B	3.139	2.132	1.385	1.073
H/B = 0.75	B	73.200	61.742	48.049	39.944
	2B	17.165	11.499	7.344	5.654
	3B	4.313	2.914	1.852	1.436
H/B = 1.00	B	78.080	68.241	54.105	45.092
	2B	21.977	14.826	9.010	6.563
	3B	5.448	3.647	2.275	1.686
H/B = 1.50	B	78.573	69.760	57.202	47.061
	2B	24.421	16.386	9.491	6.698
	3B	7.112	4.456	2.493	1.668
H/B = 2.00	B	59.242	53.327	49.036	47.931
	2B	23.436	16.769	9.627	6.149
	3B	6.442	3.476	1.557	1.198
H/B = 2.50	B	50.879	49.855	48.700	48.034
	2B	22.632	17.403	11.658	9.697
	3B	2.026	1.115	0.740	0.552
H/B = 3.00	B	49.257	48.905	48.373	48.038
	2B	14.915	13.473	12.212	11.418
	3B	0.226	0.228	0.362	0.362
Homojen Kum	B			48.219	
	2B			12.218	
	3B			1.402	

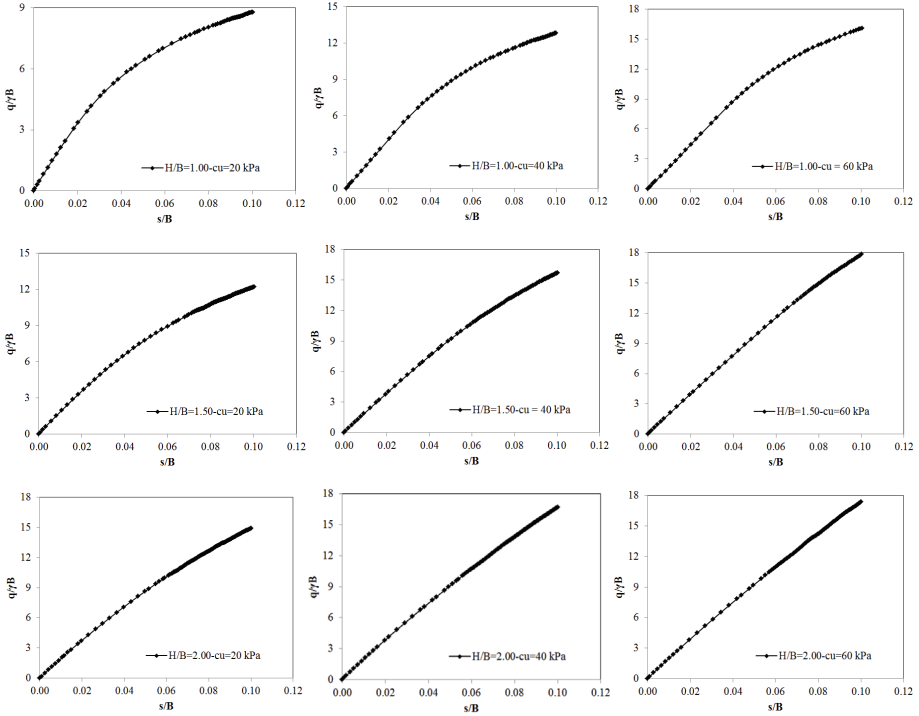
edilmiştir. Kum tabakası kalınlığının ve buna bağlı olarak da kil tabakasının yüzeyden itibaren derinliğinin artmasının bir sonucu olarak B-2B derinlikleri arasındaki oturmaların da toplam oturma içerisindeki oranı artmaktadır. Üstteki tabaka kalınlığının $H/B=1.50$, 2.00 ve 2.50 olduğu durumlarda $c_u=10$ ve 20 kPa için 2B-3B derinlikleri arasında meydana gelen oturmaların toplam oturmaya oranı yaklaşık olarak %15 iken $c_u=20$ ve 40 kPa için bu oran $< \%10$ dur.

Çizim 9’ da $B=3.0$ m genişlikteki kare temelde $c_u=10$ kPa durumunda farklı H/B oranları için $s/B-q_u/\gamma B$ ilişkileri gösterilmiştir. Çizim 9’ dan da görüldüğü gibi $H/B=0.25$ ve $H/B=0.50$ durumlarında elde edilen yük-oturma eğrileri, homojen kil zemindeki gibi elastik-tam plastik benzeri bir davranışı temsil etmektedir. Üst tabaka kalınlığı rölatif olarak küçük olduğundan göçme yüzeylerinin büyük kısmı doymuş kil zemin tabakasında gelişmektedir. $H/B=0.75$, 1.00 , 1.50 ve 2.00 durumlarında yük-oturma eğrileri elasto-plastik benzeri bir davranışı temsil ederken $H/B=2.50$ durumunda davranış doğrusal elastik davranışa yakındır. Üstteki kum tabakası kalınlığının artması ile birlikte tabakalı zeminde taşıma gücü ve oturma davranışları kum ve kil tabakalarının katkıları ile idare edilirken $H/B \geq 2.50$ durumunda kum tabakası tarafından idare edilen bir taşıma gücü ve oturma davranışı söz konusudur. Doymuş kil tabakasının mukavemet ve rijitliğindeki artış ile birlikte aynı H/B oranında farklı $c_u/\gamma B$ değerlerinde yük-oturma davranışları da farklılık sergilemektedir.



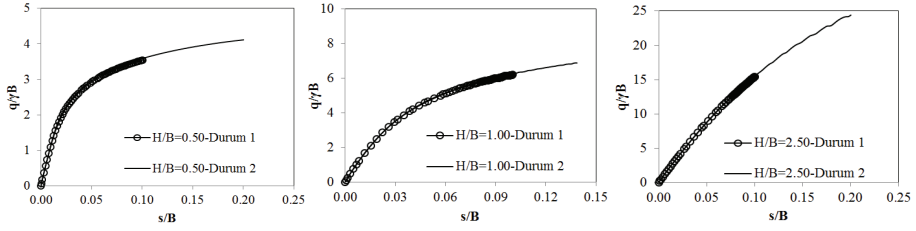
Çizim 9 - $B=3.0$ m genişlikteki kare temelde $c_u = 10$ kPa durumunda farklı H/B oranları için $s/B-q_u/\gamma B$ ilişkileri

Çizim 10' dan görüldüğü gibi artan üst tabaka kalınlığı ile birlikte daha küçük $c_u/\gamma B$ değerlerinde yük-oturma davranışları doğrusal elastik davranışa yakın hale gelmektedir. $H/B=1.00$ durumunda yük-oturma eğrisinde doğrusal elastik davranışa yakın davranış $c_u/\gamma B > 1.28$ için gerçekleşirken bu değer $H/B=1.50$ ve 2.00 için, sırası ile, $c_u/\gamma B > 0.85$ ve $c_u/\gamma B > 0.43$ için meydana gelmiştir.



Çizim 10 - $B=3.0$ m genişlikteki kare temelde farklı H/B ve c_u değerleri için $s/B-q/\gamma B$ ilişkileri

Çizim 11' de $s/B=0.1$ değerinde oturmaya neden olan yükleme durumu Durum 1, bu yüklemenin yaklaşık 2 katı değerinde yükün uygulandığı durum da Durum 2 olarak adlandırılmıştır. $H/B=0.50$ için Durum 2' de oturma değeri %100 artmış olmasına karşın taşıma gücü değerindeki artış Durum 1' e göre %16 olmuştur. $H/B=0.50$ için Durum 2' de yapılan analizde göçme meydana gelmemiştir. Analiz, $s/B=0.2$ değerinde sonlandırılmıştır. $H/B=1.0$ için Durum 2' de $s/B=0.14$ değerinde zeminde göçme meydana gelmiştir. Göçmeye neden olan boyutsuz taşıma gücü değeri $q/\gamma B=6.889$ olup Durum 1' e göre oturma değerinde meydana gelen %40' lık artışa karşılık taşıma gücü değerinde %11 değerinde artış oluşmuştur. $H/B=2.50$ için Durum 2' de oturma değerindeki %100' lük artışa karşılık taşıma gücü değerinde Durum 1' e göre %58 oranında artış meydana gelmiştir. $H/B=2.50$ için Durum 2' de yapılan analizde göçme meydana gelmemiştir. Analiz, $s/B=0.2$ değerinde sonlandırılmıştır.



Çizim 11 - $B=3.0$ m genişlikteki kare temelde $c_u=10$ kPa için Durum 1 ve Durum 2' de elde edilen $s/B-q_u/\gamma B$ ilişkilerinin karşılaştırılması

H/B oranı ve c_u değerlerinde meydana gelen değişimler yatay yöndeki deplasmanların oluşumu üzerinde de etkili olmaktadır. Yatay yöndeki deplasman hareketleri, H/B oranı ve c_u değerlerine bağlı olarak temel merkezinden itibaren $1.50B-2.00B$ mesafeye kadar etkili olmaktadır. $c_u/\gamma B < 0.85$ için yatay mesafe $1.70B-2.00B$ aralığında iken $c_u/\gamma B \geq 0.85$ için bu aralık $1.50B-1.60B$ dir.

4.2. Temel Boyutunun Etkisi

Nihai taşıma kapasitesi üzerinde temel boyutunun etkisi, sadece, homojen zeminlerde değil tabakalı zeminlerde de gözlenebilir.

ϕ_{pik} , göçme anındaki pik gerilme durumu için elde edilmiş içsel sürtünme açısı değeri olup kritik durum içsel sürtünme açısı, ϕ_{kritik} ve dilatasyon açısı, ψ' nin toplamı olarak ifade edilmektedir. ϕ_{kritik} , zeminin gerilme geçmişinden, zemindeki gerilme durumundan ve dane düzenlemesinden bağımsız iken ψ , zemin durum değişkeni olup zemin sıkılığı ve zemindeki ortalama efektif gerilme değerinden etkilenmektedir. Zemin sıkılığı arttığında ve ortalama efektif gerilme azaldığında ψ artar ve daha büyük ϕ_{pik} değerleri elde edilebilir. Analizlerde giriş parametresi olarak sabit bir ϕ_{pik} değeri kullanılmasına rağmen kayma yüzeyleri boyunca mobilize haldeki içsel sürtünme açısı değerleri farklı dilatasyon davranışları nedeni ile aynı olmayacaktır. Homojen kum zemin durumunda temel boyutunun artması ile etkili gerilme bölgesi derinliği ve çevre basıncı artacaktır. Bunun sonucu olarak kum zemindeki kayma yüzeyleri boyunca mobilize haldeki ψ değerleri ve buna bağlı olarak da $\phi_{mobilize}$ değerleri farklılaşacaktır. Temel boyutu; çevre basıncı seviyesi, kum zeminin kayma mukavemeti davranışı ve göçme mekanizması oluşumu üzerinde etkilidir. Kohezyonsuz zeminlerde ϕ açısı sabit olmayıp artan çevre basıncı ile birlikte azalmaktadır [39-43].

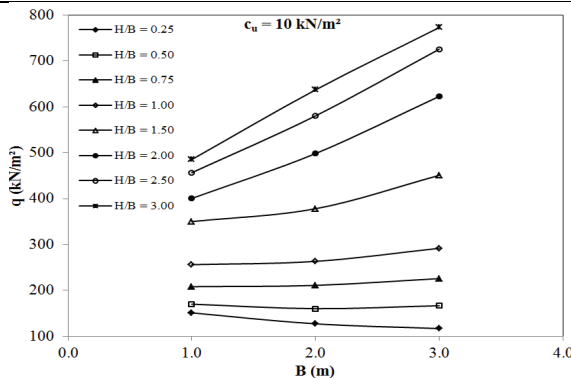
Temel boyutunun tabakalı zeminlerde taşıma gücü ve oturma davranışı üzerindeki etkisini araştırmak için $B=1.0$, 2.0 ve 3.0 m genişlikteki kare temeller ile homojen kil, homojen kum ve tabakalı zemin durumlarında bir seri üç boyutlu sonlu elemanlar analizi yapılmıştır. Analizler, her bir temel boyutu için $c_u=10$ kPa durumunda farklı H/B oranları için gerçekleştirilmiştir. Tabakalı zemin profilinde homojen kum zemin durumunda elde edilen taşıma gücü değerinin üst sınır olduğu kabul edildiğinde, $c_u=10$ kPa için, $B=3.0$ m genişlikteki kare temelde tabakalanma etkisi $H/B=2.5-3.0$ için görülmezken $B=2.0$ m genişlikteki kare temelde $H/B=3.0$ için ve $B=1.0$ m genişlikteki kare temelde de $H/B>3.0$ için tabakalanma etkisi görülmemektedir. Temel boyutu, tabakalanma davranışını etkilemekte ve

temel boyutunun artması ile birlikte tabakalanma etkisinin olmadığı H/B oranı azalmaktadır. Çizelge 5’ te verilen s_i/S oranları değerlendirildiğinde de benzer sonuca ulaşılmaktadır. B=1.0 m genişlikteki kare temelde H/B=3.0 durumunda s_i/S =%13.649 dur. B=2.0 m genişlikteki kare temelde s_i/S oranı H/B=2.5-3.0 ve B=3.0 m genişlikteki kare temelde de H/B=2.0-2.5 aralığında %10 değerinin altına düşmektedir. Diğer taraftan H/B=3.0 için s_i/S değerleri B=1.0, 2.0 ve 3.0 m genişlikteki kare temellerde, sırası ile, %13.649, 4.601 ve 0.226 olarak elde edilmiştir.

Çizim 12’ de görüldüğü gibi H/B=0.25 için temel boyutunun artması taşıma gücünde azalmaya neden olurken H/B=0.50 ve 0.75 için taşıma gücü değeri temel boyutundan etkilenmemiştir. H/B \geq 1.00 için temel boyutunun artması taşıma gücünü de artırmaktadır. Ancak; H/B oranı ile taşıma gücü arasında kurallı ve orantılı bir artış gözlenmemiştir. Her bir temel boyutu için taşıma gücündeki en büyük artış miktarı H/B’ nin 1.00 ile 1.50 değerleri arasında elde edilmiştir. H/B \geq 1.50 için tabakalanma etkisinin görülmediği H/B oranına kadar taşıma kapasitesindeki artış oranları azalmaktadır.

Çizelge 5 - Farklı boyutlara sahip kare temeller için kil tabakasında gözlenen s_i/S oranları

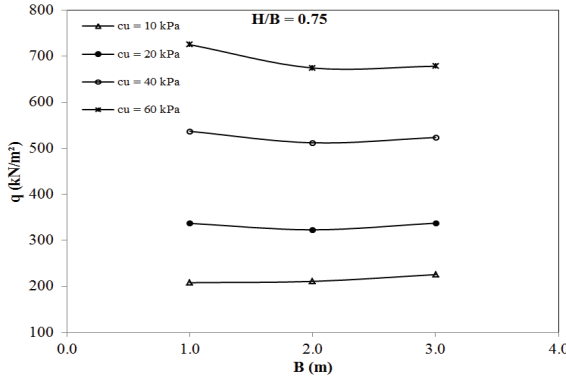
H/B	B = 3.00 m	B = 2.00 m	B = 1.00 m
	$c_u = 10 \text{ kN/m}^2$	$c_u = 10 \text{ kN/m}^2$	$c_u = 10 \text{ kN/m}^2$
	s_i / S (%)	s_i / S (%)	s_i / S (%)
0.25	98.179	98.246	98.846
0.50	96.054	95.779	94.500
0.75	89.906	87.657	87.322
1.00	78.080	76.902	85.397
1.50	48.585	56.672	62.404
2.00	23.436	32.809	41.699
2.50	7.643	14.224	22.398
3.00	0.226	4.601	13.649



Çizim 12 - Farklı H/B oranları için temel boyutunun taşıma kapasitesi üzerindeki etkisi

Zayıf kil tabakası bulunan problemlili zemin koşullarında üstte oluşturulacak kontrollü bir dolgu tabakası ile zemin iyileştirilmek istendiğinde, dolgu tabakasının kalınlığı $B > 1.0$ m genişlikteki temeller için H/B oranı minimum 0.50 olacak şekilde seçilmelidir. $B = 1.0$ m olduğu durumda bu oran minimum 0.75 olmalıdır.

Üst tabaka kalınlığının $H/B = 0.75$ olduğu durumda c_u değerindeki artışın nihai taşıma gücü ve oturma davranışı üzerindeki etkileri analiz edilmiştir. Çizim 13' den görüldüğü gibi bütün temel boyutlarında c_u değerinin artması tabakalı zeminin nihai taşıma gücünü artırmaktadır. Nihai taşıma gücündeki artış miktarı, $c_u = 20$ kPa ile $c_u = 40$ kPa ve $c_u = 40$ kPa ile $c_u = 60$ kPa arasındaki değişimlerde, göz önüne alınan bütün temel boyutları için hemen hemen aynı oranda olup, sırası ile, %58 ve %30 değerindedir. c_u değerinin artması ile birlikte taşıma gücündeki artış oranının azalması, zayıf tabaka durumundaki alttaki kil tabakasının mukavemetinin sağlam tabaka durumundaki üstteki kum tabakasının mukavemetine yaklaşması ile açıklanabilir. Temel boyutunun artması ile birlikte $c_u = 10$ kPa ile $c_u = 20$ kPa arasında meydana gelen artış oranı azalmıştır. $B = 1.0$ m genişlikteki temelde artış oranı %62 iken $B = 2.0$ m ve $B = 3.0$ m genişlikteki temeller için artış oranları, sırası ile, %53 ve %50 dir. Çizim 13' de gösterildiği gibi kil zeminin drenajsız kayma mukavemetinin sabit olduğu durumda temel boyutunun artması nihai taşıma kapasitesi üzerinde önemli olmayan değişimlere neden olmuştur.



Çizim 13 - Farklı c_u değerleri için temel boyutunun taşıma kapasitesine etkisi

Çizelge 6 - Farklı boyutlara sahip kare temeller için $H/B = 0.75$ durumunda kil tabakasında gözlenen s_i/S oranları

H/B = 0.75				
B	$c_u = 10$ kN/m ²	$c_u = 20$ kN/m ²	$c_u = 40$ kN/m ²	$c_u = 60$ kN/m ²
	s_i / S (%)	s_i / S (%)	s_i / S (%)	s_i / S (%)
3.0	89.906	83.267	73.632	66.134
2.0	87.657	81.027	72.081	65.374
1.0	87.322	81.454	71.194	64.797

Farklı temel boyutları için farklı c_u değerlerinde kil tabakası yüzeyindeki s_v/S (%) değerleri $H/B=0.75$ durumunda Çizelge 6' da verilmiştir. Çizelge 6' dan görüldüğü gibi c_u değerinin sabit olduğu durumda temel boyutunun değişmesi kil tabakasında meydana gelen oturmaları etkilememektedir. Ancak; c_u değerinin artması ile birlikte kil tabakasında meydana gelen oturma miktarı azalmaktadır. Kil tabakasının kum tabakasına göre rölatif mukavemetinin artması kum tabakasının taşıma gücüne olan katkısını arttırmakta diğer bir ifade ile kum tabakasında mobilize haldeki içsel sürtünme açısının büyümesi ile taşıma gücü artmaktadır.

4.3. Başlangıç Gerilme Durumu ve Gerilme Geçmişinin Etkisi

Geleneksel taşıma gücü teorileri; nihai taşıma kapasitesi tahmininde düşey efektif gerilme esas olduğu için sükunetteki toprak basınç katsayısı, K_0 'ın etkisini göz önüne almamaktadır. Oysaki; geliştirilmiş tasarımlar için K_0 katsayısının taşıma kapasitesi üzerindeki etkisinin araştırılması önemlidir [39-43]. Tabakalı durumda, kum tabakasında meydana gelen zımbalama davranışı ve kum bloğun düşey yüzeylerindeki sürtünme direnci yatay gerilmeler ve pasif etkilere bağlı olarak değerlendirildiğinden K_0 katsayısının tabakalı zeminlerin taşıma gücü ve deformasyon davranışları üzerinde etkili olduğu düşünülmektedir.

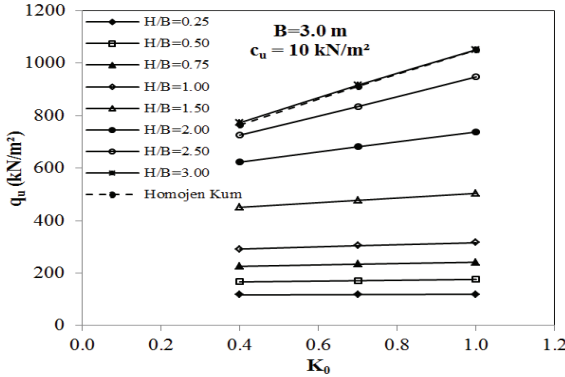
Başlangıç gerilme durumu, sadece, zeminin kendi ağırlığından kaynaklı düşey ve yatay gerilmelere değil zeminin gerilme geçmişine de bağlıdır. HS modelde OCR ya da POP parametreleri kullanılarak zeminin gerilme geçmişi göz önüne alınabilmektedir. Diğer bir seçenek ise zeminin normal konsolide kabul edilerek derinlik boyunca sabit değere sahip daha büyük bir K_0 katsayısının kullanılmasıdır. POP değeri kullanıldığında, zemin yüzeyindeki gerilme değerleri, başlangıç gerilme durumu için, sıfırdan büyük değerler alırken derinlik boyunca sabit bir K_0 katsayısı seçildiğinde başlangıç gerilmelerinin zemin yüzeyindeki değeri sıfır olmaktadır. Bununla birlikte; OCR ve POP bilgilerinin elde edilebilmesi K_0 katsayısının tahmin edilmesine göre daha karmaşıktır.

Zeminin aşırı konsolide halindeki yanal toprak basınç katsayısı normal konsolide halinden daha büyüktür. Doğal durumda, üstte yer alan ve aşırı konsolide hale gelen tabakaların kalınlıkları iklim koşulları ve tektonik hareketlere bağlı olarak değişkenlik gösterir. Zemin profilinin yüzeye yakın üst kısmında yer alan ve aşırı konsolide halde bulunan bölümlerindeki OCR oranı derinlikle birlikte azalacağından K_0 katsayısının yüzeye yakın derinliklerde daha büyük olması ve derinlikle birlikte azalarak normal konsolide durumdaki değerine yaklaşması beklenir. İnsan yapımı granüler dolgular, genellikle, kompaksiyon öncesinde normal konsolide olarak değerlendirilir. Bununla birlikte; zemin kompaksiyonu sonucunda oluşan ön konsolidasyon etkisi dolgunun aşırı konsolide hale gelmesine neden olur. Bu süreçte zemin sadece sıkışmaz aynı zamanda da ön yüklenir ve sonuçta yatay efektif gerilmelerde kalıcı bir artış oluşur. Yatay efektif gerilmelerdeki değişim, genelde dikkate alınmamasına karşılık, granüler zeminlerdeki oturmayı önemli derecede etkilemektedir. [27, 32, 42, 44-49].

Bu çalışmada, kum zeminin aşırı konsolide durumu, normal konsolide halde sahip olduğu K_0 değerinden daha büyük olan sabit K_0 katsayısı değerleri seçilerek göz önüne alınmıştır. K_0 katsayısının 0.4, 0.7 ve 1.0 değerleri için bir seri analiz gerçekleştirilerek başlangıç gerilme koşulları ve kum zeminin gerilme geçmişinin tabakalı durumdaki taşıma gücü ve oturma davranışına etkisi araştırılmıştır. Analiz sonuçları incelendiğinde K_0 katsayısının değerinin artması ile taşıma gücünün arttığı görülmektedir. $H/B < 2.0$ için artış oranları ihmal edilebilir

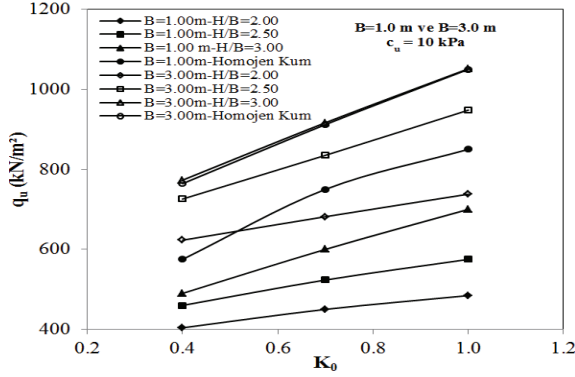
seviyelerde olup %10' dan küçük iken $H/B \geq 2.0$ için artış oranları hem $K_0=0.7$ hem de $K_0=1.0$ için %10' un üzerinde elde edilmiştir. H/B oranının artması ile birlikte taşıma gücündeki artış oranları %36' ya kadar çıkmaktadır. K_0 katsayısının 0.4' den 1.0' e artırıldığı durumda taşıma gücünde meydana gelen artış oranı, bütün H/B oranları için, 0.4' den 0.7' ye artırıldığı durumda elde edilen artış oranlarının yaklaşık iki katı kadardır. Çizim 14' den görüldüğü gibi $H/B \geq 2.0$ için taşıma gücündeki artış K_0 katsayısının artışı ile yaklaşık doğrusal olarak değişmektedir. $H/B \leq 1.0$ durumunda K_0 katsayısı ile birlikte taşıma gücündeki artış oranları %5 ve altında elde edilmiştir. $H/B=3.0$ durumunda taşıma gücünün K_0 katsayısı ile artışı homojen kum zemin durumu ile aynıdır. $B=3.0$ m genişlikteki kare temeller üzerinde yapılan analizlerden elde edilen bu sonuç ele alınan durumda tabakalanma etkisinin $H/B=2.5$ ile $H/B=3.0$ aralığında kalktığını da göstermektedir.

Farklı genişlikteki temellerde taşıma gücü değeri temel boyutundan etkilenmekte ve bununla birlikte tabakalanma etkisi farklı H/B oranlarında kalkmaktadır. Çizim 15' de temel boyutu ve K_0 katsayısının taşıma gücü üzerindeki etkisi görülmektedir. $B=1.0$ m genişlikteki kare temelde $H/B < 2.0$ için artış oranları ihmal edilebilir seviyelerde olup %10' dan küçük iken $H/B \geq 2.0$ için artış oranları hem $K_0=0.7$ hem de $K_0=1.0$ için %10' un üzerinde elde edilmiştir. H/B oranının artması ile birlikte taşıma gücündeki artış oranları %47' ye kadar çıkmaktadır. K_0 katsayısının 0.4' den 1.0' e artırıldığı durumda taşıma gücünde meydana gelen artış oranı, bütün H/B oranları için, 0.4' den 0.7' ye artırıldığı durumda elde edilen artış oranlarının yaklaşık iki katı kadardır. Çizim 15' den görüldüğü gibi $H/B \geq 2.0$ için taşıma gücündeki artış K_0 katsayısının artışı ile yaklaşık doğrusal olarak değişmekte ve tabakalanma etkisi $H/B > 3.0$ için kalkmaktadır.



Çizim 14 - Farklı K_0 değerleri için elde edilen nihai taşıma kapasitesi değerlerinin karşılaştırılması

Kil tabakası yüzeyindeki oturmaların toplam oturmaya oranı değişen H/B oranlarında farklı K_0 katsayısı değerleri için Çizim 7' de gösterilmiştir. $H/B \geq 1.0$ için K_0 katsayısındaki artış ile birlikte kil tabakası yüzeyinde gözlenen oturma miktarlarında artışlar oluşmuştur. K_0 katsayısındaki artış ile kum bloğun yatay yöndeki yerdeğiştirmeleri sınırlanmakta ve düşey yüzeylerinde daha büyük pasif direnç etkileri oluşmaktadır. Bu şekilde daha rijit hale gelen kum bloğun yatay yöndeki deplasmanları azalırken taşıma kapasitesi ve kil tabakasındaki zımbalama etkisi de artmaktadır.



Çizim 15 - Farklı K_0 değerleri için elde edilen nihai taşıma kapasitesi değerlerinin karşılaştırılması

Temel altında, deplasmanların yatay doğrultudaki dağılımları incelendiğinde, $H/B < 1.0$ için, K_0 ' in artması yatay doğrultudaki deplasman hareketlerini önemli derecede etkilememiş ve temel merkezinden itibaren $1.7B-2.0B$ mesafelerde deplasman hareketleri gözlenmiştir. $H/B \geq 1.0$ ve homojen kum zemin durumlarında ise deplasman hareketlerinin K_0 değişiminden etkilendiği ve temel merkezinden itibaren $1.2B-1.8B$ mesafelerde deplasman hareketlerinin oluştuğu görülmüştür. $H/B \geq 1.0$ için K_0 katsayısının artması ile birlikte deplasman hareketlerinin yatay yöndeki etki mesafesi azalmaktadır.

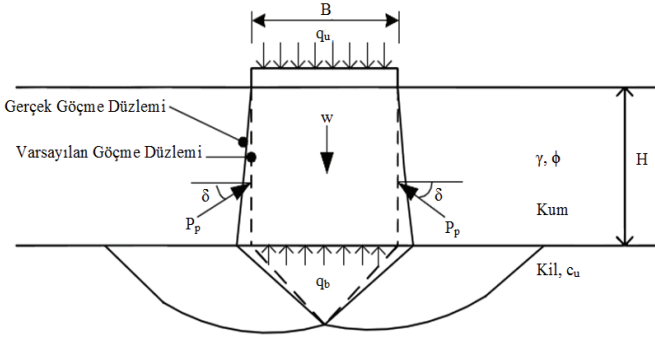
Çizelge 7 - Farklı K_0 değerleri için elde edilen s_i/S (%) değerleri

B = 3.00 m - $c_u = 10$ kN/m ²			
H/B	$K_0=0.40$	$K_0=0.70$	$K_0=1.00$
	s_i / S (%)	s_i / S (%)	s_i / S (%)
0.25	98.179	98.325	98.632
0.50	96.054	96.428	96.733
0.75	89.906	90.962	91.859
1.00	78.080	80.239	82.365
1.50	48.585	52.770	58.572
2.00	23.436	28.189	31.876
2.50	7.643	11.328	14.140
3.00	0.226	3.519	5.803

4.4. Limit Denge Yöntemine Dayalı Yarı-Deneysel Yöntemlerle Karşılaştırma

Tabakalı zeminlerde taşıma gücü probleminin çözümü için pratikte en yaygın kullanılan taşıma gücü teorisi olan zımbalama kesme yöntemi, limit denge yöntemine dayalı yarı-deneysel bir yaklaşımdır. Çizim 16’ da gösterildiği gibi zımbalama kesme yönteminde [5-7] H/B oranının rölatif olarak küçük değerleri için üstte yer alan sağlam tabakada bir zımbalama kayma göçmesi ve devamında da alttaki zayıf tabakada bir genel kayma göçmesi oluşacağı kabul edilir. Kum bloğun düşey kenarları boyunca oluşan kayma direnci, altta yer alan mevcut zayıf tabakadan dolayı, kabul edilen göçme düzlemlerinde mobilize içsel sürtünme açısındaki azalmayı da temsil eden zımbalama kesme katsayısı, K_s kullanılarak göz önüne alınmaktadır. K_s katsayısı, q_2/q_1 ’ in bir fonksiyonu olup q_2/q_1 ve ϕ_1 ’ e bağlı olarak tanımlanır. q_1 ve q_2 , sırası ile, homojen sağlam zemin ve homojen zayıf zeminin yüzeyine oturan B genişliğindeki bir temelin nihai taşıma gücü değeri iken ϕ_1 üstte yer alan kum tabakasının içsel sürtünme açısıdır. Kum tabakası kalınlığı H’ ın temel genişliği B’ den büyük olması durumunda göçme yüzeyi tamamı ile üstte yer alan sağlam tabaka içerisinde oluşacaktır. Bu durum aynı zamanda tabakalı durumdaki nihai taşıma kapasitesi için bir üst sınırdır.

Hanna ve Meyerhof [6], suya doymuş zayıf kil ($\phi_2=0$) tabakası üzerindeki sağlam kum zemine oturan dikdörtgen temellerin nihai taşıma kapasitesi için aşağıdaki eşitlikleri önermişlerdir. q_u ve q_t değerleri karşılaştırılarak küçük olan değer nihai taşıma kapasitesi olarak seçilir. q_u , tabakalı durumdaki nihai taşıma gücü değerini ifade ederken q_t , üstte yer alan tabakanın nihai taşıma kapasitesidir.



Çizim 16 - Zımbalama Kesme Yöntemi [5,13]

$$q_u = 5.14c_2 \left[1 + 0.2 \left(\frac{B}{L} \right) \right] + \left(1 + \frac{B}{L} \right) \gamma_1 H^2 \left(1 + \frac{2D_f}{H} \right) \left(\frac{K_s \tan \phi_1}{B} \right) \lambda_s + \gamma_1 D_f \leq q_t \quad (3)$$

$$q_t = \gamma_1 D_f N_{q(1)} \left[1 + 0.1 \left(\frac{B}{L} \right) \tan^2 \left(45 + \frac{\phi_1}{2} \right) \right] + \frac{1}{2} \gamma_1 B N_{\gamma(1)} \left[1 + 0.1 \left(\frac{B}{L} \right) \tan^2 \left(45 + \frac{\phi_1}{2} \right) \right] \quad (4)$$

Hanna ve Meyerhof [6] yapmış oldukları deneysel çalışmalara göre kare ya da dairesel temeller için λ_s şekil katsayısının değerinin 1.1 ile 1.27 aralığında değiştiğini ve muhafazakar bir tasarım için 1.0’ e eşit alınabileceğini belirtmişlerdir. Burd and Frydman [8], Hanna ve Meyerhof [6] tarafından geliştirilen grafik yöntemin, sadece, Hanna ve Meyerhof [6]

tarafından kullanılan zemin özellikleri, geometrik seçimler ve deneysel koşullara ait değer aralıkları için uygun olduğunu belirtmiştir.

Farklı H/B oranları ve farklı c_u değerlerine sahip tabakalı zemin profilleri için plaxis analizlerinden elde edilen nihai taşıma gücü değerleri, (3) no lu eşitlikte kullanılarak göz önüne alınan her bir durum için K_s katsayısı geri hesaplama yolu ile elde edilmiştir. Geri hesaplama işlemleri λ_s şekil katsayısının hem 1.1 hemde 1.27 değeri kullanılarak yapılmıştır. Yapılan hesaplamalar sonucunda $\lambda_s=1.27$ için elde edilen değerlerin plaxis 3D sonuçlarına daha yakın olduğu görülmüş olup elde edilen sonuçlar Çizelge 8' de verilmiştir. Zımbalama kesme yönteminde üstte yer alan tabaka kalınlığı H' in temel genişliği B' den büyük olması durumunda göçme yüzeyinin tamamı ile üstte yer alan sağlam tabaka içerisinde oluşacağı kabul edildiğinden dolayı nihai taşıma gücü değerleri arasındaki karşılaştırma H/B \leq 1.0 için yapılmıştır.

Çizelge 8 - B=3.0 m genişlikteki kare temel için Zımbalama Kesme Yöntemi (ZKY) ve Plaxis 3D' den elde edilen taşıma gücü ve K_s değerlerinin karşılaştırılması

c_u (kPa)	H/B	q_u -Plaxis 3D (kN/m ²)	q_u -ZKY (kN/m ²)	K_s -Plaxis 3D	K_s - ZKY
10	0.25	116.738	94.153	3.685	1.923
	0.50	166.559	139.926	2.650	
	0.75	225.747	206.827	2.188	
	1.00	291.779	294.854	1.897	
20	0.25	194.000	160.767	4.901	2.308
	0.50	265.765	215.705	3.675	
	0.75	337.534	296.000	2.890	
	1.00	412.408	401.650	2.400	
40	0.25	326.000	290.779	5.575	2.827
	0.50	429.750	358.071	4.784	
	0.75	523.500	456.422	3.765	
	1.00	602.000	585.830	2.965	
60	0.25	449.847	426.956	5.613	3.827
	0.50	565.071	518.052	5.111	
	0.75	678.342	651.192	4.207	
	1.00	755.000	826.376	3.218	

Zımbalama kesme yönteminde K_s katsayısı, q_2/q_1 ve ϕ_1 ' e bağlı olarak tanımlanmakta, H/B oranı ve λ_s katsayısından bağımsız olarak, sadece, kil tabakasının drenajsız kayma mukavemeti ve temel boyutu ile değişmektedir. Plaxis analiz sonuçları kullanılarak yapılan geri hesaplamalar sonucu elde edilen K_s katsayısı değerlerinin H/B oranına bağlı olarak da

değişiklik sergilediği ve bu değişimin doğrusal olmadığı görülmüştür. $H/B=0.25$ için en büyük değerine sahip olan K_s katsayısı H/B oranının artması ile birlikte azalmakta ve $H/B=1.0$ için zımbalama kesme yönteminden elde edilen K_s değeri ile uyumlu hale gelmektedir. Kil tabakasının drenajsız kayma mukavemetinin artması K_s katsayısının artmasına neden olmaktadır. c_u ve H/B oranının artması hem kum zeminin mobilize içsel sürtünme açısının artmasına hem de kum bloğun düşey yüzeyleri boyunca elde edilen pasif direnç etkisinin büyümesine neden olduğundan nihai taşıma gücü de artmaktadır.

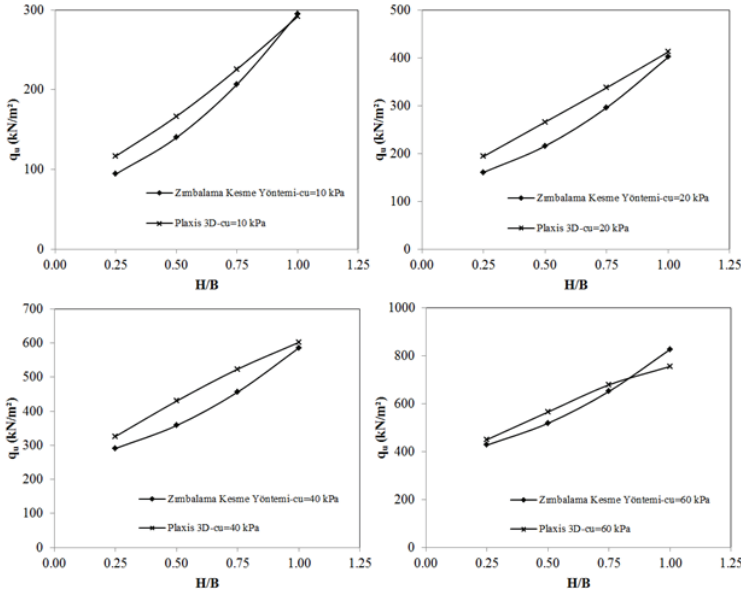
Çizelge 9 - Farklı boyutlardaki kare temeller için $c_u = 10 \text{ kN/m}^2$ durumunda Zımbalama Kesme Yöntemi (ZKY) ve Plaxis 3D' den elde edilen taşıma gücü ve K_s değerlerinin karşılaştırılması

B (m)	H/B	q_u -Plaxis 3D (kN/m^2)	q_u -ZKY (kN/m^2)	K_s -Plaxis 3D	K_s - ZKY
3.0	0.25	116.738	94.153	3.685	1.923
	0.50	166.559	139.926	2.650	
	0.75	225.747	206.827	2.188	
	1.00	291.779	294.854	1.897	
2.0	0.25	127.000	92.741	5.233	2.115
	0.50	160.111	131.467	3.093	
	0.75	210.876	185.684	2.574	
	1.00	263.196	255.391	2.204	
1.0	0.25	150.951	94.151	8.896	2.692
	0.50	169.880	128.655	4.568	
	0.75	208.000	173.017	3.602	
	1.00	256.000	227.237	3.183	

Çizelge 9' da verilen taşıma gücü değerleri incelendiğinde, temel boyutunun artması ile birlikte zımbalama kesme yöntemi ve plaxis 3D' den elde edilen q_u değerleri arasındaki farkın azaldığı görülmektedir. $H/B=1.0$ için, $B=1.0$ m genişlikteki kare temel hariç, q_u değerleri arasındaki fark oldukça az iken $B=1.0$ m genişlikteki kare temelde fark yaklaşık %12 dir. Temel boyutundan bağımsız olarak K_s katsayısı değerleri H/B oranı ile ters orantılı bir değişim sergilemektedir. $H/B=1.0$ için her iki yaklaşımla elde edilen K_s değerlerinin birbiri ile uyumlu olduğu gözlenmiştir. Zımbalama kesme yöntemi, göz önüne alınan her bir kombinasyon için muhafazakar tarafta kalan taşıma gücü değerleri üretmiştir.

Limit denge yaklaşımına dayalı zımbalama kesme yönteminde K_s katsayısı, kil tabakasının drenajsız kayma mukavemeti, kumun içsel sürtünme açısı ve temel boyutuna bağlı olup deformasyon oluşumundan, tabakaların rölatif mukavemetlerinden ve geometrik koşulların geçme mekanizmasına olan etkisinden bağımsızdır. Plaxis analiz sonuçları kullanılarak yapılan geri hesaplamalar sonucu elde edilen K_s katsayısı değerleri ise üstteki kum tabakası

kalınlığı, kumun sıklığı, kilin kayma mukavemeti, yer altı su seviyesi, yükleme koşulları, seçilen malzeme modelleri, sonlu elemanlar ağı vb. faktörlerin etkisi altındadır. Bununla birlikte; zımbalama kesme yönteminde çözüm, kabul edilen basitleştirilmiş bir göçme mekanizmasına göre gerçekleştirilirken plaxis analizlerinde belirli bir göçme mekanizması bulunmamaktadır. Plaxis analizlerden elde edilen taşıma gücü değerleri tabakaların farklı deformasyon karakterlerinden, rölatif mukavemetlerinden ve problemin geometrik koşullarından etkilenmektedir. Bu durum plaxis ve zımbalama kesme yönteminden elde edilen K_s değerlerinin birbirinden farklı olmasını açıklamaktadır.

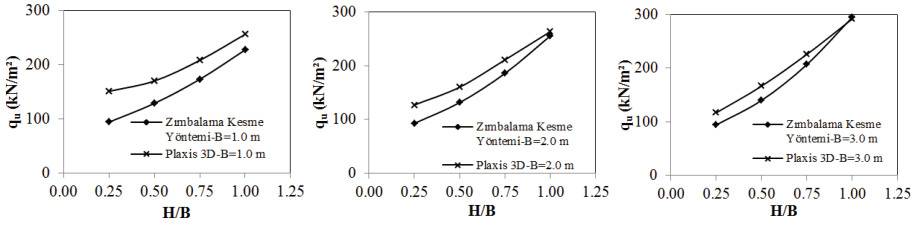


Çizim 17 - B=3.0 m genişlikteki kare temel için q_u değerlerinin karşılaştırılması

Çizim 17' de B=3.0 m genişliğindeki kare temelde H/B=0.25, 0.50, 0.75 ve 1.00 oranlarında farklı c_u değerleri için zımbalama kesme yöntemi kullanılarak elde edilen q_u değerlerinin plaxis analizlerinden elde edilen q_u değerleri ile karşılaştırması gösterilmektedir. Göz önüne alınan her bir c_u değeri için H/B=0.25, 0.50 ve 0.75 durumlarında q_u değerleri arasındaki fark %10-20 aralığında iken H/B=1.00 için her iki yöntemden elde edilen sonuçların birbirine oldukça yakın olduğu görülmektedir. $c_u=60$ kPa için bütün H/B oranlarında elde edilen hata değerleri %10' dan küçüktür.

Çizim 18' ten görüldüğü gibi temel boyutu ve H/B oranındaki artış sonucu, elde edilen q_u değerleri arasındaki fark azalmaktadır. B=3.0 m genişlikteki kare temelde H/B=0.25 için q_u değerleri arasındaki fark %24 iken H/B=0.50 ve 0.75 için, sırası ile, %19 ve %9 dur. B=2.0 m genişlikteki kare temelde q_u değerleri arasındaki fark H/B=0.25, 0.50 ve 0.75 için, sırası ile, %37, %22 ve %14 olarak elde edilmiştir. B=1.0 m genişlikteki kare temelde ise q_u değerleri arasındaki fark, sırası ile, %60, %32 ve %20 dir. Temel boyutundan bağımsız

olarak, H/B oranı ile q_u arasındaki değişim her iki yöntem için de benzer davranışı sergilemektedir.



Çizim 18 - Farklı boyutlardaki kare temeller için $c_u = 10$ kN/m² durumunda Zımbalama Kesme Yöntemi ve Plaxis 3D' den elde edilen taşıma gücü değerlerinin karşılaştırılması

5. SONUÇLAR

Bu çalışmada; temel boyutunun, kum zeminin başlangıç gerilme durumu ve gerilme geçmişinin, üstte yer alan kum tabakası kalınlığı ve altta yer alan kil tabakasının drenajsız kayma mukavemetinin tabakalı zeminlerdeki kare temellerin taşıma kapasitesi ve oturma davranışları üzerindeki etkilerini araştırmak için bir seri üç boyutlu sonlu elemanlar analizi gerçekleştirilmiştir. Sonlu eleman analizleri sonucu bulunan taşıma gücü değerleri zımbalama kesme yöntemi ile hesaplanan taşıma gücü değerleri ile karşılaştırılmış ve bunun yanı sıra K_s katsayısı değerlerinin H/B oranına ve λ_s ' e bağlı değişimi araştırılmıştır. Çalışma sonucunda elde edilen başlıca sonuçlar aşağıda özetlenmiştir.

Limit denge yöntemine dayalı teorik taşıma gücü yöntemlerinde yapılan kabulün aksine tabakalı durumun hem alttaki kil tabakasının drenajsız kayma mukavemeti hem de üstte yer alan kum tabakasının kalınlığına bağlı olarak H/B>1.0 durumunda da geçerli olduğu görülmektedir. Kil tabakasının drenajsız kayma mukavemetindeki artış taşıma gücü değerini artırırken c_u ' nun artması ile birlikte daha küçük üst tabaka kalınlıklarında homojen kum zemin durumundaki taşıma gücüne ulaşılmaktadır.

Yük-oturma eğrisi, üstte yer alan kum tabakası kalınlığının artması ile daha küçük $c_u/\gamma B$ değerlerinde doğrusal elastik davranışa yakınsamıştır.

B=3.0 m genişlikteki kare temelde $c_u=10$ kPa için Durum 1 ve Durum 2 koşullarında yapılan analizlerin sonuçları karşılaştırıldığında, aynı tabakalı zemin koşullarında temele uygulanan yük artırıldığında oturma ve taşıma gücündeki artış oranlarının birbirinden bağımsız gerçekleştiği görülmüştür. Oturma değerinde daha büyük oranda artış oluşurken, taşıma gücünde aynı oranda artışlar görülmemektedir. H/B=0.50 için Durum 2' de oturma değeri %100 artmış olmasına karşın taşıma gücü değerindeki artış Durum 1' e göre %16 olmuştur. H/B=1.0 için Durum 2' de $s/B=0.14$ değerinde zeminde göçme meydana gelmiştir. Göçmeye neden olan boyutsuz taşıma gücü değeri $q/\gamma B=6.889$ dir. Durum 1' e göre oturma değerinde meydana gelen %40' lık artışa karşılık taşıma gücü değerinde %11 oranında artış oluşmuştur. H/B=2.50 için Durum 2' de oturma değerindeki %100' lük artışa karşılık taşıma gücü değerinde Durum 1' e göre %58 oranında artış meydana gelmiştir.

K_0 katsayısının değerinin artması ile taşıma gücünün arttığı görülmektedir. $H/B \geq 1.0$ için K_0 katsayısının artması ile birlikte deplasman hareketlerinin yatay yöndeki etki mesafesi de azalmaktadır.

Zayıf kil tabakası bulunan problemlili zemin koşullarında üstte oluşturulacak kontrollü bir dolgu tabakası ile zemin iyileştirilmek istendiğinde, dolgu tabakasının kalınlığı $B > 1.0$ m genişlikteki temeller için H/B oranı minimum 0.50 olacak şekilde seçilmelidir. $B = 1.0$ m olduğu durumda bu oran minimum 0.75 olmalıdır.

K_s katsayısı değerlerinin H/B oranına bağlı olarak da değişiklik sergilediği ve bu değişimin doğrusal olmadığı görülmüştür. Temel boyutundan bağımsız olarak K_s katsayısı değerleri H/B oranı ile ters orantılı bir değişim sergilemektedir.

Tabakalı zemin davranışı, artan temel boyutu ile birlikte daha küçük H/B oranlarında kaybolmuştur.

Her bir temel boyutu için taşıma gücündeki en büyük artış miktarı H/B ' nin 1.00 ile 1.50 değerleri arasında elde edilmiştir. $H/B \geq 1.50$ için tabakalanma etkisinin görülmediği H/B oranına kadar taşıma kapasitesindeki artış oranları azalmaktadır.

Kaynaklar

- [1] Terzaghi, K., Theoretical Soil Mechanics, New York. Wiley, 1943.
- [2] Meyerhof, G.G., The Ultimate Bearing Capacity of Foundations. Geotechnique, 2, 301-332, 1951.
- [3] Hansen, J. B., A Revised and Extended Formula for Bearing Capacity. Bulletin No.28, Danish Geotechnical Institute, Copenhagen, pp. 5-11, 1970.
- [4] Vesic, A. S., Analysis of Ultimate Loads of Shallow Foundations. Journal of the Soil Mechanics and Foundations Division, ASCE, 99(SM1), 45-73, 1973.
- [5] Meyerhof, G.G., Ultimate Bearing Capacity of Footings on Sand Overlying Clay. Canadian Geotechnical Journal, 11 (2), 223-229, 1974.
- [6] Hanna, A.M., Meyerhof, G.G., Design Charts for Ultimate Bearing Capacity of Foundations on Sand Overlying Soft Clay. Canadian Geotechnical Journal, 17, 300-303, 1980.
- [7] Hanna, A.M., Foundations on Strong Sand Overlying Weak Sand. J. Geotech. Eng. Div., 107(7), 915-927, 1981.
- [8] Burd, H.J., Frydman, S., Bearing Capacity of Plane-Strain Footings on Layered Soils. Canadian Geotechnical Journal, 34, 241-253, 1997.
- [9] Uncuoğlu, E., The Bearing Capacity of Square Footings on A Sand Layer Overlying Clay. Geomechanics and Engineering, 9(3), 287-311, 2015.
- [10] Mosallanezhad, M., Moayedi, H., Comparison Analysis of Bearing Capacity Approaches for the Strip Footing on Layered Soils. Arabian Journal for Science and Engineering, 42, 3711-3722, 2017.

- [11] Tang, C., Phoon, K.K., Zhang, L., Li, D.Q., Model Uncertainty for Predicting the Bearing Capacity of Sand Overlying Clay. *International Journal of Geomechanics*, 17 (7), 2017, 04017015.
- [12] Eshkevari, S.S., Bearing Capacity of Surface Strip Footings on Layered Soils, Ph.D. Dissertation. The University of Newcastle, Australia, 2018.
- [13] Eshkevari, S.S., Abbo, A.J., Kouretzis, G., Bearing Capacity of Strip Footings on Sand Over Clay. *Canadian Geotechnical Journal*, 56, 699-709, 2019.
- [14] Zheng, G., Wang, E., Zhao, J., Zhou, H., Nie, D., Ultimate Bearing Capacity of Vertically Loaded Strip Footings on Sand Overlying Clay. *Computers and Geotechnics*, 115, 2019, 103151.
- [15] Zheng, G., Zhao, J., Zhou, H., Zhang, T., Ultimate Bearing Capacity of Strip Footings on Sand Overlying Clay under Inclined Loading. *Computers and Geotechnics*, 106, 266-273, 2019.
- [16] Pham, Q.N., Ohtsuka, S., Ultimate Bearing Capacity of Rigid Footing on Two Layered Soils of Sand-Clay. *International Journal of Geomechanics*, 21(7), 2021, 04021115.
- [17] Briaud, J.L., Gibbens, R., Large-Scale Load Tests and Data Base of Spread footings on Sand. Publication No. FHWA-Rd-97-068, November, 1997.
- [18] Briaud, J.L., Jeanjean, P., Load Settlement Curve Method for Spread Footings on Sand. *Journal of Geotechnical and Geoenvironmental Engineering*, 133(8), 905-920, 1994.
- [19] Amar, S., Baguelin, F., Canepa, Y., Frank, R., Experimental Study of the Settlement of Shallow Foundations. *Geotechnical Special Publication*, ASCE, 40(2), 1602-1610, 1994.
- [20] Lavasan, A.A., Ghazavi, M., Behavior of Closely Spaced Square and Circular Footings on Reinforced Sand. *Soils and Foundations*, 52(1), 160-167, 2012.
- [21] Cerato, A.B., Scale Effect of Shallow Foundation Bearing Capacity on Granular Material, Ph.D. Dissertation. University of Massachusetts Amherst, MA, USA, 2005.
- [22] Cerato, A.B., Lutenegeger, A.J., Scale Effect of Shallow Foundation Bearing Capacity on Granular Material. *Journal of Geotechnical and Geoenvironmental Engineering*, 133(10), 1192-1202, 2007.
- [23] Lutenegeger, A.J., Adams, M.T., Bearing Capacity of Footings on Compacted Sand, *International Conference on Case Histories in Geotechnical Engineering*. 36, 1216-1224, 1998. <https://scholarsmine.mst.edu/icchge/4icchge/4icchge-session01/36>.
- [24] Michalowski, R.L., Shi, L., Bearing Capacity of Footings Over Two-Layer Foundation Soils. *Journal of Geotechnical Engineering*, 121 (5), 421-428, 1995.
- [25] Merifield, R.S., Sloan, S.W., Yu, H.S., Rigorous Plasticity Solutions for the Bearing Capacity of Two-Layered Clays. *Geotechnique*, 49(4), 471-490, 1999.
- [26] Shiau, J.S., Lyamin, A.V., Sloan, S.W., Bearing Capacity of A Sand Layer on Clay by Finite Element Limit Analysis. *Canadian Geotechnical Journal*, 40, 900-915, 2003.

- [27] Plaxis 3D (2012), Delft, Netherlands.
- [28] Lo Presti, D. C. F., Jamiolkowski, M., Pallara, O., Pisciotto, V., Ture, S., Stress Dependence of Sand Stiffness, International Conferences on Recent Advances in Geotechnical Earthquake Engineering and Soil Dynamics, 1995, 71-76. <https://scholarsmine.mst.edu/icrageesd/03icrageesd/session01/16>.
- [29] Maeda, K., Miura, K., Confining Stress Dependency of Mechanical Properties of Sands. *Soils and Foundations*, 39, 1999, 53-67.
- [30] Tjje-Liong, G., Common Mistakes on the Application of Plaxis 2D in Analyzing Excavation Problems. *International Journal of Applied Engineering Research*, 9, 2014, 8291-8311.
- [31] Babagiray, G., Akbaş, S.O., Sığ Rijit Tabaka Üzerinde Yer Alan Kohezyonsuz Zeminlerdeki Yüzeysel Temellerin Taşıma Gücü Hakkında Sayısal Modelleleme Esaslı Parametrik Bir Çalışma. *İMO Teknik Dergi*, 494, 2018, 8185-8198.
- [32] The Hardening Soil Model-A Practical Guidebook, Z Soil. PC 100701 report, revised 21.10.2018.
- [33] Bolton, M.D., The Strength and Dilatancy of Sands. *Geotechnique*, 36(1), 65-78, 1986.
- [34] Poulos, H.G., Small, J.C., "Development of design charts for concrete pavements and industrial ground slabs" Chapter 2, *Design Applications of Raft Foundations*, Hemsley. Ed. J.A., Thomas Telford, 39-70, 2000.
- [35] Dustin, R., Initial Elastic Modulus Degradation Using Pressuremeter and Standard Penetration Test Results at Two Sites, Master of Science Theses. University of Nevada Las Vegas, 2013.
- [36] Briaud, J.L., *Geotechnical Engineering: Unsaturated and Saturated Soils*, New Jersey. John Wiley & Sons, Inc. Hoboken, 2013.
- [37] Bowles, J. E. *Foundation analysis and design* (5th ed.), New York. The McGraw-Hill Companies, Inc., 1997.
- [38] Coduto, D., Yeung, M.C., Kitch, W., *Geotechnical Engineering: Principles&Practices*, New Jersey. Pearson Prentice Hall, 2011.
- [39] Lee, J., Salgado, R., Estimation of Bearing Capacity of Circular Footings on Sands Based on Cone Penetration Test. *Journal of Geotechnical and Geoenvironmental Engineering*, 131(4), 442-452, 2005.
- [40] Nguyen, D.L., Ohtsuka, S., Hoshina, T., Isobe, K., Discussion on Size Effect of Footing in Ultimate Bearing Capacity of Sandy Soil Using Rigid Plastic Finite Element Method. *Soils and Foundations*, 56(1), 93-103, 2016.
- [41] Ueno, K., Miura, K., Maeda, Y., Prediction of Ultimate Bearing Capacity of Surface Footings with Regard to Size Effects. *Soils and Foundations*, 38(3): 165-178, 1998.
- [42] Lee, J., Salgado, R., Kim, S., Bearing Capacity of Circular Footings under Surcharge Using State-Dependent Finite Element Analysis. *Computers and Geotechnics*, 32, 445-457, 2005.

- [43] Chen, J., Dong, Y., Whittle, A.J., Prediction and Evaluation of Size Effects for Surface Foundations on Sand. *Journal of Geotechnical and Geoenvironmental Engineering*, 146(5), 2020, 04020022.
- [44] Jozsa, V., Estimation and Separation of Preconsolidation Stress Using Triaxial and Oedometer Test in Kiscelli Clay. *Periodica Polytechnica Civil Engineering*, 60(2), 297-304, 2016.
- [45] Zelger, J., Calibration of 2D Pre-Relaxation Factors in Tunnelling with 3D Finite Element Calculations, MSc. Thesis. Graz University of Technology, 2012.
- [46] Melnikov, R., Zazulya, J., Stepanov, M., Ashikkmin, O., Maltseva, T., OCR and POP Parameters in Plaxis-Based Numerical Analysis of Loaded Over Consolidated Soils. *Procedia Engineering*, 165, 845-852, 2016.
- [47] Massarsch, K. R., Westerberg, E., Broms, B.B., Footings Supported on Settlement-Reducing Vibrated Soil Nails, *Proceedings of the Fourteenth International Conference on Soil Mechanics and Foundation Engineering*, Hamburg/6-12 September 1997, 1533-1539.
- [48] Holtz, D.R., Kovacs, D.W., *An Introduction to Geotechnical Engineering*, New Jersey. Prentice-Hall, Inc. Englewood Cliffs, 1981.
- [49] Cetin, H., An Experimental Study of Soil Memory and Preconsolidation Adjacent to An Active Tectonic Structure: The Meers Fault, Oklahoma, USA. *Engineering Geology*, 57, 169-178, 2000.

TECHNICAL NOTE

Farklı Oturmalar Nedeniyle Eğik Konuma Gelmiş Binanın Jet-Grout Yöntemiyle Doğrultulup Desteklenmesi

Sadık KÖSEOĞLU¹



ÖZ

Antalya-Konyaaltı ilçesindeki 7 katlı bir bina, çok farklı kalınlıktaki zayıf zemin tabakalarının farklı oturmaları nedeniyle, kaba inşaatın tamamlanmasından sonra radye temelin açılma eğikliği $\tan \alpha = 1/107$ değerine ulaşmış ve ilgili Belediye tarafından inşaat durdurulmuştur.

Söz konusu bina ile ilgili “İMO Antalya Şubesi Bilirkişi”sinin, sonradan yapılan zemin incelemesine ve bina üzerinde yaptıkları incelemelere dayanılarak düzenledikleri raporda, binanın doğrultulup desteklenerek kazanılabileceği önerisinde bulunulmuştur.

Bina, yazarın danışmanlığı altında BST Mühendislik Firması tarafından Jet Grout yöntemi kullanılarak özel bir teknikle doğrultulup desteklendikten sonra, YTÜ-Geoteknik Dalı Yetkilileri tarafından yapılan yükleme deneyleriyle, doğrultmanın ve desteklemenin başarılı ve güvenli olduğunu kanıtlamışlardır. Binanın oturma ve deformasyonları belirli bir süre izlenmiş ve oturmaların durduğu anlaşıldıktan sonra, binaya iskan raporu verilmiştir.

Anahtar Kelimeler: Jet grout yöntemi, bina doğrultulması, bina desteklenmesi, eğik binanın doğrultulması.

ABSTRACT

An Application of the Jet-Grout Rectification Technique for a Tilted Building

For a 7-storey residential building in the Konyaaltı county of Antalya province, as a result of the differing settlements of weak soil layers of different thicknesses, it was found at the completion stage of the main structural framework that the angle of tilt of the mat foundation had reached a value given by $\tan \alpha = 1 / 107$, as a result of which the construction was halted by the Municipality.

Not: Bu yazı

- Yayın Kurulu'na 23 Mart 2023 günü ulaşmıştır. 13 Ekim 2023 günü yayımlanmak üzere kabul edilmiştir.
- 31 Mayıs 2024 gününe kadar tartışmaya açıktır.

• <https://doi.org/10.18400/tjce.1269866>

1 BST Mühendislik Proje İnşaat Taahhüt Yatçılık Tic. Ltd. Şti., Antalya, Türkiye
koseoglusaa@gmail.com - <https://orcid.org/0009-0009-0606-3866>

A Technical Report based on soil investigations and structural evaluations by an Expert Witness from the Antalya Chamber of Civil Engineers suggested that rectifying the tilt and supporting the building might be feasible.

The building was strengthened and rectified using a special application of the Jet Grout technique by the BST Engineering Firm, with the author as Project Consultant. Loading tests were conducted by the Geotechnical Division of Yıldız Technical University, and the safety of the building after completion of the procedure was established. After a period of observations wherein no foundation movements were found, the Municipality issued its Certificate of Occupancy for the building.

Keywords: Jet grout technique, straightening of buildings, stiffening of buildings, rectification of tilted building.

1. GİRİŞ

Antalya - Konyaaltı ilçesindeki 7 katlı bir binanın temeli altındaki oturma farklarından dolayı binada oluşan eğiklik, inşaat süresince artarak gözü rahatsız eder duruma gelmiştir. İnşaat ruhsatı vermeye yetkili kurum (Konyaaltı Belediyesi İmar Müdürlüğü), bu durumu gerekçe göstererek inşaatı durdurmuş ve İMO Antalya Şubesine başvurarak, binanın oluşturulacak bir bilirkişi heyeti tarafından incelenerek, sonucun bir raporla kendilerine bildirilmesini istemiştir. Bilirkişi heyeti adına “Temel İnşaatı Uzmanı Yazar” tarafından düzenlenen rapor heyet tarafından onaylanarak yetkili kuruma sunulmuştur.

2. MAKALENİN AMACI

Makale, farklı kalınlıkta zayıf zemin tabakaları üzerine oturan binaların inşaatı sırasında veya daha sonrasında, ortaya çıkan farklı oturmalarından kaynaklanan eğikliğin giderilmesi veya izin verilen eğiklik sınırının altına çekilmesi için, bina doğrultulması konusunda yeni bir yöntem olan “Jet Grout Yöntemi” nin kullanılmasını öngören bir uygulamayı ayrıntılı bir biçimde açıklamayı amaçlamaktadır. Buna benzer koşullara sahip eğik binaların doğrultulması ve desteklenmesi için yol gösterici bir özelliğe sahip olan bu uygulamanın, pratikte çalışan İnşaat Mühendisleri ve Temel İnşaatı firmaları için iyi bir rehber olacağı kanısındayım.

3. BİNA VE TEMEL ZEMİNİNE İLİŞKİN SAPTAMALAR

İşin başında zemin incelemesi yapılmadan inşaat ruhsatı verilen ve inşaat başlanan bu bina için, kaba inşaatın tamamlanma aşamasında gözle fark edilir duruma gelen eğiklikten dolayı, işin Fenni Mesulü’ nün isteğiyle sonradan bina temeli dışında zemin incelemesi yapılmıştır.

Bina ile ilgili statik ve betonarme projeler ve sonradan yapılan zemin incelemesi temel alınarak, İMO Antalya Şubesi Bilirkişi Heyeti tarafından bina üzerinde yapılan inceleme ve ölçümler sonucunda özetle aşağıdaki bulgular saptanmıştır:

- 1) Kaba inşaatı tamamlanan bina, bodrum, zemin, 4 normal ve çatı katı olmak üzere 7 kattan oluşmaktadır (bkz. Şekil 1),



Köşe Adı	Köşe Yönü	Zayıf Tabaka Kalınlığı	Göreceli Oturma
A	GB	5,5 m	18 cm
B	GD	3,5 m	0
C	KB	11,5 m	24 cm
D	KD	5,5 m	18 cm

Köşe yönlerinde; G : Güney, B : Batı, D : Doğu, K : Kuzey yönü tanımlar.

Şekil 1 - Antalya-Konyaaltı ilçesinde kaba inşaatı tamamlanma aşamasında olan 7 katlı konut binasının genel görünüşü (Fotoğrafta binanın en az oturma oluşan tarafı sağ ön köşesi (B köşesi) ve en çok oturma oluşan tarafı sol arka köşesi (C köşesi) olarak belirlenmiştir).

- 2) Binanın betonarme karkas inşaatı tamamlanmış, duvarlar örülmüş, iç ve dış sıvaları tamamlanmış, kapı ve pencere kör kasaları takılmış ve döşeme kaplamaları büyük ölçüde tamamlanmıştır. Binanın, temel tabanına etkileyen üniform taban basıncı, bir bina katının yükü (Tesviye betonu kalınlıklarının imal edildikleri andaki eğiklikten dolayı gereğinden fazla yapıldığı dikkate alınarak) $13,0 \text{ kN/m}^2$ alınmıştır. Buna göre kirişli radye temel yükünün bir normal katın yüküne ve çatı katı yükünün yaklaşık normal kat yükünün yarısına eşit olduğu varsayılırsa, aşağıdaki gibi hesaplanabilir :

$$\sigma_0 = 13,0 \times (7,5) = 97,5 \text{ kN/m}^2 \quad (1)$$

Görüldüğü gibi bu taban basıncı, kaya (traverten) tabakası üzerindeki çok zayıf zemin tabakaları üzerine etkimektedir ve zemin emniyet gerilmesinin çok üzerindedir.

- 3) Binanın zemin kat döşemesi üzerinde kot okumaları yapılmış ve en az oturma yapan güney-doğu (B) köşesi baz alındığında (Bu köşedeki oturma sıfır kabul edildiğinde), binanın güney-batı (A) ve kuzey-doğu (D) köşelerinin 18 cm ve kuzey-batı (C) köşesinin 24 cm göreceli oturma yaptığı belirlenmiştir (bkz. Şekil 2),
- 4) Oturma farkları, temel tabanında her iki doğrultuda farklı ölçüde olmak üzere, üst yapı ile birlikte rijit bir dönmeye neden olmuştur. Buna göre bina temelinde oluşan en büyük dönme, en az oturma yapan güney-doğu (B) köşesi ile en çok oturma yapan kuzey-batı (C) köşesi arasında oluşmuştur,
- 5) B ve C köşeleri arasındaki maksimum dönme (eğiklik) :

$$\tan \alpha = s_{\max}/l_{BC} = 24/2571 \text{ cm} = 1/107 > 1/300 \quad (2)$$

olarak elde edilmiştir (Burada l_{BC} ; temelin güney-doğu köşesi ile kuzey-batı köşesi arasındaki diyagonal uzaklık olup, $l_{BC} = \sqrt{(21,60^2 + 13,95^2)} = 25,71 \text{ m}$ dir).

Fakat temelin üst yapı ile birlikte 1/107 oranındaki rijit açısız dönmesi sonucu, yapının taşıyıcı sisteminde ve dolgu duvarlarda hiçbir çatlak ve aşırı zorlanma belirtisine rastlanmamıştır. Bununla birlikte Polshin/Tokar (1957) ve Skempton/Mc Donald (1956)' ya göre bacalar silolar gibi çok fazla rijit yapılarda, en büyük eğiklik olarak $\tan \alpha = 0,004 = 1/250$ değerine izin verilmektedir. Söz konusu binanın taşıyıcı sistemi çok rijit olmadığından, izin verilen eğiklik sınırının 1/300 olarak alınması uygun olur. Bu eğiklik sınırının, Bjerrum (1973)' un önerdiği açısız dönmeler için hasar sınırları kriterleri' ne de uygun düştüğünü belirtelim. Buna göre bina temelinde bir doğrultuda işlemi yapılması gerektiği açıktır (bkz. S. Köseoğlu –Temeller II, Bölüm 3, Şekil 3.9).

- 6) Binanın onaylı statik projesinde temel sistemi, kirişli radye olarak düzenlenmiş ve taban güvenlik basıncı $\sigma_{g\ddot{u}v} = 120 \text{ kN/m}^2$ alınmıştır. Kirişli radye, 40 cm plak kalınlığı ve 50/80 cm ile 60/80 cm kesit boyutları olan kirişlerden oluşturulmuştur. Kirişli radye planı ve kirişlerin aks aralıkları Şekil 2 'de gösterilmiştir.
- 7) Binanın Betonarme taşıyıcı sisteminde kullanılan malzemeler C14 (B160) ve S220 (BÇI) olduğu belirlenmiştir. Bu malzemelerin, inşaat ruhsatının onaylandığı tarihte geçerli olan TS 500 (1984) Standardına ve 1975 tarihli "Türkiye Bina Deprem Yönetmeliği"ne uygun olduğu saptanmıştır (Günümüzde geçerli olan "TBDY:2018 - Deprem Yönetmeliği"nde minimum Beton ve Çelik malzeme kaliteleri C25 ve S420C' ye yükseltilmiştir). Ayrıca konut binası betonarme taşıyıcı sisteminin beton kalitesini belgelendirmek amacıyla, İMO Antalya Şubesi beton laboratuvarı tarafından taşıyıcı sistemin değişik bölgelerinden alınan 11 adet 93 mm çaplı karot beton örnekleri üzerinde tek eksenli basınç deneyleri yapılmış ve ortalama beton basınç dayanımı $21,67 \text{ N/mm}^2$ olarak elde edilmiştir. Görüldüğü gibi, beton dayanımı C14 beton sınıfının epeyce üzerinde elde edilmiştir.
- 8) Sonradan yapılan zemin incelemesinde, bina temelinin dışında 5 adet sondaj deliği açılmış üstte bulunan zayıf zemin tabakaları için SPT deneyleri ve alttaki traverten kayası için RQD ve laboratuvarında eksenel basınç dayanımları belirlenmiştir. 15 m

derinliğinde açılmış 5 adet sondaj kuyusundan 4 adedi bina temeli köşelerinin hemen dışında ve 1 adedi CD temel kenarı ortasının hemen dışında açılmıştır (bkz. Şekil 2).

Zemin incelemesi, yazarın Geoteknik Uzmanı olarak devreye girdiği tarihten çok önce yapıldığından, ayrıntılı bir zemin incelemesi ve gerekli zemin parametrelerinin elde edilmesine yönelik zemin deneylerinin yaptırılması mümkün olamamıştır.

Şekil 2’ de, zemin incelemesinde açılan 5 sondaj kuyusundaki değişik zeminlerin tabaka kalınlıkları ve derinlikleri gösterilmiştir. Buna göre üstteki zayıf zemin tabakaları altındaki traverten (orta sertlikte kaya) tabakasının temel tabanından itibaren derinlikleri aşağıdaki gibi belirlenmiştir :

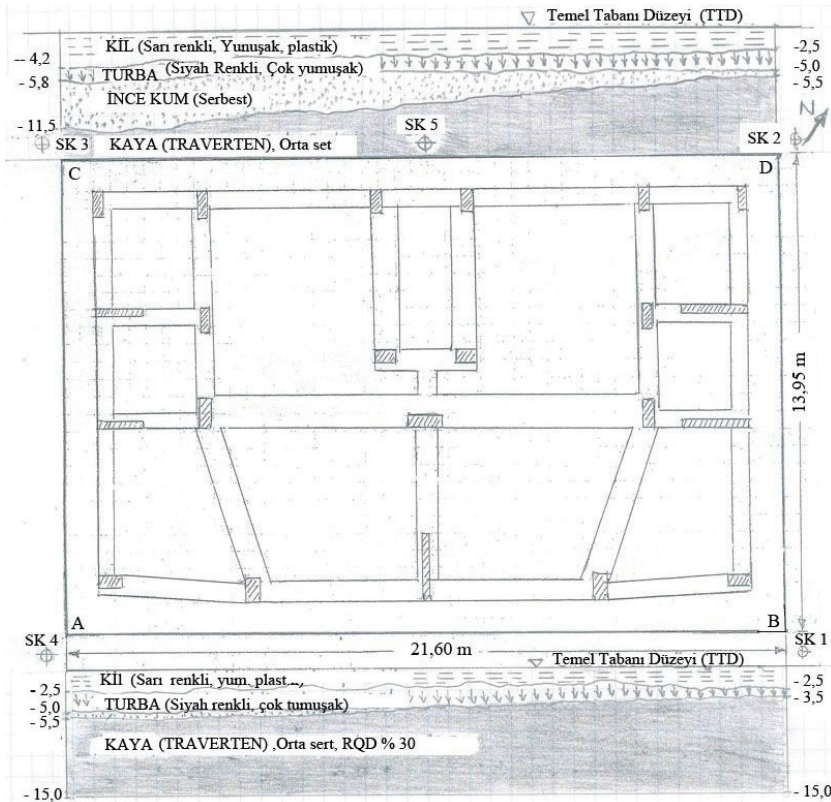
Radye temelin güney-doğu köşesi dolayında (SK1 sondaj kuyusu için) : 3,5 m,

Radye temelin kuzey-doğu köşesi dolayında (SK2 sondaj kuyusu için) : 5,5 m,

Radye temelin kuzey-batı köşesi dolayında (SK3 sondaj kuyusu için) : 11,5 m,

Radye temelin güney-batı köşesi dolayında (SK4 sondaj kuyusu için) : 5,5 m,

Radye temelin arka kenar ortası dolayında (SK5 sondaj kuyusu için) : 5,8m.



Şekil 2 - Oturma farkları nedeniyle eğik konuma gelmiş konut binasının temel planı ve zemin incelemesine ilişkin sondaj yerleri, zemin tabakalarının türleri ve kalınlıkları

Traverten tabakası üzerindeki zayıf zemin tabakasının zemin türleri ve derinlikleri Şekil 2' de gösterilmiştir. Ayrıca zayıf zemin türlerinin her bir sondaj kuyusundaki toplam kalınlığı, yukarıda verilen traverten tabakası derinliklerine eşit olacağı açıktır.

5 Adet sondaj kuyusunda yapılan SPT deneyleri sonucunda, 30 cm giriş için ortalama vuruş sayıları ; Kil için $N_{30} = 3$, Turba için $N_{30} = 1$ ve İnce Kum için $N_{30} = 7$ olarak elde edilmiştir. Bu sonuçlara göre, zayıf zemin tabakalarının hiçbir taşıma yeteneği olmadığı varsayılabilir. Zemin incelemesine göre, yeraltı suyu yoktur ve zeminde sıvılaşma riski bulunmamaktadır.

Ayrıca zemin incelemesi sırasında traverten tabakasının RQD değeri % 30 olarak belirlenmiş ve alınan 3 adet Traverten karot örnekleri üzerinde yapılan tek eksenli basınç deneyi sonucunda aşağıdaki dayanım değerleri elde edilmiştir :

SK1 Sondaj kuyusunun 5,0 m derinliğinden alınan karot örnek için : 9,91 MN/m²,

SK2 Sondaj kuyusunun 7,0 m derinliğinden alınan karot örnek için : 7,85 MN/m²,

SK5 Sondaj kuyusunun 7,0 m derinliğinden alınan karot örnek için :10,74 MN/m².

Buna göre, traverten tabakasının orta sertlikte kaya özelliklerine sahip olduğu görülmektedir.

Binadaki oturmaların zayıf zemin tabakalarının toplam kalınlığı ile orantılı olacağı açıktır. Buna göre, 24 cm' lik en büyük göreceli oturmanın 11,5 m toplam zayıf zemin tabakasına sahip kuzey-batı (C) köşesinde, 18 cm' lik ikinci büyük göreceli oturmaların 5,5 m kalınlığında toplam zayıf zemin tabakalarına sahip kuzey-doğu (D) ve güney-batı (A) köşelerinde ve en küçük oturmanın güney- doğu (B) köşesinde oluşacağı söylenebilir.

4. EĞİK BİNANIN DOĞRULTULARAK DESTEKLENMESİ İÇİN ÖNERİLER

Bina temel zemini ile ilgili yukarıda belirtilen bulguların ve değerlendirmelerin ışığı altında, binanın rehabilitasyonu için bilirkişi heyeti tarafından aşağıdaki öneriler yapılmıştır :

- 1) Bina temeli altındaki zayıf zemin tabakaları, bina taşıyıcı sistemi ve zemin özellikleri gözönünde tutularak belirlenecek uygun bir yöntemle ve bu konuda uzmanlaşmış bir firma tarafından uygulanacak bir doğrultma ve destekleme yöntemiyle, çok titiz bir çalışma sonucu binanın kullanılabilir duruma getirilmesi olanaklı görülmektedir.
- 2) Mal sahibinin isteğiyle, yazarın Teknik Danışmanlığını yaptığı BST Mühendislik Firmasınınca düzenlenerek Konyaaltı Belediyesi'ne sunulan, binanın jet grout tekniğiyle doğrultulması ve jet grout kolonları ile bina yüklerinin alttaki sağlam temel zemini tabakasına aktarılması projesi, binada ek zorlamalar oluşturmayacak biçimde titizlikle uygulandığı ve tarafsız bir kuruluş tarafından taşıma gücü için gerekli yüklemeye deneyleri yapılarak, olumlu sonuçlar elde edildiği taktirde, uygulamanın başarılı olacağı konusunda bilirkişi heyetinde genel bir kanaat oluşmuştur.
- 3) Binanın desteklenmesi nasıl yapılırsa yapılsın, sözkonusu uygulama tamamlandıktan sonra, oturma ve oturma farkları inşaat bitimine kadar (en az 3 ay süreyle) izlenmeli ve oturmaların tamamen durduğuna kanaat geldikten sonra iskan izni verilmelidir.

5. EĞİK BİNANIN DOĞRULTULMASI VE ALTTAN DESTEKLENMESİ YÖNTEMİNİN BELİRLENMESİ VE UYGULANMASI

5.1. Genel Bilgiler

Antalya-Konyaaltı ilçesi Atatürk Bulvarında inşa edilen 7 katlı konut binası kaba inşaatının tamamlanması aşamasında, temel altındaki farklı oturmalarından kaynaklanan eğiklik nedeniyle, Konyaaltı Belediyesi tarafından 24.04.1999 tarihinde inşaat durdurularak mühürlenmiştir. Bu arada mal sahibinin görevlendirdiği BST Mühendislik Firması Belediye İmar Müdürlüğüne, İMO Antalya Şubesi bilirkişi raporu doğrultusunda ve temel mühendisliği uzmanı olarak yazarın görüş ve önerilerini de dikkate alarak, sözkonusu binanın doğrultulması ve bina yüklerinin sağlam zemine aktarılması ile ilgili bir proje sunmuştur. Konyaaltı Belediyesi, İMO Antalya Şubesi Bilirkişi Raporundaki ve Akdeniz Üniversitesi-Mühendislik Fakültesi öğretim üyelerinin İMO Antalya Şubesi Bilirkişi Raporu'ndakilere paralel görüş ve önerilerine dayanarak, konuyu Belediye Encümeni gündemine taşımıştır. Konyaaltı Belediyesi Encümeni tarafından, İMO Antalya Şubesi Bilirkişisinin görüş ve önerileri doğrultusunda, eğik binanın doğrultulması ve bina yüklerinin jet grout kolonları ile sağlam zemine aktarılması projesinin kontrollü olarak uygulanmasına ve bu konuda uzman tarafsız bir kuruluşun ve Belediye teknik elemanlarının denetiminde yapılacak yükleme deneyleri sonuçlarının ilgili tarafsız kuruluş tarafından düzenlenecek olumlu bir raporun Belediye İmar Müdürlüğüne verilmesi koşuluyla, bina rehabilitasyon çalışmalarına izin verildiği belirtilmiştir.

5.2. Eğik Binanın Doğrultulması Çalışmaları

BST Mühendislik firmasının teknik danışmanı olarak Temel İnşaatı Uzmanı Yazar ve firma yetkilileri, firmanın ekipman olanaklarını da gözönüne alarak yapılan değerlendirmeler sonucunda, eğik binanın doğrultulması ve bina yüklerinin sağlam zemine aktarılması konusunda aşağıdaki yöntem ve aşamaları kararlaştırmışlardır :

- 1) Eğik binanın doğrultulması, temel altında az oturan zayıf zemin bölgelerine jet grout ekipmanı ile kontrollü bir biçimde yüksek basınçla su püskürtülerek zeminin dışarı atılmasıyla, hacminin küçültülüp temel oturmasının sağlanması,
- 2) Binanın 1/107 olan eğikliği, doğrultma çalışmaları ile 1/300 olan güvenli sınır altına çekildikten sonra, bina yükünün yeterli sayıda düzenlenecek jet grout kolonları ile sağlam zemine aktarılması çalışmalarına başlanması uygun görülmüştür,
- 3) Bina doğrultma uygulamasında, o aşamaya kadar oluşan gerçek oturma farkları ve destekleme uygulamasında toplam bina yükünün yeterli sayıda jet-grout kolonu ile doğrudan traverten (kaya) tabakasına aktarılması esas alınmıştır.

Dünya Literatüründeki bina doğrultma yöntemlerinin hemen hemen tümü, binanın fazla oturma yapan bölgesinden binayı çok sayıda hidrolik preslerle kaldırma prensibine dayanmaktadır. Bu yöntemde doğrultmanın sağlıklı ve başarılı olması için, yapı sisteminin ve temelin rijit ve taban alanının oldukça küçük olması gerekir. Doğrultulması istenen binanın taban boyutları oldukça büyük ($b_x=21.60$ m ve $b_y=13,95$ m) olan bir binadır. Bu binanın fazla oturan bölgelerinin hidrolik preslerle yalnızca temel kenarlarından (Temel

tabanı altına girilemeyeceğine göre) kaldırılması sırasında, temel plağında ve üst yapı sisteminde aşırı zorlanmalar ve hasarlar oluşması kaçınılmazdır.

Böyle bir binanın yapısal özelliklerine ve temel zemini koşullarına en uygun doğrultma yönteminin, az oturan bina bölgelerinin kontrollü olarak oturma yaptırılması ile binanın doğrultulması olduğuna karar verilmiştir. Binanın az oturma yapan bölgesinden zeminin kazılarak çıkartılması ile gerçekleştirilen bir doğrultma yöntemi, Zou (1996) [50] tarafından Çin 'de denenmiş olmasına karşın, jet grout yöntemiyle su püskürtülerek doğrultulma yöntemi, bildiğimiz kadarıyla Literatürde ilk kez uygulanmıştır. Bu yöntemle yapılacak bir bina doğrultulmasının uygun olacağı düşüncesine bizi yönlendiren üç nedenden birincisi, binanın oldukça rijit olan bir kirişli radye temele oturması, ikincisi 24 cm'lik maksimum oturma farkında bile taşıyıcı sistemde ve dolgu duvarlarda hiçbir çatlak ve aşırı zorlanma oluşmaması ve üçüncüsü ise oturma farklarının sağlam traverten tabakası ile temel tabanı arasındaki zayıf zemin tabakalarının toplam kalınlığının çok farklı (sağlam traverten tabakası üst yüzeyinin çok eğimli) olmasından kaynaklandığının kuşku duyulmaz bir biçimde belirlenmiş olmasıdır.

Şimdi esas konu, az oturma yapan bölgelerde bulunan zayıf zemin tabakalarının nasıl oturtulacağıdır. Bu amaçla geliştirilen çözüm, temel plağında açılan 60 mm çapındaki deliklerden Ø42 mm çapında olan jet grout tijinin zayıf zemin içine sokularak, memelerden 300 ila 350 bar basınçla zemine su püskürtülmesidir. Yüksek basınçlı su jeti sırasında, zemin tümüyle örselenerek ince daneler radye temelde açılan Ø60 mm çapındaki deliklerden su ile birlikte dışarı atılmaktadır. Bu zayıf zemin tabakalarını oturtulmasına yardımcı olan öteki bir önlem, bu bölgelerdeki zemin kat döşemesi üzerine, gerekli önlemler alınarak, uygun ölçüde ağırlık (safra) konulmasıdır.

Jet grout kolonlarının imalinde 42 mm çapında jet grout tiji kullanılmıştır. Bu Jet grout tijinin ucunda 2 adet 2 mm çapında püskürtme memesi bulunmaktadır. Zeminin örselenmesi ve ince danelerin temel plağında açılmış Ø60 mm'lik deliklerden dışarı atılması için, zayıf zemin tabakalarını derinliği boyunca yüksek basınçla su jeti püskürtülmüştür. Burada önemli olan nokta, su jeti ve döşeme üzerindeki ağırlıkla temelin oturması sağlanırken, temelin düzensel olarak oturması ve temelde önemli ölçüde kasıntı ve deformasyon oluşmamasıdır. Bu amaçla elimizde üç olanak bulunmaktadır: Birincisi zemine püskürtülecek su jetinin fazla oturma yaptırılacak bölgelerde daha çok sayıda ve az oturma yaptırılacak bölgelerde daha az sayıda uygulanması, ikincisi tijin fazla oturma yaptırılacak bölgelerde daha uzun süreli (tijin çok sayıda batırılıp çekilmesiyle) ve az oturma yaptırılacak bölgelerde daha kısa süreli uygulanmasıdır. Üçüncü olanak ise, işlem sırasında temel plağı üzerinde sık sık oturma kontrollerinin yapılmasıdır. Bu belirlemelerin ışığı altında, jet grout yöntemiyle yüksek basınçlı su püskürtülerek zemine oturma yaptırılmasında aşağıdaki gibi hareket edilmiştir:

Jet grout yöntemiyle su püskürtmeye başlamadan önce, fazla oturma yapan C köşesine komşu temel plağı kenarlarının fazla oturan bölgeleri, çalışmalar sırasında daha fazla oturmaması için, 2 sıra jet grout kolonu ile oturma yapamayacak şekilde askıya alınarak desteklenmiştir. Daha sonra, üst yapıdan gelen kolon yüklerinin yoğunluğuna uygun olarak açılan deliklerden zemine sokulan jet grout tiji ile, B köşesinden C köşesine doğru dalgalar halinde pek çok kez tekrar edilerek, kademe kademe yüksek basınçlı su püskürtülmüştür. Yukarıda da belirtildiği gibi, su püskürtme işlemi, fazla oturma yaptırılması gereken bölgelerde, jet grout tijinin zemine çok sayıda uygulanması ve çok sayıda sokulup çekilmesi ile gerçekleştirilmiştir. Bu

işlemlerin her aşamasında, oturmalar temel plağı üzerindeki kot okumaları ile sık sık kontrol edilerek jet grout yöntemiyle su püskürtme işlemi buna göre yönlendirilmiştir.

Eğik binaların doğrultulması sırasında, gözden kaçırılmaması gereken çok önemli bir nokta daha vardır. Çok eğimli kaya üst yüzeyi üzerinde çok fazla sıkışabilen zayıf zemin tabakalarının bulunduğu temel zeminine oturan binalarda, oturma ve oturma farkları temel plağı dökülür dökülmez başlamakta ve her yeni imalat yükünün eklenmesiyle artmaya devam etmektedir. Bu binada asansör boşluğu iskeletinin imal edildiği aşamada, 7 cm'lik bir oturma farkı bulunduğu ölçmeler sonucunda belirlenmiştir. Kat döşemelerinin tesviye betonları ve asansör rayları bu eğikliğe göre düzenlendiği için, bina temeli oturma farkı sıfır olacak şekilde doğrultulursa, asansör raylarında ters tarafa doğru 7 cm'lik bir eğiklik oluşacak ve bu eğiklikten dolayı asansör normal çalışamaz duruma gelecektir. Bu dedenle temelin B ve C köşeleri arasındaki oturma farkı sıfır olduğunda değil, $(24 - 17) = 7$ cm olduğunda doğrultma işlemine son verilmiştir. Bu durumda açılacak eğiklik :

$$\tan \alpha = 7 \text{ cm} / 2571 \text{ cm} = 0,0027 = 1/367 < 1/300 \quad (3)$$

olduğundan, doğrultma işlemi sonucu eğiklik, izin verilen sınırın altına düşürülmüştür.

Temel plağı üzerinde yapılan kot okumaları ile, doğrultmanın hedeflenen düzeye geldiği anlaşıldıktan sonra, içine su püskürtülen zayıf zemin tabakalarının kuruması için çalışmalara birkaç gün ara verilmesinde yarar vardır.

5.3. Bina Temelinin Sağlam Zemine Kadar Jet Grout Kolonları ile Desteklenmesi

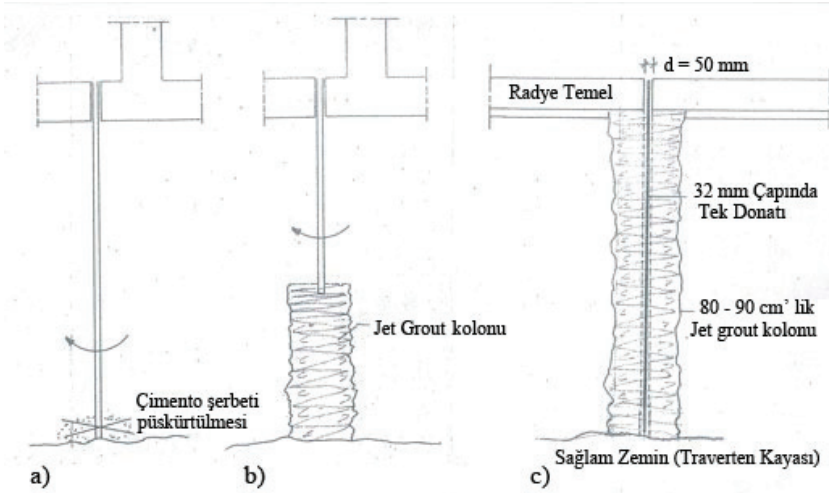
Şimdi su jeti için açılan deliklerden, sağlam temel zemini (traverten) tabakasına kadar uzanan jet grout kolonları ile bina yükünün sağlam zemine aktarılması gerekmektedir (bkz. Şekil 3).

Binanın kat tabiyesi yükü (BA karkas + Dolgu duvarlar + Döşeme kaplaması + sıva ağırlığı ve hareketli yük dahil) $13,0 \text{ kN/m}^2$ alınır, toplam bina yükü aşağıdaki gibi hesaplanır :

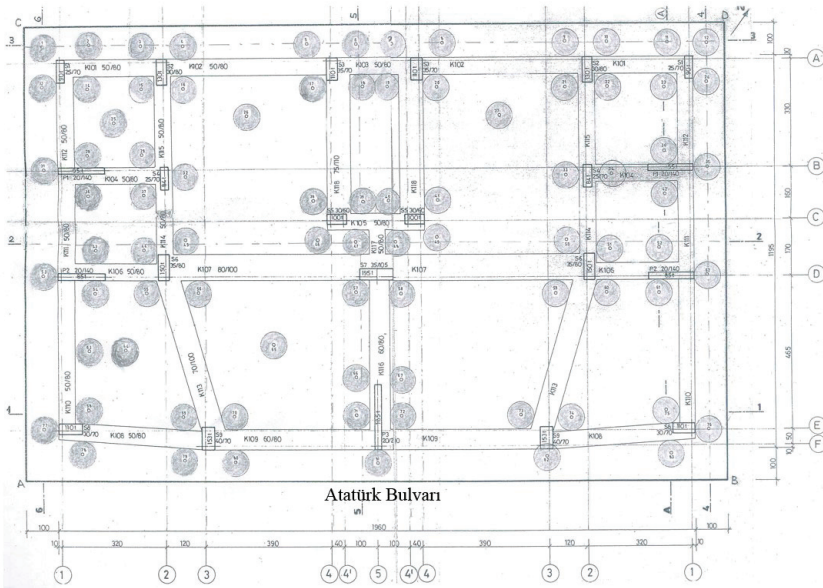
$$P_{\text{top}} = 13,0 \times 7,5 \times (21,60 \times 13,95) = 29\,379 \text{ kN} = 29,379 \text{ MN} \quad (4)$$

Bu yükün sağlam temel zeminine (traverten tabakasına) aktarılabilmesi için, 83 adet düşey jet grout kolonu imal edilmiştir. Toplam yükün jet grout kolonlarına eşit dağılmayabileceği gözönüne alınarak, en büyük jet grout kolonu yükü % 10 artırılarak : $1,10 \times 29\,379/83 \approx 400 \text{ kN}$ olarak belirlenmiştir. Traverten tabakası ile radye tabanı arasındaki zayıf zemin tabakalarının hiçbir yük taşımadığı varsayılmıştır. Jet grout kolonlarının çapı zemin türüne göre 60 cm ile 90 cm arasında, uzunlukları ise 4 m ile 14 m arasında gerçekleştirilmiştir. Zemin incelemesinde traverten tabakasının en derin noktası C köşesinde 11,5 m derinlikte gösterilmiştir. İmalat sırasında 14 m uzunluğunda jet grout kolonunun gerçekleşmiş olması, traverten üst yüzeyinin düzlemsel olmadığı, yer yer çukurluklar bulunduğu anlamına gelmektedir.

Bina temeli altındaki jet grout kolonları imalatına başlamadan önce, bina dışındaki arazide deneme amaçlı jet grout kolonları imal edilmiş ve başarılı sonuçlar elde edilmiştir. Jet grout kolonlarının imali için, 2 mm çapında 2 adet püskürtme memesi kullanılmış ve meme aralıkları 2,5 cm seçilmiştir. Püskürtülecek çimento şerbetinin su/çimento oranı 1/1 olarak ve sistem basıncı 300 ila 350 bar olarak seçilmiştir. Jet grout tijinin dönüş hızı 15 devir/dakika olarak alınmış ve tijin çekilmesi otomatik olarak 4 cm'lik kademelerle gerçekleştirilmiştir.



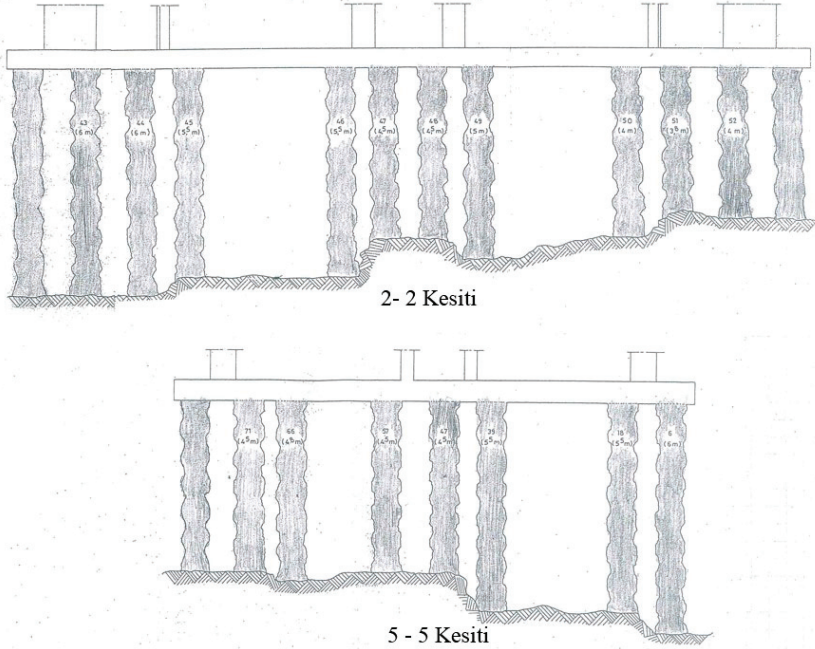
Şekil 3 - Bina içinde yapılan jet grout kolonu çalışmalarının imalat aşamaları



Şekil 4 - Temel planı üzerinde jet grout kolonlarının yerlerinin ve sıra numaralarının gösterilişi

Şekil 4'de radye temel planı üzerinde jet grout kolonlarının yerleri ve sıra numaraları gösterilmiştir (Fazla oturma yapan temel bölgesi kenarlarında düzenlenen 2 sıra kolon dahil). Ayrıca x doğrultusunda 2-2 kesitinde ve y doğrultusunda 5-5 kesitinde düzenlenen jet grout kolonlarının yandan görünüşü, çapları ve boyları ile birlikte şekil 5 'te gösterilmiştir.

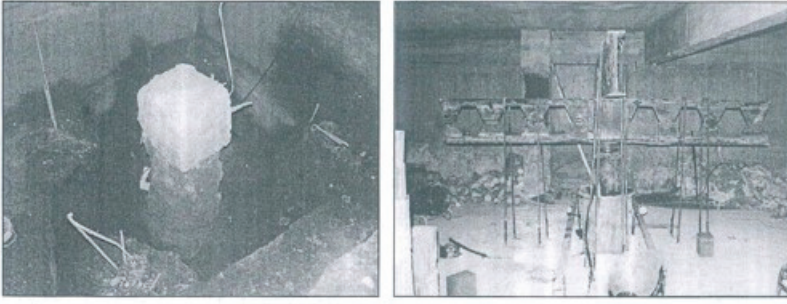
Temel planında radye temel altına jet grout kolonlarının yerleştirilmesinde, radye temelin eğilme zorlanmalarını düşük tutmak için, jet grout kolonlarını bodrum kattaki üst yapı kolonlarının etki bölgelerinde yoğunlaştırılmasına ve kolon yüklerine uygun sayıda jet grout kolonu düzenlenmesine dikkat edilmelidir. Burada Temel tabanı altından sağlam zemin tabakasına kadar düşey jet grout kolonlarından oluşturulan bu destekleme sistemi, boşlukta düzenlendiğinde çoğunlukla kararsız dengeye sahip bir statik sistem oluşturmasına karşın, jet grout sütunları ile iyileştirilmiş zayıf zemin içinde yatay kuvvetlerin, zeminin toprak direnci ile karşılanması sonucu stabil bir sistem olarak alınabilir.



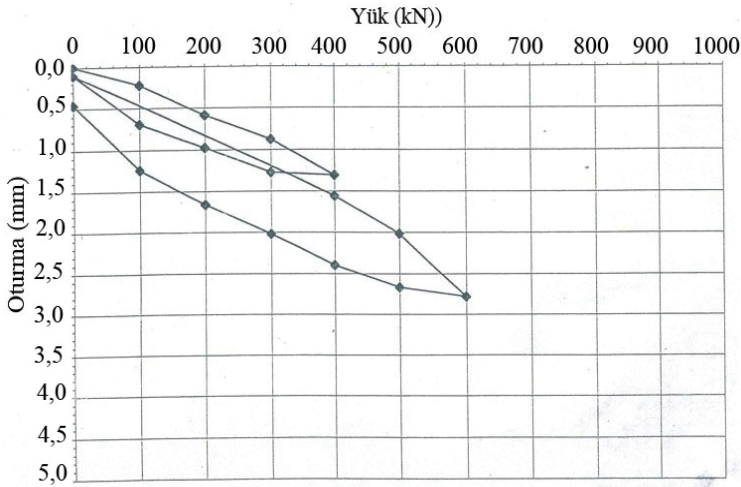
Şekil 5 - x Doğrultusundaki 2-2 kesitinde ve y doğrultusundaki 5-5 kesitindeki jet grout kolonlarının numaraları ve temel plağı tabanı ile traverten tabakası üst yüzeyi arasındaki yükseklikleri

6. BİNANIN DESTEKLENMESİ İÇİN İMAL EDİLEN JET GROUT KOLONLARININ YÜKLEME DENEYİ İLE TAŞIMA GÜCÜNÜN KONTROLÜ

Antalya-Konyaaltı ilçesindeki 7 katlı eğik konut binasının doğrultma ve destekleme çalışmaları tamamlandıktan sonra, BST Mühendislik firması tarafından uygulaması yapılan temel destekleme projesinde, imal edilen jet grout kolonlarının hedeflenen taşıma gücünü doğrulamak amacıyla, konunun uzmanı tarafsız bir kurum (YTÜ, İnş. Fak., Geoteknik Dalı) tarafından, binada oturmanın en fazla olduğu temel köşesinde (C köşesinde) jet grout kolonları ile çevrilmiş alanın ortasındaki jet grout kolonunda bir yükleme deneyi gerçekleştirilmiştir (bkz. Şekil 6 a ve 6 b).



Şekil 6 - a) Desteklenen binanın temel tabanı altında imal edilmiş jet grout kolonu (BST Mühendislik Firm.) b) Desteklenen binanın temeli altında imal edilmiş bir jet grout kolonu üzerinde yapılan yükleme deneyi



Şekil 7 - Bir jet grout kolonu üzerinde yapılan yükleme deneyinin Yük-Oturma eğrisi

Proje kazıkları için CIRIA (1985)' de belirtilen aşamalarla gerçekleştirilen bu deneyde, jet grout kolonu başının deplasmanı, 0,01 mm duyarlılığı olan saatler yardımıyla ölçülmüş ve deplasman değeri, okuma değerleri ortalaması olarak alınmıştır. Şekil 7'de gösterildiği üzere, birinci çevrimde proje yükü olan yaklaşık 400 kN 'da toplam oturma 1,3 mm ve kalıcı oturma 0,1 mm, proje yükünün 1,5 katında (600 kN 'luk yükleme altında) ise toplam oturma 2,8 mm ve kalıcı oturma 0,5 mm olarak gözlenmiştir. Bu değerler, yükleme deneyini gerçekleştirilen ve elde edilen sonuçları 08.06.2000 tarihinde düzenlenen bir Raporla Konyaaltı Belediyesi-İmar Müdürlüğüne sunan tarafsız kurum tarafından, jet grout kolonları için öngörülen 400 kN 'luk proje yükünün güvenle taşınabileceği şeklinde yorumlanmıştır.

Konut binasının doğrultulması ve bina temelinin desteklenmesi işinin tamamlanmasından başlayarak, işin sonuna kadar (en az 3 ay süreyle) periyodik ölçümler yapılarak, binada hiçbir

oturma ve oturma farkı olmadığı saptanmış ve Konyaaltı Belediyesi İmar Müdürlüğü'ne yazılı olarak bildirilmiştir. Ancak Belediye, ondan sonra binaya iskan ruhsatı vermiştir. Ayrıca binaya ilişkin doğrultma, destekleme ve yükleme deneyi çalışmalarının tamamlanma tarihi olan Haziran 2000 tarihinden sonra, kontrol aralıkları giderek artırılmak suretiyle 2022 yılı sonuna kadar izlenmiş ve binada hiçbir oturma ve oturma farkı oluşmadığı saptanmıştır.

7. SONUÇLAR

Varolan zemin ve yapı sistemi koşulları altında, jet grout yöntemiyle eğik bir binanın doğrultulması ve desteklenmesi uygulamasından çok başarılı bir sonuç elde edilmiştir. Uygulamanın başarısında, öncelikle çok titiz ve kontrollü çalışmanın büyük payı olduğu açıktır. Bunun dışında, uygulamanın öngörülen hedefleri sağlayıp başarılı olmasının diğer önemli iki nedeni ;

- 1) Bina eğikliğinin neden kaynaklandığının çok açık bir biçimde belirlenmiş olması,
- 2) Temel sisteminin üst yapı ile birlikte rijit bir toplam sistem oluşturması sonucu, binanın oturma farklarından dolayı zemin üzerinde rijit bir dönme yapması ve bu dönme sırasında taşıyıcı sistemde ve dolgu duvarlarda hiçbir çatlama ve aşırı zorlanma ortaya çıkmamasıdır.

Binanın jet grout yöntemiyle doğrultulup desteklenmesiyle kazanılması, çok ekonomik ve rasyonel bir çözüm olmuştur. Eğer sözkonusu bina jet grout yöntemiyle başarılı ve güvenli bir biçimde doğrultulup desteklenmeseydi, kaba inşaatı tamamlanmış bina için ilgili Belediye tarafından yıkılma kararı alınıp kesinlikle yıkılacaktı. Binanın kaba inşaatının tamamlanması aşamasında yıkılıp yeniden yapılması, yaklaşık 540 000 \$ 'lık milli servetin yok olması dışında, yaklaşık bir yıllık zaman kaybına neden olacaktı. Ayrıca mal sahibi veya yüklenici, binadan inşaat aşamasında daire satın alan şahısların haklı yasal talepleriyle karşı karşıya kalacaktı.

Kaynaklar

- [1] Baumann, V./Samol, E. (1980) -Soilcrete-Verfahren-Hochdruckinjektion zur Lastübertragung und Abdichtung in fein-und grobkörnigen Bodenschichten. Vortraege Baugrundtagung Mainz, S. 437 – 463.
- [2] Bijerrum, L – Allowable settlemente of structures Geot. Inst. Oslo 198 (1973)
- [3] Brandl, H. (1989) – Underpinning. Proc. 12 th ICSMFE Bio de Janerio, S. 2 227 –2 258.
- [4] Brandl, H. (1992) – Fundamentsicherung einsturzgefaehrder Brücken. Vortage Baugrundtagung Dresden, S. 256 – 280.
- [5] Cambefort, H. (1969) – Bodeninjektionstechnik. Deutsche Übersetzung von K. Back nach der Französischen Ausgabe von 1964. Wiesbaden : Bauverlag.
- [6] Gravert, F. W. (1975) – Ein Beitrag zur Gründung von Hochhaeusern auf bindigen Boden. Deutsch Konferenz Hochhaeuser, Int. Verein Brückenbau Hochbau (IVBH).

- [7] Greenwood, D. (1987) – Underpinning by grouting. *Ground Engineering* 20, S. 21 – 30.
- [8] Köseoğlu, S. (2017) – Temeller II-Statığı ve Konstrüksiyonu, Lord Matbaası-İstanbul.
- [9] Marinas, P.G. /Koukis, G.C. (1988) – The Engineering Geology of Ancient Works, Monuments and Historical Sites. Proc.INT. Symposium Athen. Ed. Balkema.
- [10] Meissner, H./Petersen, H. (1990) – Einpresstechniken zur Erddruckerhöhung und zum Anheben von Bauwerken. *Bauingenieur* 65, S. 83 – 89.
- [11] Polshin/Tokar – Maximum allowable nonuniform settlement of structures Proc. IV. Int. Conf. Soil Mech. London 1957, Bd I S. 402-405.
- [12] Raabe, E.W./Ersters, K. (1986) – Injektionstechniken von Stillsetzung und zum Rückstellen von Bauwerksetzungen. *Vortraege der Baugrundtagung Hamburg*,
- [13] Schubert, A./v.SooS,P. (1990) – Schadenrisiken beim Einsatz des Jet-Grouting-Verfahrens. 5. Christian Veder Kolloqium Graz, 15 S.
- [14] Skempton/Mc Donald – Settlement of building Proc. Inst. Civ. Eng. London 5 (1956)..
- [15] Smolczyk, U. (1981) – Saving Old Cites. General Report Sees 9, x. ICSMFE Stockh.
- [16] Smolczyk, U. (1992) –Grundbau-Taschenbuch (1992), Teil 3, Kapitel 2.3, S. 87-107.
- [17] Sommer, H. (1976) – Setzung von Hochhaeusern und benachbarter flachen Anbauten nach Theorie und Messung. *Vortrage Baugrundtagung Nürnberg*, S. 141 – 169. Deutsch Gesellschaft für Erd-und Grundbau, Essen
- [18] Stockhammer, P. (1990) – Aisführung der Hochdruckboden vermörtelung nach dem Soilcrete-Verfahren. 5. Christian-Veder-Kolloqium Graz, 15 S.
- [19] Zou, Y. (1996) – Ein neues Verfahren zum Aufrichten geneigter Gebaeude, *Bautechnik* 73, 437 – 442.

Standartlar ve Yönetmelikler

- [1] DIN 4123 (2013) – Ausschachtungen, Gründungen und Unterfangungen, im Bereich bestehender Gebaeude.
- [2] DIN 4124 (2012) – Baugruben und Graeben-Böschungen, Verbau, Arbeitsraumbreiten.
- [3] Türkiye Bina Deprem Yönetmeliği (TBDY-2018).
- [4] TS 500 (2000) – Betonarme Yapıların Tasarım ve Yapım Kuralları

Turkish Journal of Civil Engineering (formerly Teknik Dergi)

Manuscript Drafting Rules

1. The whole manuscript (text, charts, equations, drawings etc.) should be arranged in Word and submitted in ready to print format. The article should be typed on A4 (210 x 297 mm) size paper using 10 pt (main title 15 pt) Times New Roman font, single spacing. Margins should be 40 mm on the left and right sides and 52.5 mm at the top and bottom of the page.
2. Including drawings and tables, articles should not exceed 25 pages, technical notes 10 pages.
3. Your contributed manuscript must be sent over the DergiPark system. (<http://dergipark.gov.tr/tekderg>)
4. The text must be written in a clear and understandable language, conform to the grammar rules. Third singular person and passive tense must be used, and no inverted sentences should be contained.
5. Title must be short (10 words maximum) and clear, and reflect the content of the paper.
6. Sections should be arranged as: (i) abstract and keywords, (ii) title, abstract and keywords in the other language, (iii) main text, (iv) symbols, (v) acknowledgements (if required) and (vi) references.
7. Both abstracts should briefly describe the object, scope, method and conclusions of the work and should not exceed 100 words. If necessary, abstracts may be re-written without consulting the author. At least three keywords must be given. Titles, abstracts and keywords must be fitted in the first page leaving ten line space at the bottom of the first page and the main text must start in the second page.
8. Section and sub-section titles must be numbered complying with the standard TS1212.
9. Symbols must conform to the international rules; each symbol must be defined where it appears first, additionally, a list of symbols must be given in alphabetic order (first Latin, then Greek alphabets) at the end of the text (before References).
10. Equations must be numbered and these numbers must be shown in brackets at the end of the line.
11. Tables, drawings and photographs must be placed inside the text, each one should have a number and title and titles should be written above the tables and below the drawings and photographs.
12. Only SI units must be used in the manuscripts.
13. Quotes must be given in inverted commas and the source must be indicated with a reference number.
14. Acknowledgement must be short and mention the people/ institutions contributed or assisted the study.
15. References must be numbered (in brackets) in the text referring to the reference list arranged in the order of appearance in the text. References must include the following information:

If the reference is an article: Author's surname, his/her initials, other authors, full title of the article, name of the journal, volume, issue, starting and ending pages, year of publication.

Example : Naghdi, P. M., Kalnins, A., On Vibrations of Elastic Spherical Shells. J. Appl. Mech., 29, 65-72, 1962.

If the reference is a book: Author's surname, his/her initials, other authors, title of the book, volume number, editor if available, place of publication, year of publication.

Example : Kraus. H., Thin Elastic Shells, New York. Wiley, 1967.

If the reference is a conference paper: Author's surname, his/her initials, other authors, title of the paper, title of the conference, location and year.

If the source is a thesis: Author's surname, his/her initials, thesis title, level, university, year.

If the source is a report: Author's surname, his/her initials, other authors, title of the report, type, number, institution it is submitted to, publication place, year.
16. Discussions to an article published in Turkish Journal of Civil Engineering (formerly Teknik Dergi) should not exceed two pages, must briefly express the addressed points, must criticize the content, not the author and must be written in a polite language. Authors' closing remarks must also follow the above rules.
17. A separate note should accompany the manuscript. The note should include, (i) authors' names, business and home addresses and phone numbers, (ii) brief resumes of the authors and (iii) a statement "I declare in honesty that this article is the product of a genuinely original study and that a similar version of the article has not been previously published anywhere else" signed by all authors.
18. Copyright has to be transferred to UCTEA Turkish Chamber of Civil Engineers. The standard copyright form signed by the authorised author should therefore be submitted together with the manuscript.



UCTEA Turkish Chamber of Civil Engineers

TMMOB İnşaat Mühendisleri Odası

Necatibey St. No: 57, Kızılay, Ankara / Türkiye

Tel: +90.312.294 30 00 - Faks: 294 30 88

www.imo.org.tr